SAIMM
JOURNAL OF THE SOUTHERN AFRICAN INSTITUTE OF MINING AND METALLURGY
FOUNDED 1894
VOLUME 118 NO. 5 MAY 2018

We are World Leaders in Slurry Systems Engineering
www.PatersonCooke.com

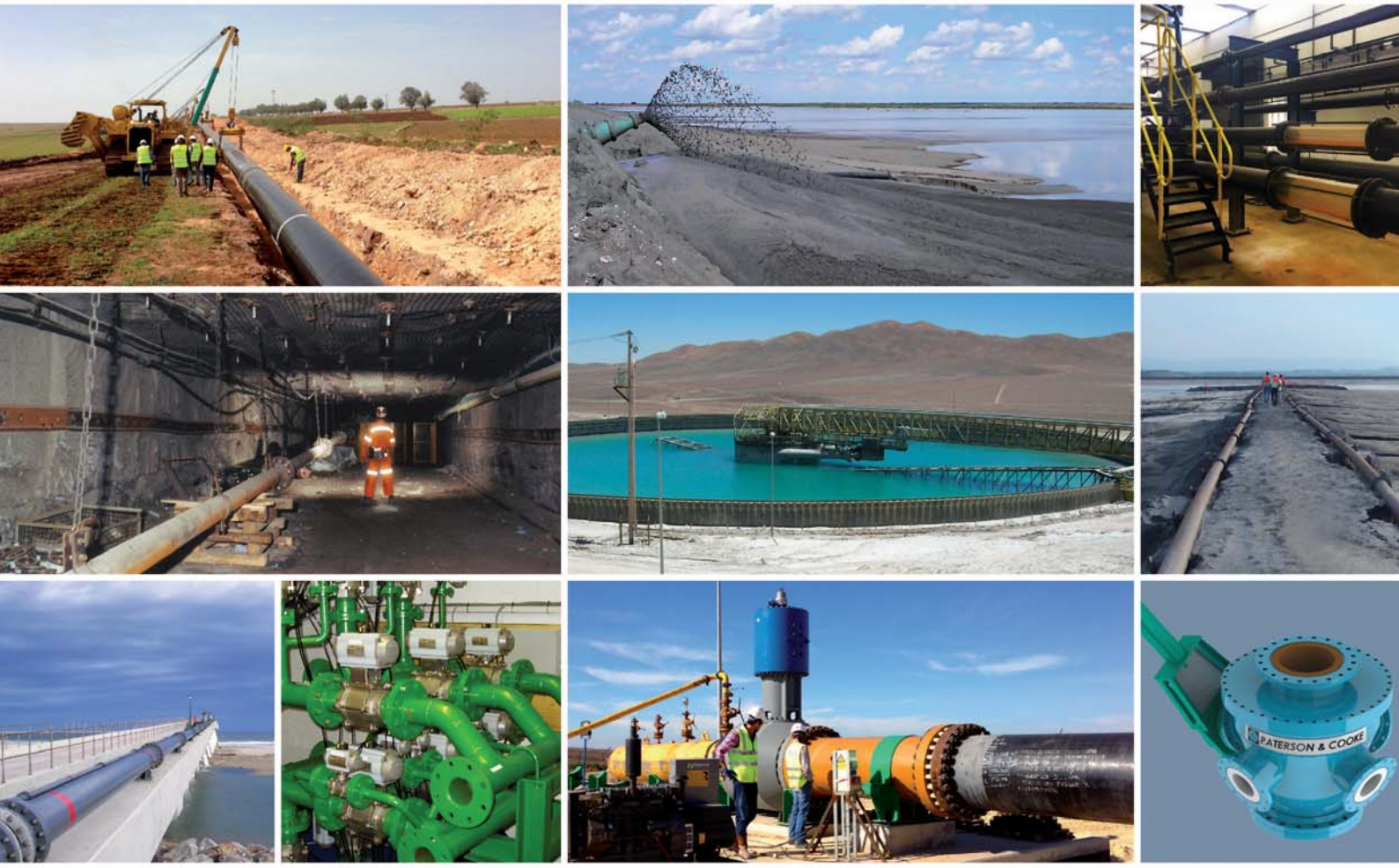

PATERSON & COOKE
ESTABLISHED 1991

We are World Leaders in Slurry Systems Engineering

www.PatersonCooke.com

- Long Distance Slurry Pipelines
- Tailings
- Mine Backfill
- Slurry & Process Test Work
- Process Engineering
- Specialist Engineering
- Marine & Coastal
- Field Services
- Specialised Products
- Hydraulic Ore Hoisting
- Courses

Paterson & Cooke has extensive experience in designing long distance slurry pipelines, conventional and paste tailings pipeline systems and mine backfill and paste plant systems. Together, our engineers have been involved in engineering many of the long distance slurry pipeline systems operating throughout the world today, and have been at the forefront of advancing high density thickened and paste tailings pumping systems in water scarce regions.

Deep mine backfilling technology has been a core expertise of Paterson & Cooke since we began in 1991, and our knowledge of mining and backfill support requirements, supported by our extensive network of laboratories, means we design mine backfill and paste fill systems that are specifically tailored to each application.

We undertake all phases of systems engineering, from process test work, studies to detail design, construction support, commissioning and operator training.

- AUSTRALIA (Perth)
- CANADA (Sudbury, Calgary, Vancouver)
- CHILE (Santiago)
- SOUTH AFRICA (Cape Town, Johannesburg)
- UNITED KINGDOM (Cornwall)
- USA (Denver)

PATERSON & COOKE

ESTABLISHED 1991

Our key strength is the intellect, commitment and creativity of the people who work for Paterson & Cooke

Proposed book

The story of the decline of the South African mining industry

Ian Robinson

Rob Croll

Two authors with extensive experience in the South African mining industry, Rob Croll and Ian Robinson, are embarking on writing a book describing the current situation in the South African mining industry and the story of the transformation of the industry from its status as a world mining superpower in 1980 to a shadow of its former self.

The book will tell the story of the evolution of the South African mining industry since 1980 and recount personal experiences and opinions of people who have played important roles in the industry.

The industry is in a state of anarchy. Former prosperous mining towns have become ghost towns; illegal miners scavenge abandoned mines; companies with political connections strip mining properties with impunity; labour disputes have degenerated into strife and violence; environmental degradation in the Mpumalanga coalfields and Witwatersrand Basin has polluted the soil and water and threatens the health of local communities.

The industry is also in a state of paralysis. Mining's contribution to national GDP fell to 6,6% in 2017 compared with 19,4% in 1980 and the number of employees on South African mines has nearly halved from a peak of 829 235 in 1986 to 455 109 in 2017. At a mining conference in Perth, Australia in October 2017 CEO of the Minerals Council (formerly Chamber of Mines), Roger Baxter said that mining companies in South Africa had essentially frozen all investments in the country because of policy and regulatory uncertainty. There has been no major mineral discovery in South Africa since the Venetia diamond deposits in the 1980s.

We invite suggestions and contributions from SAIMM members.

Contact the authors:

Ian Robinson: irob@mweb.co.za · Rob Croll: robcmas@netactive.co.za

OFFICE BEARERS AND COUNCIL FOR THE 2017/2018 SESSION

Honorary President
Mxolisi Donald Mbuyisa Mgojo
President, Minerals Council South Africa

Honorary Vice-Presidents
Samson Gwede Mantashe
Minister of Mineral Resources, South Africa

Rob Davies
Minister of Trade and Industry, South Africa

Mmamoloko Kubayi-Ngubane
Minister of Science and Technology, South Africa

President
S. Ndlovu

President Elect
A.S. Macfarlane

Senior Vice-President
M.I. Mthenjane

Junior Vice-President
Z. Botha

Immediate Past President
C. Musingwini

Honorary Treasurer
J.L. Porter

Ordinary Members on Council

V.G. Duke
I.J. Geldenhuys
M.F. Handley
W.C. Joughin
E. Matinde
M. Motuku
D.D. Munro
G. Njowa
S.M Rupprecht
A.G. Smith
M.H. Solomon
D. Tudor
D.J. van Niekerk
A.T. van Zyl

Past Presidents Serving on Council

N.A. Barcza
R.D. Beck
J.R. Dixon
M. Dworzanowski
H.E. James
R.T. Jones
G.V.R. Landman
R.G.B. Pickering
S.J. Ramokgopa
M.H. Rogers
D.A.J. Ross-Watt
G.L. Smith
W.H. van Niekerk
R.P.H. Willis

G.R. Lane–TPC Mining Chairperson
Z. Botha–TPC Metallurgy Chairperson

A.S. Nhleko–YPC Chairperson
K.M. Letsoalo–YPC Vice-Chairperson

Branch Chairpersons

Botswana	L.E. Dimbungu
DRC	S. Maleba
Johannesburg	J.A. Luckmann
Namibia	N.M. Namate
Northern Cape	W.J. Mans
Pretoria	R.J. Mostert
Western Cape	R.D. Beck
Zambia	D. Muma
Zimbabwe	S. Matutu
Zululand	C.W. Mienie

Corresponding Members of Council

Australia:	I.J. Corrans, R.J. Dippenaar, A. Croll, C. Workman-Davies
Austria:	H. Wagner
Botswana:	S.D. Williams
United Kingdom:	J.J.L. Cilliers, N.A. Barcza
USA:	J-M.M. Rendu, P.C. Pistorius

PAST PRESIDENTS

*Deceased

* W. Bettel (1894–1895)
* A.F. Crosse (1895–1896)
* W.R. Feldtmann (1896–1897)
* C. Butters (1897–1898)
* J. Loevy (1898–1899)
* J.R. Williams (1899–1903)
* S.H. Pearce (1903–1904)
* W.A. Caldecott (1904–1905)
* W. Cullen (1905–1906)
* E.H. Johnson (1906–1907)
* J. Yates (1907–1908)
* R.G. Bevington (1908–1909)
* A. McA. Johnston (1909–1910)
* J. Moir (1910–1911)
* C.B. Saner (1911–1912)
* W.R. Dowling (1912–1913)
* A. Richardson (1913–1914)
* G.H. Stanley (1914–1915)
* J.E. Thomas (1915–1916)
* J.A. Wilkinson (1916–1917)
* G. Hildick-Smith (1917–1918)
* H.S. Meyer (1918–1919)
* J. Gray (1919–1920)
* J. Chilton (1920–1921)
* F. Wartenweiler (1921–1922)
* G.A. Watermeyer (1922–1923)
* F.W. Watson (1923–1924)
* C.J. Gray (1924–1925)
* H.A. White (1925–1926)
* H.R. Adam (1926–1927)
* Sir Robert Kotze (1927–1928)
* J.A. Woodburn (1928–1929)
* H. Pirow (1929–1930)
* J. Henderson (1930–1931)
* A. King (1931–1932)
* V. Nimmo-Dewar (1932–1933)
* P.N. Lategan (1933–1934)
* E.C. Ranson (1934–1935)
* R.A. Flugge-De-Smidt (1935–1936)
* T.K. Prentice (1936–1937)
* R.S.G. Stokes (1937–1938)
* P.E. Hall (1938–1939)
* E.H.A. Joseph (1939–1940)
* J.H. Dobson (1940–1941)
* Theo Meyer (1941–1942)
* John V. Muller (1942–1943)
* C. Biccard Jeppe (1943–1944)
* P.J. Louis Bok (1944–1945)
* J.T. McIntyre (1945–1946)
* M. Falcon (1946–1947)
* A. Clemens (1947–1948)
* F.G. Hill (1948–1949)
* O.A.E. Jackson (1949–1950)
* W.E. Gooday (1950–1951)
* C.J. Irving (1951–1952)
* D.D. Stitt (1952–1953)
* M.C.G. Meyer (1953–1954)
* L.A. Bushell (1954–1955)
* H. Britten (1955–1956)
* Wm. Bleloch (1956–1957)
* H. Simon (1957–1958)
* M. Barcza (1958–1959)
* R.J. Adamson (1959–1960)
* W.S. Findlay (1960–1961)
* D.G. Maxwell (1961–1962)
* J. de V. Lambrechts (1962–1963)
* J.F. Reid (1963–1964)
* D.M. Jamieson (1964–1965)
* H.E. Cross (1965–1966)
* D. Gordon Jones (1966–1967)
* P. Lambooy (1967–1968)
* R.C.J. Goode (1968–1969)
* J.K.E. Douglas (1969–1970)
* V.C. Robinson (1970–1971)
* D.D. Howat (1971–1972)
* J.P. Hugo (1972–1973)
* P.W.J. van Rensburg (1973–1974)
* R.P. Plewman (1974–1975)
* R.E. Robinson (1975–1976)
* M.D.G. Salamon (1976–1977)
* P.A. Von Wielligh (1977–1978)
* M.G. Atmore (1978–1979)
* D.A. Viljoen (1979–1980)
* P.R. Jochens (1980–1981)
G.Y. Nisbet (1981–1982)
A.N. Brown (1982–1983)
* R.P. King (1983–1984)
J.D. Austin (1984–1985)
H.E. James (1985–1986)
H. Wagner (1986–1987)
* B.C. Alberts (1987–1988)
C.E. Fivaz (1988–1989)
O.K.H. Steffen (1989–1990)
* H.G. Mosenthal (1990–1991)
R.D. Beck (1991–1992)
* J.P. Hoffman (1992–1993)
* H. Scott-Russell (1993–1994)
J.A. Cruise (1994–1995)
D.A.J. Ross-Watt (1995–1996)
N.A. Barcza (1996–1997)
* R.P. Mohring (1997–1998)
J.R. Dixon (1998–1999)
M.H. Rogers (1999–2000)
L.A. Cramer (2000–2001)
* A.A.B. Douglas (2001–2002)
S.J. Ramokgopa (2002-2003)
T.R. Stacey (2003–2004)
F.M.G. Egerton (2004–2005)
W.H. van Niekerk (2005–2006)
R.P.H. Willis (2006–2007)
R.G.B. Pickering (2007–2008)
A.M. Garbers-Craig (2008–2009)
J.C. Ngoma (2009–2010)
G.V.R. Landman (2010–2011)
J.N. van der Merwe (2011–2012)
G.L. Smith (2012–2013)
M. Dworzanowski (2013–2014)
J.L. Porter (2014–2015)
R.T. Jones (2015–2016)
C. Musingwini (2016–2017)

Honorary Legal Advisers
Scop Incorporated

Auditors
Genesis Chartered Accountants

Secretaries
The Southern African Institute of Mining and Metallurgy
Fifth Floor, Minerals Council South Africa Building
5 Hollard Street, Johannesburg 2001 • P.O. Box 61127, Marshalltown 2107
Telephone (011) 834-1273/7 • Fax (011) 838-5923 or (011) 833-8156
E-mail: journal@saimm.co.za

Editorial Board
R.D. Beck
P. den Hoed
M. Dworzanowski
B. Genc
M.F. Handley
R.T. Jones
W.C. Joughin
H. Lodewijks
J.A. Luckmann
C. Musingwini
S. Ndlovu
J.H. Potgieter
N. Rampersad
T.R. Stacey
M. Tlala

Editorial Consultant
D. Tudor

Typeset and Published by
The Southern African Institute of Mining and Metallurgy
P.O. Box 61127
Marshalltown 2107
Telephone (011) 834-1273/7
Fax (011) 838-5923
E-mail: journal@saimm.co.za

Printed by
Camera Press, Johannesburg

Advertising Representative
Barbara Spence
Avenue Advertising
Telephone (011) 463-7940
E-mail: barbara@avenue.co.za

ISSN 2225-6253 (print)
ISSN 2411-9717 (online)

Directory of Open Access Journals

THE INSTITUTE, AS A BODY, IS NOT RESPONSIBLE FOR THE STATEMENTS AND OPINIONS ADVANCED IN ANY OF ITS PUBLICATIONS.

Copyright© 2018 by The Southern African Institute of Mining and Metallurgy. All rights reserved. Multiple copying of the contents of this publication or parts thereof without permission is in breach of copyright, but permission is hereby given for the copying of titles and abstracts of papers and names of authors. Permission to copy illustrations and short extracts from the text of individual contributions is usually given upon written application to the Institute, provided that the source (and where appropriate, the copyright) is acknowledged. Apart from any fair dealing for the purposes of review or criticism under ***The Copyright Act no. 98, 1978, Section 12***, of the Republic of South Africa, a single copy of an article may be supplied by a library for the purposes of research or private study. No part of this publication may be reproduced, stored in a retrieval system, or transmitted in any form or by any means without the prior permission of the publishers. ***Multiple copying of the contents of the publication without permission is always illegal.***

U.S. Copyright Law applicable to users In the U.S.A.
The appearance of the statement of copyright at the bottom of the first page of an article appearing in this journal indicates that the copyright holder consents to the making of copies of the article for personal or internal use. This consent is given on condition that the copier pays the stated fee for each copy of a paper beyond that permitted by Section 107 or 108 of the U.S. Copyright Law. The fee is to be paid through the Copyright Clearance Center, Inc., Operations Center, P.O. Box 765, Schenectady, New York 12301, U.S.A. This consent does not extend to other kinds of copying, such as copying for general distribution, for advertising or promotional purposes, for creating new collective works, or for resale.

SAIMM
JOURNAL OF THE SOUTHERN AFRICAN INSTITUTE OF MINING AND METALLURGY
VOLUME 118 NO. 5 MAY 2018

Contents

Proposed Book: The story of the decline of the South African mining industry
by I. Robinson and R. Croll i

Journal Comment: Where will our future metallurgists come from?
by Q. Campbell v

Open Journal System
by D. Tudor vi

President's Corner: The future of Africa is not so dark
by S. Ndlovu vii

STUDENT PAPERS

Optimization of the load-and-haul operation at an opencast colliery
by O. Pasch and S. Uludag 449
The results of a literature review, on-site time studies, and statistical data analysis were combined in order to determine the best loader-truck fleet combinations for increased production. A number of relevant key performance indicators (KPIs) for the identification and evaluation of productivity improvement opportunities were defined.

Test work to examine the potential for improving gold leaching performance at Navachab Gold Mine, Namibia
by M.N. Amwele and D.R. Groot 457
Bottle roll leach tests were conducted to investigate the effect of pH and cyanide concentration on gold extraction and cyanide consumption. The effect of introducing lead nitrate on the leach performance was also investigated. The results indicate areas for further investigation in order to improve leaching performance.

PAPERS OF GENERAL INTEREST

Numerical analysis and case study on the mitigation of mining damage to the floor of no. 5 coal seam of Taiyuan Group by grouting
by A. Li, Y. Liu, L. Mou, and K. Li 461
A numerical analysis of the stability and water permeability characteristics of the floor aquiclude before and after grouting was conducted using Rock Failure Process Analysis (F-RFPA2D). The dynamic development, extension, and distribution of the cracks in the aquiclude are discussed. This exercise provided invaluable experience in preventing water inrush hazards.

Surrounding rock control mechanism in the gob-side retaining entry in thin coal seams, and its application
by J.Z. Li, M. Zhang, Y. Li, and H. Hu 471
An analysis of the mechanical failure mechanism of the roadside filling body was carried out, and numerical simulations and field experiments were subsequently performed to characterize the stress environment of the roadside filling body under caving and gob filling conditions. The results of this study contribute to the theory and technology of gob-side entry retention and provide a basis for an effective stress adjustment and structural control method in the area.

International Advisory Board
R. Dimitrakopoulos, *McGill University, Canada*
D. Dreisinger, *University of British Columbia, Canada*
E. Esterhuizen, *NIOSH Research Organization, USA*
H. Mitri, *McGill University, Canada*
M.J. Nicol, *Murdoch University, Australia*
E. Topal, *Curtin University, Australia*

SAIMM
JOURNAL OF THE SOUTHERN AFRICAN INSTITUTE OF MINING AND METALLURGY
VOLUME 118 NO. 5 MAY 2018

Contents *(continued)*

PAPERS OF GENERAL INTEREST

Experimental study on the stability of surrounding soft rocks of gob-side entry retaining in fully mechanized caving
by P.S. Zhang, Z.H. Kan, W. Yan, B. Shen, Y.P. Zhao, and S.X. Wu 481
This study shows that mining the upper and lower panels causes a superposition effect to the gob-side entry retaining road way. An innovative support method was developed which provided excellent support for roadways with fractured roofs.

Determination of stable spans in UG2 excavations
by B.P. Watson, and R. Gerber. 493
Research was carried out to determine the interaction of support with the rock mass in both conventional and mechanized UG2 workings. The results provide insight into stable span determination where excavations are intersected by a shallow-dipping thrust structure.

Effect of mould geometry, coating, and plate thickness on the thermal profile of continuous casting moulds
by A. Gupta, R.K. Singh, A. Paul, and S. Kumar 505
A three-dimensional model for heat transfer analysis of continuous casting mould plates has been developed to predict the hot face temperature. The model takes into consideration the presence of bolt holes as well as the effect of nickel coating on the hot face.

Automatic generation of feasible mining pushbacks for open pit strategic planning
by X. Bai, D. Marcotte, M. Gamache, D. Gregory, and A. Lapworth 515
Automatic generation of practical pushbacks is a highly desirable feature in an open pit mine. An algorithm which is based on modification of sets of blocks obtained by parametric optimization of the pit using a maximum flow method was developed. Case studies show that the proposed method generates practical pushbacks with all geometrical constraints fulfilled.

A new approach for predicting bench blasting-induced ground vibrations: a case study
by X. Hu and S. Qu. 531
The concepts of equivalent path and equivalent distance are introduced to take into account the effects of topographic features and rock and rock-mass properties on ground vibrations induced by bench blasting. The resulting equivalent–path-based equation can easily be used in open pit mines where the factors such as the equivalent path and distance, rock density and wave velocity, and integrity coefficient of the rock mass, can be easily measured.

Effect of cooling conditions on the leachability of chromium in Cr_2O_3-containing steelmaking slag
by Y. Yu, D. Wang, J, Li, M. Li, and Z. Xue. 539
The influences of temperature and atmosphere during cooling on the leachability of chromium from stainless steel slags were investigated. The results indicate that it is necessary to adopt a neutral or reducing atmosphere for slag cooling in order to supress the formation of hexavalent chromium.

Mathematical simulation and water modelling of liquid steel interaction with an argon bubble curtain in a one-strand continuous casting tundish
by A. Cwudzinski 545
Investigations were conducted under a range of thermal conditions with the aim of increasing the active liquid steel flow in the tundish without using standard flow control devices. Numerical simulations showed that the argon flow rate, gas-permeable barrier (GPB) location, and thermal conditions influence the liquid steel motion in the tundish. The best GPB positions were identified based on the lowest value of stagnant flow.

Particle size distribution and energy consumption during impact crushing of single granite particles
by H. Fang, J. Yang, and Q. Chen 555
A custom-made experimental rig was used for impact crushing tests on single particles of granite. The results showed that the particle size distribution of the crushed granite under the range of different experimental parameters was in accordance with a continuous probability distribution (Weibull distribution). It was also found that an optimal impact velocity exists at which the energy consumption per unit of sand product is minimized.

Where will our future metallurgists come from?

The 14th Annual SAIMM Student Colloquium 2017 was held at Mintek on 25 October 2017. This is a prestigious annual event where mining and metallurgy students at tertiary institutions can showcase results of their projects to an audience from the greater Southern Africa mining community. The top students are invited to publish their papers in a special issue of the *Journal*. Looking at the papers in this edition, it is clear that the type of research conducted by students increasingly reflects the priorities in the industry, and that the outcomes are applicable, current, and of very high quality. This is a very encouraging sign, and it does go far to dispel the notion that only 'pie-in-the-sky' research is being done at our tertiary institutions. We are indeed successfully contributing to the creation of prosperous and empowered young professionals, to paraphrase the slogan of the Colloquium. Anybody with any interaction with these bright young minds can confirm that the industry will be in good hands in the future.

But will this be enough? While the quality of education of our future mining professionals seems to be ensured, the numbers are worrying. We have been experiencing a steady but significant drop in enrollment numbers for metallurgy- and mineral processing-related qualifications at most, if not all, of the big universities. The effect of this is that there is a high probability that there will not be enough of these young professionals in four or five years' time to cater for our job market. The South Africa mining industry (and the rest of the world as well, probably) has always been locked in this lead-lag dilemma on the supply of, and demand for, qualified professionals. One can recall the situation in the early to mid-1980s, when we had to look overseas to supplement the demand for young metallurgists to service the boom in the gold and platinum industries, in particular. Yes, the times were good then, but we all know that our game is a highly cyclic affair. And we know that the past few years were abysmal. But we need to question ourselves if we are geared to support a new optimism in the mining sector as far as trained and educated professionals are concerned. Remember, it takes more than four years of foresight to plan our future in terms of qualified talent. And who knows what will happen in the industry in four or five years' time?

So why don't we currently get the young feet flowing to our institutions? Capacity is certainly not the problem, and I don't believe we can blame the school system this time. To find a solution, we need to ask the same questions young potential students ask themselves: How will I pay for my studies? and; will I have a secure and satisfying career?

Unfortunately, the answer to the first question is not easy. All academics in this field agree that the number of industry-funded bursaries has decreased drastically over the last ten years. We do not see the abundance of bursaries that we saw in the 'nineties. This is perfectly understandable, given the state of the industry, but the question is whether any scenario planning about future professional requirements is being done. We may be caught napping once again.

Another issue around bursaries is the rise of emerging miners, coupled with the fragmentation of the once mighty mining houses. And while nobody is questioning the strategic and social importance of this change, it is true that small emerging players simply do not have the capacity – financial or otherwise – to invest in talent development.

The answer to the second question, about the future prospects in a career in mining, is rather obvious: the perception about the state of mining in the country has never been worse. It is not surprising that students do not see themselves operating in such an unsecure industry while the policy-makers are still trying to get their ducks in a row. The damage to the future of the industry in terms of acquiring young talent is terminal. Added to that are the many qualified mining and metallurgical engineers not being able to find employment in their disciplines. We will not attract top talent while there is a perception that a career in mining is not a good option.

Thank goodness for the few students, like the authors of these papers, who are prepared to gamble on a very bright future – one in which they themselves may very well be the change agents for the better. Now is the time for universities and employers to invest in the few who are willing, and to develop them to reach their potential. We are going to need special people in the foreseeable future.

Q. Campbell

Open Journal System

The SAIMM has adopted the Open Journal System (OJS) with the objective of optimizing the management of the paper reviewing process for the *Journal*.

Paper submissions will no longer be accepted *via* the SAIMM Journal submission form on the SAIMM website. Only papers that are currently in the system will follow the existing reviewing process.

You can now submit manuscripts and peer reviews online. The OJS assists you with every step of the reviewing process. Authors can also check the status of their papers online and referees will receive automated reminders for their reviews.

We request that you register as an Author and/or Referee on the system. To access the OJS website please follow the link: http://saimmjournal.co.za/

Any query or comment on your experiences with OJS should be communicated to the Journal Co-ordinator, Kelly Matthee at Kelly@saimm.co.za and 0118341273.

Thank you for your cooperation.

D. Tudor
SAIMM Editorial Consultant

Learn more:
www.geobrugg.com/rockfall

GEOBRUGG
BRUGG
Safety is our nature

Why choose Geobrugg?

- For the most valuable asset in life - our safety
- High tensile steel mesh
- Blast resistant
- Different mesh types for different ground conditions
- Proven static and dynamic performance
- Cutting edge corrosion protection
- Tailor-made sheet sizes

Geobrugg Southern Africa (Pty) Ltd | Unit 3 Block B Honeydew Business Park | 1503 Citrus Street | Honeydew 2170 | South Africa | T +27 11 794 3248 | info@geobrugg.com | www.geobrugg.com

The future of Africa is not so dark

This month's *Journal* edition celebrates the impressive research achievements of some of the 2017 graduates in the mining and metallurgical sector. However, of the eight papers that were selected from the Student Colloquium in October last year, only four were submitted for the reviewing process. Two papers were subsequently accepted for publication and two are being reworked. This is a little disappointing because the *Journal* aims to profile, each year, a number of papers that are the outcomes of research presented by students at the well-established annual SAIMM Student Colloquium. The presentations are a reflection of the wide variety of research being conducted in various institutions of mining and metallurgy in Southern Africa, and showcase the magic that happens when students challenge the status quo in their fields. It is a missed opportunity not to have this work published. Through novel scientific fundamentals and unique combinations of knowledge, these young researchers produce surprising results and new discoveries that can create the foundation for many innovative opportunities and technologies in Africa. And Africa is in great need of innovative African-driven technologies to solve its problems.

Africa has long been known as the Dark Continent due to its slow rate of development. However, there are at least two treasures in which Africa trumps other continents; its natural resources, and its young and dynamic generation which can make up a strong human resource force. The sterling work by the mining and metallurgical graduates presented in this issue of the *Journal* gives us a glimpse into those riches that Africa holds in abundance. The riches that will make the continent a potential economic *tour de force* in the future. Africa, therefore, needs to convert its comparative advantage to a competitive edge. For this to happen, Africa as a continent must work as a whole to safeguard and intelligently invest in its mineral resources and development of human capital.

Mineral wealth can provide the African continent with a tremendous opportunity for economic development by providing the funding for investment and growth. In recent years, there has been a significant push by African countries to cooperatively develop policies, strategies, and programmes that strengthen the capabilities and capacities to fully develop and utilize mineral resources for effective socio-economic development of the continent. In 2009, for example, the African heads of state adopted the Africa Mining Vision (AMV), a holistic approach enabling the transparent, equitable, and optimal exploitation of mineral resources to underpin broad-based sustainable growth and socio-economic development in Africa. The AMV is meant to address the disparity that tends to exist between African's mineral wealth and the poor socio-economic conditions in most African countries, and one of the approaches to close this gap is to move away from being an exporter of cheap raw materials to a manufacturer and supplier of knowledge-based services. While discussing on the AMV initiative, a friend recently suggested that just as oil-producing countries have 'cartels' such as OPEC, which control the price of oil, Africa should also have its own cartels that will control the exploitation and utilization of its minerals. My response was that only a united, focused Africa with a vision can change its future. It's nearly ten years since the AMV initiative and commitment from the African states is essential to ensure that this does not remain only as a paper agreement.

The development of human capital through empowerment with the relevant skills and knowledge is also critical to the success of the African vision. The right people with the right skills across Africa can be an enabling tool that ensures the proper management and development of the mineral sector and other resources available on the continent for a sustainable economy. Africa contains an enormous pool of dynamic young people who can be trained to provide that critical mass. In 2015, sixteen of Africa's leading universities came together in Dakar to establish the African Research Universities Alliance (ARUA). ARUA is intended to build capacity and develop local research excellence through a collaborative network. ARUA's vision reflects what Africa needs; making African researchers and institutions globally competitive while contributing to the generation of knowledge for socio-economic transformation.

The ARUA and AMV initiatives are but two examples showing that African countries are waking up to the fact that they need to work together to find solutions to development problems facing the continent. I am happy to say that the SAIMM is doing its part by bringing together different young researchers and professionals from Southern Africa, through events such as the Student Colloquium and many other conferences and workshops. Because it is only through uniting and working together that the African continent can shed its image as a resource-cursed Dark Continent.

S. Ndlovu
President, SAIMM

DESIGNED TO DELIVER

ELECTRIC
WHEELED CONE PLANT
WC 1000
WORKS FOR YOU

TEREX
Minerals Processing Systems

ELB EQUIPMENT
HEAD OFFICE:
+27 (0)11 306 0700
Elb@elbquip.co.za

BRANCHES & DEALERS SOUTH AFRICA:

BRITS • CAPE TOWN • DURBAN
EAST LONDON • GEORGE
KIMBERLEY • MIDDELBURG
POLOKWANE

DEALERS – SOUTHERN AFRICA:

BOTSWANA • LESOTHO
MOZAMBIQUE • NAMIBIA
•SWAZILAND • ZAMBIA
ZIMBABWE

www.elbequipment.com

Distribution and Product Support by:
ELB EQUIPMENT
A Member of the ELB Group

Global Mining Standards and Guidelines Group

Creating community to drive operational excellence

27 June 2018

www.globalminingstandards.org

Mandela Mining Precinct, Cnr Rustenburg and Carlow Roads, Melville, Johannesburg

Facilitators
Andrew Scott
Jean-Jacques Verhaeghe

WORKSHOP

Interoperability and Underground Communications Infrastructure

Interoperability

This workshop aims to engage broad industry participation in the GMSG Interoperability Definitions and Roadmap Project.
The project, to be complete by Q3 2018, will enable industry-wide alignment and identify a collaborative path forward to address mining interoperability including the identification of initiatives and projects and fostering increased collaboration across the sector. As part of this project, volunteers will join a multi-stakeholder innovation ecosystem, sharing expertise and building meaningful relationships with potential collaborators.

The outcome is generating input for the much-needed international roadmap: a landscape of interoperability initiatives, projects, organizations and resourcing that are aligned, collaborative, and supportive of interoperability developments in other organizations.

During the workshop, participants will work together to:

- Determine common industry interoperability definitions, scope, principles and references
- Develop a consensus on what the desired end state looks like
- Identify existing projects and organizations that have developed/are developing interoperability-related solutions
- Identify industry barriers and success factors to move interoperability forward

Underground Communications Infrastructure

This workshop will enable participants to ensure the GMSG Underground Communications Infrastructure guideline suite is relevant and applicable to the Southern African mining industry. This year, the project committee has made strong progress towards publishing Section 3 of the guideline suite – a high-level overview of factors for mine operators to consider for their unique communications needs – by year end.
The Guideline is intended to provide mine owners and operators with an overview of best practices for electronic communications across a mine's lifespan. GMSG published Section 1 and Section 2 of the Guideline in early 2017. The Guideline is divided into five sections:

1) Positioning and Needs Analysis
2) Scenarios and Applications
3) General Guidelines
4) Business Case Development
5) Planning, Deploying, and Support Considerations

The published Guideline will continue to support underground operations developing their communications infrastructure into robust, cost-effective and user-friendly installations.

Space is limited due to room size, therefore please RSVP as soon as possible, no later than 18 June 2018 to Yolanda Ndimande at yolanda@saimm.co.za. or for more information contact Jennifer Curran at jcurran@globalminingstandards.org.

For further informaton contact:
Conference Co-ordinator, Yolanda Ndimande
Tel: +27 11 834-1273/7 · E-mail: yolanda@saimm.co.za

SAIMM
THE SOUTHERN AFRICAN INSTITUTE OF MINING AND METALLURGY

Partner Organizations

CIM ICM · AusIMM THE MINERALS INSTITUTE · SME Society for Mining, Metallurgy & Exploration · SMART Surface Mining Association For Research & Technology

http://dx.doi.org/10.17159/2411-9717/2018/v118n5a1

Optimization of the load-and-haul operation at an opencast colliery

by O. Pasch and S. Uludag

Paper written on project work carried out in partial fulfilment of BEng (Mining Engineering) degree

Synopsis

The current coal mining climate is characterized by coal price volatility, political instability, high labour costs, and increasing operational costs. This is exacerbated by a steady decline in the growth of global coal demand due to the increased use of alternative and renewable fuels in the energy industry. Locally, the overall mining cost inflation indices shows a yearly increase of 2% over the national consumer inflation. In order for coal mines to survive and mine profitably, they need to capitalize on the opportunity to improve their productivity and focus on one factor they can control: operational efficiency. Increasing productivity is one of the key drivers to counter diminishing profit margins. Increasing production effectively reduces operating costs. However, the emphasis should not only be on increasing output with the same input, but increasing the output while decreasing the input, and ultimately adding optimum value to current resources. Research shows that an increase in production will ultimately decrease the operation's unit cost, especially fixed costs.

In this study a load-and-haul fleet optimization approach has been used to identify the opportunities for operational improvement at an opencast colliery. The study combines the results of a literature review, on-site time studies, and statistical data analysis in order to determine the best loader-truck fleet combinations for increased production. Several relevant key performance indicators (KPIs) for the evaluation and identification of productivity improvement opportunities were defined during this study. These KPIs are bucket fill factor, loading conditions, loading cycle time, utilization, and deviations from schedule. The priority delays determined by on-site time studies compared to the time book for each delay showed that idle or waiting time by the loaders, face preparation and relocation, and process delays had significant deviations. However, the results showed that this operation is under-trucked, hence optimizing the loader-related inputs proved less effective than optimizing truck-related inputs. The results indicated that a homogeneous truck fleet consisting of five Caterpillar 789C trucks, combined with a Caterpillar 994K loader, is the most efficient fleet option and will produce 1455 t/h. The combined optimized effect of each identified KPI of production led to a tonnage improvement opportunity of 5421 t per shift.

Keywords
optimization, productivity, load-and-haul fleet, KPIs, under-trucked, tonnage improvement opportunity.

Mine background

The opencast coal mining complex extends over two mines within the Witbank Coalfield, to the south of Emalahleni, Mpumalanga Province. The target pit is currently a mature opencast strip-mining operation that extracts multi-layered coal seams, exercising a throw-over method to the low-wall side to the north and advancing in a southerly direction. The area was previously mined using a conventional underground bord-and-pillar method.

The mining complex produced a total of 30.4 Mt in the preceding financial year, about 8.5 Mt/ of which was produced at the opencast colliery. The mine was established in 2010 and consists of a mixture of greenfield and brownfield operations that supply energy coal to both local and export markets. Coal is supplied to Eskom's power station via a conveyor system, while a higher quality export grade is supplied to mainly European and Indian markets.

Project background

In recent years, the global effort towards utilization of alternative and renewable energy resources has driven the demand for energy from coal downward. In addition to this, various sources have highlighted that fact that coal is a finite resource; it is inevitable that coal resources are heading towards depletion. Meanwhile, supplying coal has become increasingly more challenging. This is because mining operations usually extract the reserves nearest to the surface or the most conveniently accessible reserves. Coal deposits that have been left in situ by previous operations may now be sterilized, or if the extraction opportunity exists, will require sizeable financial investments. Operational costs for South African mines are increasing at a rate that diminishes the margin to mine profitably. The developing South African economy has had difficulty maintaining a positive GDP growth rate, weakening the rand to US dollar exchange rate. Not only does this play a decisive role in the mining industry's export sector, but it also increases mining operational input costs significantly. Most operational expenses like

* *School of Mining Engineering, University of Pretoria, South Africa.*
© *The Southern African Institute of Mining and Metallurgy, 2018.* *ISSN 2225-6253. Paper received May 2018.*

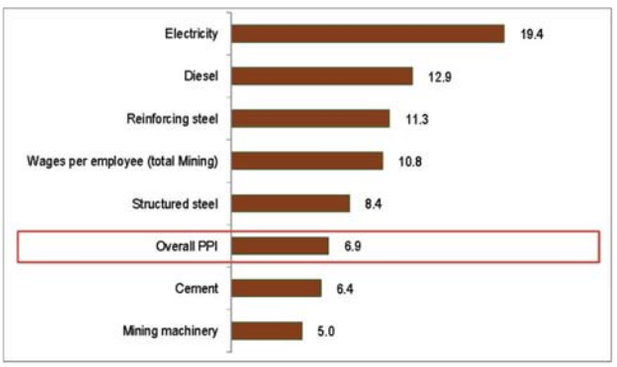

Figure 1—Cost inflation (%) affecting the mining sector (annual average increase from 2008 to 2014) (Baxter, 2015)

consumables, electricity, equipment, fuel, and various overhead costs are heavily inflated by a weaker rand.

Production challenges

Pillar mining is one of the most challenging coal extraction methods in an opencast environment. Remnant coal pillars in old workings are also susceptible to spontaneous combustion. Not only does this degrade the quality of the coal, it also creates an extremely hazardous operating environment. As a result, overheating of equipment occurs frequently, which leads to regular production stoppages. The ambient environment caused by the smoke reduces operator visibility and generates uncomfortable operating conditions. The uneven and undulating country rock results in water accumulation on the pit floor. This contributes to productivity losses in a number of ways, including trapping of equipment by mud, pumping arrangements, unseen potholes damaging tyres, and material losses from loaded haul trucks. Another factor that affects productivity is operator proficiency. Operators may be tempted to ignore reporting and logging responsibilities as a result of working in a strenuous environment.

The exposure of country rock underneath the coal seams also adds to the challenges. This results in poor road conditions that affect hauling by increasing travel time, causing excessive wear on haul truck tyres, and increasing safety risks, to mention only a few. Hauling coal from a pit some 60 m below surface means that loaded trucks must travel upwards at steep inclines. This reduces the speed trucks can travel at and adds considerable time to the hauling cycle. As extraction advances with each strip, the hauling distances to the tipping points increase, in turn increasing the truck cycle time.

Objectives and methodology

The following objectives were formulated.

- Determine and quantify the main factors that affect the productivity of the load-and-haul fleet at the mine by means of value drivers.
- Identify, compare, and analyse the major delays that have created shortcomings in the current extraction process to arrive at the potential capacity of the mine's extraction process.
- Identify the tonnage improvement opportunity associated with each KPI.
- Recommend practical improvements that target priority KPIs in order to increase productivity at the target pit.
- Develope an optimized fleet solution for the current coal extraction operation through the basic mining equations.
- Conduct a basic cost evaluation for each improved KPI based on benchmarking and industry standards.

A literature review was conducted to gain understanding of the background of the project as well as to limit the context to the milieu of the investigation. In addition, the literature was used to gain knowledge of industry standards in order to benchmark costs where applicable. Various literature sources were continuously reviewed to add knowledge and understanding to the problem statement throughout the investigation. Preliminary research related to the theme of the study includes conventional data-gathering techniques like interviews with employees of the mine and group-based discussions. These insights added qualitative value and support to a mainly quantitative investigation. Documents, records, and statistical data were also retrieved from the mine's online Integrated Management System and utilized. Information relevant to the project scope was made available to the investigator with permission from the General Manager of the operation. The third method of investigation was based on a time study where the investigator recorded overall loading and hauling cycle times over 15 twelve-hour shifts. Simultaneously, side-by-side on-site observations were recorded. This allowed the investigator to record multiple 'day-in-the-life-of' observations whereby half-hourly events could be logged. These methods can be categorized as visual observations done over a period of 180 hours. Quantitative data obtained was used to calculate a benchmarked improvement tonnage opportunity target.

The Time Usage Model, proposed under the ownership of the mine was applied during the course of the study, which drives a consistent approach to measure productivity. This model provides a standard methodology to calculate time-related parameters for equipment at the mine. Time-related parameters are one of the most fundamental aspects in measuring the relative performance of mines, hence this model contributes to the continuous iteration in order to achieve optimum productivity.

Scope of study

The investigated extraction processes are limited to the targeted pit's loading and hauling fleet. Only KPIs and value drivers from extraction processes will be considered in creating a benchmark for the mine. A generic methodology on how to adapt the in-pit extraction processes is only applicable to similar operations. *i.e.* opencast collieries. Due to the confidential nature of mining financials, relative measures for operational costs of the mine are used unless stated otherwise.

Literature review

Production

The following key excerpts were taken from various sources relevant to the company's coal market.

- South Africa supplied 66 Mt for the global coal supply in 2016 (Anon., 2016)
- South African collieries produced 176.9 Mt in 2007 to supply the local market (Anon., 2016)
- The company produced 14.85 Mt in FY16 for export, of which an estimated 8.25 Mt were produced at the targeted mine (Anon., (2015). A decrease to 12.8 Mt in FY18 is expected by the company (Anon., 2016)
- The targeted mine supplied Eskom with 8 Mt in FY15. The company plans to decrease the mine's contribution to 6.75 Mt in FY 17 (Anon., 2015).

A common focus for a mining operation is to improve productivity to reduce cost pressures. However, two increasingly important and inevitable factors remain critical, which mining companies must continuously analyse and evaluate in order to maintain profitability – the depletion of coal resources and the shift towards alternative energy (renewable energy sources).

Productivity in mining terms can be generally defined as the same output for less input. Baxter (2015) argues that productivity gain should be measured as a form of optimization. In other words, the drive to productivity should focus on increasing the ratio of output to input. This is evident from Figure 2, which highlights the general motivation to increase the product or output but reduce the input or cost per unit.

Load-and-haul operation

The load-and-haul operation can be seen as a continuous cycle that is made up of different production steps or activities. The load-haul cycle time is the total time to complete a full cycle. The critical cycle steps, as time fractions of the total cycle, have been identified by Krause (2006):

- Spotting at loading is the time required for a truck, as soon as it arrives near the vicinity of the loader, to manoeuvre into a stopping position for loading.
- Loading time is the total time for the loader to load the bucket of the truck to its required payload.
- Hauling-full time is the total travelling time for a loaded truck to reach the dump site from the loading site.
- Travel empty time refers to the total travelling time to for an empty truck to reach the load site from the dump site.

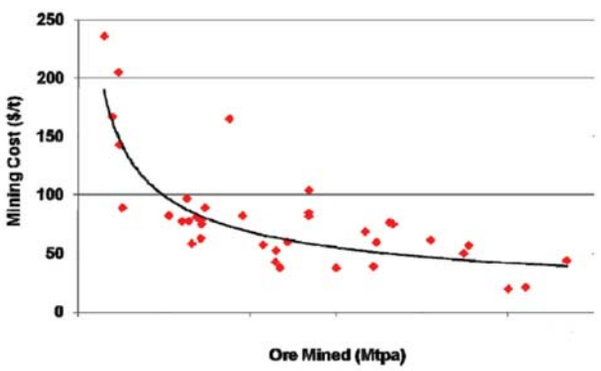

Figure 2—The general trend in mining productivity where mining cost decreases as the product, or output, increases (EY, 2015)

- Queuing time is the total time an empty truck has to wait in line before it can manoeuvre into a position for loading.

Another factor that is commonly ignored is the waiting time of a loader. 'Waiting at dump', 'Queuing', and lastly 'Waiting time of loader' are the three noteworthy delays that are not directly caused by the performance of the equipment, but rather due to load-haul equipment combinations.

Time usage model

The company promotes the use of a standardized method by which productivity can be measured and calculated, in addition to the reporting and documenting of equipment usage. Figure 3 illustrates a typical time usage model. The time usage model illustrates time factors that are related to the total time that equipment is not performing its required, planned, and intended function. However, the total time under consideration when equipment is performing its required, planned, and intended function is referred to as Equipment Production Time or Direct Operating Hours (DOH). The DOH is defined by the time when measurable throughput in the process is established. This is generally considered to be the product of the available time for equipment to perform work and the actual utilization time to maintain a productive cycle. Various equipment performance metrics that will determine the productivity of an operation can be derived from the time factors. These relative measures are generally called key performance indicators (KPIs) (Choudhary, 2015).

Equipment match factor

In a load-and-haul operation, the capacities of the loaders should be compatible with the capacities of the truck fleet. Choudhary (2015) presents a simplified model to determine if a fleet is under-trucked or over-trucked. This is represented by the following formula:

$$No.of\ truck\ require = \frac{Total\ truck\ cycle\ time\ (\text{min})}{Sum\ of\ the\ spotting\ time\ an\ loading\ time\ (\text{min})} \quad [1]$$

If the current fleet operates with a number of trucks exceeding the value determined by Equation [1], the fleet is said to be over-trucked, and if less than the value, under-trucked. Equation [1] does not consider the queuing times, thus it can only be applied as a comparison whereby two ideal fleets are considered.

The equipment match factor (MF) between two interdependent pieces of equipment takes into account the total cycle time of the equipment. According to Choudhary (2015) and Krause (2006), the equipment match factor refers

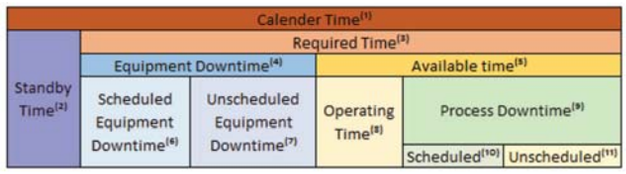

Figure 3—A diagram illustrating a typical time usage model (derived from the mine's IMS; Pasch, 2015)

to the ideal capacity and number of trucks that are paired in operation with a loader and how well they are suited to each other. The variables in Equation [2] are dependent on the equipment specifications as well as fixed performance capacities, *i.e.* payload, truck height, and loader reach to name a few.

$$Match\ Factor = \frac{No.\ of\ trucks \times loader\ cycle\ time}{No.\ of\ loader \times trucks\ cycle\ time} \quad [2]$$

The match factor, which provides a measure of the productivity of the fleet, can be calculated by Equation [2]. Although the MF ratio does not take into account the equipment capacities and specifications, it is inherently considered by applying the equipment cycle times in the equation. Choudhary (2015) notes that the MF ratio is not to be applied to the efficiency of the production itself, but only to the efficiency of the selected combined fleet. Choudhary (2015) goes on to state that an MF of 1.0 indicates that the fleet is 100% compatible regarding size and timing, but in this instance the combination can only produce 10% of the capacity of a fleet that has an MF of 0.5. The mining industry would rather opt for a lower MF limit, as this will correlate with a lower operating cost. Choudhary (2015) states that the MF is best applied in combination with other approaches, such as experiential and iterative methods, for determining the haulage fleet size.

Equipment specification

The mine has become accustomed to the exclusive use of CAT equipment for their load-and-haul operation. According to CAT Mining (2017), the 993K loader with a standard coal bucket is sized to load 90 t in three to four passes to the 777D, and load 136 t in six passes to the 785C. This amounts to an average of approximately 22.5 t per load. The 994K loader with a standard coal bucket is sized to load 136 t in four passes to the 785C and 177 t in five passes to the 789C. It is also capable of loading 227 t to the 793 in six passes. Hence, in theory, the 994K loader can average approximately 36 t per load. Bucket selection is a critical factor in any extraction process. According to CAT Mining (2017), in-seam coal is best mined with a rock-type bucket, and they recommend that serrated edge buckets be used as this provides the highest penetration rates.

Bucket fill factor (BFF) is used to determine how well the volume of a bucket is utilized. Bucket fill factor is very useful to determine the productivity of a combined fleet. Mathematically, it is expressed in Equation [3] (Mohammadi, Rai, and Gupta, 2015). Bucket fill factors are usually impractical to obtain from in-field measures but an estimation scale can be used to objectively rate each bucket load accordingly.

$$Bucket\ fill\ factor = \frac{Volume\ of\ materials\ in\ the\ bucket}{Bucket\ capacity} \quad [3]$$

Productivity for coal haul trucks is not limited by the nominal payload *per se*, but rather by the volumetric design and dimensions of the bucket. Due to the low relative density of coal, which is amplified by the swell factor of broken coal during loading, there is no theoretical limitation to the output per ton and the truck payload.

Results and interpretation

The total fleet sizes seen in Table I and Table II indicate the available equipment for the duration of the study. The sample size includes the equipment from the fleet on which observations, measurements, and recordings were made and from which relevant data was collected. However, the most significant amount of data was measured and recorded from 994K loaders and 789K haul trucks.

It can be argued from the total and sampled fleet sizes that the load-and-haul coal extraction operation is under-trucked. However, under-trucking or over-trucking varies with the time parameters in the truck cycle time. According to CAT (2017), each loader has been benchmarked to service at least three to five trucks. From Table I and Table II, looking at the sampled fleet size, it is seen that one 994K loads on average loads two trucks, which indicates that the operation is under-trucked.

Bucket fill factor

Table III shows that each loader-truck combination deviates

Table I

The mine's coal extraction haul truck fleet

Total	Sampled	Equipment	Type	Volume (m^3)	Mass [t]
-	-	Cat 793F	Rock	160	244
20	8	Cat 789C	Coal	105	160.125
18	4	Cat 785C	Coal	78	118.95
-	-	Cat 777C	Coal	60	91.5

Table II

The mine's coal extraction loader fleet

Total	Sampled	Equipment	Type	Volume (m^3)	Mass [t]
6	3	994K	Rock	19	28.975
3	1	993K	Rock	13,8	21.045
-	-	992K	Rock	10,7	16.32

Table III

Actual average passes with load-haul combinations

Load-haul pairing	Average passes @ Pit	Benchmarked standard	% deviation	BFF
994K - 789C	6.4	5	28.0%	74.1%
994K - 785C	4.6	4	15.0%	87.0%
993K - 789C	9.2	7	31.4%	76.1%
993K - 785C	6.7	5	34.0%	74.6%

significantly from the benchmarked passes or loader loads prescribed by CAT Mining (2017). The 994K-789C pairing deviates 26% from benchmarked practice, effectively resulting in a 74.1% BFF for the loader (see Figure 1).

Optimizing the loader BFF to a mine-ideal standard will inevitably decrease the passes per load. Increasing the BFF of the loader results in two improvements the overall productivity. The first is a decrease in passes, which will shorten the loading time while still maintaining the same mass per loading cycle. This results in a 90 t/h increase (see Table IV). However, if the cycle is under-trucked, reducing the loader cycle time will not necessarily add direct production value. This is because the loader has to wait for trucks in an under-trucked cycle. No additional tonnage can be hauled unless another truck is added to the cycle. Additional available time 'created' in this improvement can, however, be spent on face preparation for the next load. A second option may be considered whereby an additional load can be loaded, making six loads per loading cycle. This will increase the BFF of the trucks to 90.5% (144.9 t). This results in a total increase of 156 t/h (see Table IV). Applying this method will evidently increase the tonnage produced in an under-trucked cycle since more tons are added while operating at the same loading and truck cycle time.

The Australian Department of Resources, Energy and Tourism (2014) has indicated that with an increase in the average payload, the fuel cost per ton decreases as more tons are being hauled. The aforementioned source also states that the fuel usage does not increase significantly when the payload is increased from 80% to a 95% BFF (Australian Government, 2014). By comparing only fuel costs of the current BFF to the second tonnage improvement opportunity, the net opportunity profit per hour resulted in a R19.6 per ton decrease in unit cost.

Table IV

A comparison of the two available optimizing options related to the BFF

Theoretical current production		
Cycle time	= (10 min x 60 s)	600 s
Cycles per hour	= (60 min / 10 min)	6
Tons per loading cycle	= (From Table VI)	128.6 t
Tons per hour	= (6 x 128.6 t)	771.6 t
Av passing time	=	60 s
Av passes per load	=	6
Loading time	=	360 s
Option 1		
Av passes per load	=	5
Av passing time	=	60 s
Loading time	= (5 x 60 s)	300 s
New cycle time	=	540 s
Actual time saved	=	60 s
Cycles per hour	=	6.7
Tons per loading cycle	=	128.6 t
Tons per hour	=	861.62 t
862 -772 t = 90 t/h increase (↑ 11.65%)		
Option 2		
Tons per loading cycle	= (Truck BFF of 90.5%)	144.9 t
Tons per hour	= (using current cycle times	869.4 t
869 -772 t = 97 t/h increase (↑ 12.60%)		

Loading conditions

Loading conditions in-pit differ greatly from stockpile loading conditions. Loading times from the pit and from the stockpile will also differ from theoretical loading times, as well as benchmarked loading times and assumed conditions. In the case of this study, stockpile loading conditions are presumed to be either ideal or near-ideal for the following observed reasons.

- The stockpile floor grade is periodically maintained by graders, thus providing a flat and horizontal load floor that improves loading performance.
- The coal stockpiles are loosely packed against the angle of repose; hence minimum penetration force is used over the shortest possible time at an angle that is ideal for bucket designs to maximize bucket fill factors.
- Less spontaneous combustion on stockpiles, as the time the coal spends on the stockpiles is kept to a minimum. This allows for loader operators to plan and execute loading methods at a high accuracy and in the shortest possible time.
- If stockpiles are effectively managed, the loader can be ideally positioned for the loading method used, with sufficient space to move around.

The following conditions and practices were observed at in-pit loading operations.

- Uneven floor conditions as toes and irregularities in the footwall of the coal seam occur frequently, resulting in low bucket fill factors and consequently increasing loading time.
- Increased breakout force is required by the loaders to break coal from *in situ* conditions, thus increasing loading time.
- Limited space and changing coal face conditions in the pit led to frequent manoeuvring and positioning for loading trucks. This caused the loading method to change frequently, adding to time wasted.
- Spontaneous combustion caused extreme loading conditions, preventing the operator from loading efficiently. Operators have to continuously assess the ambient conditions and manoeuver into positions that enable the loader to remain at a safe distance from the burning coal but still access the coal face.

Cycle times

A mine ideal standard was developed to compare actual results against a targeted mine potential. The mine ideal was determined by benchmarking equipment specifications, supported by the upper quartile data distribution of recorded data obtained from the mine. This means that the mine ideal is now standardized and based on the best cycle activity time that had been reached in a quarter of the time over which the data were recorded. The cycle times were recorded (see Table V) for 161 truck cycles for the combination of 994K loader and 789C haul truck. The most significant contributor to the overall cycle time deviation is the loading activity, which contributed 37%. This is mainly due to mitigating the hazardous loading conditions *i.e.* water-spraying, floor grading, and face preparation. It was also determined that 27% of the total deviation is due to the queuing time. The results indicated that the current extraction technique or

Table V

Load-haul cycle time breakdown of a 994K – 789C combination

Cycle activities	Actual site average	Mine ideal	Deviation
Spotting at loading	00:55	00:55	00:00
Loading	05:48	04:19	01:29
Hauling full	09:39	09:00	00:39
Tipping	01:26	01:26	00:00
Travel empty	07:30	06:40	00:50
Queuing	01:06	00:00	01:06
Total	**26:24**	**22:20**	**04:04**

loading cycles could possibly be over-trucked, or the loader is not fully utilized for loading the trucks. This is in contrast with the results from the fleet sizes, which showed an under-trucked operation. The queuing times can be explained by a few localized events where either all trucks were dispatched to one loader when the other loaders were unavailable, or downstream process downtime due to crusher maintenance.

Table VI highlights the tonnage opportunity per shift or production improvement opportunity when only the cycle time is optimized to a mine ideal. It is important to keep in mind that the above summary is presented on the assumption that there is no queuing time, which is expected in an under-trucked operation, but frequently impractical. Yet, with the reduction in cycle time of four minutes and four seconds, the total improvement is 154 t per shift per truck for the 994K-789C combination.

In the case of improved cycle times, the payload per cycle will remain constant, in conjunction with all other factors, *ceteris paribus*, *i.e.* maintenance, tyres, and operator/labour costs. The fuel costs may increase due to the increase in the total haulage distance per shift, but this may be considered as negligible as the fuel cost associated with idling at queuing are assumed to be used for hauling. The total cost opportunity due to the increase in tonnage per shift amounted to a net decrease of R1.94 per ton.

Equipment match factor

According to Equation [1], the optimal number of 789C trucks paired with one 994K loader is five. Currently, the fleet

Figure 4—Stockpile loading with a 75% bucket fill factor (Pasch, 2015)

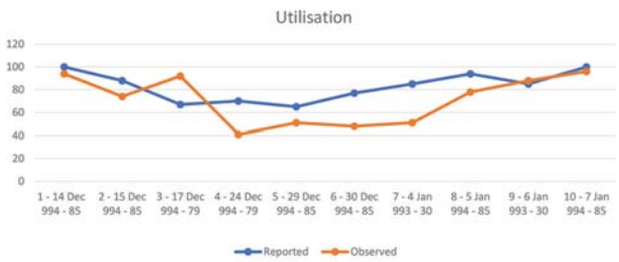

Figure 5—Reported and actual utilization over the duration of the study

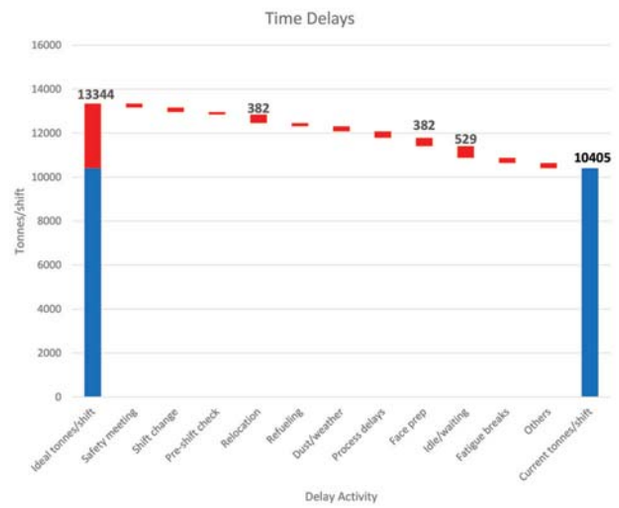

Figure 6—Tonnage opportunity associated with each delay

is operating at an average MF of 0.59. This confirms that the operation is currently under-trucked. According to Equation [2], the mine ideal MF ratio should be 0.96. The MF ratio can now be used as an index of the overall fleet efficiency or as a relative efficiency measure. Including the waiting and queuing times recorded in the study will provide a more accurate insight into cases where mixed fleets are used, as is the case at this mine. Results show that the optimum fleet in terms of tons produced per hour consists of one 994K loader and five 789C haul trucks. This yielded a total of 1455 t/h. Alternatively, removing one 789C truck in this fleet will decrease the tonnage by approximately 75 t/h. From the results, it can be deduced that there may be a linear relationship between the MF and the queuing times. In reducing the queuing time, the MF will tend to 1.0, which indicates a perfect MF. Combinations with the lowest queuing times does not necessarily reflect the best possible production fleet. The MF ratio for the optimized fleet yielded the largest MF ratio in this specific case, yet it resulted in the best possible production fleet. Thus, these MF calculations cannot be used in isolation from other fleet optimizing measures.

Productivity

Due to the nature of time studies and the associated methodology, the study focused on activities associated with delays in the extraction process. The average reported availability over the study period was 86.6%, according to

data collected from the mine's Integrated Management System (IMS). Figure 5 compares the observed and reported utilization. In eight out of ten days, the observed utilization was lower than what was reported. The average IMS reported utilization is 83.2%, whereas the average measured results show a 71.3% utilization. For the period between Christmas Day and New Year's Day, utilization reduced significantly. This period is generally known in the mining industry as the 'Silly Season', which typically reflects increased lost-time injury (LTI) trends.

Table VII shows the contribution of each delay to the total measured lost time. The main contributors to these delays are idle or waiting time. Using the rate of production, 1445 t/h, this amounts to a total of 10 405 t per shift and consequently 20 810 t/d. If delays could be reduced so that the full 602 minutes available could be utilized, a total of 26 688 t/d could theoretically be achieved for the targeted pit.

Figure 6 highlights the opportunity tonnage associated with each delay. An additional 2 940 t per shift is achievable, which could increase revenue by 18%.

Table VI

Tonnage opportunity using mine ideal cycle time comparison for the 994K – 789K combination

Actual		Mine ideal	
Cycles/shift/truck	= (7h x 60 min)/29.6 min	Cycles/shift/truck	= (7 h x 60 min)/22.3 min
*7 h DOH	= 420/26.4	*7 h DOH	= 420/22.3
	= 15.9 ≈ 16 cycles		= 18.83 ≈ 18 cycles
Tons/shift/truck	= 16 x 128.6 t	Tons/shift/truck	= 18 x 128.6 ton
*Truck BFF of 80%	= 2058 ton	*Truck BFF of 80%	= 2315 t
*80% Availability	= 2058 t x 0.8 x 0.75	*80% Availability	= 2315 t x 0.8 x 0.75
*75% Utilization	= 1235 ton/shift	*75% Utilization	= 1389 ton/shift

Total ton improvement/shift/truck = 1389 - 1235 = 154 t

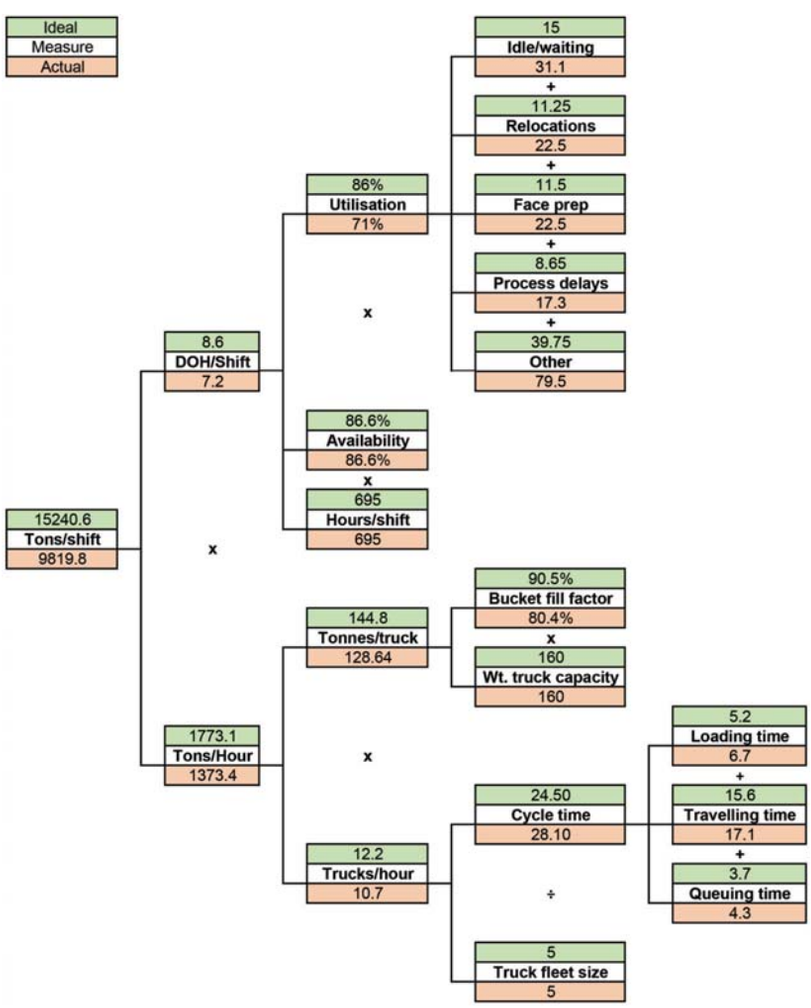

Figure 7—A value driver tree illustrating the total mine ideal opportunity tonnage for all KPIs *versus* the actual measured KPIs

Table VII

Top delays within shift breakdown

Total shift time	= (12 x 60)	= 720 min
Available time	= (720 - 125)	= 695 min
Availability	= (695 x 86.6%)	= 602 min
Reported utilization	= (602*83.2%)	= 501 min
Measured utilization	= (602*71.3)	= 429 min
Reported time lost	= (602-501)	= 101 min
Measured time lost	= (602-429)	= 173 min

SAFETY MEETING	10.4 min
SHIFT CHANGE	12.1 min
PRE-SHIFT CHECK	6.9 min
RELOCATE	22.5 min
REFUELING	8.7 min
DUST/WEATHER	13.8 min
PROCESS DELAYS	17.3 min
FACE PREP	22.5 min
IDLE/WAITING	31.1 min
FATIGUE BREAKS	13.8 min
OTHER	13.8 min

Table VIII

Tonnage improvement opportunities and recommendations for the identified KPIs

KPI	Tonnage improvement	Recommendation
Bucket fill factor	1% BFF increase @ loader = 1% ton produced increase	1) Improve operators proficiency by continuous and specialized training in typical conditions 2) Increase capacity of buckets *i.e.* installing coal buckets on the loaders 3) Continuous grading of the loading floor during scheduled loader downtime 4) Introduce improved ground engaging tools on the bucket teeth to improve penetration rate 5) Introduction of payload monitors that are frequently calibrated and monitored will increase awareness of actual BFF on which can be immediatly responded
Loading conditions	N/A	1) Continuous grading of haul roads and loading areas 2) Spray down of flames during breaks, maintenance, shift changes and other production equipment downtime 3) Face prep can be done during loader waiting times to ease the next loading activity
Cycle time	1 min cycle time improvement = 24.25 t/min produced increase (1455 thp increase)	1) Provide freeflow communication between loader and truck operator so that each load can be continuously assessed 2) Improving the BFF will decrease average passes per load and effectively decrease cycle time 3) Improving road conditions by applying effective road maintenance measures *i.e.* backfilling of potholes 4) The continuous review of queuing times as coal faces advance to adapt the fleet size accordingly
Time utilization	1 min delay reduction = 17 t/min production increase (1019 t/h increase)	1) A daily DOH target can be set for the operators 2) Control and monitor operators' start-of-operation time, working time, break time, and end-of-operation time 3) Optimize parking bay area by; conluding pre-shift checks at park-bay and refuelling during shift changes

Conclusions

The targeted pit is a high-producing asset for the mine, and the company is heavily dependent on this pit as an operation and a company. Several relevant KPIs for the evaluation and identification of productivity improvement opportunities were defined during this study. These KPIs are bucket fill factors, loading conditions, cycle and loading time, time utilization, and deviations from schedule. The combined tonnage improvement opportunity can be viewed in Figure 7, which reflects a theoretical improvement of 49.4%. From the research, it is evident that an increase in production will ultimately decrease the operational unit cost, which could increase profit margins significantly.

Recommendations

Recommendations for each KPI are summarized in Table VIII.

Suggestions

- An investigation is necessary to confirm the use of the correct buckets. Bucket costs are relatively expensive in consideration of operational costss. In addition, an analysis can be conducted to consider additional bucket protection as this can affect the performance of the machine through higher horsepower demand, higher fuel consumption, and reduced productivity.
- It is suggested that future studies that are largely dependent on statistics should be analysed by means of statistical approaches, for instance, Monte Carlo simulations and chi-square tests. This will increase the accuracy of any conclusions reached in conjunction with a significant amount of measured field data. If this is made available to the investigator, a substantial value can be drawn from such investigations.

References

Anon. 2016. FY16 Financial Results & Outlook.

Anon. 2015. Equity Research, Australia: CreditSuisse

Australian Government. 2014. Analyses of diesel use for mine haul and transport operations. Department of Resources, Energy and Tourism. https://www.eex.gov.au/sites/g/files/net1896/f/files/2014/06/Analyses-of-Diesel-Use-for-Mine-Haul-and-Transport-Operations.pdf [accessed 30 May 2017].

Baxter, R. 2015. RSA coal mining industry - Economic overview and realising the potential of the sector. Chamber of Mines, Johannesburg.

CAT Mining. 2017. Products - Equipment. https://www.cat.com/en_ZA/products/new/equipment/wheel-loaders.html [accessed 14 April 2017].

Choudhary, R.P. 2015. Optimization of load-and-haul mining systems by OEE and Match Factor for surface mining. *International Journal of Applied Engineering and Technology*, vol. 5, no. 2 (April-June). pp. 96–102.

Mohammadi, M., Rai, R, and Gupta, S. 2015. Performance measurement of mining equipment. *International Journal of Emerging Technology and Advanced Engineering*, vol. 5, no. 7. pp. 240–248

Krause, A.J. 2006. Shovel - truck cycle simulation methods in surface mining. MSC thesis, University of the Witwatersrand, Johannesburg. http://hdl.handle.net/10539/4763 [accessed 18 May 2018] ◆

http://dx.doi.org/10.17159/2411-9717/2018/v118n5a2

Test work to examine the potential for improving gold leaching performance at Navachab Gold Mine, Namibia

by M.N. Amwele and D.R. Groot

Paper written on project work carried out in partial fulfilment of B.Eng (Metallurgical Engineering) degree

Synopsis

The Navachab Gold Mine is an open-pit gold operation located in Namibia. The metallurgical flow sheet consists of crushing, milling, leaching by CIP (carbon in pulp), and electrowinning. Extraction in the leach section is approximately 67%, increases to approximately 86% by the end of carbon adsorption, indicating that extraction in the leach section is far from complete. The purpose of this study was to examine the potential for improving the performance of the leach section. Bottle roll leach tests were conducted using different parameters to observe their impact on gold extraction and cyanide consumption. The factors varied included the cyanide concentration and pH. The effect of introducing lead nitrate on the leach performance was also investigated. Furthermore, it is suspected that constituents in the ore that adsorb gold from solution (known as preg-borrowing constituents) suppress the overall extraction of gold, and thus the benefit of CIL (carbon in leach) was investigated. Finally, bottle roll tests as well as plant tests were conducted to determine the influence of residence time, as it was thought that this may be a limiting factor. An increase in extraction was observed when the cyanide levels were increased and when lead nitrate was introduced. The CIL test also showed an improvement in extraction compared to the normal leach tests. An increment in the pH did not show the same benefit, however. Plant tests showed a decline in the solid residue grade with an increase in residence time. The results indicate possible areas for further research in order to improve leach performance.

Keywords

gold leaching, CIP, CIL, cyanidation, lead nitrate, optimization.

Introduction

The Navachab Gold Mine is an open-pit operation that started production in 1989 at an average gold grade of 2 g/t. Ore mineralization includes pyrrhotite, chalcopyrite, arsenopyrite, sphalerite, molybdenite, scheelite, and uraninite (Nortemann *et al.*, 2000). The metallurgical flow sheet comprises crushing, milling, carbon-in-pulp leaching, and electrowinning.

Figure 1 shows the layout of the leach section, which consists of one pre-oxidation tank and eight leach tanks with a total residence time of approximately 18 hours. The throughput is 200 t/h with the feed at 75% passing 75 µm and pulp density 50% solids. Oxygen is injected into the tanks to obtain DO (dissolved oxygen) levels of approximately 25 ppm, while the cyanide concentration is maintained at approximately 200 ppm. The pH ranges between 9.6 and 10.2.

The plant currently achieves an extraction of approximately 67% in the leach section and a final extraction of 86% after adsorption. It is undesirable for leaching to be far from completion before the slurry contacts the carbon because firstly, oxygen as well as cyanide is limited, which limits the amount of gold that actually goes into solution. Secondly, carbon flows countercurrent to the slurry, thus gold losses are likely to occur (especially in the last tank) as the carbon will be pumped upstream without accessing the rest of the soluble gold. The unsatisfactory extraction in the leach section could be attributed to:

- The presence of sulphides like pyrrhotite and arsenopyrite, which can consume cyanide as well as oxygen during leaching.
- Preg-borrowing constituents in the ore, which results in a high content of gold in the leach residue, which is subsequently desorbed from the preg-borrowing constituent by competitive adsorption onto the more active activated carbon in CIP.
- Insufficient residence time in the leach section for the current throughput.

The aim of this research was therefore to investigate whether it is possible to improve the leaching performance, by investigating the following:

- Whether varying certain leach parameters can improve the extraction
- The impact of adding lead nitrate on gold extraction and cyanide consumption
- The possible benefits of CIL (carbon in leach)
- The impact of extending the residence time.

* *Department of Mining and Process Engineering, Namibia University of Science and Technology, Namibia.*

© *The Southern African Institute of Mining and Metallurgy, 2018.* *ISSN 2225-6253. Paper received Apr. 2018.*

Test work to examine the potential for improving gold leaching performance at Navachab

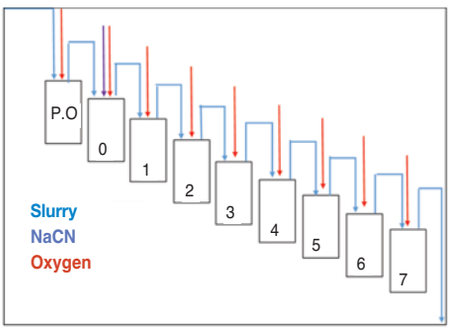

Figure 1—Layout of the leach section

Experimental

Factorial design tests

The three factors investigated were cyanide concentration, pH, and lead addition (as lead nitrate). In order to allow all combinations of factors and levels to be incorporated, a full factorial design was generated using Minitab (2010). Table I shows the different factors and the levels at which they were investigated. Each run was replicated.

The leach tests were carried out using the standard bottle roll method. A slurry sample was collected from the leach feed distribution box. The sample was then filtered and dried. Tap water was added to achieve the desired pulp density of 50% solids. Sodium hydroxide was used for pH modification and 99.5% pure oxygen was bubbled into the slurry. The dissolved oxygen (DO) levels were maintained above 8 mg/l for the duration of each test. Lead nitrate, when used, was added during the first hour. A 20% NaCN (sodium cyanide) solution was then added to achieve the desired concentration and the bottle was rolled for 48 hours. The pH was monitored regularly and adjusted with sodium hydroxide. Samples were taken at 2-hour intervals and filtered, and the filtrate and residue were submitted to the Navachab laboratory for analysis. All samples were analysed for gold to determine the metal extraction. The filtrate was also analysed for final cyanide concentration by titration with silver nitrate.

CIL tests

The objective of this test was to observe the effect of adding carbon earlier during leaching. This test was carried out using the standard bottle roll procedure as outlined above. Table II shows the parameters for the CIL test.

Extended residence time tests

The objective of this test was to observe the effect of extending the residence time on the extraction. A sample of 4 litres was collected from tank 7 (the last tank in the leach train) and subjected to further leaching using bottle roll tests. Table III shows the parameters for the extended residence time test. The test was duplicated.

Monitoring of batch reactor

The Navachab team was also interested in investigating how an extended residence time would affect the extraction on a plant scale. Tank 7 was bypassed and allowed to run in batch mode for 24 hours. The conditions in the reactor mimicked those of the plant in terms of pH, cyanide and dissolved oxygen concentration, and slurry density. Two runs of this test were conducted. Samples were taken at predetermined time intervals. The filtrate and solids were analysed to determine the gold extraction as well as cyanide concentrations. Table IV shows the parameters for the extended residence time test.

Results and discussion

Factorial design tests

It can be observed from Figure 2 that an increase in the cyanide concentration from 200 ppm to 400 ppm resulted in a 0.5% increase in extraction. An increase in cyanide concentration accelerates leach kinetics.

According to Miguel (2014), sulphide ions adsorb strongly onto the gold surface, which suppresses gold leaching. The introduction of lead nitrate resulted in a 2.28% increase in extraction. Studies have shown that the addition of lead nitrate can be beneficial to gold leaching kinetics.

Table I

Factors and their levels for the full factorial design experiment

Level	Pb ion concentration (ppm)	pH range	Initial cyanide concentration (ppm)
1	0	9.6–10.2	200
2	100	10.5–11	400

Table II

CIL test parameters

pH	% solids	Target DO concentration (mg/l)	Leach time (h)	Carbon concentration (g/l)
9.6–10.2	50	>8	48	30

Table III

Extended residence time test parameters

Target CN concentration (ppm)	pH	% solids	Target DO concentration (mg/l)	Leach time (h)
150	9.6–10.2	50	>8	24

Table IV

Plant residence time test parameters

Target CN concentration (ppm)	pH	% solids	Target DO concentration (mg/l)	Leach time (h)
150	9.6–10.2	50	>8	24

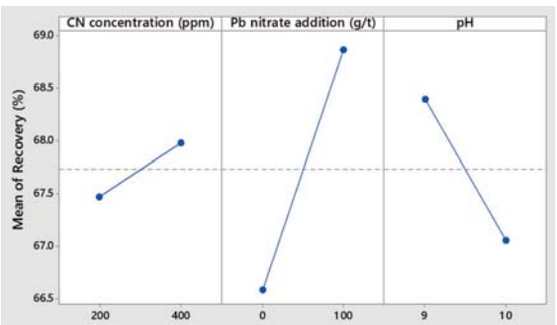

Figure 2—Main effects plot for extraction

Lead passivates the surface of reactive sulphides and forms insoluble lead sulphide, thus effectively preventing the solution from contacting the sulphides. Lead also decreases complexation with cyanide, thereby reducing cyanide consumption.

An increase in the pH range from 9.6–10.2 to 10.5–11 resulted in a 1.34% decrease in extraction. The electrochemical driving force for gold dissolution is maximized at pH values between 9.0 and 9.5 (Marsden and House, 2006). Thus, it can be inferred that the leach kinetics were likely faster at lower pH values of 9.6–10.2.

Figure 3 shows the main effect of each factor on the cyanide consumption. An increase in the cyanide concentration from 200 ppm to 400 ppm resulted in a 23 g/t increase in cyanide consumption.

The introduction of lead nitrate resulted in a 34 g/t decrease in cyanide consumption. According to La Brooy, Linge, and Walker (1994), reactions involving sulphides may consume cyanide and oxygen and produce various solution species that can decrease the efficiency of gold leaching. Pyrrhotite is the most reactive iron sulphide mineral in cyanide:

Pyrrhotite >>> Marcasite > Arsenopyrite > Pyrite

The addition of lead nitrate could have resulted in the passivation of these cyanide consumers, resulting in a decrease in the amount of cyanide consumed.

An increase in the pH range from 9.6–10.2 to 10.5–11 resulted in an 11.9 g/t decrease in cyanide consumption. This is probably due to the fact that less cyanide is lost as hydrogen cyanide gas at higher pH values. At a pH of around 9.3, half of the total cyanide is available as HCN (hydrogen cyanide) and half as free cyanide ions. Above pH 10, more than 90% of the total cyanide is available as free cyanide ions, while at a pH of around 8.4 more than 90% of the total cyanide is present as hydrogen cyanide gas. In order to reduce cyanide loss as HCN, cyanide leaching is usually conducted at a pH between 10 and 11 (Marsden and House, 2006).

Higher order interactions were calculated using Minitab (2010) and found to be minimal, and are thus neglected.

CIL tests

Figure 4 shows that the CIL test achieved the highest average extractions based on both solids and solution analysis. Carbonaceous components in the ore can adsorb dissolved gold during leaching, thus reducing gold extraction. It has been reported that in some cases, as little as 0.1% carbon can have preg-robbing (removing gold from solution irreversibly) or preg-borrowing (removing gold from solution reversibly) properties (Marsden and House, 2006). The higher extractions by CIL are an indication of possible preg-borrowing during the normal leach, which is eliminated by the addition of activated carbon during leaching, thus indicating the benefit of CIL.

Extended residence time and batch reactor tests

Extending the residence time by 4 hours resulted in a significant decrease in the solid residue grade, from 0.66 g/t to 0.43 g/t. This benefit is also confirmed by the extraction curves (Figure 5), which show an increase in the extraction of more than 5% with the longer residence.

Figure 6 shows the trend lines obtained from the results of the tank 7 test. It can be observed that the extraction increases with time, which shows the potential benefits of adding an extra tank to the leach circuit. The retention time determines the contact time between gold particles and reagents. Typical residence times in a leach section may range from 12–48 hours, depending on the head grade and nature of the ore (Marsden and House, 2006). In practice, most gold plants tend to operate between 24–36 hours' residence time.

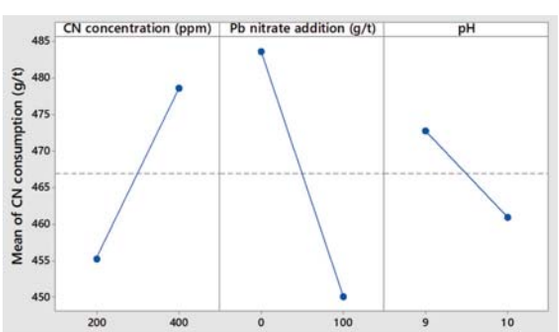

Figure 3—Main effects plot for cyanide consumption

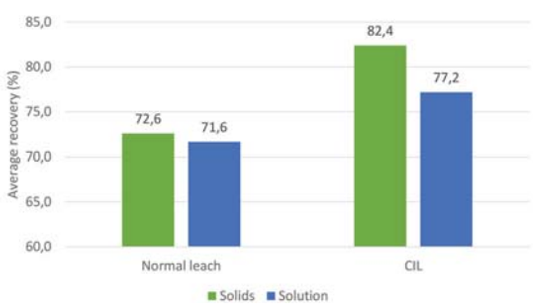

Figure 4—Comparison of extraction by CIL and normal leaching

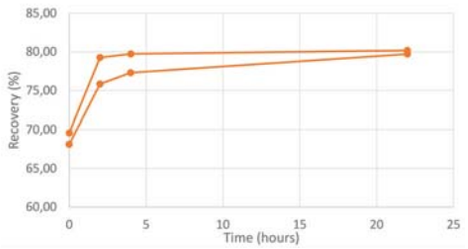

Figure 5—Gold extraction *vs.* additional leaching time for leach solids from tank 7

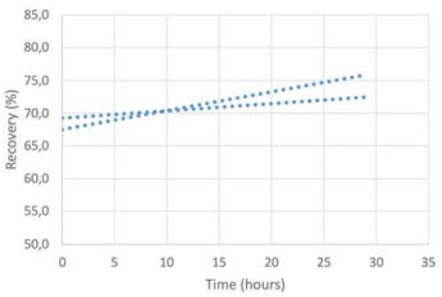

Figure 6—Gold extraction in tank 7 *vs.* time

Cost analysis

Table V shows the cost analysis that was done for the month of July 2017. The gold price used is that for 17 August 2017.

An increase in cyanide dosage resulted in a 0.5% increase in gold extraction and a 23 g/t increase in cyanide consumption. Adding lead nitrate to leaching increased the extraction by 2.3% and decreased the cyanide consumption by 34 g/t. The lead nitrate consumption was 100 g/t. Increasing the pH decreased the extraction by 1.3% and decreased cyanide consumption by 12 g/t. A higher sodium hydroxide addition was necessary to maintain the higher pH levels.

The cost benefit of changing each parameter was calculated and evaluated as a percentage of the revenue that Navachab achieved for the month of July. The cost analysis showed that an increase in the cyanide concentration and the introduction of lead nitrate can have potential financial benefits. However, an increase in the pH value resulted in a negative net benefit.

Conclusions

An increase in the cyanide levels improves gold extraction but results in increased cyanide consumption. However, the cost analysis showed an overall benefit of increasing the cyanide levels. The addition of lead nitrate improves extraction and reduces cyanide consumption. The introduction of lead nitrate could be very advantageous to Navachab's leaching circuit. An increase in pH reduces cyanide consumption but also reduces gold extraction. This resulted in a negative net benefit.

CIL shows potential benefits in terms of extraction. The ore might contain preg-borrowing matter to the point where it is limiting the extraction of gold. On the other hand, extending the residence time showed similar results to the CIL tests. Thus adding an extra tank to the circuit might be more beneficial to the process than choosing a CIL route. Finally, the results indicate that there is possibly leaching taking place after 18 hours of residence time.

The following measures are recommended.

- Increase cyanide levels but monitor the amount of cyanide lost to the tailings to prevent any environmental issues.
- Plant trials should be performed to verify the benefit of lead nitrate addition. Navachab can decide whether the lead nitrate will be purchased in solution form or as dry crystals. If it is bought in solid form, then a make-up facility will be required. The lead nitrate can be dosed before or during leaching. According to Miguel (2014), these trials can last up to 3 months, and the benefits should be observable after a month.
- Maintain current pH levels.
- Conduct more trials on tank 7, as only two runs were conducted during the course of this research.
- Further test work should be conducted on the benefits of CIL and increasing the residence time.

Acknowledgements

The authors wish to acknowledge Navachab Gold Mine for facilitating this project and the Navachab laboratory team for working tirelessly to analyse all the samples on time. The guidance of Mr Hildebrand Wilhelm, Mr Innocent Matsika, Mr Georg von Oppen, Mr. Jakobus Apollus. and the staff of the Department of Mining and Process Engineering, Namibia University of Science and Technology, is greatly appreciated.

References

La Brooy, S.R., Linge, H.G., and Walker, G.S. 1994. Review of gold extraction from ores. *Minerals Engineering*, vol. 7, no. 10. pp. 1213–1241.

Marsden, J.O. and House, C.I. 2006. The Chemistry of Gold Extraction. 2nd edn. Society for Mining, Metallurgy & Exploration, Littleton, CO.

Miguel, B. 2014. Lead into gold- A review of the use of lead nitrate to extract more gold. *Proceedings of ALTA 2014 Gold-Precious Metals Sessions*, Perth, Australia, 29-30 May 2014. ALTA Metallurgical Services. pp. 139–150.

Minitab, 2010. Minitab 17 Statistical Software. State College: Minitab, Inc.

Nortemann, M., Mucke, A., Weber, K., and Meinert, L. 2000. Mineralogy of the Navachab skarn deposit, Namibia: an unusual Au-bearing skarn in high-grade metamorphic rocks. *Communications of the Geological Survey of Namibia*, vol. 12. pp. 169–177. ◆

Table V

Cost analysis for the month of July 2017

	Increased cyanide	Lead nitrate addition	Higher pH range
Extraction (%)	+ 0.5	+ 2.3	- 1.3
Cyanide consumption (g/t)	+ 23	- 34	- 12
Lead consumption (g/t)		+ 100	
NaOH consumption (g/t)			+ 426
Cost benefit as a percentage of revenue (%)	0.61	3.1	- 1.9

- Decrease + Increase

http://dx.doi.org/10.17159/2411-9717/2018/v118n5a3

Numerical analysis and case study on the mitigation of mining damage to the floor of no. 5 coal seam of Taiyuan Group by grouting

by A. Li*, Y. Liu†, L. Mou†, and K. Li‡

Synopsis

Based on the geological condition of panel 22507 of the no. 5 coal seam at Dongjiahe coal mine, numerical analysis of the stability and water permeability of the floor aquiclude before and after grouting was conducted using Rock Failure Process Analysis (F-RFPA2D). The dynamic development, extension, and distribution of the cracks in the aquiclude are discussed. It is shown that grouting can increase the effective thickness of the aquiclude, reduce the floor damage depth, and control the floor water inrush path, thus effectively improving the overall strength and water blocking capability of the aquiclude. These numerical study results were applied to facilitate relevant engineering work at Dongjiahe coal mine. The mitigation measures involved grouting the floor of the no. 5 coal seam, allowing panel 22507 to be mined safely above confined water. This exercise provided invaluable experience in preventing water inrush hazards.

Keywords
grouting, aquiclude, aquifer, numerical analysis, field practice.

Introduction

As the mining depth in the Chenghe mining area of the Weibei coalfield has increased, the coal seam floor has been subject to increasing pressure from the Ordovician limestone overburden, which in turn has increased the potential hazard of water inrush (Li, Gu, and Chen, 2013; Wang and Park, 2003; Wei *et al.*, 2010; Wu, Jiang, and Zhai, 2011; Zhang and Shen, 2004; Zhang, 2005). The Dongjiahe coal mine is one of the major mines in the Chenghe mining area (Li *et al.*, 2015). Following decades of mining, the upper seams are almost mined out and most of the mining activities have moved to the lower no. 5 coal seam. The no. 5 seam is located above the Ordovician limestone and K2 aquifers of the Taiyuan Group, with the former posing the main threat to mining safety. The distance between the no. 5 seam and the Ordovician limestone aquifer is about 25–35 m, leading to a very high possibility of water inrush hazard. Currently, considerations of cost, environmental impact, and feasibility dictate that mining under high water pressure is the main method used to extract the coal resources above confined water (Li *et al.*, 2015; Lu *et al.*, 2015). However, the water inrush risk associated with this method is high (Feng and Jiang, 2015; Li and Wang, 2003), making it very important to protect the coal seam floor effectively (Guan, Li, and Lu, 2003; Liu, 2008; Yang *et al.*, 2007). Much fruitful research has been conducted on the mechanism of floor water inrush (Duan, 2014; Jiang, 2011; Liu and Hu, 2007; Liu *et al.*, 2013; Wang *et al.*, 2004; Wang 2012). However, very little has been done to better understand how to protect coal seam floors, although a few studies have assessed issues such as floor damage during mining, stress distribution, and seepage before and after coal seam floor mitigation (Chen, Xie, and Jing, 2006; Lu and Wang, 2015; Yuan, Li, and Jiao, 2015).

In this study, the lithology of the floor strata of the no. 5 coal seam in Dongjiahe coal mine was used as a basis for a systematic assessment of coal seam floor damage under high water pressure before and after floor mitigation. The Rock Failure Process Stress-Seepage Coupling Analysis software (F-RFPA2D) was used to model coal seam floor damage in detail under the coupling of seepage and stress fields. The dynamic process of initiation, development, connection, and forming of water-conducting paths was analysed. The numerical modelling results were used to design and plan a floor grouting field test on the K2 aquifer. This theoretical analysis and field floor grouting test provide significant insight into water inrush prediction, mining method optimization, and safety evaluation for both the no. 5 seam and the Chenghe mining area as a whole.

* *School of Architecture and Civil Engineering, Xi'an University of Science and Technology, China.*
† *Hydrogeological Research Institute, China Coal Technology & Engineering Group, China.*
‡ *Department of Mining Engineering, West Virginia University, USA.*

© *The Southern African Institute of Mining and Metallurgy, 2018.* *ISSN 2225-6253. Paper received Nov. 2015; revised paper received May 2016*

Hydrogeological conditions

Panel 22507 of the no. 5 coal seam in Dongjiahe coal mine was selected for field testing. The panel is located at the east side of the downhill belt entry of the second mining area, with solid coal to the north and a 30 m barrier pillar to the south. The average thickness of the coal seam is 3.6 m and the elevation of the panel is around +255 to +273 m. The length of the panel in the strike direction is 910 m and the width in the dip direction is 114 m. The panel is mined using longwall extraction with roof caving. The average inclination of the coal seam is 3°. The no. 5 coal seam is located in the upper section of the Taiyuan Group. The immediate roof is hard grey K4 medium sandstone with a thickness of 10.9–18.15 m. The immediate floor is dark grey coarse siltstone with a thickness of 0.2–3.21 m, while the main floor is fine K3 quartz sandstone or siltstone with a thickness of 3.4–7.8 m. Based on documented data, the panel is in a very complicated hydrogeological condition and is mined above confined water. The distance between the bottom of the coal seam and the top of the Ordovician limestone is about 28 m, which poses a high potential for water inrush.

The hydrogeological data shows that the roof of panel 22507 is composed of medium-grained and other types of sandstone, while the floor of the no. 5 coal seam is composed of medium-grained sandstone, mudstone, and thin limestone. This section of the strata has medium consolidation, good compactness, and very few cracks, indicating a high-quality aquiclude that blocks water inrush from the Ordovician limestone. However, there is a weak to medium karst fracture aquifer between the no. 5 seam and the Ordovician limestone aquifer. This aquifer is composed of Upper Carboniferous Taiyuan Group quartz sandstone and K2 limestone, with a high water content at high pressures. These characteristics and the short distance between the aquifer and the no. 5 seam constitute a significant threat to the mining of the seam.

Numerical simulations

Rock Failure Process Stress-Seepage Coupling Analysis software (F-RFPA2D) was employed to study the mitigation of K2 aquifers using floor grouting. Based on this stress-seepage coupling analysis, the dynamic process of fracture initiation, development, connection, and formation of water-conducting paths at the floor aquiclude of panel 22507 was simulated and analysed.

Numerical model

The physical and mechanical parameters used in the numerical simulation were derived from the roof and floor strata lithologies of panel 22507 and are listed in Table I. Figure 1 shows the mechanical model of the panel, with mining occurring above the confined water level, used for numerical simulation. The model is 230 m in length and 100 m in height, with 230 × 100 (total 23 000) elements. From top to bottom, the strata in the model are main strata, main roof, immediate roof, coal seam (4 m), upper aquifer (14 m), K2 aquifer (7 m), lower aquiclude, and Ordovician limestone aquifer. The aquiclude at the top of the Ordovician limestone aquifer comprises the no. 10 coal seam and aluminous mudstone. The water head at the Ordovician limestone aquifer is 140 m.

The bottom of the model was fixed in the vertical direction and the two corner points at the bottom and side were fixed in both the vertical and horizontal directions. The

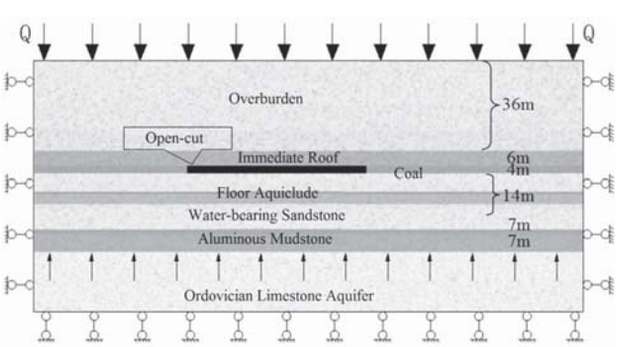

Figure 1—Mechanical model for numerical simulation

Table I

Physical and mechanical parameters

Lithology	Thickness (m)	Young's modulus *E* (Mpa)	Tensile strength f_c (Mpa)	Angle of friction *Φ* (°)	Poisson's ratio *μ*	Unit weight γ (kg·m-3)	Permeability (K/m·d-1)	Pore pressure factor *α*
Siltstone	18	8800	4.5	26	0.24	2500	0.1	0.04
Medium sandstone	10	8500	2.9	28	0.26	2450	0.1	0.04
Fine sandstone	8	7800	2.4	29	0.28	2450	0.1	0.04
Sandy mudstone	6	2850	0.7	32	0.33	2200	0.01	0.002
No. 5 coal	4	1650	0.8	36	0.32	1500	0.02	0.002
Quartz sandstone	2	8850	4.8	25	0.24	2650	0.1	0.04
Fine sandstone	4	8500	3.3	26	0.28	2400	0.1	0.04
No. 6 coal	1	1700	0.7	36	0.32	1540	0.02	0.002
Sandy mudstone	4	3500	1.2	36	0.34	2200	0.01	0.002
Thin siltstone	3	8200	3.5	28	0.26	2450	0.1	0.04
K_2 aquifer	7	8850	3.7	26	0.25	2650	60	0.6
No. 10 coal	1	2000	0.8	38	0.33	1520	0.02	0.002
Aluminous mudstone	6	2800	0.7	35	0.35	2050	0.01	0.002
Ordovician limestone	26	10 000	8.0	30	0.26	2600	100	1.0

two sides were fixed in the horizontal direction. The top and bottom of the model consisted of water-confining boundaries. The overburden depth was 350 m, which was loaded on top of the model as a distributed stress (Q) of 6.6 MPa based on an average overburden strata density of 2150 kg/m^3. The numerical simulation was conducted in a stepwise manner: in the first step, the self-weight of the strata was balanced; in the following steps, mining commenced 65 m from the left boundary. The mining distance for each step was 8 m, with a total mining distance of 96 m over 13 mining steps.

Numerical simulation analysis without grouting

The first numerical model iteration simulated the mining process without grouting of the floor. The development and distribution of floor fractures, abutment pressure, and floor seepage characteristics are discussed in the following sections.

Floor fracture development and distribution

Figure 2 shows the dynamic development and extension of the floor fractures and their distribution in the floor aquiclude of the no. 5 seam. Four steps with face advances of 16, 48, 56, and 72 m were selected for demonstration.

As the coal seam is mined, the roof and floor strata begin to break. When the face advances to 16 m, the immediate mudstone roof over the gob area breaks for the first time, with a roof break height of 6 m. Some tensile shear failure zones develop in the floor under the gob area, with a damage depth of about 2 m. The floor demonstrates good water-blocking capability. Slight floor heave of about 46.2 mm occurs in the centre of the gob area, as shown in Figure 2 (step 3).

When the face advances to 48 m, the fractures in the roof rock beam propagate upward continuously and the first weighting occurs on the main roof. The roof caving height is about 11 m. The floor tensile shear failure zone extends deeper, inducing serious damage to the main floor extending to 7 m depth The floor heave increases to about 53.2 mm, as shown in Figure 2 (step 7).

When the face advances to 56 m, the fractures in the roof strata continuously propagate to the medium sandstone layer. The first periodic weighting occurs on the main roof. The voids under the gob area increase and the fractures on the floor continuously extend to the low-strength sandy mudstone layer owing to tensile and compressive shear action. The overlying hard rock strata all fail and lose their water-blocking characteristics. At this point, the floor damage reaches 10 m depth. Erosion by water in the K2 aquifer leads to the creation of a 1 m thick progressive fracture zone about 2 m away from the floor damage zone, which stops the development of fractures. The maximum floor heave is about 85.6 mm, as shown in Figure 2 (step 8).

When the face advances to 72 m, periodic weighting continues on the main roof. However, owing to the strong sandstone layer in the overburden, the roof fracture does not propagate to the surface. The floor aquiclude is now in a state of unloading, and the floor tensile shearing failure continues to develop under the combined effects of mining abutment pressure and seepage fields. The fractures finally penetrate the fine sandstone layer above the aquifer and connect to the progressive fracture zone in the K2 aquifer, forming a water-conducting path. Water confined within the aquifer seeps through the fractures in the floor aquiclude and enters the gob area, resulting in a floor water inrush. The floor bending heave increases rapidly to a maximum of 433.8 mm, as shown in Figure 2 (step 10).

Abutment pressure distribution

Figure 3 shows the shear stress distribution on the floor of the seam. The various degrees of brightness represent changes in the magnitude of the shear stress. Figure 4 and Table II show the floor strata shear stress, support pressure, major and minor principal stresses, and peak stresses at the open cut and face front areas as the longwall face advances.

As the face advances, stress redistribution around the mining area induces symmetrically distributed shear stress on the sidewall of the gob, as shown in Figure 3 (step 3). Stress concentration occurs at the open cut and face front areas. When the face advances to 16 m, first weighting occurs on the immediate roof. At this moment, the floor peak shear stresses are 4.6 and 5.2 MPa at the open cut and face front areas respectively, the corresponding support peak stresses are 13.8 and 14.9 MPa, the major principal stress peaks are 14.6 and 14.9 MPa, and the minor principal stress peaks are 5.2 and 4.8 MPa, as shown in Figure 4 and Table II.

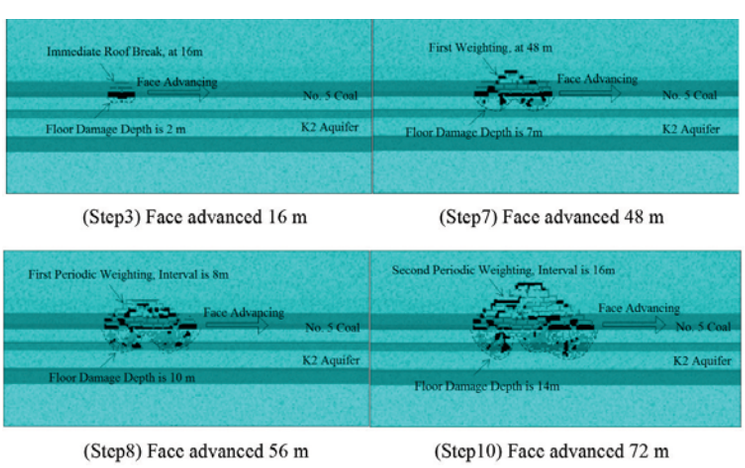

Figure 2—Dynamic development of floor fractures and their distribution

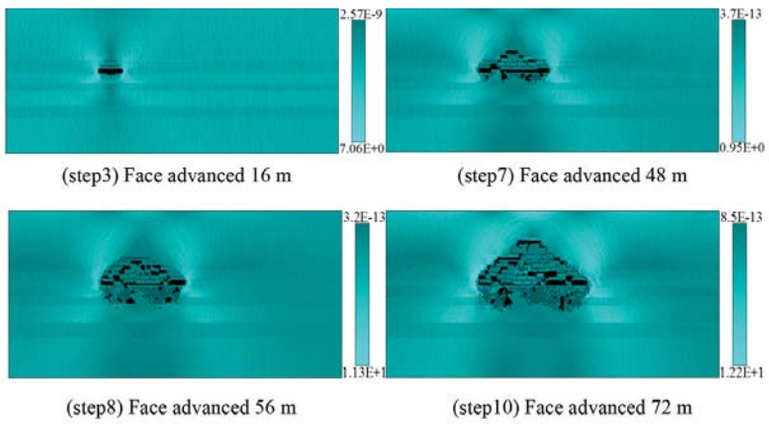

Figure 3—Shear stress distribution and shear failure zone of floor strata

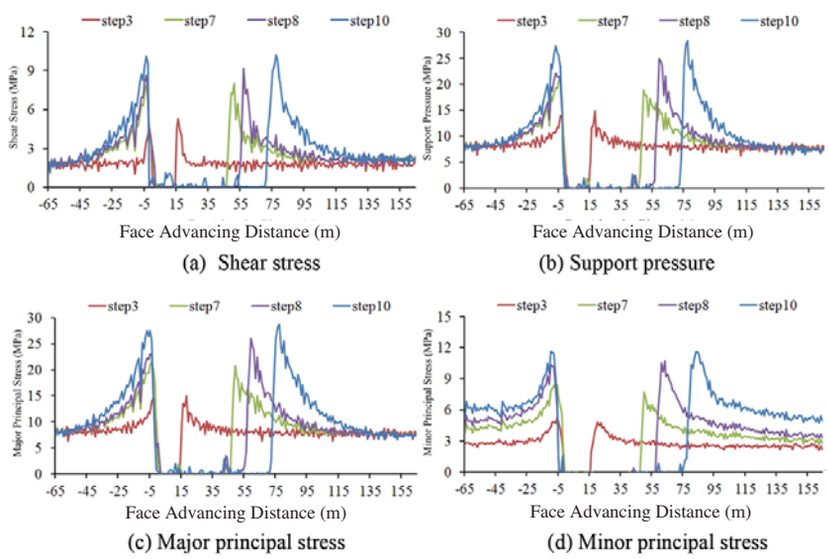

Figure 4—Stress distributions on floor

Table II

Floor peak stresses at different mining stages

Location	Step	Shear stress σ_{rmax} (MPa)	Support pressure σ_{vmax} (MPa)	Major principal stress σ_{1max} (MPa)	Minor principal stress σ_{3max} (MPa)
Open cut	Step 3	4.6	13.8	14.6	5.3
	Step 7	7.8	20.7	21.5	8.4
	Step 8	8.5	22.2	22.9	10.6
	Step 10	10.2	27.4	27.4	11.5
Face front	Step 3	5.2	14.9	14.9	4.8
	Step 7	8.0	18.8	20.7	7.6
	Step 8	9.1	25.0	25.8	10.7
	Step 10	10.3	28.5	28.6	11.8

The shear failure area on the gob sidewalls increases as the face advances, with the shear stress symmetrically distributed as shown in Figure 3 (step 7). When the face advances to 48 m, the stress concentration increases at both the open cut and face front areas, inducing the first weighting of the main roof. The damage zone in the floor under the gob extends downward and the area of tensile shear failure increases. At this point, the floor peak shear stresses are 7.8 and 8.0 MPa at the open cut and face front areas, respectively, the corresponding support peak stresses are 20.7 and 18.8 MPa, the major principal stress peaks are 21.5 and 20.7 MPa, and the minor principal stress peaks are 8.4 and 7.6 MPa.

As the face advances, the floor shear failure area under gob increases from the combined effects of abutment pressure and water pressure. The stress concentrations at the

open cut and face front areas both increase. When the face advances to 56 m, a 1 m-thick progressive fracture zone forms in the fine sandstone layer at the top of the K2 aquifer. At this point, the floor peak shear stresses are 8.5 and 9.1 MPa at the open cut and face front areas, respectively, the corresponding support peak stresses are 22.2 and 25.0 MPa, the major principal stress peaks are 22.9 and 25.8 MPa, and the minor principal stress peaks are 10.6 and 10.7 MPa.

When the face advances to 72 m, the floor deformation increases rapidly owing to the combined effect of mine abutment pressure and seepage. There is a large tensile shear failure area in the floor aquiclude and the damage depth exceeds 13 m. The mining-induced floor fractures connect with the progressive fracture zone in the sandstone layer and form a water-conducting path. As shown in Figure 3 and Table II, the stress concentrations at the open cut and face front areas are fairly high. At this point, the floor peak shear stresses are 10.2 and 10.3 MPa at the open cut and face front areas, respectively, the corresponding support peak stresses are 27.4 and 28.5 MPa, the major principal stress peaks are 27.4 and 28.6 MPa, and the minor principal stress peaks are 11.5 and 11.8 MPa

Floor seepage analysis

Figure 5 shows the floor water flow rate vector distribution for the seam and the floor vertical flow volume curves under the gob area. Table III shows the maximum floor flow rate at each mining step.

As the face advances, the water flow rate and volume increase under the gob area. When the face advances to 16 m, the floor water flow rate is relatively small – only about 1.66×10^{-2} m/h – and the floor water inrush is mainly from the fracture water in the mining fracture zone of the immediate floor. The water flows through the open cut area and the mining face into the gob area. At this point, a sandy mudstone layer still exists between the floor fracture zone and the K2 aquifer, despite the aquifer's water pressure, and the top of the aquifer does not connect to the floor fracture zone. (Figure 5, step 3)

When the face advances to 48 m, the floor water flow rate increases to 8.51×10^{-2} m/h and the water inrush is mainly from the fractures in the quartz sandstone and fine sandstone layers in the immediate floor. The water outlet locations are mostly in the gob area. The effective aquiclude above the K2 aquifer still has very good water-blocking capability.

When the face advances to 56 m, the floor tensile shear failure range of the aquiclude increases under the combined effect of abutment pressure and high water pressure. This damage propagates to the sandy mudstone layer above the K2 aquifer, with a damage depth of about 10 m, and the water flow rate increases to 2.45×10^{-1} m/h, as shown in Table III. The water outlet locations are mostly in the centre of the gob area, the open cut area, and the mining face area. Owing to the effects of erosion due to the high pressure water, a 1 m forward fracture zone occurs in the K2 aquifer. The floor fracture zone still does not connect to the K2 aquifer and no water-conducting path forms.

When the face advances to 72 m, the floor damage depth extends downward and the effective thickness of the floor aquiclude decreases. The high-pressure water in the K2

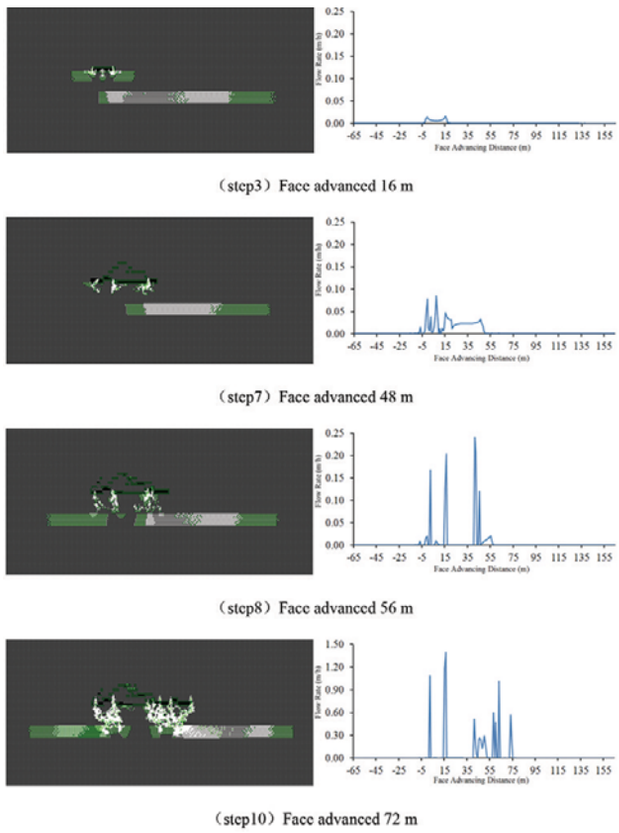

Figure 5—Floor water flow rate vector distribution and the floor water flow volume under gob area

Table III

Maximum water flow rates (m/1) at each mining step

Step 3	Step 4	Step 5	Step 6	Step 7	Step 8	Step 9	Step 10
1.66E-2	2.98E-2	4.33E-2	5.67E-2	8.51E-2	2.45E-1	3.87E-1	1.39

aquifer breaks the sandstone layer and the floor fracture zone and connects to the gob area, forming a water-conducting path. The floor water flow volume increases rapidly and the floor water flow rate increases to 1.39 m/h, which is three times the flow rate before the water inrush. Finally, the combined effects of the abutment pressure and seepage field causes the high-pressure water in the aquifer to flow into the gob area through the conducting path in the floor aquiclude, resulting in a water inrush.

Discussion

Based on the above numerical simulation results, the following observations can be made.

Taking the floor strata lithology into consideration, the floor strata between the no. 5 coal seam and the Ordovician limestone aquifer are essentially composed of soft and hard rock layers, a strata composition that has good water blocking qualities. The top of the floor aquiclude comprises a high-strength, hard rock layer, while the top of the Ordovician limestone aquifer comprises a thick aluminous

mudstone with a high water-blocking capacity. However, the middle of the floor aquiclude consists of the K2 aquifer composed of quartz sandstone and K2 limestone, with highly developed fractures. The presence of this K2 aquifer reduces the stability and the water-blocking capability of the floor aquiclude.

Based on the numerical simulation results, the influence of mining activity on floor deformation will be very small in the initial stage of mining, even with a confined aquifer within the floor aquiclude. As the mining face advances, the floor damage depth will be extended as the aquiclude above the aquifer is impacted by confined water seepage. Finally, when the progressive fracture zone connects with the floor damage zone, a water-conducting path is formed. The water in the sandstone layer will rush into the gob area through the water-conducting path with an inrush volume proportional to the water pressure of the aquifer.

Compared to the high-pressure and high-volume water in the underlying Ordovician limestone aquifer, the water inrush from the K2 aquifer is relatively small. If the floor damage zone is not connected to the Ordovician aquifer, the water inrush from the K2 aquifer will not cause serious problems. However, if a potential water-conducting path exists between the quartz sandstone or K2 limestone layer and the Ordovician limestone aquifer, the water in the latter will refill the aquifer and flow to the mining face, resulting in a hazardous water inrush accident.

Numerical simulation analysis with floor grouting

Numerical analysis was conducted to determine the effects of mitigation of the coal seam floor on the K2 aquifer. Mitigation measures to improve the total strength and water-blocking characteristics of the floor's effective aquiclude were assessed. The simulation used the numerical model shown in Figure 1. The rock mechanics parameters were identical for each stratum, save for the strength, permeability, and pore pressure of the 7 m thick K2 aquifer. Table IV shows a comparison of the rock mechanics parameters before and after mitigation.

The numerical simulation was conducted in a stepwise manner: first, the self-weight of the strata was balanced, and then mining commenced at 65 m from the left boundary in 14 steps of 8 m out to a total mining distance of 104 m.

Floor fracture development and distribution

Figure 6 shows the dynamic development and extension of the floor fractures and their distribution on the floor aquiclude of the no. 5 coal seam after K2 aquifer grouting mitigation. Four steps with face advance distances of 40, 56, 88, and 96 m are selected for demonstration.

As the coal seam is mined, stress concentrations occur at the open cut and mining face areas, and the roof and floor strata start to break. When the face advances to 40 m, the main roof of fine sandstone over the gob area undergoes first weighting, and the roof break height is about 11 m. The floor under the gob area develops some tensile shear failure zones and the damage depth is about 5 m. A slight floor heave of only 18.7 mm occurs in the center of the gob area, as shown in Figure 5 (step 6).

When the face advances to 56 m, the first periodic weighting occurs on the main roof and the fractures in the roof rock beam propagate upward continuously to a depth of about 14 m. The floor tensile shear failure zone extends deeper, inducing serious damage to the main floor, and the floor damage depth reaches 7 m. The floor heave increases to about 27 mm, as shown in Figure 5 (step 8).

Table IV

Comparison of the rock mechanics parameters of K_2 aquifer before and after mitigation

K_2 aquifer	Thickness (m)	Young's modulus *E* (MPa)	Strength *Σc* (MPa)	Friction angle *Φ* (°)	Poisson's ratio *μ*	Density *γ* (kg·m^{-3})	Permeability K/m·d^{-1}	Pore pressure factor *α*
Before	7	8850	36.5	26	0.25	2650	60	0.6
After	7	8850	40	26	0.25	2650	0.4	0.08

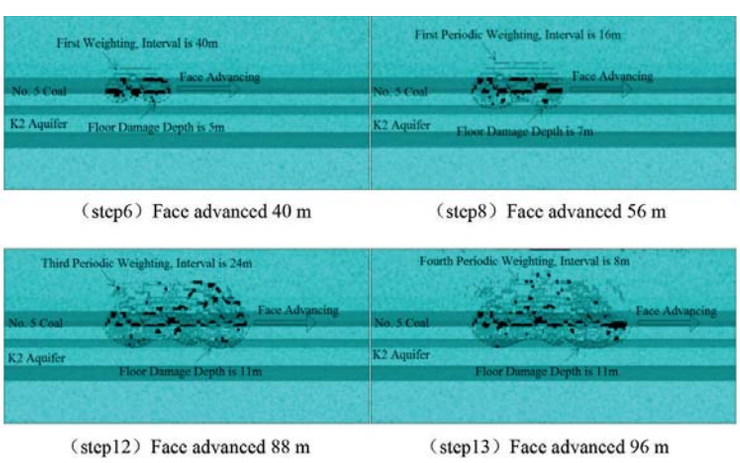

(step6) Face advanced 40 m (step8) Face advanced 56 m

(step12) Face advanced 88 m (step13) Face advanced 96 m

Figure 6—Dynamic development of floor fractures and their distribution after K_2 aquifer grouting mitigation

When the face advances to 88 m, the main roof has already undergone three periodic weightings and the fractures in the roof strata continuously propagate to the medium sandstone layer. The voids under the gob area increase and the fractures in the floor continuously extend to the low-strength sandy mudstone layer owing to tensile and compressive shear action. The hard rock strata above have all failed and have lost their water-blocking characteristics. At this point, the floor damage depth reaches 11 m. The maximum floor heave is about 85.6 mm, as shown in Figure 5 (step 12).

When the face advances to 96 m, periodic weighting occurs again on the main roof. The roof fracture propagates to the surface owing to breakage of the strong sandstone layer in the overburden. The floor tensile shear fractures cease to propagate downward, and the floor damage depth reaches its maximum value of 11 m. The floor bending heave is compacted with caved roof rocks, and the floor heave reduces to 63.5 mm, as shown in Figure 5 (step 13).

Abutment pressure distribution

Figure 7 shows the floor strata shear stress, support pressure, and major and minor principal stresses after K2 aquifer grouting.

The advance of the mining face induces stress redistribution around the mining area. When the face advances to 40 m, first weighting occurs on the immediate roof. At this point, the peak floor shear stress, support pressure, and major and minor principal stresses are 6, 19.5, 19.6, and 6.5 MPa, respectively, at the open cut area. The peak floor shear stress, support pressure, and major and minor principal stresses at the face front area are 5.1, 16.6, 17.0, and 5.8 MPa, respectively.

When the face advances to 56 m, the stress concentration at the open cut and face front areas increases and induces the first periodic weighting of the immediate roof. At this point, the peak floor shear stress, support pressure, and major and minor principal stresses are 9.4, 21.6, 21.6, and 8.4 MPa, respectively, at the open cut area. The peak floor shear stress, support pressure, and major and minor principal stresses at the face front area are 8.8, 19.2, 19.5, and 7.4 MPa, respectively.

As the face advances further, the stress concentration at the open cut and face front areas continues to expand and increase. When the face advances to 88 m, the immediate roof above the gob area has already undergone three periodic weightings. At this point, the peak floor shear stress, support pressure, major principal stress, and minor principal stress are 11.2, 31.3, 31.9, and 12.2 MPa, respectively, at the open cut area. The peak floor shear stress, support pressure, and major and minor principal stresses at the face front area are 12.8, 34.0, 34.1, and 12.8 MPa, respectively,.

When the face advances to 96 m, the immediate roof has incurred additional periodic weightings, the sandstone key stratum breaks, and the floor stress drops back to the *in situ* stress condition. At this point, the peak floor shear stress, support pressure, and major and minor principal stresses are 9.3, 22.1, 22.3, and 8.4 MPa, respectively, at the open cut area. The peak floor shear stress, support pressure, and major and minor principal stresses at the face front area are 8.5, 21.3, 21.6, and 5.7 MPa, respectively.

Floor seepage analysis

Figure 8 shows the floor water flow rate vector distribution of no. 5 coal seam and the floor vertical flow volume curves under the mine gob area after mitigation of the K2 aquifer by grouting.

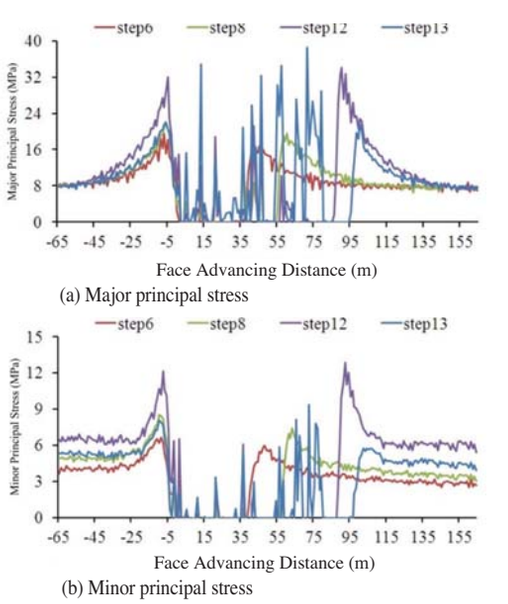

Figure 7—Stress distribution on floor after K_2 aquifer grouting mitigation

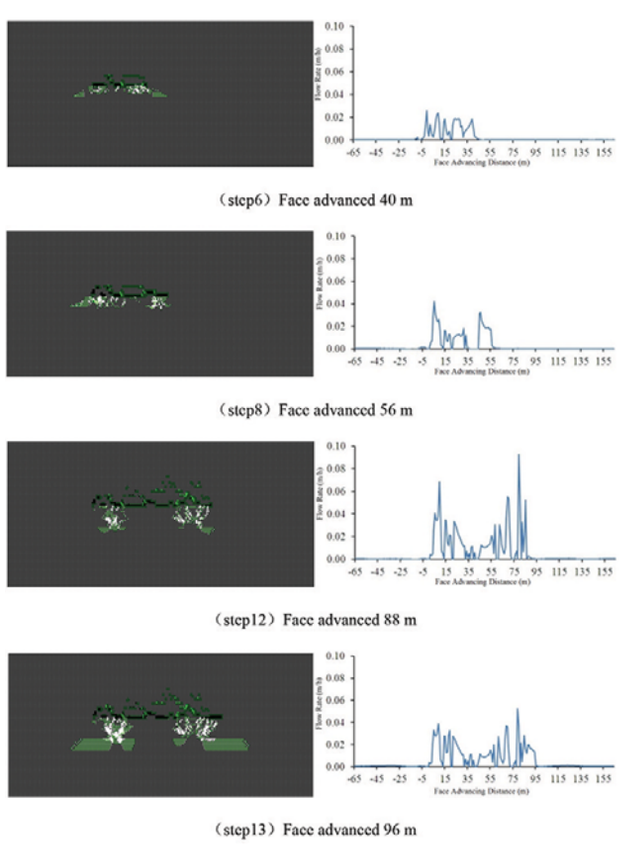

Figure 8—Floor water flow rate vector distribution and the floor water flow volume under gob area after K_2 aquifer grouting mitigation

As the face advances, the water flow rate and volume increase under the gob area. When the face advances to 40 m, the immediate roof undergoes the first weighting and the floor water flow rate is relatively small at only 2.58 × 10^{-2} m/h. The floor water inrush is mainly from the fracture water in the mining fracture zone of the immediate floor. The water flowing outlets are mainly in the gob area, as shown in Figure 8 (step 6).

When the face advances to 56 m, the floor water flow rate increases to 4.21 × 10^{-2} m/h and the water inrush is mainly from the fracture water in the quartz sandstone and fine sandstone layers in the immediate floor. There is an insignificant impact on the water-blocking characteristics of the effective floor aquiclude, as shown in Figure 8 (step 8).

When the face advances to 88 m, the immediate roof has undergone three periodic weightings and the floor damage depth reaches 11 m. The floor water flow rate increases to 9.25 × 10^{-2} m/h. The water outlet locations are mostly in the open cut and gob areas. The floor fracture zone still does not connect to the K2 aquifer and no water-conducting path forms, as shown in Figure 8 (step 12).

When the face advances to 96 m, the roof sandstone key strata break and compact the debris in the gob. The water inrush slows and the water flow rate decreases to 5.25 × 10^{-2} m/h, as shown in Figure 8 (step 13). At this point, the floor damage depth remains 11 m. The floor fracture zone still does not connect to the K2 aquifer and no water-conducting path forms. The floor aquiclude retains its very good water-blocking characteristics. This result indicates that grouting of the K2 aquifer has significantly improved the total strength of the floor aquiclude and the water-blocking characteristics.

Discussion

Based on the results produced by the two numerical models (before and after K2 aquifer grouting mitigation), it can be concluded that grouting can change the K2 aquifer into an aquiclude or weak aquifer, which not only increases the floor water-blocking capability and the total strength, but also reduces the depth of floor damage. The floor water inrush path can be effectively controlled in order to prevent water inrush from the Ordovician limestone aquifer. The numerical simulation methodology and results provide a scientific basis for the engineering practice of floor grouting mitigation for the purpose of preventing water inrush.

Field experiment on floor grouting mitigation

The numerical simulation results described above were applied using field engineering techniques to the floor of panel 22507 of the no. 5 coal seam at Dongjiahe coal mine. The objectives of the exercise were to improve the water-blocking capability and effective thickness of the floor aquiclude (the K2 aquifer) in order to prevent water inrush hazards and ensuring safe production in the mine.

Floor grouting mitigation theory

Based on the effective diffusion radius of grout from a single borehole, it is necessary to drill a sufficient number of grouting boreholes into the floor aquifer at the headgate and tailgate entries. When the designed grouting pressure is applied, the grout material will squeeze into aquifer voids, structural fractures, and water-conducting paths, then consolidate or gelatinize, forming an integrated water-blocking structure. The K2 aquifer will be changed into an effective aquiclude or weak aquifer, which will improve the water-blocking capability and the total strength of the floor aquiclude, reduce the amount of water in the K2 aquifer, and ensure the safety of the retreat mining face.

Procedure

Based on the floor strata lithology and Ordovician limestone aquifer properties and the geological and hydrogeological conditions during the development of the panel, it was decided to construct an exploratory drilling site during development and to drill into the floor in order to inject grout for the purposes of floor condition mitigation. The grout would fill the floor sandstone fractures and change the aquifer into an effective aquiclude or weak aquifer, enabling safe mining above the confined water level.

Layout of the drilling site

Drilling was conducted at the side of the panel. The grouting

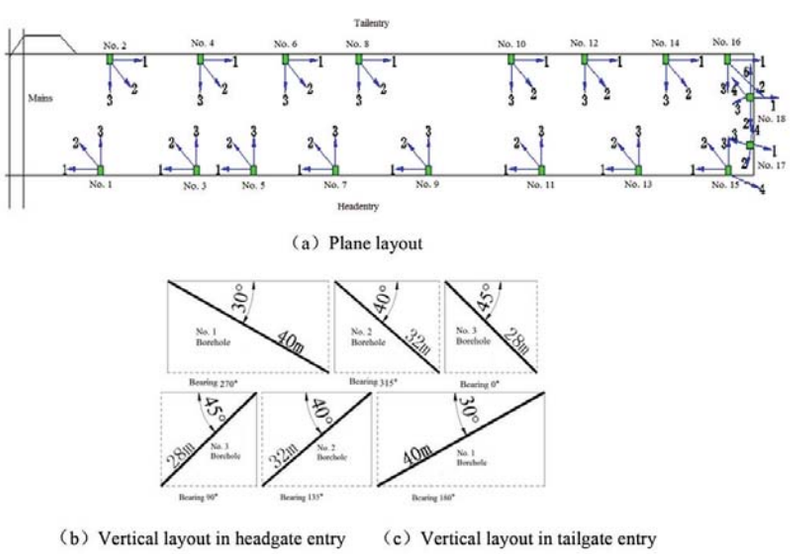

(a) Plane layout

(b) Vertical layout in headgate entry (c) Vertical layout in tailgate entry

Figure 9—Grouting borehole layout at Dongjiahe coal mine

area was determined by the length (910 m) and width (115 m) of the longwall panel. Headgate and tailgate entries were constructed with eight drilling sites each; two drilling sites were also located at the open cut area for a total of 18 drilling sites. The drilling sites were numbered from the beginnings of the entries as 1, 3, 5, 7, 9, 11, 13, and 15 for the headgate entry; 2, 4, 6, 8, 10, 12, 14, and 16 for the tailgate entry; and 17 and 18 for the open cut area. The length, width, and height of the drilling sites were 4 m, 4 m, and 3 m, respectively.

Borehole layout

Based on previous underground grouting experience in the Chenghe mining field, the grout diffusion radius was estimated to be 30–60 m. The grouting depth was selected to be 3 m below the level of impact on the K2 aquifer by mining abutment pressure. In order to inject the grout effectively into the K2 aquifer and reinforce it, the grouting boreholes were designed and planned as shown in the plane layout and vertical views in Figure 9.

There were three boreholes at each drilling site. At the headgate entry, the boreholes were laid at angles of 270°, 315°, and 0° in the vertical plane (plane layout) and at 30°, 40°, and 45° in the horizontal plane. At the tailgate entry, the boreholes were laid at 90°, 135°, and 180° in the plane layout and at 30°, 40°, and 45° to the horizontal plane.

All boreholes were drilled and cored according to this design. For boreholes at different depths, three levels of protection casings were installed, *i.e.*, φ 168 at the first level, φ 108 at the second level, and φ 89 at the third level. Pure cement grout was used to seal the boreholes.

Grouting material

In order to ensure effective grouting and water blocking and reduce the engineering costs, clay grout and cement grout were injected into the floor alternately. Pure cement grout was used when necessary.

Grouting effectiveness

The drilling sites and boreholes were constructed and drilled according to the above design requirements. Figure 10 shows the drilling and grouting process. The overall drilling and grouting process for the panel took 344 days and entailed a total drilling distance of 3796.9 m. Grouting of current boreholes and drilling of future borehole were conducted simultaneously, and the total grouting volume was 41 232.75 m^3. The injection pressures of all boreholes reached the designed value and the pressure stabilization times satisfied the standards requirements. Underground survey and measurements confirmed that all boreholes in the exploration area had no or very little water outflow.

The water flow rates of the boreholes were around 0–0.5 m^3/h, which satisfied the design requirement of 1 m^3/h. Rock sampling and electrical surveying were conducted before and after grouting to verify the grouting effectiveness. The test results show that the floor grouting had significant water-blocking effects and that the mitigation project satisfied design requirements. All boreholes were sealed after grouting.

Prior to grouting mitigation, the water inrush flow rate at panel 22507 was estimated to be 200 m^3/h; after floor grouting mitigation, the measured rate was reduced to less than 60 m^3/h. This represents a saving of up to one million RMB in water drainage cost. The floor-mitigated panel is currently retreat-mined and 375 000 t of coal has been safely extracted, representing an income of about 147.2 million RMB for the company.

Conclusions

A numerical analysis on the simulation of grouting mitigation of the floor of the no. 5 coal seam at panel 22507 of Dongjiahe coal mine was conducted. Based on the geological condition of panel 22507, Rock Failure Process Analysis (F-RFPA2D) software was used to analyse the stability and water-blocking characteristics of the floor aquiclude before and after grouting. The numerical study results were applied at the mine in order to facilitate engineering works, and the proposed mitigation measures employing grouting of the floor of the seam were implemented. As a result, panel 22507 can now be mined safely above the confined water level. This exercise provided valuable experience in preventing water hazards and has resulted in significant economic and social benefits.

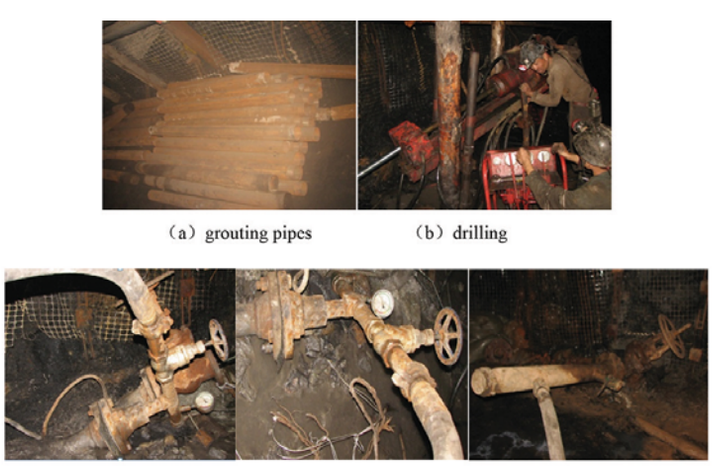

Figure 10—Grouting borehole drilling and grouting at Dongjiahe coal mine

Based on the geological condition of panel 22507, numerical analysis using Rock Failure Process Analysis (F-RFPA2D) was used to predict dynamic crack development, expansion, and distribution in the floor aquiclude under the combined effects of seepage and stress field. Mining damage to the floor aquiclude, stress distribution, and seepage features were analysed.

The results produced by numerical simulation of the panel before and after K2 aquifer grouting mitigation demonstrated that grouting mitigation could change the aquifer into an aquiclude or weak aquifer, which not only increases the floor water-blocking capability and total strength, but also reduces the floor damage depth. The floor water inrush path can be effectively controlled in order to prevent water inrush from the Ordovician limestone aquifer. The numerical simulation methodology and results provided a scientific basis for the engineering practice of floor grouting mitigation for the purpose of preventing water inrush.

The numerical simulation results were applied in a field engineering exercise in which floor grouting mitigation was applied to the floor aquiclude of the K2 aquifer with the goal of preventing water inrush hazards and ensuring safe coal production. The injection pressures of all boreholes reached the designed value and the pressure stabilization times satisfied standards requirements. Underground survey and measurements confirmed that all boreholes had zero or minimal water outflow. The water flow rates of the boreholes were around 0–0.5 m^3/h, which satisfied the design requirement of 1 m^3/h. Rock sampling and electrical surveying were conducted before and after grouting to verify grouting effectiveness, with the test results showing that the floor grouting had significant water-blocking effects and that the project satisfied the design requirements.

The grouting mitigation project solved the problem of water inrush hazard during retreat mining; this effectively reduced the water drainage costs, improved the recovery ratio, and most importantly, ensured the safe mining of the panel. These research results suggested new ideas for mitigating the water inrush hazard at Dongjiahe coal mine and also provided valuable experience for future panel mining above confined water.

Acknowledgements

The authors gratefully acknowledge financial support from National Natural Science Foundation for Young Scientists (41402265). The acquisition of the modelling skills and equipment necessary to complete this project would not have been possible without this support.

References

Chen, X., Xie, W., and Jing, S. 2006. Determination of mechanics parameters of mining induced rock mass for numerical simulation. *Journal of Mining & Safety Engineering*, vol. 23, no. 3. pp. 341–345.

Duan, H. 2014. Analysis on failure features and failure depth of coal seam floor during mining process. *Coal Science and Technology*, vol. 42, no. 5. pp. 17–20.

Feng, Q. and Jiang, B. 2015. Analytical solution for stress and deformation of the mining floor based on integral transform. *International Journal of Mining Science and Technology*, vol. 25, no. 4. pp. 581–586.

Guan, Y., Li, H., and Lu, J. 2003. Research of no. 9 coal seam floor's fracture regularity in Xian-Dewang coal mine. *Journal of China Coal Society*, vol. 28, no. 2. pp. 121–125.

Jiang, Z.H. 2011. Numerical analysis of the destruction of water-resisting strata in a coal seam floor in mining above aquifers. *Mining Science and Technology* (China), vol. 21, no. 4. pp. 537–541.

Li, A., Gu, S., and Chen, F. 2013. Theoretical analysis and numerical simulation of destroyed depth of coal seam floor during bearing mining: with seam no. 5 in Dongjiahe Mine, Chenghe Mining Area, Shaanxi as example. *Coal Geology & Exploration*, vol. 41, no. 4. pp. 56–60.

Li, A., Liu, Y., and Mou, L. 2015. Impact of the panel width and overburden depth on floor damage depth in no. 5 coal seam of Taiyuan group in Chenghe Mining Area. *Electronic Journal of Geotechnical Engineering*, vol. 20, no. 6. pp. 1603–1617.

Li, K. and Wang, C. 2003. The technique measuring the stress of rock mass used in the study of the mechanism of the water-inrush from coal floor. *Coal Geology & Exploration*, no. 3. pp. 31–33.

Li, S., Liu, B., Nie, L., Liu, Z., Tian, M., Wang, S., Su, M., and Guo, Q. 2015. Detecting and monitoring of water inrush in tunnels and coal mines using direct current resistivity method: A review. *Journal of Rock Mechanics and Geotechnical Engineering*, vol. 7, no. 4. pp. 469–478.

Liu, W., Cao, G., Shen, J., Zhang, L., and Xintai, C.I.B. 2013. Field measurement and simulation research on floor failure depth. *Journal of Liaoning Technical University*, vol. 32, no. 12. pp. 1585–1589.

Liu, Y. 2008. Numerical analysis of breaking depth of coal floor caused by mining pressure. *Journal of Xi'an University of Science of Technology*, vol. 28, no. 1. pp. 11–14.

Liu, Z. and Hu, Y. 2007. Solid-liquid coupling study on water inrush through faults in coal mining above confined aquifer. *Journal of China Coal Society*, vol. 32, no. 10. pp. 1046–1050.

Lu, H., Yao, D., Shen, D., and Cao, J. 2015. Fracture mechanics solution of confined water progressive intrusion height of mining fracture floor. *International Journal of Mining Science and Technology*, vol. 25, no. 1. pp. 99–106.

Lu, Y. and Wang, L. 2015. Numerical simulation of mining-induced fracture evolution and water flow in coal seam floor above a confined aquifer. *Computers and Geotechnics*, vol. 67, no. 6. pp. 157–171.

Wang, J.A. and Park, H.D. 2003. Coal mining above a confined aquifer. *International Journal of Rock Mechanics and Mining Sciences*, vol. 40, no. 4. pp. 537–551.

Wang, K., Wei, A., Chen, Y., and Yue, Q. 2004. Predicting method and its application of water inrush from coal floor based on catastrophe theory. *China Safety Science Journal*, vol. 14, no. 1. pp.11–14.

Wang, Y., Yang, W., Li, M., and Liu, X. 2012. Risk assessment of floor water inrush in coal mines based on secondary fuzzy comprehensive evaluation. *International Journal of Rock Mechanics and Mining Sciences*, vol. 52, no. 6. pp. 50–55.

Jiuchuan, W.E.I., Zhongjian, L., Longqing, S.H.I., Yuanzhang, G.U.A.N., and Huiyong, Y.I.N. 2010. Comprehensive evaluation of water-inrush risk from coal floors. *Mining Science and Technology*, vol. 20, no. 1. pp. 121–125.

Wu, J., Jiang, Z., and Zhai, X. 2011. Research on controlling of rock mass structure on water inrush from coal seam floor in Huaibei Mining Area. *Procedia Engineering*, vol. 26. pp. 343–350.

Yang, T., Tang, C., Tan, Z., Zhu, W., and Feng, Q. 2007. State of the art of inrush models in rock mass failure and developing trend for prediction and forecast of groundwater inrush. *Chinese Journal of Rock Mechanics and Engineering*, vol. 26, no. 2. 268–277.

Yuan, R., Li, Y., and Jiao, Z. 2015. Movement of overburden stratum and damage evolution of floor stratum during coal mining above aquifers. *Procedia Engineering*, vol. 102. pp. 1857–1866.

Zhang, J. 2005. Investigations of water inrushes from aquifers under coal seams. *International Journal of Rock Mechanics and Mining Sciences*, vol. 42, no.3. pp. 350–360.

Zhang, J. and Shen, B. 2004. Coal mining under aquifers in China: a case study. *International Journal of Rock Mechanics and Mining Sciences*, vol. 41, no. 4. pp. 629–639. ◆

http://dx.doi.org/10.17159/2411-9717/2018/v118n05a4

Surrounding rock control mechanism in the gob-side retaining entry in thin coal seams, and its application

by J.Z. Li*†, M. Zhang*, Y. Li‡, and H. Hu*

Synopsis

The stability of the roadside filling body is the key to successful gob-side entry retention in a thin coal seam. However, the existing failure mechanism of the roadside filling body is unclear, and no proactive measures for the high-stress regulation of the roadway-surrounding rock have been proposed. Taking the 2704N working face of Xinyang mine, China, as an example, this study aimed to elucidate the failure mechanism and characterize the mechanical environment of the roadside filling body in order to implement proactive stress adjustment in gob-side entry retention and measures for the structural control of the surrounding rock. The mode of failure of the roadside filling body was analysed, and numerical simulations and field experiments were subsequently performed to characterize the stress environment of the roadside filling body under caving and gob-filling conditions. Finally, regulatory measures for regional stress were proposed. The results showed that adjusting the three-dimensional stress fields in the surrounding rock causes the majority of the principal deviatoric stress to concentrate on the filling body, thus causing the surrounding rock to fail. Therefore, decreasing the subsidence space of the roof strata and preventing the accumulation of excessive principal deviatoric stress on the roadside filling body are crucial for regulating the regional field stress in gob-side entry retention and structurally controlling the roadway-surrounding rock. After gob filling, neighbouring units in the 'coal–roadside filling body–immediate roof-filling body in the gob' support system jointly form a skeleton structure that supports the overlying rock through contact force. A powerful force chain network is stored in the skeleton structure. The strong force chains in the gob-filling body bear the majority of the stress imparted by the overlying rock. Relative movement between key blocks is restricted because the key blocks compress each other. Thus, the principal deviatoric stress on the roadside filling body decreases and stability is significantly improved. A new technology that combines a mechanized gob-side entry in a thin coal seam and proactive roof guarding in the gob filling behind the hydraulic supports was designed in accordance with the 'green mining' concept of underground separation of coal from gangue and the requirements for pumped filling materials. The results of this study contribute to the theory and technology of gob-side entry retention and provide a basis for an effective stress adjustment and structural control method in the gob-side entry retention area.

Keywords

gob-side entry retention, roadside filling body, failure mechanism, principal deviatoric stress, stress adjustment.

Introduction

Gob-side entry retention can decrease mine driveage ratio and eliminate the adverse effect of stress concentration on coal pillars that support a roadway in a thin coal seam. Gob-side entry retention is an important development for non-coal pillar mining in China, since it decreases the stress reduction area to achieve a Y-ventilation system for the working face, which the transfinite gas problem at the face (Xie, Zhang, and Gao, 2016. The yield and mining efficiency in thin coal seams can be improved by increasing the mining rate, *in situ* gangue backfilling, and relieving lifting and transportation pressure on the mine (Li, Yang, and Liang, 2011).

Many researchers have conducted long-term and in-depth investigations of gob-side entry retention. Roadside filling bodies have been developed from gangue picking for wall building, dense individual props, and concrete blocks to novel support materials such as high- and ultrahigh-water materials and pasty fluid materials (Mohammad, Reddish, and Stace, 1997; Golshani *et al.*, 2007). Support modes in roadways have developed from shed-type support systems, like I-beams and U-shaped steels, into the present high-strength anchor bolt support system, which has been successfully applied in many mining regions in China (Mark *et al.*, 2007; Schumacher and Kim, 2014).

The retention roadway along the gob is influenced by the intensive mining of the working face and the next working face. Stress from extensive mining causes failure of the roadside filling body and intense deformation of the roadway, and complicates maintenance (Chen, 1994). In addition, a high driveage ratio and large gangue content are prominent problems that restrict the mining of thin coal seams that are developed along geological structures such as faults. Therefore, the failure mechanism and proactive high-stress

* *Anhui Province Key Laboratory of Mining Reponse and Disaster Prevention, and Control in Deep Coal Mine, Anhui University of Science and Technology, Huainan, Anhui, China.*

† *School of Resource and Safety Engineering, Anhui University of Science and Technology, Huainan Anhui, China.*

‡ *School of Resource and Safety Engineering, China University of Mining and Technology, Beijing, China.*

© *The Southern African Institute of Mining and Metallurgy, 2018.* *ISSN 2225-6253. Paper received Jan. 2017; revised paper received Oct. 2017.*

regulation of the roadside filling body in gob-side entry retention are problems that urgently require solutions. Thus, studying the influence of this problem on gob-side entry retention has considerable practical value in engineering applications.

State of the art

Retention roadways along gobs are usually located at the gob edge, and the structural stability of the roadway-surrounding rock is related to stratum activities in the stope. Chinese and foreign scholars have performed numerous studies on the theory and technology of gob-side entry retention through theoretical modelling, laboratory tests, and field experiments. In Germany, roadside supports are filled with low-water materials, such as Portland cement mixed with anhydrite, with gangue added to the cementing materials. This technology is deployed in over 50% of the mining areas in Germany. Britain and Poland have also developed this technology. Research on gob-side entry retention problems in China began in the 1950s. Smart and Haley (1987) proposed a roof-beam tilt theory and indicated that the roof slant angle and position of the rotator pivot are two important parameters in roadside support design. The researchers posited that roadside support most likely controls the main roadway roof and recommended controlling the roof slant angle to maximize the working resistance and yielding ability of the roadside support. Shabanimashcool and Li (2013) developed a Wilson model of stope mining pressure and proposed the detached block theory to describe the structure–static force relationship for a rock mass. Bai *et al.* (2004) proposed a new gob-side entry retention technology for cemented roadside filling. Zhang, Mao, and Ma (2002) studied the stability control of a filling body in gob-side entry retention in a fully mechanized caving face. They also performed an experimental study on the deformation characteristics of rock bodies surrounding a gob-side entry and proposed technology for gob-side entry retention in a fully mechanized caving face. Ma *et al.* (2007) analysed the support resistance of the filling body in a retained gob-side entry in a fully mechanized roadway and found that the stability of the surrounding rock is related to the support resistance of the filling body and the internal support of the entry. Zhang *et al.* (2013) studied the optimal width of a roadside filling body under solid stowing, as well as *in situ* gob-side retention technology in a fully mechanized solid filling. Zhang, Chen, and Chen (2015) believed that gob-side entry retention should be developed to proactively improve the stress environment in the roadway-surrounding rock and comprehensively optimize roadway driveage, entry retention, and repair.

To summarize, existing studies on support materials in and along the roadway, the stress-bearing capacity of the roadside support body, and the rigidity of the roadside support system are based mainly on the hypothesis that the lateral strata overlying the roadside form after the key strata have fractured. These previous studies found that the success of gob-side entry retention is highly dependent on the strength and durability of the roadside filling body. These studies, however, neglected the effect of roof strata on the gob. Gob-side entry retention under a hard floor in a thin coal seam has unique features and strict requirements for roadway deformation and gangue consumption in a nearby region to realize green mining. Therefore, this study aimed to propose an effective stress adjustment and structural control method in the gob-side entry retention area. To achieve this objective and to provide a theoretical basis for gob-side entry retention in thin coal seams, the failure mechanism and environment of the roadside filling body under different coal mining methods were studied.

Method

Engineering overview

The 2704N mining face in the no. 2 panel of Xinyang mine, Shandong Xinwen Mining Group, China is located in the central to eastern section of the coalfield. The northeast region in the no. 2 panel, the western region of shaft station, and the adjacent east 2703N working face have been mined, whereas the no. 3 mining area in the west has not. The coal transport roadway begins at the seventh stratum in the no. 2 panel south of the DF_{17} (H = 0–32 m, angle 68°) stratum in the north. The burial depth of the coal seam is 464.7–517.4 m. The strike lengths range from 335 m to 359 m with an average of 347 m. The inclined length is 150 m. Coal seam dip angles range from 2° to 9° with an average value of 5°. Mining height is 1.2 m. The upper roof is 10.5 m thick and is composed of fine sandstone. The immediate floor is 2.6 m thick and is composed of siltstone. The hard floor is 5.5 m thick and is composed of medium sandstone. The shaft location of the 2704N working face is shown in Figure 1.

Numerical simulation

Establishment of the numerical method

The three-dimensional (3D) model of 2704N working face was established using the numerical simulation software FLAC3D. A total of 12.9 MPa vertical stress was applied at the upper boundary of the model to simulate stratum stress; the static earth pressure coefficient was unity; the lateral boundaries of the model restrict the horizontal displacement and the bottom boundary restricts the vertical displacement. The upper boundary is free. Paste filling materials were used for the roadside support body, and the width and height of the roadway cross-section after entry retention were 1.5 m and 1.2 m, respectively. The complete caving and gob-filling methods were adopted to simulate stress distribution in the rock surrounding the retained gob-side entry, with the condition that other parameters remained constant.

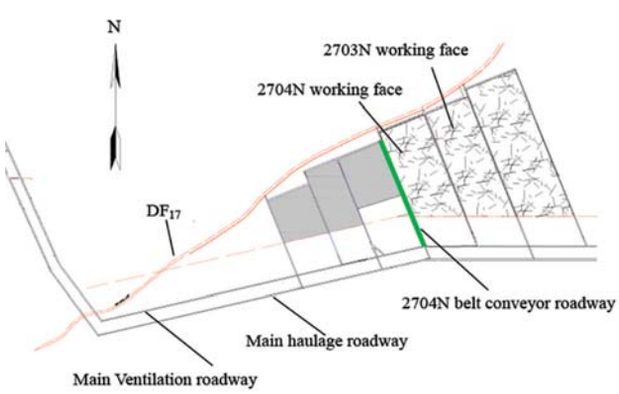

Figure 1—Location of the 2704N working face

To further investigate the failure mechanism of the filling body along the gob and the effect of gob filling on the gob-side entry, a numerical simulation using particle flow code (PFC) was carried out.

Numerical calculation parameters

Field sampling and rock mechanics test results revealed that the rock mass underwent failure under maximum load strength. The residual strength of the rock mass gradually decreased with the development of deformation during a post-peak plastic flow process. Therefore, the Mohr–Coulomb yield criterion was used to calculate the failure of the rock mass (Equation [1]). The strain softening model was used to reflect the gradual degradation of the residual strength of the coal body after failure with the development of deformation (Huang *et al.*, 2011).

$$f_s = \sigma_1 - \sigma_3 \frac{1+sin\varphi}{1-sin\varphi} - 2c\sqrt{\frac{1+sin\varphi}{1-sin\varphi}} \quad [1]$$

where f_s is the shear failure index of the material, σ_1 and σ_3 are the maximum and minimum principal stresses, respectively, and c and φ are the cohesion force and frictional angle, respectively. When $f_s > 0$, the material will undergo shear failure. As the tensile strength of the rock mass is very low, the likelihood of the rock mass undergoing tensile failure can be determined on the basis of the tensile strength criterion ($\sigma_3 \geq \sigma_T$).

Gob caving materials feature macroscopic continuity and irreversible compressive deformation, and caving gangues exhibit permanent bulk shrinkage and strain hardening under isotropic pressure. This bulk hardening behaviour is described using the bulk hardening model (Figure 2).

Gangue materials inside the gob are compacted as the working face advances during mining. Gangue caved from the gob presents a type of loose medium. The mechanical effect of gangue caving on the supporting root can be macroscopically approximated as a supporting body with irreversible deformation. Notably, with the advance of the working face and time, gangue is gradually compacted under the effect of overlying strata, and the material density, elasticity modulus, and Poisson's ratio increase over time.

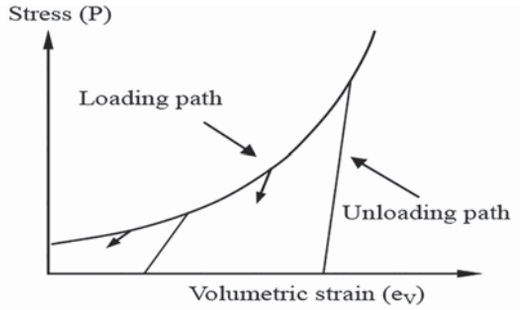

Figure 2—Hardening constitutive model for caving gangues

Existing studies have shown that change rules can be expressed by Equations [2]–[4].

$$\rho = 1400 + 800(1-e^{-1.25t}) \quad [2]$$

$$E = 15 + 200(1-e^{-1.25t}) \quad [3]$$

$$v = 0.05 + 0.2(1-e^{-1.25t}) \quad [4]$$

where ρ is material density (kg/m^3), t is time (years), E is elasticity modulus (MPa), and υ is Poisson's ratio. Equations [2]–[4] reflect the changing relationships of ρ, E, and υ. These parameters exhibit exponential growth with time until finally becoming constant values.

The main stratum parameters of the model are presented in Table I.

Field observation scheme

Three groups of anchor bolt stress measurement stations and roadway surface displacement measurement stations were arranged over the gob-side entry retention period of the 2704N working face. The interval between each measurement station was 50 m. Anchor bolt stress was monitored using an anchor bolt force meter installed at the tail of the anchor bolt. A KDW-1 multipoint displacement meter placed 50 m ahead of the anchor bolt force meter was used to monitor the

Table I

Mechanical parameters of the rock mass

Rock type	Cohesion (MPa)	Frictional angle φ (°)	Bulk modulus (MPa)	Shear modulus (MPa)	Tensile strength σ_T (MPa)
Fine sandstone	2.78	40	13,333	10,000	1.35
Siltstone	2.95	40	15,119	10,410	1.55
Mudstone	1.2	30	6076	3472	0.605
Sandy mudstone	2.19	30	2571	2348	0.72
Quartz sandstone	2.06	45	12,000	8011	2.13
Coal	1.24	32	4561	1985	0.16
Filling body	2.1	35	2450	2125	0.69

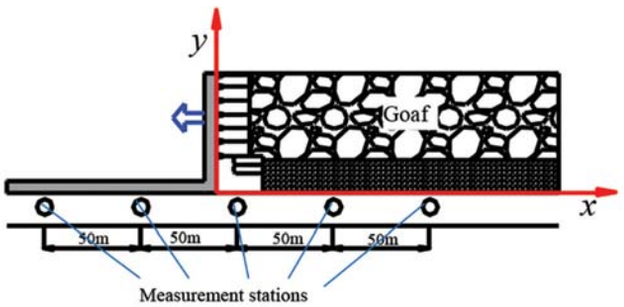

Figure 3—Layout of the measurement stations

surface displacement of the roadway. The layout of measurement stations is shown in Figure 3. To facilitate data processing, the coordinate value of the *x*-axis on the working face was defined as zero. The front of the working face was positive, whereas the rear was negative; for example, the coordinate value of axis *x* was –50 within 50 m inside the gob in the rear of the working face.

Results and discussion

Fracture criterion of the roadside filling body

Coal seam mining disrupts the initial stress balance. Stress fields in the stope-surrounding rock gradually migrate, concentrate, and finally achieve a quasi-static balance to adapt to the mining environment. The stress state of any point in the stope-surrounding rock can be expressed as multiple forms, and a special circumstance among all descriptions, namely, three principal stresses $\sigma_i (i = 1, 2, 3)$, arranged in vertical pairs, is found. The average stress is set as

$$\sigma_m = (\sigma_x + \sigma_y + \sigma_z)/3 = \frac{1}{3}\sum^{i}\sigma_i$$

where $\sigma_1 \geq \sigma_2 \geq \sigma_3$.

The stress state of any point in the roadside filling body can be decomposed into the sum of the spherical and deviatoric stresses. The spherical tensor of stress only gives rise to the elastic change of the bulk roadside filling body, and the deviatoric tensor of stress results in the plastic deformation of the roadside filling body. The maximum principal deviatoric stress σ_1 controls the degree of failure of the stope-surrounding rock, and its value can obtained through Equation [5] (Xu, Wei, and Xiao, 2015).

$$\sigma_1' = \frac{2}{3}\sigma_1 - \frac{1}{3}(\sigma_2 + \sigma_3) \quad [5]$$

The coal seam floor is formed through specific geological processes and is subjected to a specific geological environment. The initial maximum principal deviatoric stress is zero; the mining process disrupts the initial ground stress balance and causes the maximum principal deviatoric stress field in the roadside filling body to change. The surrounding rock undergoes plastic failure when the maximum principal deviatoric stress σ_1 exceeds the ultimate strength of the filling body.

Movement laws of lateral roof in the stope and rock beam structure

Plate theory (Xu *et al.*, 2009) provides the macroscopic

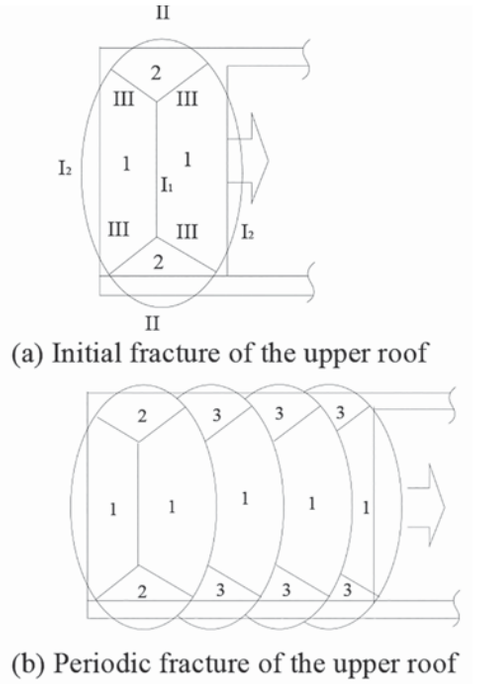

Figure 4—Overlying stratum movement of gob-side entry retention

explanation for the fracture of the upper roof. When applying the caving method, the rock mass fails under maximum principal deviatoric stress, and the stope-surrounding rock expands from the shallow to the deep region toward the unsteady state, specifically manifesting during mining of the working face. The immediate roof caves, and the hanging upper roof stratum fractures when it reaches ultimate strength under the effects of overlying strata and self-weight. Fracture line I is first formed at two long edges during fracture. Subsequently, fracture line II appears at a short edge, the surrounding cracks thread in an 'O' shape, and the bending moment in the middle of the plate reaches the maximum value. Crack I1 is formed after the maximum strength of the rock mass is exceeded. Finally, an X-shaped failure forms, and the upper roof strata move and rotate along I and II, causing fracture line III to form structural blocks 1 and 2 of the upper roof failure. The movement of the upper roof decreases as the upper beam of the rock roof first contacts the gangue in the middle of the gob. The plane figure of the upper roof after initial fracture presents as an ellipse and is called an 'O–X' fracture structure (Xu and Qian, 2000). The fracturing process of the rock stratum is shown in Figure 4.

When the complete caving method is used to manage the roof after fracture, key strata mutually extrude to form a beam-like, semi-arched temporary structure with self-stabilizing balance. Three mutually occlusive key blocks – A, B, and C – form in the side direction of the gob, and the rock beam structure is formed after the fracture of key strata, as shown in Figure 4a. The retained gob-side entry is located underneath key block B, and the solid coal side and filling body side in the retained gob-side entry provide widely different mechanical environments. Specifically, key block B is unstable under the supporting effect of immediate roof caving and horizontal extrusion stresses of key blocks A and C. The compaction of the immediate roof and settling of key

block C causes key block B to rotate and sink. The 'filling body–immediate roof–floor' jointly constitute the roadside support system, and the rotation and subsidence of key block B constitute the main stress sources in the system. Therefore, controlling the movement of key block B is the key for successful gob-side entry retention. The roadside support system cannot control the rotary deformation of key block B before the upper roof movement is completed, and the support system is mainly characterized by yielding.

The roadside filling body and gob filling body undergo compression during the rotation and subsidence of key block B. The final subsidence of key block B is given as:

$$S_E = h - m_z(K_A - 1) \quad [6]$$

where S_E is the rotary subsidence of key block B, h is the mining height, m_z is the thickness of the immediate roof, and K_A is the expansion coefficient of the broken rock.

If backfilling is adopted, the effect of the gob filling body on the movement of the overlying strata is equivalent to the reduction of mining height and is replaced by the equivalent mining height. Equivalent mining height M_e is expressed as Equation [7] in accordance with the features of the gob paste filling (Miao, Zhang, and Guo, 2010).

$$M_e = M - (h_1 + h_2 + h_3 + h_4 + h_5) \quad [7]$$

where h_1 is the subsidence of the upper roof after the support is advanced (in mm); h_2 is the restricted deformation quality of hydraulic support; h_3 is the designed thickness of the upper beam of the hydraulic support (in mm); h_4 is the upper roof subsidence during the paste filling process in the gob (in mm); h_5 is the final settling volume of the immediate roof when the paste is compacted (in mm); h_1 is the uncontrollable engineering quantity related to rock pressure; and h_2–h_5 are controllable engineering quantities related to the design of the hydraulic support and filling technology. Field mining height M is a fixed value. The effective feasible approach to decrease the equivalent mining height is to decrease h_2–h_5, namely, by decreasing the subsidence of the roof in the support area, timely filling, and shortening the setting time of the filling body.

One end of key block B is located inside the roadside coal body, whereas the other end rotates and subsides towards the gob. The 'coal body–roadside filling body–immediate roof' support system fails to resist deformation and passively accepts this 'given deformation' state. The amount of deformation is given by Equation [8] (Zhang *et al.*, 2012).

$$S = \frac{l[(1 - K_0)h_r + M_e]}{L} \quad [8]$$

where l is the distance from a point in key block B to a fracture line at the roadside coal body, and K_0 is the expansion coefficient of the caved rock strata. The expansion coefficient of broken hard sandstone is 1.3–1.35, whereas that of mudstone with relatively low strength is 1.25–1.28. The greater the K_0 value, the smaller the given deformation of key block B; namely, the more the movement of key block B is restricted, the smaller the load borne by roadside filling body. In Equation [8], hr is the thickness of the immediate roof, and L is the length of key block B.

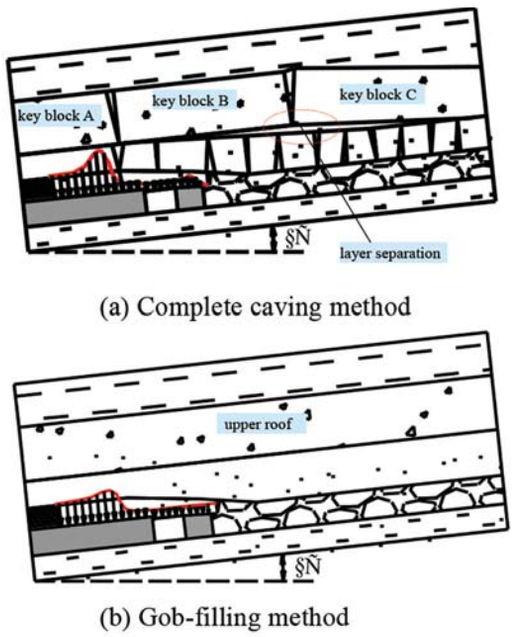

Figure 5—Lateral roof movement process and rock mass fracture structure of the gob-side entry

Equations [7] and [8] show that the effect of the gob paste filling is equivalent to a reduction in mining height. The subsidence space of the overlying strata is restricted and the immediate roof does not completely cave. The fracture structure shown in Figure 5a is not formed; however, it is in a broken-like state. The structure of the overlying strata after gob filling is shown in Figure 5b.

Dispersed particles are the basic components of the PFC. Material parameters include particle density, modulus of deformation of particles, normal/tangential stiffness ratio of particles, modulus of deformation of parallel bonds, coefficients of particle friction, and normal and tangential binding strength of parallel bonds. The parallel bond model was used as the mechanical constitutive model. The PFC simulation results demonstrated that the coal body in front of the working face, side coal body of the working face, filling body in the gob, immediate roof, and filling body along the roadway extrude mutually. Adjacent particle units form the bearing structure that supports the overlying rock movement through contact forces. Stress migrates and concentrates in the stope-surrounding rock during mining of the working face. Accompanied by the redistribution of rock strata stresses, a powerful force chain network is stored inside the skeleton structure (Figure 6). The force chain network includes strong force chains and weak force chains and exhibits extremely strong self-organizing and energy transfer capabilities. In Figure 6, weak force chains are represented by light gray lines, strong force chains are represented by black lines, and the intensity of force chains are expressed by line thickness. Strong force chains bear the majority of overlying stratum stress despite their low numbers in the gob-filling body. The minor disturbance of the overlying strata caused by the strong force chains in the gob-filling body is of a nonlinear response nature. Their bifurcation or instability would very easily cause the avalanche-like fracture of the key

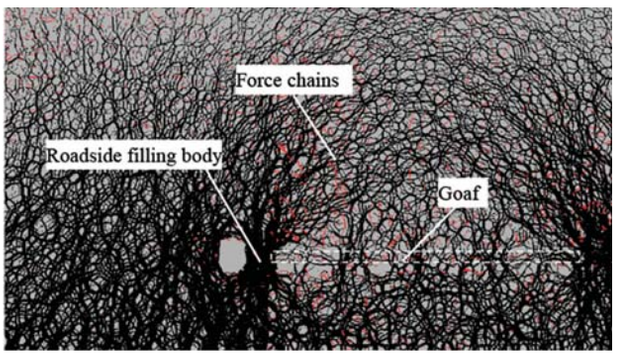

Figure 6—Distribution of force chains in the surrounding rocks

strata, resulting in the intense, large deformation of the roadside filling body. Therefore, the gob-filling body should be stable and effectively support the roof.

Mechanical environment of roadside filling body and optimization of regional stress

The distributions of the mechanical environment in the stope-surrounding rock in response to different mining methods are shown in Figure 7. Figure 7 was derived using FLAC3D numerical simulation software. Figure 8 shows the maximum principal deviatoric stress values of slant section 20 m at the rear part of the working face. The calculation results indicate that when the caving method is used, the fracture, rotation, subsidence, and contacting of gangue with the main roof induce a high-stress field to concentrate in the area of the roadside filling body. The maximum principal deviatoric stress borne by the roadside filling body is 34.5 MPa. After the gob is filled, the separation of stratum between the immediate and main roofs could be prevented to decrease the subsidence of the roof strata, exert a pressure 'yielding' effect on the roof strata, and prevent the accumulation of an excessively high principal deviatoric stress on the roadside filling body. The maximum principal deviatoric stress borne by the roadside filling body is approximately half of that when the complete caving method is used to manage the roof. Therefore, selecting the appropriate mining method is the most direct and effective method to ensure successful gob-side entry retention and adjust the uncontrollable remote stress of the roadside filling body.

Filling scheme and coal–gangue separation technology

Performance requirement for filling materials

The roadside filling body should have high deformability and a high load-bearing strength to seal the gob and support the roof while satisfying pumping requirements. Gob-filling behind hydraulic supports should sufficiently consume redundant gangue during underground mining and drifting processes while avoiding influencing regular production. Therefore, the mould for the gob-filling body behind the hydraulic supports should be removed after 3–4 hours to ensure that the working face can be mined as normal.

The optimal proportioning schemes of the roadside filling body and gob filling materials were selected through laboratory experiments and are presented below.

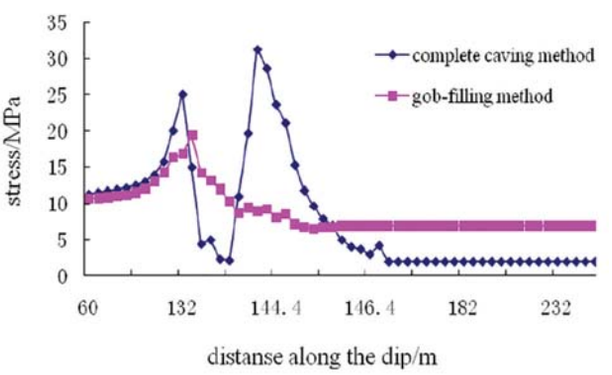

Figure 8—Distribution of maximum principal deviatoric stress along the coal seam

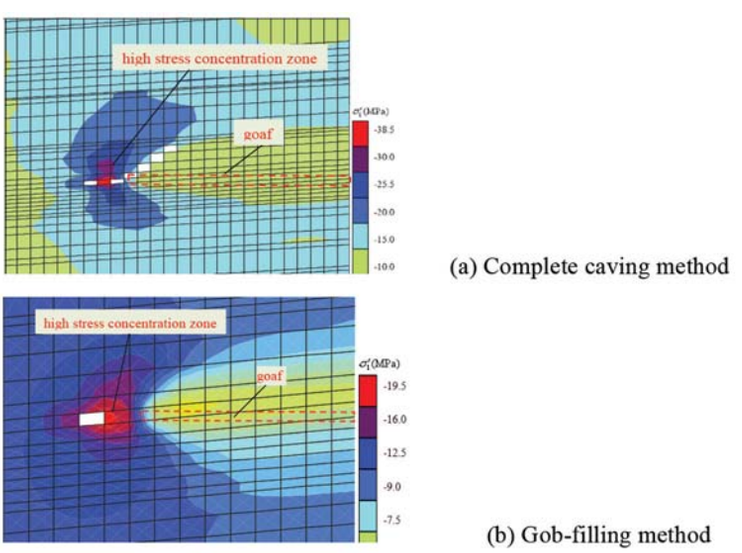

Figure 7—Distribution of principal deviatoric stress in stope-surrounding rock

The composition of the roadside filling body is 42.5 ordinary Portland cement, river sand, gangue, and additive in proportions of 1, 3, 8, and 0.9 by weight, with compressive strengths at 3 hours, 1 day, 3 days, 7 days, and 28 days of 0.34, 11.3, 16.1, 19.9, and 29 MPa, respectively. When the mould is removed after 3 hours, the support body is filled and self-stabilized. The slump is greater than 160 mm. The pumping distance can reach 500 m.

Gob-filling materials should contain as much gangue as possible to decrease costs and realize a pumping distance of 500 m. Moreover, the filling materials should undergo self-compaction after being pumped to the mould. The weight ratio of the optimal proportioning scheme is water: gangue: coal ash: additive = 13.23: 79.23: 6.15 .

Shallow slot method for the underground separation of coal and gangue using heavy media

The shallow trough separator for heavy media is characterized by a small volume (5.5 × 3.9 m), strong adaptability to feeding stability, small loss caused by gangue mixing with coal (<0.5%), facile and convenient operation, and a high degree of automation. Therefore, the ground 'diamond-style' shallow trough for separation by heavy media was changed to a 'cavern long strip-style' separation unit after miniaturization and displacement by equipment to separate raw block coal in the 50–250 mm size range. The early separation of gangue from the panel was accomplished and on-specification raw coal and pure gangue were produced. The pure gangue was used for backfilling to realize green and environmentally friendly mining (Xu *et al.*, 2009.

Case study A

Field research was conducted at 2704N working face in no. 2 panel of Xinyang coal mine to verify the effects of the new fully mechanized gob-side entry retention and gob filling technology behind hydraulic supports on stress adjustment and the structural control of gob-side entry retention area.

Design of filling system

Owing to the imbalance of underground production and many uncertain factors, if a large quantity of gangue was available and a surplus remained after filling for gob-side entry retention, the redundant materials were filled in the gob. The filling system for 2704N working face was designed as a parallel gob-side entry retention system and gob-filling system after support had been installed. Two sets of filling pumps were located inside the main roadway. The filling pumps did not move when the working face was mined. The mould base of the gob-side entry retention and hydraulic support of the filling template behind the hydraulic supports were arranged inside the working face and continuously formed new filling spaces as the workface was mined. The filling system was designed primarily to ensure gob-side entry retention. Gob filling was implemented only when the quantity of gangue was greater than was required for gob-side entry retention. Specifically, gob filling behind the hydraulic supports was done with the objective of consuming gangue (Qian, Miao, and Xu, 2007).

The existing coal bunker in the no. 2 panel and connecting roadway in the gangue bunker were transformed and the main separation system was arranged. The width and height of the connection roadway were increased to 6.8 m × 7.0 m, and coal–gangue separation equipment was arranged in the connecting roadway. To facilitate installation and overhaul of the clean coal and coarse slime screen, a pressure filter was installed inside the sealed and unused coal transportation roadway in the 2701N working face, and crushed gangue was stored in the roadway. Qualified and diluted medium pools were arranged inside the connecting roadway for subsidence treatment and automatically flowing qualified media were collected. The installation and maintenance requirements for the separation equipment were fully considered so as not to interfere with the gangue crushing system, thus ensuring the smooth implementation of the filling work. The layout of the underground coal–gangue separation roadway is shown in Figure 9.

The material preparation system was set up in accordance with the dual system design. Crushed gangue was used to fill the retained gob-side entry through a set of mixed material proportioning, blending, and pumping systems. Gob filling behind the hydraulic supports was implemented through another set of mixed material proportioning, blending, and pumping systems. The flow chart of this dual filling system is shown in Figure 10.

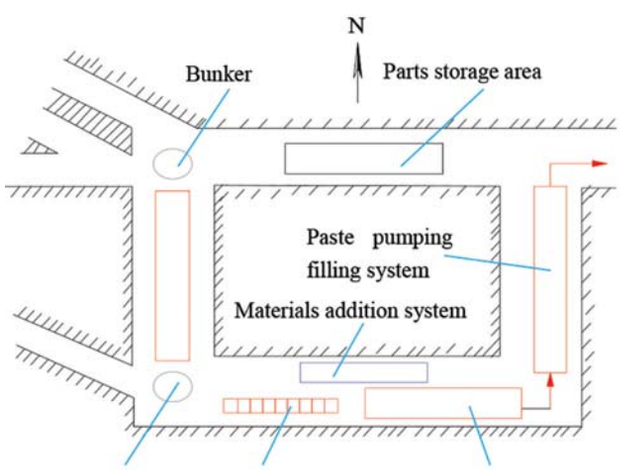

Figure 9—Layout of the underground coal–gangue separation roadway

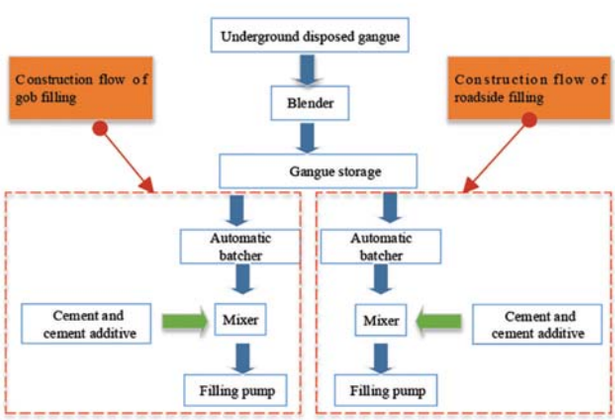

Figure 10—Dual filling process for gob-side entry retention and gob filling

Filling technology

Filling technology for gob-side entry retention

Filling beside the roadway was implemented once for every three slices of coal cut. Coal mining and roadside mining could be conducted simultaneously, and a filling body with dimensions of 1.8 m (length) × 1.3 m (height) × 2.5 m (width) (5.85 m³) was formed behind the hydraulic supports once filling was implemented. To facilitate removal of the template, plastic film was laid on the template support and surface before filling. During roadway filling, a metal or plastic net, originally used to protect the coal body inside the coal transportation roadway in the working face, was cut off and used to reinforce the filling body.

Template supports (Figure 11) used for gob-side entry retention in the working face were all in lagging support forms. The support was advanced after the scraper conveyor when the coal body was cut by a coal cutter. Filling was started only when the template supports had advanced for three cycles, and filling and coal cutting could be implemented simultaneously. Filling work could be completed after the cutting of the third cycle was completed.

Gob-filling technology after support

The cutting depth of the coal cutter in the 2704N working face was 0.6 m. Template supports (Figure 12) could be filled forward after two slices of coal were cut from the working face and the scraper conveyer was moved. This would not influence the cutting of the third slice of coal. A 1.8 m × 1.2 m × 1.5 m (3.51 m3) filling space was formed after the template supports were removed, and the 3.51 m³ space was used for concrete filling each time. The construction processes proceeded simultaneously, and the gob was filled once the templates were moved. To ensure the appropriate moisture content of filling materials during freezing and for the convenience of moving the filling templates, plastic films were laid down on the template supports and template surfaces before filling.

Figure 11—Template supports for gob-side entry retention

Figure 12—Hydraulic support used specifically for gob filling

Support reinforcement scheme for gob-side entry retention

Roof support was reinforced in the gob-side entry retention area during the mining of the 2704N working face. The spacing between anchor bolts was 1.35 m, and the row spacing was 1.0 m. The filling method was used to form a concrete wall at the rear of the support after anchor bolts were installed to maintain the roadway, and the width of filling body was 2.5 m. Three rows of single hydraulic props were used for support reinforcement within 50 m of the front of the working face, and two rows of single hydraulic props were set within 200 m influence range of dynamic pressure at the rear of the working face. The amount of deformation of the surrounding rock in the retained gob-side entry was controlled within the permitted range, and props were removed after the movement of the stratum overlying the mined working face stabilized. The original three-support temporary support on the end of working face was replaced by the mould base of the gob-side entry retention. The support reinforcement mode for gob-side entry retention is shown in Figure 13.

Field measurement of the entry retention effect

Figure 14 shows the results of anchor bolt stress tests for roof management in the retained gob-side entry. The results revealed considerable changes in stress, with a peak stress of 11.5 MPa within the distance of 50 m from the measurement station to the coal mining face. When the distance from the face was 60 m, the immediate roof was forced to subside because of the rotation of the key blocks. Support inside the roadway did not change the movement mode of the large structure in the surrounding rock. The anchor bolt stress increased slightly after entering the gob, reaching a maximum value of 4.8 MPa at approximately 40 m from the rear of the working face. As the movement of the surrounding rock tended to be stable, the anchor bolt stress tended to be mild. The rotary subsidence of the roof after gob

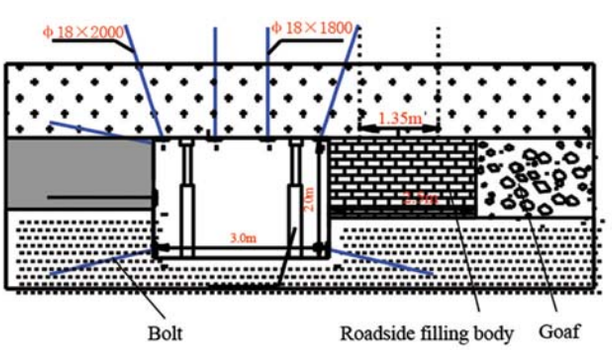

Figure 13—Support reinforcement scheme for gob-side entry retention

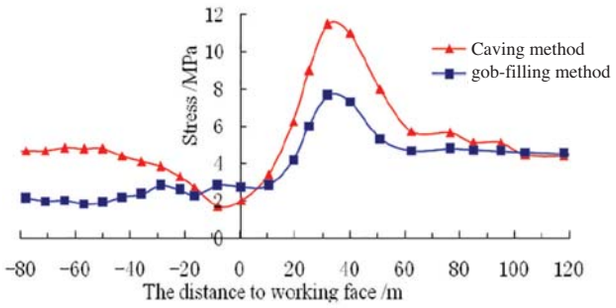

Figure 14—Change in anchor bolt stress on the roadway roof

filling was restricted, thus preventing separation of the overlying strata and the development of fractures. The anchor bolt stress decreased significantly to a peak value of 7.7 MPa. Field observation revealed that the high stress generated by the movement of the surrounding rock was not controlled solely through the roadside support and the basic support inside the roadway, since the deformation space permitted by gob-side entry retention in thin coal seams was limited. Gob filling enhanced control of the roof strata and had a beneficial effect on regulating high stress on the roadside filling body.

Figure 15 shows the deformation of the rocks surrounding the gob filling in the retained gob-side entry. The mechanical environment of the roadside support body was improved because the gangue filling inside the gob bore the majority of the pressure from the overlying strata. Thus, the maximum cumulative displacement of the roof and floor was only 203 mm. Since the mining face was exploited until the roadside filling body lagged the mining face by 87 m, displacement between the roadway roof and floor gradually increased. This indicated that the overlying stratum moved within this range. In the meantime, the horizontal stress concomitant with the vertical deformation of the filling body inside the gob was transferred to the roadside filling body. The phenomena in the surrounding rock of the retained gob-side entry could be divided into a slow subsidence phase (0–16 m behind the working face), accelerated subsidence phase (16–42 m behind the working face), decelerated subsidence phase (42–85 m behind the working face), and stable phase (87 m behind the working face). These phases are influenced by the rapid, slow, and constant increases of the filling body intensity in the gob area. The roof underwent subsidence mainly by bending, whereas the floor underwent base swelling. The entry retention section was maintained above 89% of the original section, thus meeting the use requirement for the next working face. The actual effect of gob-side entry retention is shown in Figure 16.

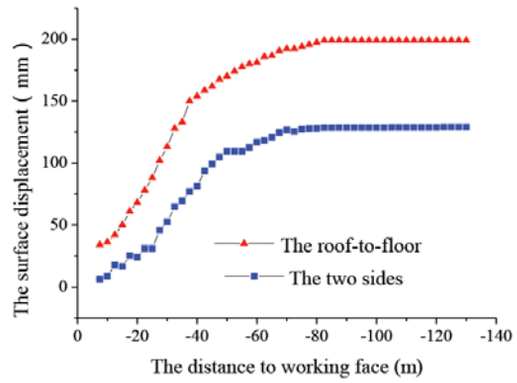

(a) Surface displacement

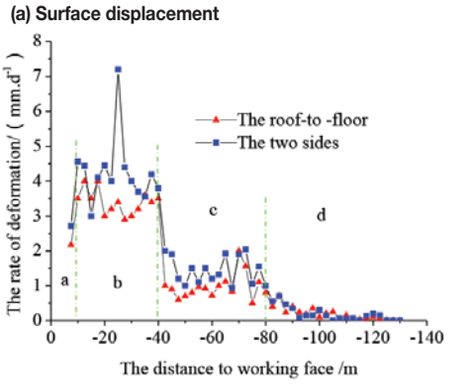

(b) Deformation rate. a: Slow subsidence phase; b: accelerated subsidence phase; c: decelerated subsidence phase; d: stable phase

Figure 15—Surrounding rock deformation curves

Figure 16—Photograph of the entry retention effect

Conclusion

This study aimed to characterize the failure mechanism of the roadside filling body and to achieve gob-side entry retention in thin coal seams. Thus, the distribution laws of deviatoric stresses of the roadside filling body under two roof management conditions – caving method and gob filling – were described on the basis of elastic–plastic mechanics and mining pressure theory, stress adjustment, and structural control theory in the gob-side entry retention area. A new proactive roof-support technology that combines fully mechanized gob-side entry retention in thin coal seams and gob filling at the rear of hydraulic supports was designed. The following conclusions can be drawn.

- Different mining methods result in different distributions of mechanical environments in stope-surrounding rocks. Decreasing the uncontrollable high stress borne by the roadside filling body is the most direct and effective method of controlling the accumulation of excessive principal deviatoric stress on the roadside filling body.

- Filling gobs with gangue has an effect equivalent to decreasing the mining height, since it restricts the available space for subsidence of the overlying strata. The strong force chains in the gob-filling body bore the majority of the stresses from the overlying strata. Key blocks were in a near-broken state under high extrusion stresses at the two sides, and the stability of the rock mass surrounding the retained entry was significantly improved.
- A novel technology that combines proactive roof support with fully mechanized gob-side entry retention is proposed for application in thin coal seams, with gob filling behind hydraulic supports. A mutually independent rapid filling technology was designed to improve the mechanical environment of the roadside support body, significantly decrease displacement of the roof and floor, and satisfy the cross-section requirement of retained entry ventilation for the next working face.

In conclusion, this study proposes a clear and simple mechanism for the plastic deformation of a roadside filling body under deviatoric stresses. This mechanism is proposed on the basis of stress adjustment and structural control theory and technology. However, only increments in anchor bolt stress, anchor rope stress, and roadside vertical stress, as well as deformation in the rock surrounding the gob-side entry retention, were monitored owing to the lack of instruments for monitoring 3D stress fields in real time. 3D stress meters are required for the characterization of the dynamic evolution of deviatoric stress in a filling body along a retained gob-side entry during coal mining. The development of such instruments will contribute significantly to characterization of the stability of a filling body along a retained gob-side entry and enable the proactive regulation of high stress.

Acknowledgments

This research was supported by the National Key Research and Development Program of China (2017YFC0804202), the State Key Program of National Natural Science Foundation of China (U1361208), the National Natural Science Foundation of China (51504005, 51304007), and Anhui Provincial Natural Science Foundation (1408085MKL42).

References

Bai, J.B., Zhou, H.Q., Hou, C.J., and Yue, D.Z. 2004. Development of support technology beside roadway in goaf-side entry retaining for next sublevel. *Journal of China University of Mining and Technology*, vol. 33, no. 2. pp. 59–62.

Chen, S. 1994. Calculation of additional stresses in soil produced by infinite long ladder-shaped distribution load. *Suzhou Institute of Urban Construction and Environmental Protection*, vol. 7, no. 3. pp. 29–32.

Golshani, A., Oda, M., Okui, Y., Takemura, T., and Munkhtogoo E. 2007. Numerical simulation of the excavation damaged zone around an opening in brittle rock. *International Journal of Rock Mechanics and Mining Sciences*, vol. 66, no. 4. pp. 835–845.

Huang, Y.L., Zhang, J.X., Zhang, Q., and Zanm D.F. 2011.Technology of gob-side entry retaining on its original position in fully mechanized coalface with solid material backfilling. *Journal of China Coal Society*, vol. 36, no. 10. pp. 1624–1628.

Li, L.C., Yang, T.H., and Liang, Z.Z. 2011. Numerical investigation of ground water outbursts near faults in underground coalmines. *International Journal of Coal Geology*, vol. 85, no. 3. pp.276–288

Ma, L.Q., Zhang, D.S., Chen, T., and Fan G. 2007. Study on packing body supporting resistance of enter-in packing for *in situ* gob-side entry retaining in fully-mechanized top-coal caving mining face. *Chinese Journal of Rock Mechanics and Engineering*, vol. 26, no. 3. pp. 544–550.

Mark, C., Gale, W., Oyler, D., and Chen, J. 2007. Case history of the response of a longwall entry subjected to concentrated horizontal stress. *International Journal of Rock Mechanics and Mining Sciences*, vol. 44, no. 2. pp. 210–221.

Miao, X.X., Zhang, J.X., and Guo, G.L. 2010.Study on waste-filling method and technology in fully-mechanized coal mining. *Journal of China Coal Society*, vol. 35, no. 1. pp.1–6.

Mohammad, N., Reddish, D., and Stace, L. 1997.The relation between in situ and laboratory rock properties used in numerical modeling. International *Journal of Rock Mechanics and Mining Sciences*, vol. 34, no. 2. pp. 289–297.

Qian, M.G., Miao, X.X., and Xu, J.L. 2007. Green mining of coal resources harmonizing with environment. *Journal of China Coal Society*, vol. 32. pp. 1–7.

Schumacher, F.P. and Kim, E. 2014. Evaluation of directional drilling implication of double layered pipe umbrella system for the coal mine roof support with composite material and beam element methods using FLAC3D. *Journal of Mining and Safety Engineering*, vol. 55, no. 2. pp. 335–348.

Shabanimashcoo, L.M. and Li, C.C. 2013.A numerical study of stress changes in barrier pillars and a border area in a longwall coal mine. *International Journal of Coal Geology*, vol. 106. pp. 39–47.

Smart B.G.D. and Haley S.M. 1987. Further development of the roof strata tilt concept for pack design and the estimation of stress development in a caved waste. *Mining Science and Technology*, vol. 5, no. 2. pp. 121–130.

Xie, H.P., Zhang, Z.T., and Gao F. 2016. Stress-fracture-seepage field behavior of coal under different mining layouts. *Journal of China Coal Society*, vol. 41, no. 10. pp. 2405–2417.

Xu, J.L. and Qian, M.G. 2000. Method to distinguish key strata in overburden strata. *Journal of China University of Mining and Technology*, vol. 29, no. 5. pp. 463–467.

Xu, J.L., Wang, X.Z., Liu, W.T., and Wang, Z.Q. 2009. Effects of primary key stratum location on height of water flowing fracture zone. *Chinese Journal of Rock Mechanics and Engineering*, vol. 28, no. 2. pp. 380–385.

Xu, L., Wei, H.X., and Xiao, Z.Y. 2015. Engineering cases and characteristics of deviatoric stress under coal pillar in regional floor. *Rock and Soil Mechanics*, vol. 36, no. 2. pp. 561–568.

Zhang, D.S., Mao, X.B., and Ma, W.D. 2002.Testing study on deformation features of surrounding rocks of gob-side entry retaining in fully-mechanized coal face with top-coal caving. *Chinese Journal of Rock Mechanics and Engineering*, vol. 21, no. 3. pp. 331–334.

Zhang, J.X., Jiang, H.Q., Miao X.X., Zhou, N., and Zan, D.F. 2013.The rational width of the support body of gob-side entry in fully mechanized backfill mining. *Journal of Mining and Safety Engineering*, vol. 30, no. 2. pp. 159–164.

Zhang, N., Chen, H., and Chen, Y. 2015. An engineering case of gob-side entry retaining in one kilometer-depth soft rock roadway with high ground pressure. *Journal of China Coal Society*, vol. 40, no. 3. pp. 494–501.

Zhang, Q., Zhang, J.X., Huang, Y., and Feng, J. 2012. Backfilling technology and strata behaviors in fully mechanized coal mining working face. *International Journal of Mining Science and Technology*, vol. 22, no. 2. pp. 151–157. ◆

http://dx.doi.org/10.17159/2411-9717/2018/v118n5a5

Experimental study on the stability of surrounding soft rocks of gob-side entry retaining in fully mechanized caving

by P.S. Zhang*†, Z.H. Kan†, W. Yan†, B. Shen†, Y.P. Zhao†,•• and S.X. Wu†

Synopsis

Theoretical and field investigations were combined to analyse and determine the design parameters for a field roadway and roadside support. A gob-side entry retaining model was created with similar materials, and physical tests and numerical simulation were carried out to study the stability of surrounding soft rocks in fully mechanized caving using specific roadway and roadside supports with different stress states. The study shows that mining the upper and lower panels causes a superposition effect to the gob-side entry retaining roadway, and the deformation of the surrounding rock is further exacerbated during mining of the lower panel. Moreover, the lateral residual abutment stress in the gob area could easily cause the entire roadside support to topple. A support method coupling 'long/short anchor cable plus bolts plus net' to a composite suspension beam provided excellent support for roadways with fractured roofs. As long as the roadside support strength is maintained, the secondary support provided by roof-contact yielding material will facilitate benign deformation of the roadway roof to release energy and stabilize the roadside support.

Keywords

gob-side entry retaining, similar material, simulation test stress states, fully mechanized caving, physical model.

Introduction

Gob-side entry retaining in fully mechanized caving is a crucial technology for resolving gas accumulation and overstressing issues on working faces in high-yield and high-efficiency fully mechanized caving by the Y-shaped ventilation method. This method is advantageous because it eliminates panel coal pillars, improves the resource recovery ratio, reduces roadway development work, alleviates alternation problems during excavation, and eliminates isolated working faces (Zhang and Lin, 2014; Wang, Zhang, and Wang, 2015; Wang, Zhang, and Gao, 2015; Zhang *et al.*, 2015). In recent years, numerous researchers have conducted extensive studies on gob-side entry retaining technology for fully mechanized caving faces from various aspects, including theoretical investigations (Ma *et al.*, 2007; Wang *et al.*, 2001), simulations (Zhang *et al.*, 2016a), and field operations (Ma and Zhang, 2004; Li., 2005). Deng and Wang, (2014) analysed the feasibility of gob-side entry retaining in steep coal seam mining using numerical modelling. Zhang *et al.* (2014) explored the deformation and failure characteristics as well as control mechanisms of the roof in gob-side entry retaining of a steep thin coal seam. Tan *et al.* (2015) analysed the roadside support body of gob-side entry retaining under the condition of hard roof. Zhang *et al.* (2015) analysed the application of high-water packing materials in gob-side entry retaining in a high-gas mine using numerical analysis. Yang *et al.* (2016) studied the soft roof failure mechanism and supporting method for a gateway in gob-side entry retaining. Yang *et al.* (2015) evaluated the effect of six geological factors on the design of a gob-side entry retaining structure. Han *et al.* (2015) combined theoretical and numerical methods to explore the stress relief and structure stability mechanism of a gob-side entry retaining structure under the condition of hard roof. Li *et al.* (2016) investigated the fracture position of the key rock block and crack evolution processes using a gob-side filling wall by numerical modelling. These studies provided a solid theoretical foundation and technical guidance for the implementation and promotion of gob-side entry retaining technology for fully mechanized caving faces. However, due to constraints such as the testing equipment, design, and cost, only limited studies on gob-side entry retaining technology for fully mechanized caving faces using similar material test methods have been conducted (Xu and Wang., 2015).

* *State Key laboratory of Mining Disaster Prevention and Control Co-funded by Shandong Province and Ministry of Science and Technology, Shandong University of Science and Technology, China.*

† *Key Laboratory of Safe and Efficient Coal Mining Co-funded by Anhui Province and Ministry of Education, Anhui University of Science and Technology, China.*

© *The Southern African Institute of Mining and Metallurgy, 2018.* *ISSN 2225-6253. Paper received Feb. 2017; revised paper received Feb. 2018.*

Experimental study on the stability of surrounding soft rocks of gob-side entry

Similar material simulation testing is a conventional experimental method that is still employed in laboratory studies to resolve real-world problems using a defined mathematical model and relatively simple geological conditions. In recent years, various industries such as mining, tunnelling, and geotechnical engineering have widely adopted similar material simulation tests (Zhang *et al.*, 2016b; Franciss., 1997; Ren *et al.*, 2011). In this paper, a two-dimensional simulation test platform and the actual geological conditions of the 30105 working face of the Shiquan coal mine were used to design a 2D similar material test model for gob-side entry retaining. Using this model we analysed the stability of roadway surrounding rock for gob-side entry retaining with different stress states. This study provides theoretical support for successful field implementation.

Geological conditions and design of the entry retaining support plan

Geological conditions

The primary coal mining layer at the 30105 working face of the Shiquan coal mine is the no. 3 coal seam. The seam is 5.05–7.20 m thick (average of 6.11 m), the bulk density is 1.4 t/m^3, the and the dip angle is 5–7°. The working face elevation is 397–535 m above sea level and the ground elevation is 890–954 m, hence the average depth below surface is 523 m. The strike length and inclined length of the working face are 2236.7 m and 230 m, respectively. The lithology of coal, roof, and floor is shown in Figure 1.

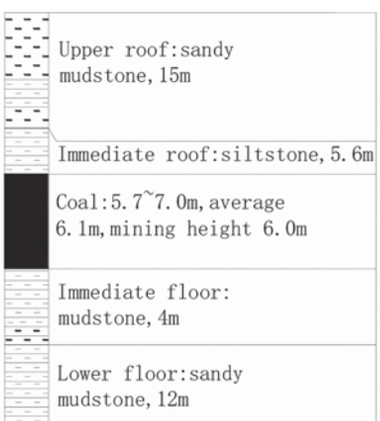

Figure 1—Lithology of coal, roof, and floor

The 30105 working face is excavated by fully mechanized coal mining methods, such as strike longwall retreat and low position full caving. Mining is based on bottom-cut-top-caving and one-cut-one-caving cyclic operations. The designed mining height is 3.0 m, the mining-caving ratio is 1:1, the overall mining rate is 85%, the cyclic drilling depth is 0.6 m, and the daily advance is 2.4 m. The layout plan of the working face is shown in Figure 2.

Design of entry retaining support plan

Roadside support is crucial for ensuring successful gob-side entry retaining. Based on research and field observations, the proposed gob-side entry retaining surrounding rock structure model (Han *et al.*, 2015; Deng *et al.*, 2011; Su and Hao, 2002) is shown in Figure 3. The formula used to calculate the roadside support's critical resistance is as follows:

$$P_f = [h_b \gamma_b L_{max} + h_a \gamma_a (x_o + c + d)]/2 \qquad [1]$$

where P_f is the filling support resistance (kN), γ_a and γ_b are the bulk densities of the immediate roof and main roof, respectively (kN/m^3), x_0 is the width of ultimate balance area in the coal mass (m), h_a is the thickness of the immediate roof (m), h_b is the thickness of the imbalanced rock in the main roof (m), and L_{max} is the maximum period weighting pace of the main roof (m).

Based on the ultimate balance of the working face, the width of the ultimate balance area of the coal mass is calculated by the following formula:

$$x_0 = \frac{m}{2f\xi} \ln \frac{K_\gamma H + c_0 cot\Psi_0}{\xi (c_0 cot\Psi_0 + p_1} \qquad [2]$$

where c_0, ψ_0 are the cohesion and internal friction angle respectively of the interfaces between the coal seam and the roof-floor rocks (MPa), f is the interface friction factor, p_1 is the support resistance of the coal wall (MPa), γ is the average

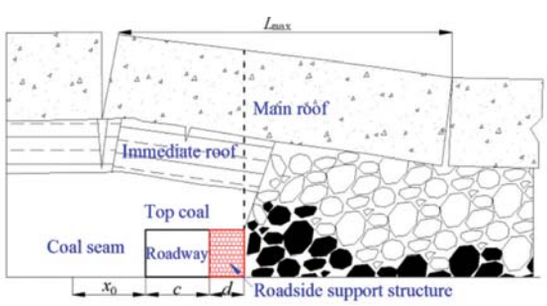

Figure 3—Simplified model of surrounding rock structure for gob-side entry retaining

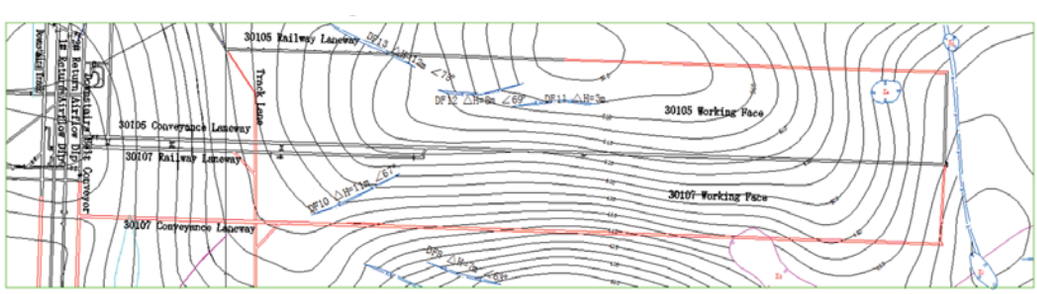

Figure 2—The layout plan of the working face

bulk density of the overlying strata (kN/m3), K is the stress concentration coefficient, H is the mining depth (m), m is the coal seam thickness (m), and ξ is the triaxial stress coefficient ($\xi = (1+\sin\psi_0)/(1-\sin\psi_0)$).

The parameters of the 30105 working face are as follows: h_a = 5.6 m, h_b = 25 m, L_{max} = 20 m, c = 4.8 m, d = 1.5 m, H = 523 m, m = 3 m, c_0 = 0.5 Mpa, p_1 = 0.375 Mpa, γ_a = 24 $\frac{kN}{m^3}$, γ_b = 26 $\frac{kN}{m^3}$, γ = 25 $\frac{kN}{m^3}$, $\psi_0 = 25^0$, f = 0.3, and K = 2. These parameters are substituted into Equations [1] and [2] to obtain x_0 = 4.12 m and the required support resistance at the initial stage of roadside filling P_f = 7200 kN/m.

Roadside support is based on a novel concrete auto-lock entity wall (Zhang *et al.*, 2016c), which is formed by concatenated concrete blocks of various sizes. Auto-locking between the blocks enhances the wall integrity and its resistance to lateral pressure and deformation. According to Chinese Standard GB50010-2010, the Code for Design of Concrete Structure (MHURC-PRC, 2010), the formula for calculating the bearing capability of a concrete auto-lock entity wall is as follows:

$$N_{cu} = \varphi\left(Af_c + f'_y A'_s\right) \quad [3]$$

where N_{cu} is the ultimate compressive strength of the axial compression structure (kN), φ is the stability coefficient, f_c is the concrete axial compressive strength (concrete peak stress) (MPa), f'_s is the rebar yield strength (MPa), A is the structure cross-sectional area (m2), and A'_s is the cross-sectional area of all longitudinal compression rebars (m2).

The parameters of a one linear metre concrete auto-lock entity wall are as follows: wall height l_0 = 3.1 m, wall width d = 1.5 m, wall section short side size b = 1 m, and l_0/b = 3.1/1 = 3.1. According to the specifications, φ is equal to unity. Testing is based on a C30 concrete block with an axial compressive strength f_c of 12.41 MPa. In each block, there are two HRB335 rebar sets r = 3 mm, and their yield strength f'_y is 300 MPa. The structure's section area unit length is $A = d$ = 1.5 m2, and $A'_s = \frac{2\pi r^2 l_0 d}{v}$, where v is the volume of a single block (1.5 × 10-2 m3). The calculation shows that N_{cu} = 23871 kN, therefore the maximum bearing capacity of a 1 m roadside auto-lock entity wall is 23 871 kN. The theoretical calculated safety coefficient is $l = \frac{Ncu}{P_f}$ = 3.3, which indicates that the support structure is safe.

Proper roadway support facilitates the formation of the gob-side entry retaining substructure, which is a basic condition for ensuring entry retaining stability (Bai *et al.*, 2015). Based on actual mine production data, the roadway support plan is finally determined by theoretical calculations combined with field experience. The roadway roof support is based on the 'long/short anchor cable plus bolt plus net' coupling support method plus 'single pillar plus hinged roof-bar'. Support at both sides of the roadway is based on the 'bolt plus net' method. The entry retaining support design is shown in Figure 4.

Similar material simulation experiment

Physical model

Current research findings (Li *et al.*, 2016; Chen *et al.*, 2012; Chen., 2012) show that the deformation of gob-side entry retaining surrounding rock in fully mechanized caving can be divided into three phases: abutment pressure in front of the upper working face, residual abutment pressure in the dip direction in the rear of the working face, and abutment pressure in front of lower working face. The direction of progress of the gob-side entry retaining working face is parallel to the entry retaining direction, which cannot be theoretically simulated in two-dimensional models. However, when spatial relationships are ignored, similar simulations of the three main deformation phases of the gob-side entry retaining surrounding rock can be performed using a two-dimensional model. Based on similarity theory, the constructed model for the different phases of gob-side entry retaining is shown in Figure 5.

Similar conditions

The tests were carried out using the two-dimensional test platform of the State Key Laboratory of Mining Disaster Prevention at Shandong University of Science and Technology, China. The dimensions are as follows: 1900 mm

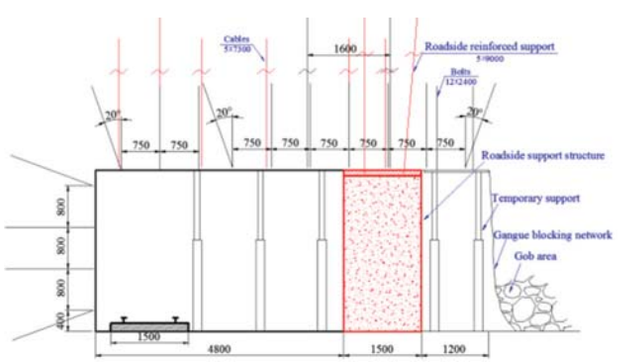

Figure 4—Entry retaining support design

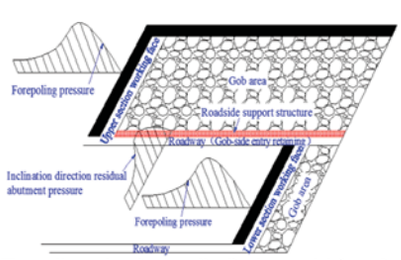

(a) Three-dimensional stress distribution model for gob-side entry retaining

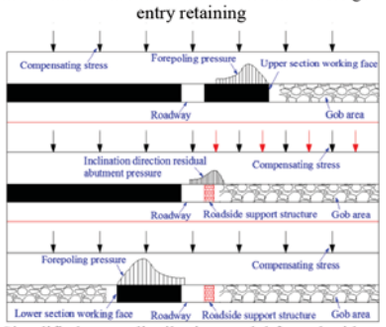

(b) Simplified stress distribution model for gob-side entry retaining based on two-dimensional similar simulations

Figure 5—Different stress influencing phases of gob-side entry retaining

(length) × 220 mm (width) × 1800 mm (height). According to the actual design for gob-side entry retaining and the actual geological data for the 30105 working face in the Shiquan coal mine, the width of the simulated gob-side entry retaining roadway is 8 m, the height is 6 m, and the coal thickness is 6 m. Because the dip angle of the coal seam is shallow, the coal seam and rock strata are assumed horizontal in the model. The simulated overburden thickness is 114 m above the coal seam (including the coal seam thickness) and 26 m below the seam. The overall rock stratum height is 140 m. Based on similarity theory (Zhang Mao, and Ma, 2002; Gu., 1995; Zhao and Zhang, 2015), the model's geometrical similarity constant is $C_l = \frac{lm}{lp} = 1{:}\ 100$ where m represents the model parameter, p represents the prototype parameter, and C_l is the similarity ratio (similarly hereafter). The bulk density similarity constant is $C_p = \gamma_p \gamma_m = 1{:}1.5$, the strength similarity constant of similar material (stress ratio/gravity ratio/hydro-pressure) is $C_\sigma = C_l \times C_p = 1{:}150$, and the time similarity constant is $C_t = \frac{tm}{tp} = \sqrt{C_l} = 1{:}10$. According to the geological data, the average density of the coal seam is 1.4 g/cm3, the uniaxial compressive strength is 16 MPa, the internal friction angle is 300 degrees, and the cohesive force is 1.8 MPa. The experimental materials including sand, calcium carbonate, plaster, and water were selected to carry out the orthogonal tests in accordance with different ratios to obtain test parameters meeting the requirements of the similarity theory and experiment. The experiment coal seam has a density of 0.989 g/cm3 and uniaxial compressive strength of 0.075 MPa. Parameters for the other strata are shown in Table I. The anchor cable was simulated by an aluminum wire 1.8 mm in diameter with a 65 N tensional strength, and the bolt was simulated by an aluminum wire 1.5 mm in diameter with a 55 N tensional strength. Because of the constraints of the testing conditions, providing anchor cable support during entry excavation is difficult. To facilitate operations during testing, anchor cables are laid in position in advance as designed using similarity theory.

Deployment of the measurement points

To study the influence of the abutment pressure in front of the upper working face, the residual abutment pressure in the dip direction in the rear of working face, and the abutment pressure in front of the lower working face on the stability of the roadway surrounding rock, 14 stress sensors are deployed in this simulation. The sensor measurement points S_1–S_4 are located in the upper working face coal seam roof within a certain distance from the roadway section, and the horizontal spacing between measurement points is always 8 m. Measurement points S_5–S_7 are located in the rock stratum within 2 m of the roadway roof, and the horizontal spacing between the measurement points is 4.75 m. S_6 is located in the centre line of the roadway roof. Measurement points S_8–S_{11} are located at the lower working face coal seam roof within a certain distance from the roadway section, and the horizontal spacing between measurement points is always 8 m. Measurement points S_{12}–S_{14} are located in the rock stratum within 2 m of the roadway floor, and the horizontal spacing between measurement points is 4.75 m. S_{13} is located in the centre line of the roadway floor. A detailed measurement point layout is shown in Figure 6.

To study the surrounding rock deformation at different phases throughout the entire gob-side entry retaining process, nine displacement measurement points are deployed around the roadway. Points D_1–D_3 are located in the rock stratum within 1 m of the roadway roof, and the horizontal spacing between measurement points is 3 m. D_2 is located in the centre line of the roadway roof. D_4–D_6 are located in the rock stratum within 1 m of the roadway floor, and the horizontal spacing between measurement points is 3 m. D_5 is located in the centre line of the roadway floor. D_7 and D_8 are located at the 1 m deep coal seam on each side of the roadway. After mining of the upper working face is completed, measurement point D_7 replaces measurement point D_7. Displacement is monitored using the total station method. A detailed layout of the measurement points is shown in Figure 7.

Table I

Parameters of different strata

Lithology	Thickness of stratification for model (cm)	Cumulative height (cm)	Ratior numbe	Bulk density g/cm3	Material dosage (kg)			
					Sand	Calcium carbonate	Plaster	Water
Fine sandstone	6	131	782	1.6	45.65	5.22	1.30	5.22
Siltstone	21	116	755	1.6	159.76	11.41	11.41	18.26
Coal	6	32	864	1.35	39.12	2.93	1.96	4.40
Mudstone	1	6	864	1.5	7.25	0.54	0.36	0.82
Sandy mudstone	5	5	864	1.6	38.64	2.90	1.93	4.35

Figure 6—Layout of the stress measurement points

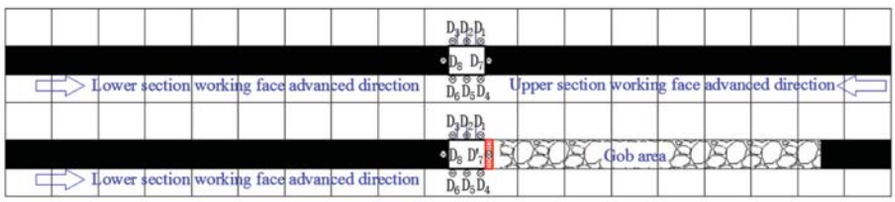

Figure 7—Layout of the displacement measurement points

Mining design

In the test model, roadway development is completed before the upper working face is mined. Subsequently, bolt support for the roadway is deployed in a similar configuration. At each side of the model, a 15 m boundary coal pillar is left. The working face moves from the model boundary towards the roadway. After mining of the upper working face is completed, the suspension roof at the roadside support is immediately reinforced. Next, a roadside support structure with dimensions of 220 mm (length) × 60 mm (height) × 15 mm (width), which was pre-arranged to provide a similar strength, is filled at the roadside, and the roof-contact yielding material (plastic foam with dimensions of 220 mm (length) × 5 mm (height) × 15 mm (width)) is applied at the support roof to simulate actual roof-contact yielding material (wooden pillar, Figure 8). After the support is in place, the model is loaded under stress for 1–2 days to simulate roadway and roadside support deformation caused by residual abutment pressure in an inclined direction in the rear of working face. The final step is mining of the lower working face. In the model, the mining height is 6 cm, which is equivalent to the actual mining height of 6 m, and the mining progresses at 2.4 cm in intervals of 1 hour, which is equivalent to the 2.4 m progress that occurs each day.

Analysis of the test results

Influencing phase of abutment pressure in front of upper section working face

For the upper working section, the vertical stress variation in the roadway roof and floor as well as the coal seam roof is shown in Figure 9. The displacement variation curve for the roadway surrounding rock is shown in Figure 10.

Figure 9a shows that with continuous progress of the working face, the stress on the coal seam roof always increases at the initial stage and then decreases. Moreover, prior to the working face reaching a measurement point, the magnitude of variation is larger at points closer to the working face. Variations are observed at measurement points S_1, S_2, S_3, and S_4 when the working face progresses to 12 m, 14.4 m, 21.6 m, and 31.2 m, respectively, and when the working face progresses to 36 m, 45.6 m, 52.8 m, and 61 m, respectively, the stress reaches its peak. When the working face passes the measurement point, the stress at the measurement point changes to a negative value, and the

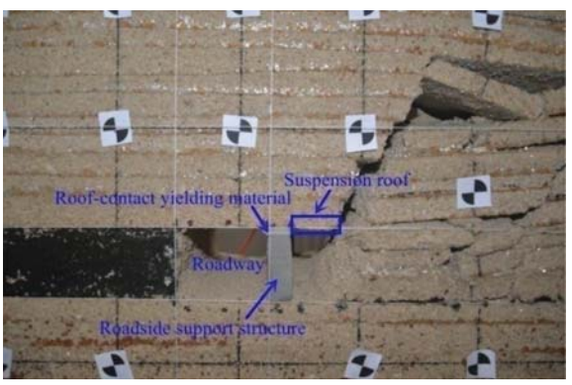

Figure 8—Simulation test for roadside support

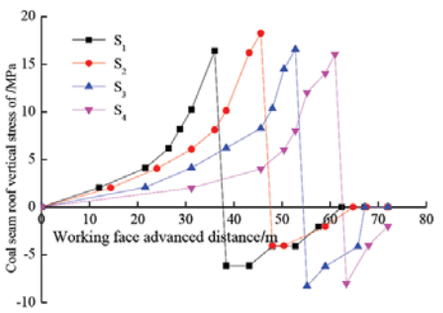

(a) Coal seam roof stress variation

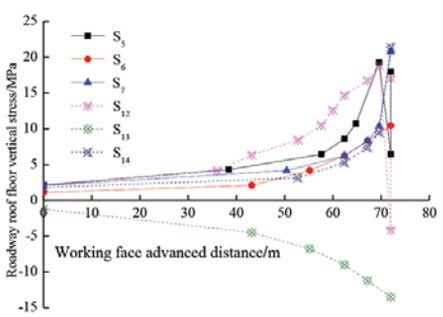

(b) Roadway roof floor stress variation

Figure 9—Stress variation – upper section working face

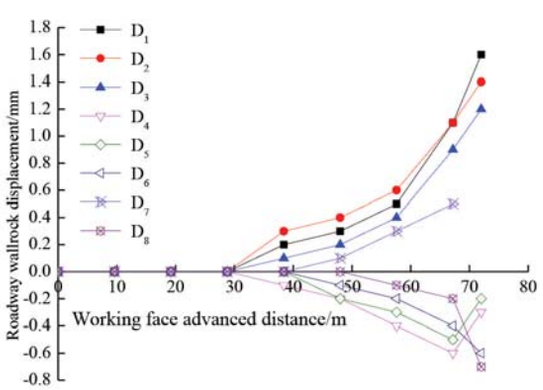

Figure 10—Displacement variation in roadway surrounding rock – upper section working face

measurement point becomes invalid. Based on the stress variation trend for measurement points S_1–S_4, the analysis shows that the abutment pressure is effective within 33 m in front of the working face. In addition, the peak value of abutment pressure is located in 2–3 m in front of the working face, where the peak values are within the range of 16–18 MPa.

Figure 9b shows that the roadway roof and floor stress increase with the progress of the working face, and after the stress values at the measurement points S_5 and S_{12} reach peak values, they undergo a sharp decrease and then increase again. The initial stress values at the measurement points S_5, S_6, and S_7 are 2.15 MPa, 1.1 MPa, and 2.08 MPa, respectively. Because the measurement points S_5 and S_7 are located at both sides of the roadway roof and measurement point S_6 is located in the centre line of the roadway roof, the concentrated stress accumulates at both sides of the roadway roof after roadway excavation is completed, which leads to an increase in stress at measurement points S_5 and S_7 before the working face and a relatively small stress of 1.1 MPa at the roadway roof measurement point S_6. The stresses at measurement points S_5, S_6, and S_7 reach peak values of 19.3, 10.4, and 20.7 MPa when the working face progresses to 69.6 m, 72 m, and 72 m, respectively. The peak stress at measurement point S6 is relatively small because when the roadway is under abutment pressure in front of the working face, the roadway roof begins to sink and releases energy. When the working face passes measurement point S_5, measurement point S_5 still bears pressure because of the effect of the immediate suspension roof; however, the stress decreases to 6.4 MPa. The initial stress values at measurement points S_{12}, S_{13}, and S_{14} are 2.1, -1.2, and 1.8 MPa, respectively. Measurement point S_{13} is under reducing stress, and the value is negative. The cause of the differences in the initial stress values is similar to the cause of the differences at the roadway roof measurement points S_5, S_6, and S_7. The stress values at measurement points S_{12}, S_{13}, and S_{14} reach peak values of 18.9 MPa, -13.5 MPa, and 21.4 MPa when the working face progresses to 69.6 m, 72 m, and 72 m, respectively. Because of significant roadway floor deformation, rock at S_{13} releases energy, which results in a relatively small stress. When the working face progresses to 72 m, the gob area and roadway are connected. Because of the effect of roadway support, the roadway roof can resist deformation to a certain degree. Long suspension roof spans lead to higher peak stress values at measurement point S_{14} than at measurement point S_{12}. The stress values at measurement points S_5 and S_{12} decline sharply, and after the roadside support is completed, the stress values at measurement points S_5 and S_{12} rise sharply.

Figure 10 shows that before the working face progresses to 38.4 m, the deformation of the roadway surrounding rock is zero. When the face reaches 38.4 m, the roadway surrounding rock starts to displace. As the working face progresses further, the displacement gradually increases, and after measurement points D_4 and D_5 reach peak values, the displacements then decrease. Before the working face progresses to 72 m, among all roadway roof measurement points, measurement point D_2 shows the largest reduction, and measurement point D_3 the smallest. When the working face progresses to 72 m, measurement point D_1 shows the largest reduction, because before the working face progresses to 72 m, measurement points D_1 and D_3 are affected by roadway support on both sides, and they show a smaller reduction than measurement point D_2. When the working face progresses to 72 m, the right side of the roadway loses support, and the stress reduction at measurement point D_1 increases instantaneously. The roadway floor has a smaller displacement than the roof, and measurement point D_4 shows the largest displacement, while measurement point D_6 shows the smallest. When the working face progresses to 72 m, the right side of the roadway has a developed gob, and the roof fails to reach the floor, which leads to decreases in the displacement at the floor at measurement points D_5 and D_6. The displacement values at measurement points D_7 and D_8 at both sides of the roadway increase gradually with the progress of the working face, and the rate accelerates. Overall, the primary mining-induced deformation of the roadway surrounding rock is relatively small, which facilitates roadway maintenance in the stable phase of entry retaining.

Influencing phase of residual abutment pressure in inclination direction in the rear of working face

After the upper working face is completed, the residual abutment pressure from the gob area is readjusted. The stress variation in the roadway roof and floor that occurs over time as the working face progresses further is shown in Figure 11. The roadway displacement curve is shown in Figure 12.

Figure 11 shows that after the upper working face is completed, the residual abutment pressure is adjusted. Over time, the stress in the roadway surrounding rock increases and eventually stabilizes. Among the roof measurement points S_5–S_7, measurement point S_5 has the most significant stress increment and measurement point S_6 the least. Measurement point S_5 is located in the roof rock immediately above the support structure and receives the most influence from the residual abutment pressure of the gob area, which leads to a significant stress increment. Measurement point S_6, in the centre line of the roadway roof, develops a relatively large deformation and releases energy, which leads to relatively small stress variations. Among the roadway floor stress measurement points S_{12}–S_{14}, measurement point S_{12} has the most significant stress increment (similar to measurement point S_5), measurement point S_{13} has the least significant stress increment (similar to measurement point S_6), and measurement point S_{14} is affected by concentrated

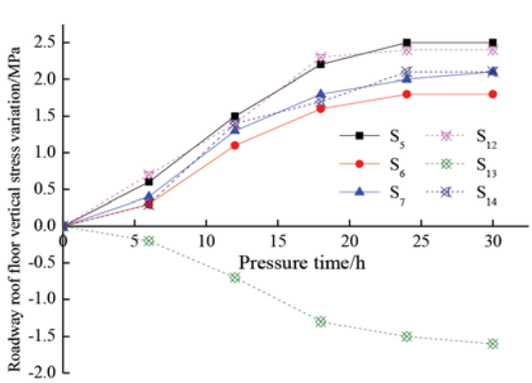

Figure 11—Stress variation in roadway roof and floor – residual abutment pressure

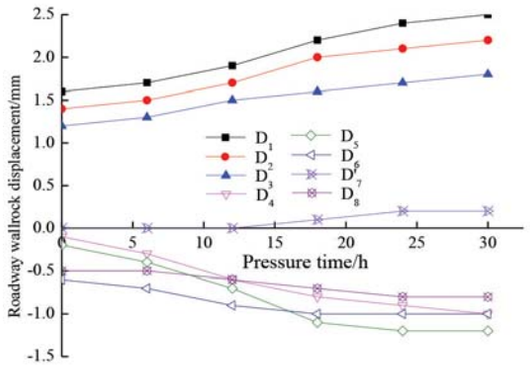

Figure 12—Displacement variation in roadway surrounding rock – residual abutment pressure

stress from the coal wall at the left side of the roadway. The stress at this point gradually increases and eventually stabilizes.

Figure 12 shows that after the upper working face is completed, the lateral residual abutment pressure in the gob area results in roadway deformation. Over time, the deformation rate stabilizes. Among all of the roadway roof measurement points D_1~D_3, measurement point D_1 has the largest reduction in displacement and measurement point D_3 the smallest. Because measurement point D_1 is the closest to the roadside support structure, the roadside roof-contact yielding material is affected by the concentration load of the overlying strata and begins to deform, which leads to the largest deformation at measurement point D_1. Measurement point D_3 is located above the left side coal wall, and because of the support of the roadway coal wall, has the smallest deformation. The floor heave at the roadway floor measurement points D_4–D_6 increases over time, and measurement point D_5 has the largest final floor heave. The displacements at points D_7–D_8 at both sides of the roadway also increase gradually over time. However, because of the high rock strength of the roadside block, the displacement at measurement point D_7 is relatively small and primarily manifested as a tilting of the entire support structure toward the roadway. In contrast, the coal wall is at the left side, and has a lower strength. Affected by the concentrated stress on the coal wall, measurement point D_8 has a larger relative displacement. The roadway deformation during this phase increases over time and eventually stabilizes. However, the variations are relatively small and do not have an impact on lower working face mining.

Influencing phase of abutment pressure in front of lower working face

The vertical stress variation in the roadway roof and floor as well as the coal seam roof during mining of the lower working face is shown in Figure 13. The roadway displacement variation curve is shown in Figure 14.

A comparison of Figure 13 and Figure 9 shows that during the lower mining phase, the stress variation trend in the coal seam roof and roadway roof /floor is the same as that during the upper mining phase. Based on the stress variation trend at measurement points S_8–S_{11}, the analysis shows that the influencing zone of abutment pressure is within 35 m of the front of the lower working, the peak value

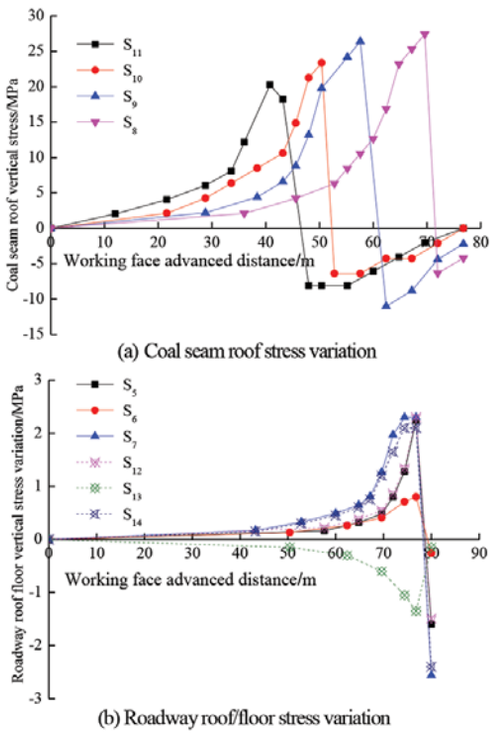

Figure 13—Stress variation – lower working face

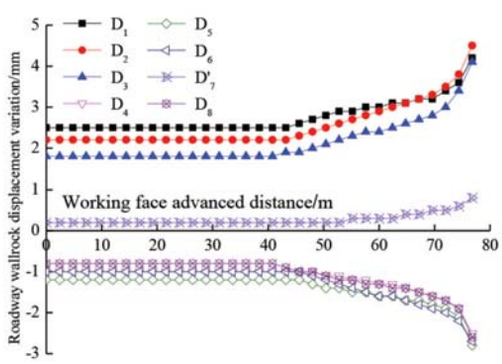

Figure 14—Displacement variation in roadway surrounding rock – lower working face

of abutment pressure is located in 4–5 m in front of the working face, and the maximum stress is larger than the maximum stress at the upper section coal seam roof. With increased testing time, the moisture content of the simulated rock changes accordingly, resulting in variations of the zone of influence of the abutment pressure, peak stress area, and span of the roof cantilever. Figure 13b shows that the stress in the roadway roof and floor increases as the lower working face progresses further. Affected by abutment pressure, the stress variation rate accelerates and the stress reaches a peak when the working face progresses to approximately 76.8 m. Subsequently, the roadway develops a significant deformation and the stress decreases sharply.

Figure 14 shows that as the lower working face progresses, deformation of the roadway surrounding rock is initially stable. When the working face progresses to 43.2 m, the surrounding rock deformation starts to accelerate. When the working face progresses to approximately 76.8 m, the peak abutment pressure has an effect on the roadway. At this

moment, the roadway deformation rate reaches its peak. Because of the high strength of the roadside support structure, the deformation is relatively small and primarily takes the form of tilting of the entire structure. Overall, the deformation of the entire roadway is significant. However, the roadway still satisfies the requirement for lower working face mining.

After the lower working is completed, the reserved upper roadway will no longer be used. The roadway is located in the gob area and develops a significant deformation, as shown in Figure 15.

Figure 15 shows photographs of the surrounding rock deformation after the entry retaining structure is abandoned. The roadway roof and floor and two sides show significant deformation, and the roof anchor cable is exposed. The roadside support structure undergoes a relatively small actual deformation during the tilting of the entire structure. Therefore, in field implementations, measures should be taken to reinforce the integrity and anti-toppling capability of the roadside support structure.

Numerical model verification

FLAC3D (Itasca, 2009), is selected as the computing software. The total size of the model is 505 m × 192 m × 79 m, with 52 m roof thickness of coal seam and 27 m floor thickness of coal seam (including the coal seam). The model is divided into 560 400 basic units and 605 772 grid nodes. The burial depth of the coal seam is 523 m, and the thickness is 6 m. The coal seam is set horizontal due to the small actual dip angle. The working face is 220 m long. The size for gob-side entry retaining is rectangular with a cross-section of 5 m × 3 m. Because the paper focuses on the influence of mining in the upper and lower panels on the confining pressure of gob-side entry retaining, the grids at the location of gob-side entry retaining, which is the main research area, are finer. The initial model is shown in Figure 16.

The horizontal displacement constraints are set around the model, and the fix constraint is set on the base. The upper interface is a stress boundary, whose load is determined by the load imparted by the overlying strata (Bu and Mao, 2009). The caving mining method is used to manage the roof, and the Mohr-Coulomb model is simulated. The lithology parameters are shown in Table II.

To analyse the displacement and stress variation in the surrounding rock of the retained roadway during mining of the upper and lower sections, the displacement measuring points D_1–D_4 are set respectively in the roadway roof, floor,

(a) Overall model diagram

(b) Partial deformation of the entry retaining surrounding rock

Figure 15—Photographs showing the entry retaining surrounding rock

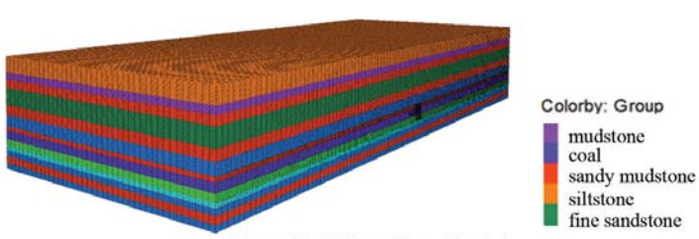

Figure 16- Grid partition of model

Figure 16—Grid partition of model

Table II

Physical and mechanical parameters of rock mass

Lithology	Bulk modulus (MPa)	Shear modulus (GPa)	Bulk density (kg.m^{-3})	Cohesion (MPa)	Internal friction angle (°)	Tensile strength (GPa)
Siltstone	4	3	2550	3.5	33	2.2
Mudstone	2.8	1.9	2200	3.4	32	1.8
Sandy mudstone	3.6	2.9	2450	2.35	32	1.32
Fine sandstone	3.3	2.4	2600	8.2	32	2.8
Coal	1.8	1.4	1420	1.8	30	0.9
Roadside support	3.0	2.2	2700	6.2	30	2.1

and midpoints of two sides. The stress points S_1 and S_2 are set at 4 m on left side of the roadway and in the roadside support structures on the right. The displacement and stress measuring lines are set in the strata 1 m from the roadway roof as well as the floor. The layout of the measuring points is shown in Figure 17.

Figure 18 shows the rock stress variation on two sides of retained roadway with the advance of the working face during mining of the upper section.

From Figure 18, stresses at measuring point S_1 and S_2 increase as the working face advances. However, stress at point S_2 increases dramatically before caving of the overlying strata of gob, and then increases slowly after periodic caving of the overlying strata of gob with further advance of the working face.

Figure 19 shows the displacement variation of the rock surrounding the retained roadway as the working face advances. The vertical displacement at measuring point D_1 and the horizontal displacement at measuring point D_3 increase continuously as the face advances, but the variation of the vertical displacement is larger than that of the horizontal displacement. The vertical displacement at measuring point D_2 and the horizontal displacement at measuring point D_4 vary slightly initially, but when the working face advances a certain distance, the variation increases sharply, and then as the working face continues to advance, the vertical displacement at D_2 decreases, that is, floor heave diminishes, while the horizontal displacement at D_4 increases inversely in a narrow range.

Figures 20 and 21 respectively describe the displacement and stress in the roadway roof and floor in the measurement lines. Figure 20 shows that the vertical displacements of

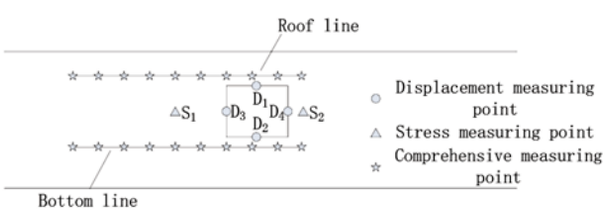

Figure 17—Layout of measuring points around roadway

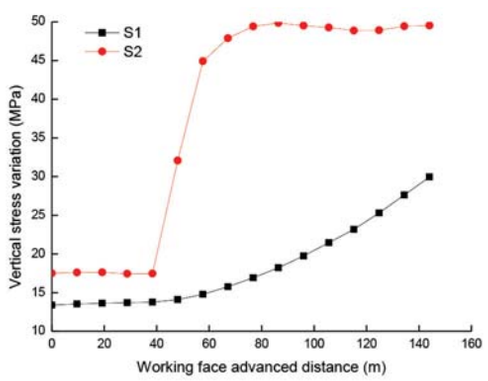

Figure 18—Stress variation – retained roadway sides

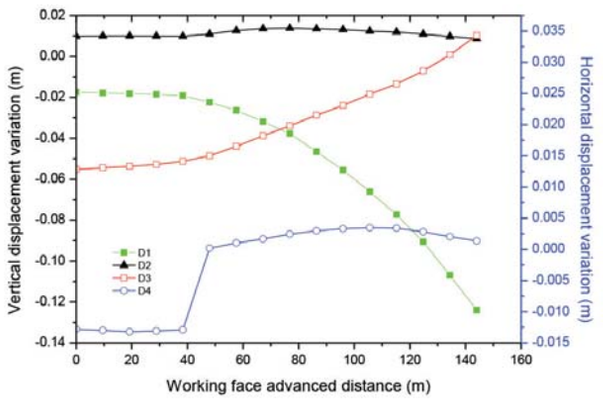

Figure 19—Displacement variation – retained roadway sides

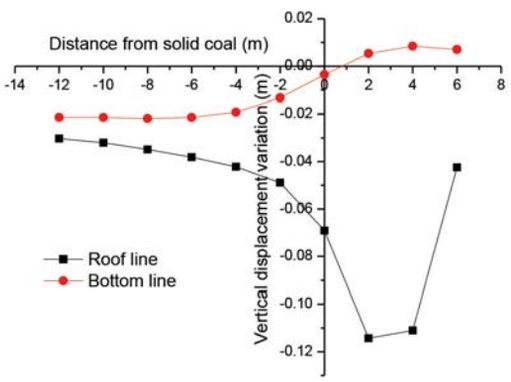

Figure 20—Displacement variation – roadway roof and floor

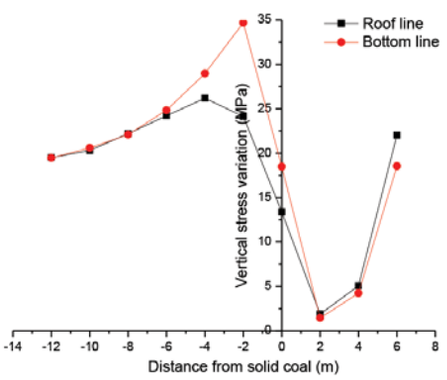

Figure 21—Stress variation – roadway roof and floor

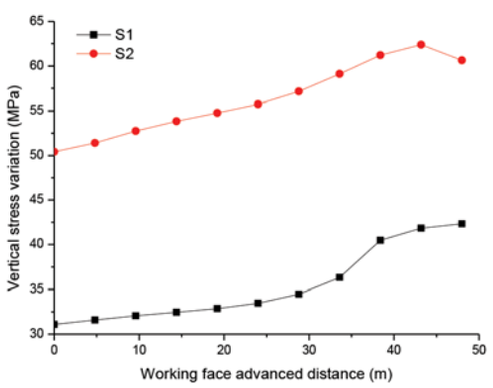

Figure 22—Stress variation – retained roadway sides

measuring points on the coal wall decrease with increasing distance from the roadway axis, and the roof subsidence displacement is larger than floor heave displacement, which is supported by the stress variation shown in Figure 21. Figure 21 shows that the stress concentrates on both sides of roadway, while the stress in the roof and floor releases due to the excavation.

The variation of in stress and displacement on both sides of the retained roadway during mining of the lower panel, are shown in Figures 22 and 23.

Figure 22 shows that the roof and floor stresses increase as the working face advances in the pre-influencing phase of mining of the lower section, which is consistent with the trends shown in Figure 18. From Figure 23, the vertical displacement of the roof measuring points D1 and the floor measuring points D_2, as well as the horizontal displacement of measuring point D_3, all increase with advance of the working face. The variation in vertical displacement is larger than that of horizontal displacement; but the horizontal displacement at measuring point D_4 on the side of the roadside support changes as mining progresses, indicating the instability of the roadside support. This is corroborated by the failure of the roadside support (Figure 13).

The distribution of the plastic zone of the surrounding rock in the retained roadway and the actual field observation as the upper and lower working faces are mined are shown in Figures 24 and 25 respectively.

From Figure 24a, mining of the upper section has an effect on roadside support, leading to damage in the upper plastic zone, but the support is stable overall and is very

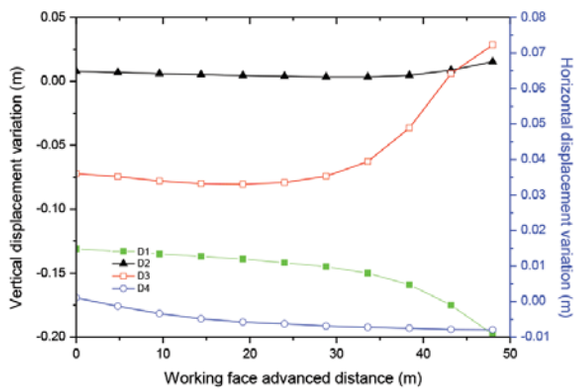

Figure 23—Displacement variation – retained roadway sides

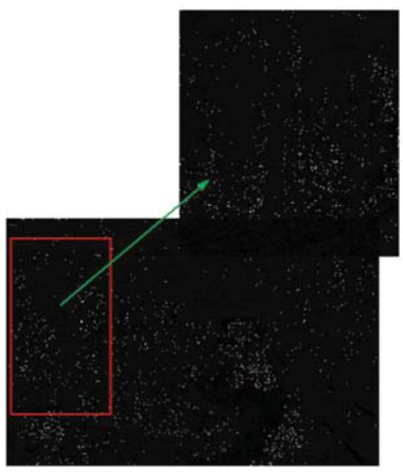

Figure 25—Field observation of retained roadway

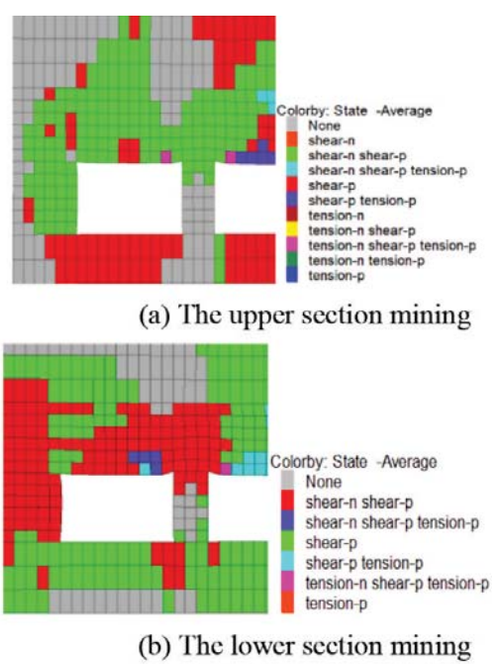

Figure 24—Distribution of plastic zone of surrounding rock in retained roadway

effective, as verified by the similar material test (Figure 8) and the engineering application (Figure 25). Mining of the lower section has a more serious effect on roadside support (Figure 24b), and plastic zones form on the top and bottom of the roadside support, increasing the instability, which is again consistent with the failure of the roadside support (Figure 13).

Discussion of the method

The similar material simulation test is based on the similarity theory proposed by Kuznetsov, and is an experimental research method leading from physical testing, mechanical analysis, and model testing to a practical engineering guide (Qian *et al.*,1958; Li., 1988). It is widely used in such industries as mining, water conservancy, and underground engineering, and is a mainstream research method in natural science and engineering technology (Cheng, Qi, and Hong,2016; Gong, Hu, and Zhao, 2005; Liu, Cai, and Zhou, 2015; Shi, Zhang, and Li, 2011; Yao, Feng, and Liao, 2017). With the rapid development of computerized methods in rock mechanics, much experimental work has been replaced by numerical simulation (Zhang, 1999; Zhang *et al.*, 2016b; Wang, Zhang, and Gao, 2015). Meanwhile, the traditional point-measurement method, which takes points as the basic measuring locations (Yao, Feng, and Liao, 2017) is still used in the similar material simulation test, but suffers from low measurement accuracy and difficulty in stress measurement as well as displacement in the internal part of model, which may be solved in the future by optical fibre sensing technology that can offer measurement along lines (Chai, Wang, and Liu, 2015; Cornelia and Marcel, 2003; Yang, Bhalla, and Wang, 2007). As one of the experimental rock mechanics methods, however, the similar material simulation test is still widely used in the study of coal mining, which has incomparable advantages in the field of a wider range of rock caving and movement than numerical simulation (Luo, Wu, and Liu, 2016; Fan, Mao, and Xu, 2016; Wu, Xie, and Wang,2010).

Conclusions

Based on detailed geological conditions and field design plans, a similar material simulation experiment and numerical simulation were performed to study the stress and deformation variations of the roadway surrounding rock at different states of gob-side entry retaining in fully mechanized caving. The following conclusions can be drawn.

(1) Roadway surrounding rock of gob-side entry retaining in fully mechanized caving has three critical influencing phases: the phase of abutment pressure in front of the upper working face, the phase of residual abutment pressure in the dip direction in the rear of the working face, and the phase of abutment pressure in front of the lower working face.

(2) Gob-side entry retaining in fully mechanized caving is also affected by mining superposition, and roadway deformation is further exacerbated with the progress of the lower working face. To ensure that the entry retaining structure satisfies production requirements at the lower working face, roadway surrounding rock at the roadway development phase and during mining of the upper section should be monitored and the support structure at the entry retaining phase should be reinforced.

(3) A 'long/short anchor cable plus bolt plus net' coupling support method provides excellent support for roadways with fractured roofs. The bolts reinforce a fractured roof, forming a 'composite beam' which is suspended by a long anchor cable in the competent main roof, and the short anchor cable increases the support strength.

(4) Roadside support using roof-contact yielding material facilitates benign roadway roof deformation for energy release and improves structural stability. When gob-side entry retaining is implemented in dipping and steeply dipping coal seams, the strength of the roadside support structure must be ensured and effective measures should be taken to enhance the structural integrity and resistance to toppling of the roadside support.

Acknowledgements

The study presented in this paper was jointly supported by grants from the National Natural Science Foundation of China (grants no. 51379119, 51109124, 51509149, and 41472281), the Specialized Research Fund for the Doctoral Program of Higher Education of China (grant no. 20113718120009), the National Basic Research Program of China (grant no. 2012CB72310401), the Specialized Funds for 'Taishan Scholar' construction of Shandong Province, the Funds for innovative team of Coal Pillar Performance and Overburden Rock Control, and the Fund for Outstanding Young Scientist Research Award of Shandong Province (grant no. BS2011SF016), Key Laboratory of Safety and High-efficiency Coal Mining, Ministry of Education (grant no. JYBSYS2014106), and the international cooperation training projects for excellent teachers in Shandong Province universities.

References

Bai, J.B., Shen, W.L., Guo, G.L., Wang, X.Y., and Yu, Y. 2015. Roof deformation, failure characteristics, and preventive techniques of gob-side entry driving heading adjacent to the advancing working face. *Rock Mechanics and Rock Engineering*, vol.48, no. 6. pp. 2447–2458, 2015. doi: 10.1007/s00603-015-0713-2.

Bu, W.K. and Mao, X.B. 2009. Research on effect of fault dip on fault activation and water inrush of coal floor. *Chinese Journal of Rock Mechanics and Engineering*, vol. 28, no. 2. pp. 386-394.

Chai, J., Wang, Z.L., and Liu, W.G. 2015. Monitoring movement laws of overlying key strata for coal mining in similar model. *Journal of China Coal Society*, vol. 40, no. 1. pp. 35 – 41. doi: 10.13225 /j.cnki jccs.2013.1777

Chen, Y. 2012. Study on stability mechanism of rockmass structure movement and its control in gob-side entry retaining. China University of Mining and Technology, Xuzhou.

Chen, Y., Bai, J.B., Wang, X.Y., Ma, S.Q., Xu, Y., Bi, T.F., and Yang, H.Q. 2012. Support technology research and application inside roadway of gob side entry retaining. *Journal of China Coal Society*, vol. 37, no. 6. pp. 903–910.

Cheng, Z.H., Qi, Q.X., and Hong, Y. 2016. Evolution of the superimposed mining induced stress-fissure field under extracting of close distance coal seam group. *Journal of China Coal Society*, vol. 41, no. 2. pp. 367–375. doi:10.13225/ j.cnki.jccs.2014.15903-4

Cornelia, S.H. and Marcel, N.G.B. 2003. Fiber Bragg grating strain measurements in comparison with additional techniques for rock mechanical testing. *IEEE Sensor Journal*, vol. 12. pp. 50–55.

Deng, Y.H., Tang, J.X., Zhu, X.K., Yong, F., and Hu, H. 2011. Industrial test of concrete packing for gob-side entry retained in gently inclined medium-thickness coal seam. *Journal of Southwest Jiaotong University*, vol. 46, no. 3. pp. 523–528.

Deng, Y.H. and Wang, S.Q. 2014. Feasibility analysis of gob-side entry retaining on a working face in a steep coal seam. *International Journal of Rock Mechanics and Mining Sciences*, vol. 24, no. 4. pp. 499–503.

Fan, Z.Z., Mao, D.B., and Xu, G. 2016. Analysis on the scale effect in the fully mechanized mining panel width with large mining height and dip angle. *Journal of China Coal Society*, vol. 41, no. 3. pp.581–585. doi: 10.13225/j.cnki.jccs.2015.0589

Franciss, F.O. 1997. Weak Rock Tunneling, Balkema, Rotterdam, The Netherlands.

Ministry of Housing and Urban-Rural Development of the People's Republic of China. 2010.GB50010-2010 Code for Design of Concrete Structures, China Architecture & Building Press, Beijing.

Gong, P.L., Hu, Y.Q., and Zhao, Y.S. 2005. Three-dimensional simulation study on law of deformation and breakage of coal floor on mining above aquifer. *Chinese Journal of Rock Mechanics and Engineering*, vol. 24, no. 3. pp. 4396–4401.

Gu, D.Z. 1995. Equivalent Material and Similar Models. China University of Mining and Technology Press, Xuzhou. pp. 6–56.

Han, C.L., Zhang, N., Li, B.Y., Si, G.Y., and Zheng, X.G. 2015. Pressure relief and structure stability mechanism of hard roof for gob-side entry retaining. *Journal of Central South University*, vol. 22, no. 11. pp. 4445–4455. doi: 10.1007/s11771-015-2992-x

Li, H.C. 1988, The Similitude Material Model Test on the Rock Pressure. China University of Mining and Technology Press, Xuzhou. pp. 1-2.

Li, X.H., Ju, M.H., Yao, Q.L., Zhou, J., and Chong, Z.H. 2016. Numerical investigation of the effect of the location of critical rock block fracture on crack evolution in a gob-side filling wall. *Rock Mechanics and Rock Engineering*, vol.49, no. 3. pp. 1041–1058. doi: 101007/s00603-015-0783-1

Li, J.P. 2005. Study on the technology of gob-side entry retaining with longwall top coal caving system and its application in Lu'an mining district. China Coal Research Institute, Bingjing.

Liu, F.M., Cai, Q.X., and Zhou, W. 2015. Experimental study on the rainfall infiltration rule in the dump slope of surface mines. *Journal of China Coal Society*, vol. 40, no. 7. pp. 1534–1540. doi: 10.13225/j.cnki.jccs.2015.0100

Luo, S.H., Wu, Y.P., and Liu, K.Z. 2016. Study on the shape of the space stress arch shell in steeply dipping coal seam mining. *Journal of China Coal Society*, vol. 41, no. 12. pp. 2993–2998. doi: 10.13225/j.cnki.jccs.2016.0539.

Ma, L.Q. and Zhang, D.S. 2004. Industrial test of road-in packing for gob-side entry retaining in fully-mechanized coalface with top-coal caving. *Journal of China University of Mining & Technology*, vol. 33, no. 6. pp. 54–58.

Ma, L.Q., Zhang, D.S., Chen, T., and Fan, G.W. 2007. "Study on packing body supporting resistance of enter-in packing for in-situ gob-side entry retaining in fully-mechanized top-coal caving mining face. *Chinese Journal of Rock Mechanics and Engineering*, vol. 26, no. 3. pp. 544–550.

MHURC-PRC (Ministry of Housing and Urban-Rural Construction of the People's. Republic of China). 2010. GB 50010-2010. Code for Design of Concrete Structures. https://www.chinesestandard.net/PDF-Excerpt/ShowPDFExcerpt.aspx?ExcerptID=GB%2050010-2010

Qian, M.G., Isnard, A.M., Xi,- M.B., and Brezhnev, L. 1958. Research of pressure used by similar material simulation method. *Journal of Beijing Institute of Mining*, vol. 14, no. 1. pp. 28–48.

Ren, S., Guo, S.T., Jiang, D.Y., and Yang, C.H. 2011. Study of creep similar model and creep equivalent material of salt rock. *Rock and Soil Mechanics*, vol. 32, no. 1. pp. 106–110.

Shi, X.Q., Zhang, Z.Q., and Li, H.Y. 2011. Experimental study of pre-reinforcement technology for weak surrounding rock of tunnel. *Chinese Journal of Rock Mechanics and Engineering*, vol. 30, no. 9. pp. 1803–1809.

Su, Q.Z. and Hao, H.J. 2002. Modeling of support resistance in roadside packing for retaining entry along gob-side. *Coal Mining Technology*, vol. 7, no. 4. pp. 32–35.

Tan, Y.L., Yu, F.H., Ning, J.G., and Zhao, T.B. 2015. Design and construction of entry retaining wall along a gob side under hard roof stratum. *International Journal of Rock Mechanics and Mining Sciences*, vol. 77. pp. 115–121. doi: 10.1016/j.ijrmms.2015.03.025

Itasca. 2009. FLAC3D-Fast Lagrangian Analysis of Continua.4th edn. Itasca Consulting Group Inc.. Minneapolis, MN.

Wang, H., Zhang, P.S., and Wang, M.H. 2015. Numerical study on the stability of surrounding rock of gob-side entry retaining along the fully mechanized working face in inclined seam. *China Science Paper*, vol. 10, no. 21. pp. 2568–2573.

Wang, J.A., Zhang, J.W., and Gao, X.M. 2015. Fracture mode and evolution of main roof stratum above longwall fully mechanized top coal caving in steeply inclined thick coal seam (I) - initial fracture. *Journal of China Coal Society*, vol. 40, no. 6. pp. 1353-1360. doi: 10.13225/j.cnki.jccs.2015.0407

Wang, W.J., Hou, C.J., Bai, J.B., and Li, X.H. 2001. Mechanical deformation analysis and principle of floor heave of roadway driving gob in fully mechanized sub-level caving face. *Rock and Soil Mechanics*, vol. 22, no. 3. pp. 319–322.

Wu,Y.P., Xie, P.S., and Wang, H.W. 2010. Incline masonry structure around the coal face of steeply dipping seam mining. *Journal of China Coal Society*, vol. 35, no. 8. pp. 1252–1256.

Xu, H.Y. and Wang, Y. 2015. Similar simulation study on moving rule of surrounding rock of gob-side entry retaining at fully mechanized caving face. *Coal Technology*, vol. 34, no. 8. pp. 73–75.

Yang, H.Y., Cao, S.G., Li, Y., Sun, C.M., and Guo, P. 2015. Soft roof failure mechanism and supporting method for gob-side entry retaining. *Minerals*, vol. 5, no. 4. pp. 707-722. doi: 10.3390/min5040519

Yang, H.Y., Cao, S.G., Wang, S.Q., Fan, Y.C., Wang, S., and Chen, X.Z. 2016. Adaptation assessment of gob-side entry retaining based on geological factors. *Engineering Geology*, vol. 209. pp. 143–151. doi: 10.1016/j.enggeo.2016.05.016

Yang, Y.W., Bhalla, S., and Wang, C. 2007. Monitoring of rocks using smart sensors. *Tunneling and Underground Space Technology*, vol. 22. pp. 206–221.

Yao, Q., Feng, T., and Liao, Z. 2017. Damage characteristics and movement of inclined strata with sublevel filling along the strike in the steep seam. *Journal of China Coal Society*, vol. 42, no. 12. pp. 3096–3105. doi: 10.13225/j.cnki jccs.2017.0509

Yao, Q., Feng, T., Wang, W.J., Liao, Z., and Ma, C.F. 2017. On preparing the materials as close as possible in the experimental ratio and mechanical properties with those gained from mining. *Journal of Safety and Environment*, vol. 17, no. 6. pp. 2129-2134.

Zhang, D.S., Mao, X.B., and Ma, W.D. 2002. Testing study on deformation features of surrounding rocks of gob-side entry retaining in fully-mechanized coal face with top-coal caving. *Chinese Journal of Rock Mechanics and Engineering*, vol. 21, no. 3. pp. 331–334.

Zhang, J.Y. 1999. Study on 3D finite element method simulation of strip mining of great inclined and multiple coal seams. *Journal of China Coal Society*, vol. 24, no. 3. pp. 242–246.

Zhang, P.S. and Lin, D.C. 2014. Technology of the Retaining Gob-Side Entry. China University of Mining and Technology Press, Xuzhou. pp. 10–27.

Zhang, P.S., Kan Z.H., Li, K., Zhao, S.J., Miao, W. Wu, S.X., Zhao, Y.P., and Wang, J.W. 2016c. A novel concrete precast block auto-lock entity wall. Chinese patent ZL201520901992.5. 22 June 2016.

Zhang, P.S., Kan, Z.H., Wang, M.H., Zhao, S.J., Li, K., and Miao, W. 2016a. Numerical study on the stability of surrounding rock of gob-side entry retaining along the fully mechanized working face in inclined seam. *Safety in Coal Mines*, vol. 47, no. 8. pp. 37–44.

Zhang, P.S., Yan, W., Zhang, W.Q., Shen, B.T., and Wang, H. 2016b. Mechanism of water inrush due to damage of floor and fault activation induced by mining coal seam with fault defects under fluid-solid coupling mode. *Chinese Journal of Geotechnical Engineering*, vol. 38, no. 5. pp. 877–889.

Zhang, Y.Q., Tang, J.X., Xiao, D.Q., Sun, L.L., and Zhang, W.Z. 2014. Spontaneous caving and gob-side entry retaining of thin seam with large inclined angle. *International Journal of Rock Mechanics and Mining Sciences*, vol. 24, no. 4. pp. 441–445.

Zhang, Z.Z., Bai, J.B., Chen, Y., and Yan, S. 2015. An innovative approach for gob-side entry retaining in highly gassy fully-mechanized longwall top-coal caving. *International Journal of Rock Mechanics and Mining Sciences*, vol. 80. pp. 1–11. doi: 10.1016/j.ijrmmis.2015.09.001

Zhao, Y. and Zhang, Z.G. 2015. Mechanical response features and failure process of soft surrounding rock around deeply buried three-centered arch tunnel. *Journal of Central South University*, vol. 22, no. 10. pp. 4064–4073. doi: 10.1007/s11771-015-2951-6 ◆

http://dx.doi.org/10.17159/2411-9717/2018/v118n5a6

Determination of stable spans in UG2 excavations

by B.P. Watson*, and R. Gerber†

Synopsis

The hangingwall of the UG2 Reef is characterized by stratification in the form of thin and weakly cohesive chromitite stringers that can vary in number and height above a stope. These stringers, in conjunction with shallow-dipping thrust faulting, endemic across the platinum-bearing reefs of the Bushveld Complex, affect the maximum span that can be safely mined. The paper describes the research that was carried out to determine the interaction of support with the rock mass in both conventional and mechanized workings, and provides insights into stable span determination where excavations are intersected by a shallow-dipping thrust structure. Four important issues are highlighted.

1. Mine pole and pack support has a greater influence on stability than span in the context of the studied database for conventional mines.
2. Shallow-dipping discontinuities are a dominant feature in stability analyses.
3. The height of the vertical tensile zone does not restrict the fallout height if persistent shallow-dipping structures are present.
4. In the context of the numerical modelling shown in the paper, a span of 6 m is safe when 1.8 m long, full-column resin bolts are used at a support resistance of 48 kN/m^2, regardless of the k-ratio or height of the triplets (intersections must be dealt with separately).

Several leading practices have been developed in recent years to identify and timeously support hazardous structures.

Keywords
thrust fault, dome structure, stable span, triplets, conventional mining, mechanized mining, UG2 Reef, vertical tensile zone.

Introduction

The UG2 Reef is widely mined in the South African Bushveld Complex (Figure 1). It is a tabular, gently dipping orebody as shown in Figure 2. The hangingwall of the UG2 Reef is characterized by stratification in the form of thin and weakly cohesive chromitite stringers (triplets) that can vary in number and height above a stope. Traditionally this reef has been extracted conventionally (Figure 3) using mine poles and packs as support. Increasingly it is extracted using mechanized (Figure 3) or partially mechanized mining methods, and these stopes or zones have to be supported on tendons.

The analyses described in this paper are based on work performed on a PlatMine project (Watson *et al.*, 2007). Most of the original PlatMine work was done in conventional stopes, and was included in this paper to highlight the impact of persistent shallow-dipping discontinuities on stability. Sensitivity analyses were done on mechanized stopes supported on tendons. The paper describes stable span determination in both conventional and mechanized stopes where a shallow-dipping thrust structure has been intersected. There are some interesting findings that are applicable to both mining methods, which are highlighted in the conclusions. Significantly more work has been added to the original PlatMine project in the paper.

For any given situation, the stability of a UG2 hangingwall depends upon the presence or absence of shallow-dipping thrust structures, height and spacing of the chromitite bands (triplets) above the reef (Figure 2), the stoping span, the rock mass rating, the support resistance, and depth of penetration (if tendons are used). The conditions for stability, incorporating all these variables and their interactions, have to be determined in order to develop a design methodology to determine stable spans for the mining of the UG2 Reef.

Three research approaches were employed to evaluate the comparative significance of the stability parameters, and to determine stable panel spans:

- Rock mass rating systems
- Hangingwall failure mechanisms
- Numerical modelling, including calibration and sensitivity analyses.

The first approach involved a suitable rock mass rating system to address the unique problems associated with the chromitite bands above the UG2 Reef. Secondly, modes of failure were determined from documented

* *Visiting Professor - School of Mining Engineering, University of the Witwatersrand, Johannesburg.*
† *Anglo American Platinum, Amandelbult Complex, Thabazimbi.*

© *The Southern African Institute of Mining and Metallurgy, 2018.* *ISSN 2225-6253. Paper received Oct. 2017; revised paper received Apr. 2018.*

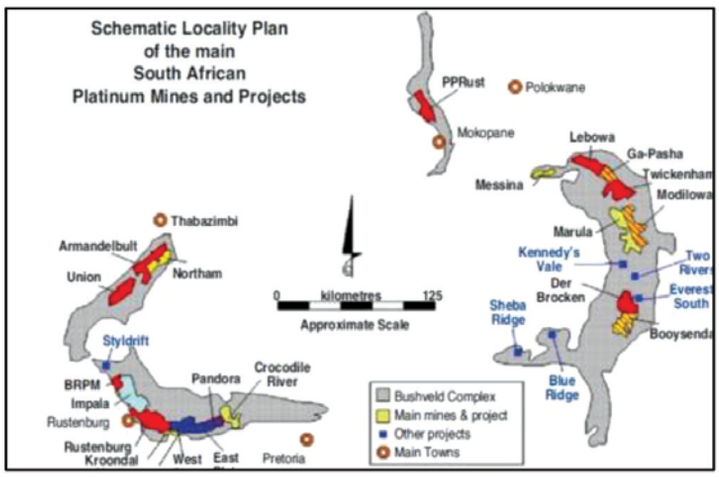

Figure 1—Map showing the western and eastern lobes of the Bushveld Complex and the locations of the platinum mines

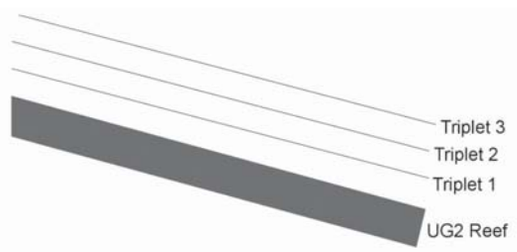

Figure 2—Typical UG2 Reef and the weakly cohesive chromitite stringers (triplets)

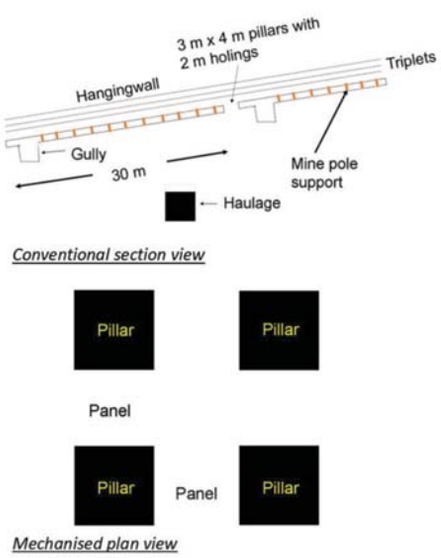

Figure 3—Typical conventional and mechanized mining layouts

collapses. Finally, numerical modelling was used to perform sensitivity analyses on various stability parameters and support configurations.

Literature review

Kirkaldie (1988) identified a total of 28 parameters that may influence the strength, deformability, permeability, or stability behaviour of rock masses. Of these parameters 10 are related to rock material properties, 10 to properties of discontinuities, and 8 are hydrogeological properties. Because it is often difficult or impossible in a general characterization to include the many variables in such a complex natural material, it is necessary to develop suitable systems or models in which the complicated reality of the rock mass can be simplified through the selection of a limited number of representative parameters.

Rock mass classification systems are empirical methods (based on case studies) that quantify the integrity of the rock mass and which can be used to estimate mechanical properties for excavation and support design. Rock mass classification systems consider combinations of some of the following components making up a rock mass:

- Intact rock strength
- Field stresses
- Joint persistence
- Joint spacing
- Joint surface condition
- Joint orientation
- Groundwater.

Some important considerations required for rock mass evaluations in shallow-dipping, tabular stopes are discussed below.

- Discontinuity orientation. Brummer *et al.* (1988) suggested that faults or persistent joints striking parallel to pillar lines (Figure 4) are considerably less stable than those perpendicular to the pillar lines.
- Joint alteration. Instability often occurs when the joint filling is thicker than 3 mm (Watson, 2003).
- Joint dip angle with respect to the orientation of the stope hangingwall. This is an important consideration for the evaluation of shallow-dipping, tabular stopes (Watson, 2003).
- Joint persistency. This factor would be in multiples of 10 m. It was suggested that a factor of 2 or greater would be considered persistent enough to cause a panel collapse if pillar lines were sub-parallel to such a joint set (Roberts, 2002).
- Stress condition. High horizontal stress can create fractures that curve into the hangingwall, providing release surfaces for large falls of ground (FOGs). Very

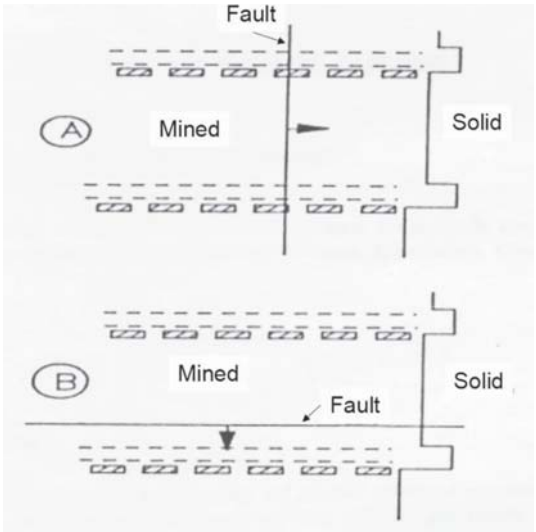

Figure 4—Favourable (A) and unfavourable (B) orientations of fault planes with respect to the yield pillar layouts (after Brummer, 1988)

low stress conditions can also be problematic, resulting in blocks sliding out of the hangingwall even in otherwise good rock mass conditions (Watson, 2003).
- Presence of water. Water lubricates and hence reduces the frictional resistance of joints to movement.

Fourteen rock mass rating systems were assessed by Watson (2003). Of these rock mass classification systems, four were considered relevant for the evaluation of stability in shallow-dipping, tabular panels. These findings agree with an assessment by Swart *et al.* (2000) for the Bushveld Complex chrome mines. The systems are:

- the Geomechanics Classification or Rock Mass Rating (RMR) system developed by Bieniawski (1989)
- the Norwegian Geotechnical Institute rock quality index (Q) system developed by Barton, Lien, and Lunde (1974)
- the Mining Rock Mass Classification or Modified Rock Mass Rating (MRMR) system developed by Laubscher (1990)
- the Modified Stability Graph method through the use of the Modified Stability Number (N'), originally developed by Mathews *et al.* (1981) and later modified by Potvin (1988) and others.

The N' system was found to correlate consistently to observed conditions underground (Watson, 2003) and is simple to use. This system was employed as a basis for development of the New Modified Stability Graph Method (N"), specifically for the platinum industry (Watson, 2003). The N" method was used in rock mass rating analysis and a database of evaluated stable, unstable, and collapsed sites was collected for the UG2 Reef by a number of rock engineers across the Bushveld Complex. Statistical analyses were performed on the collected data to determine the relevance of each parameter.

Statistical analyses of geotechnical data

A database of records, including the parameters that make up N", along with depth, physical dimensions, and support arrangements was collected for 159 panels – ample data for back-analysis by regression. All of the data was from conventional mining stopes with various configurations of mine pole and pack support (a full description of the database is provided in the PlatMine report (Watson *et al.*, 2007). The aim was to determine the comparative influence of the rating parameters, span, and support on stability. The physical dimensions of the panels were described by hydraulic radius (HR) as shown in Equation [1].

$$\mathrm{HR} = \frac{w \times h}{2w + 2h} \quad [1]$$

where w and h are the width and length of a panel.

The relative contributions of the parameters in the N" system to stability were determined by logistic regression analysis. It was established that the relationship between HR and the probability of panel collapse does indeed effectively correlate with panel failure (Figure 5): fitted into a logistic regression model with HR, it predicts collapse with an accuracy of around 77%, although with a large overlap.

The overlap could have arisen because the range of spans in the database was limited to what would normally be stable. Conversely, the analysis showed a relatively strong relationship between support resistance and probability of stability.

A statistical evaluation and reworking of the N" equation (Equation [2]) was done to provide a best fit between collapsed and stable panels. A significantly better fit was found (confidence level: about 93 %) when Equation [5] ($N'^{(3)}$) was compared to support resistance (SR) and a factor describing the joint filling. The analysis suggests that support resistance plays a more influential role than span for a given discontinuity condition, within the context of the spans in the database. Note that the dominant parameter in this equation is the B-value, which is a factor accounting for the dip orientation of the most influential discontinuity (Figure 6). The The C-value (Equation [1]) accounts for the influence of gravity on the hangingwall blocks (Figure 7).

$$N'' = Q \times B \times C \quad [2]$$

where

$$Q = \frac{RQD}{Jn} \times \frac{Jr}{Ja} \times \frac{Jw}{SRF} \quad [3]$$

RQD is calculated from the Palmström (1982) equation (Equation [4]).

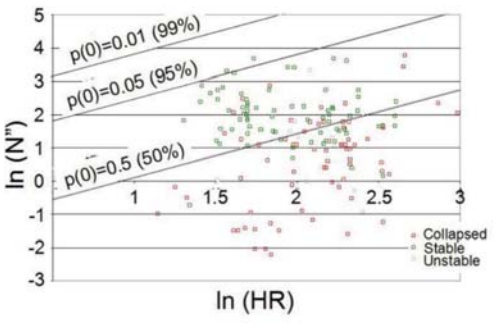

Figure 5—Design chart for N"

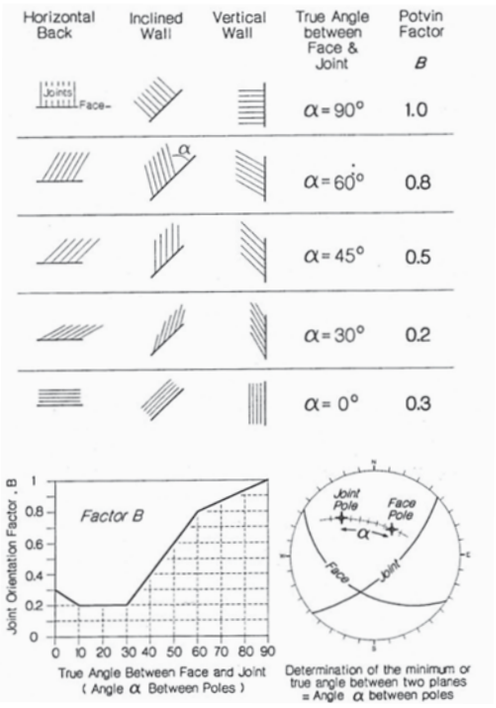

Figure 6—Factor for joint orientation 'B' (after Mathews *et al.*, 1981 and revised by Hutchinson and Diederichs, 1996)

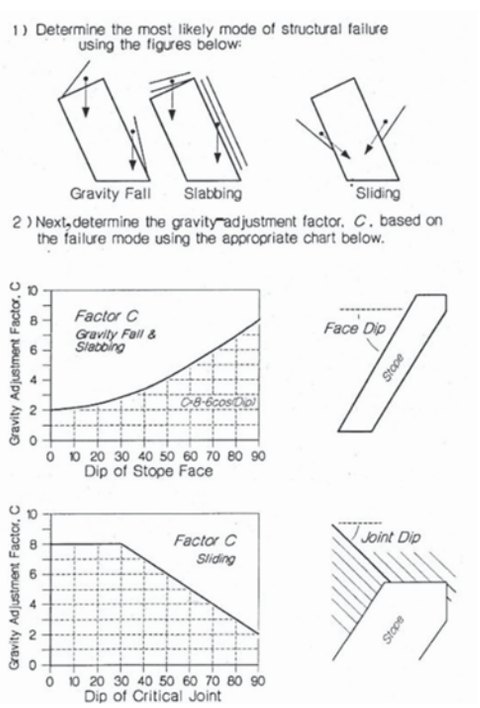

Figure 7—Gravity adjustment factor 'C' (after Mathews *et al.*, 1981 and revised by Hutchinson and Diederichs, 1996)

$$RQD = 115 - 3.3J_v \quad [4]$$

where J_v is the average number of joints in a cubic metre. J_a, J_r, J_n, J_w, and *SRF* are the parameters used in the Q rock mass rating system originally developed by Barton, Lien, and Lunde (1974) and modified slightly to suit local conditions (Watson, 2003).

$$N^{(3)} = 45.85 - 52.68.B - 0.75UCS + 0.81UCS.B - 0.48J_n \quad [5]$$

where *UCS* is the uniaxial compressive strength of the rock.

Note that although J_a was important in influencing the statistical evaluation, $N^{(3)}$ did not depend on this factor. The evaluation showed a synergistic effect of SR and J_a and because of it, these two factors could not be completely separated. Therefore, three variables were involved, and a single two-dimensional chart was insufficient. In Figure 8, the blue surface separates upper and lower regions of stability and instability, respectively (probability of collapse < 5%). Importantly, the analysis shown in the figure did not depend on HR. The derivation of Equation [5] is well described in the original PlatMine report (Watson *et al.*, 2007).

Evaluation and summary of the empirical RMR approach

The statistical evaluation of the geotechnical data suggested that the most significant stability parameter is persistent, shallow-dipping or curved discontinuities. Generally, these features are associated with thrust fault structures, which appear to be endemic across the platinum-bearing orebodies of the Bushveld Complex. These discontinuities dip in and out of the reefs, resulting in the development of dome structures in the hangingwall during mining (Figure 9).

The results of the empirical evaluation also indicate that, under the conditions of the panels in the database, changing the support resistance would yield better results than changing the panel span. However, this should be understood in the context of a maximum minor span of 30 m, the mine pole support used in the evaluated panels, and the depth below surface range of between 32 m and 970 m.

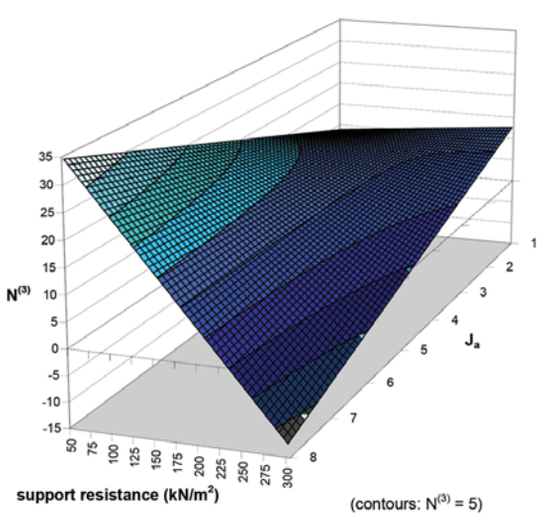

Figure 8—Surface showing a probability of a collapse at <5%

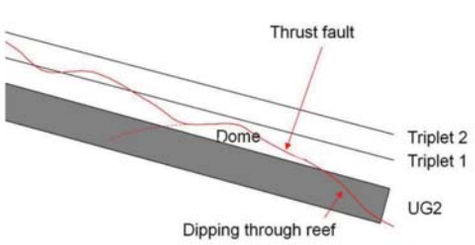

Figure 9—Diagram showing a section through an actual thrust structure

Analyses of panel collapse reports

Reports on 69 collapsed sites in the database were investigated to determine the most common causes of panel collapse.

The majority of collapse occurred on persistent, shallow-dipping or curved discontinuities (thrust faulting features). None of the collapses could be positively connected to high stress conditions or fracturing. In some cases, visible sagging of the hangingwall towards the centre of the panel suggested parting on the triplets some 3.5 m above the stope, indicating excessive panel spans for this middling between the stope and the triplets. The heights of collapses recorded without the assistance of shallow-dipping or curved joints were invariably controlled by the Leader seam or triplets. Parting in the hangingwall can theoretically occur only within the vertical tensile zone (VTZ). The FOGs with a fallout thickness greater than the VTZ height all occurred on shallow-dipping or curved structures, showing that the height of the VTZ does not restrict the fallout height if these structures are present. Since most of the FOGs studied in the PlatMine project involved shallow-dipping or curved discontinuities as the primary release surface, it was considered necessary to include the effects of such discontinuities on stability in the numerical models.

Numerical modelling to determine the effects of a shallow-dipping discontinuity

Case study on a conventional stope

A highly appropriate 2D case study was made available at 'mine A'. Stopes were mined from one side of a raise line, from 2 m to a planned 30 m width on strike and about 120 m on dip (Figure 10). A shallow-dipping thrust fault dipped in and out of the reef, causing several panel collapses that were used to calibrate the model. The joint sets at the site were similar to the common joints observed generally across the platinum mines.

2D UDEC models (Shi and Goodman, 1987) were set up with the Barton-Bandis joint addition. The models incorporated the two commonly observed joint sets, the triplets, and a thrust fault structure at 20° to the strata. The analyses were performed using laboratory-derived input parameters and actual measurements made at the mine (Tables I–III). A k-ratio of 0.16 was assumed due to the proximity of the workings to the side of a mountain.

A suite of models was run without the thrust structure and without support. The models were set up using the input parameters provided in Tables I–III so that an initial span of 3 m could be increased in steps of 2 m. The models were terminated when the unsupported span reached 40 m. No failure occurred (stable conditions), although parting took place on the triplets and the plane at 4.1 m above the stope, as shown in Figure 11. The maximum vertical deformation was 15 mm at a minor span of 40 m.

The model above was modified to include thrust faults and a suite of tests was run without support as shown in Figure 12. Blocks that formed between the shallow-dipping

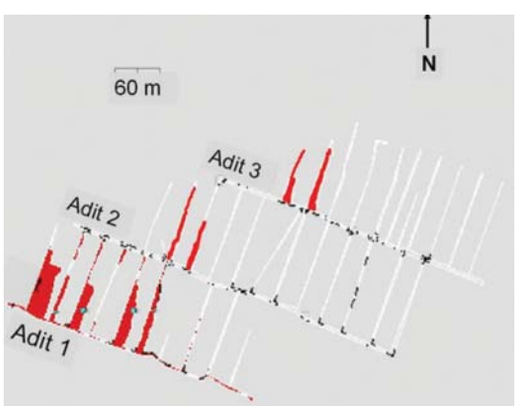

Figure 10—Plan view of the workings at the time of the 'mine A' investigations

Table I

Rock properties used in the UDEC model for a horizontal stress of 3 MPa

Property	Value
Shear modulus (G)	40 GPa
Bulk modulus (K)	42 GPa
Friction angle	48°
Cohesion	14.6 MPa
Tensile strength	8.9 MPa

Table II

Discontinuity properties used in the UDEC model for a horizontal stress of 3 MPa

Discontinuity	Friction angle	Cohesion (MPa)	Tensile strength (MPa)
Joint set I	36°	0.13	0
Joint set II	37°	0.27	0
Triplets	30°	0	7.1
Thrust structure	30°	0	0

Table III

Orientations and depths of geological discontinuities in the model

Discontinuity	Height above stope (m)	Dip angle (degrees)
Triplet I	1.3	0
Triplet II	2.0	0
Triplet III	2.7	0
Thrust fault	4.1 and 6.1	0
Thrust fault		20
Joint set I		80
Joint set II		-85

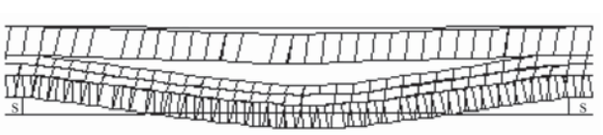

Figure 11—Results of a UDEC model without support and without the thrust structure, a span of 40 m. Vertical deformation exaggerated 35×

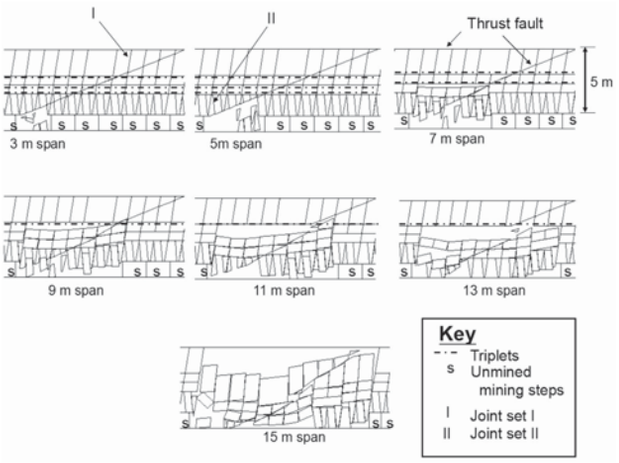

Figure 12—Results of a UDEC model without support

thrust fault and the two joint sets fell out as the span was increased, showing that there is no stable, self-supporting span. At a span of 5 m the rock mass collapsed up to triplet I (1.3 m above the stope). An increase of the span by 2 m resulted in a migration of the unstable zone up to triplet II at 2.0 m above the stope. The conditions at spans of both 5 m and 7 m were observed underground at mine A in unsupported or under-supported panels. At a span of 9 m, the entire rock mass below triplet III (at a height of 2.7 m) became unstable. At a span of 15 m, a collapse occurred up to the horizontal thrust fault at 4.1 m above the stope.

A support system of 170 mm diameter mine poles spaced 2 m × 2 m on dip and strike was originally used at the mine. A downrated support resistance of 50 kN/m² was assumed from underground measurements. A curve for the elongate support system is provided in Figure 13. The results of the models are shown in Figure 14. Stable conditions were predicted up to a span of 9 m. At a span of 11 m the model showed that parting had occurred on all three triplets as well as at 4.1 m above the stope. A collapse occurred up to triplet III at a span of 13 m, which is a modest improvement of 4 m over the unsupported scenario.

A new support system was introduced to the mine, which included larger diameter mine poles and packs. This condition was modelled assuming a downrated support resistance of 135 kN/m². In the model, only the mine poles were prestressed (to 150 kN) and the profile of support resistance to closure was determined from underground measurements (Figure 15). A great improvement, both in stable panel span and rock mass conditions, was achieved by this support system (Figure 16). Unstable conditions occurred at a span of 19 m and a final collapse at 22 m. Note that parting initiated at 4.1 m above the hangingwall, when the span reached 17 m. The modelled unstable conditions were observed underground.

A support system which was prestressed to 100 kN/m² at installation and provided a peak resistance of 200 kN/m² (Figure 17) was introduced to the mine. This support system was technically able to support a rock height of 5 m, with only about 5 mm deformation. To ensure worst-case conditions in the model, a second horizontal discontinuity,

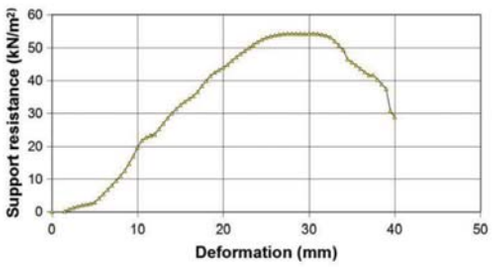

Figure 13—Support resistance with a 99% confidence, assuming large blocks (supported by at least three poles)

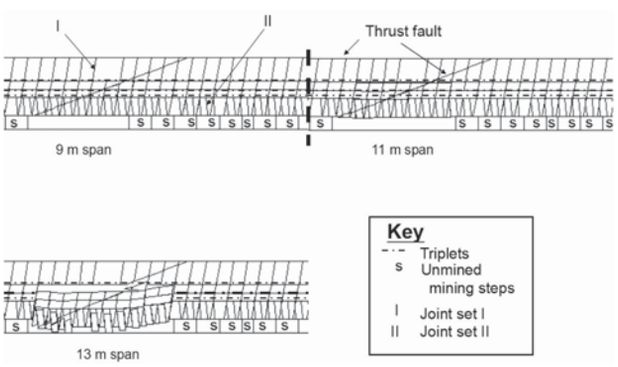

Figure 14—Results of a UDEC model with a support resistance of 50 kN/m²

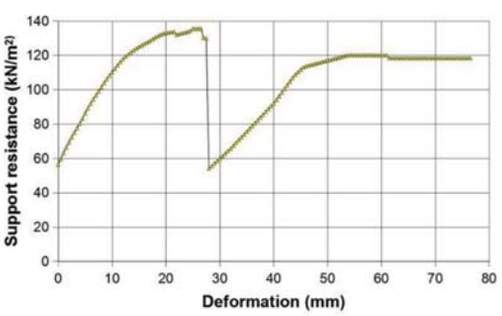

Figure 15—Support resistance profile for the second support system

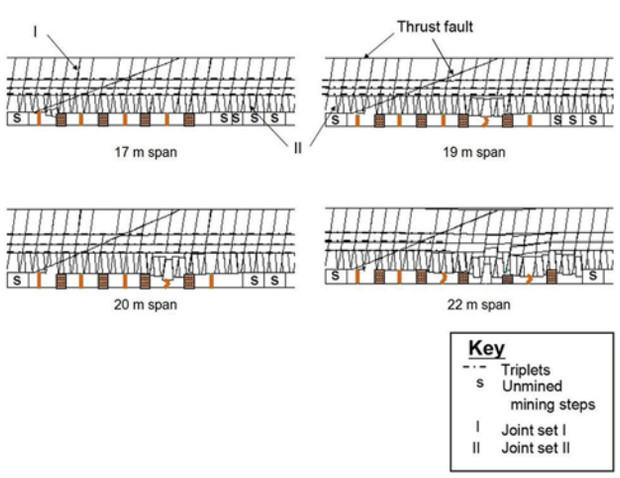

Figure 16—Results of the UDEC model for a pack-elongate support system with a support resistance of 139 kN/m²

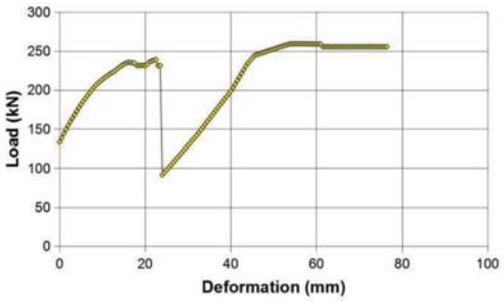

Figure 17—Final support resistance profile (100 kN/m² at installation)

with properties similar to the thrust fault, was set up at 6.1 m above the stope. This was slightly higher than the support capacity. The results are shown in Figure 18. Spans were increased in the model to a maximum of 36 m and stable conditions were predicted in all runs. However, it should be noted that FOGs occurred in the face area when the maximum support-to-face distance was 3.6 m. These FOGs did not occur in the model when the support-to-face distance was reduced to 2.8 m, and this was also confirmed by underground observations. The peak support resistance used at this mine was very high, and it may be unrealistic to apply as a best practice for preventing large-scale instabilities. Mitigation strategies based on knowledge of the height and behaviour of potentially hazardous structures are preferred.

Sensitivity analyses on mechanized scenarios

The calibrated model used in the case study was modified to provide a better representation of the general UG2 Reef conditions and to cater for mechanized stopes where only roofbolts are used:

- The second set of joints that only extended up to the first triplet at mine A was extended up to 6.1 m above the model to provide a worst-case scenario
- k-ratios of 0.5 and 2 were applied
- Models were run at depths of 200 m, 400 m, and 1000 m below surface.

All models included thrust structures that were inclined at 0° and 20° or 30° to the strata. The horizontal structures were located at 4.1 m and 6.1 m above the stope. Note that the models do not cater for intersections, where most collapses occur. This issue will be discussed later in the paper. Tunnel widths were increased in 2 m span intervals to determine the maximum stable span with the imposed conditions. A vertical exaggeration of ten was used to highlight vertical deformation in all the diagrams from Figures 19 to 28.

Sensitivity analyses were performed on:

- The height of the parting planes
- Length and spacing of bolts
- Prestressing of bolts
- Depth of workings below surface
- k-ratio.

The first model (Figure 19) shows the unsupported base case. All the parameters shown in Table I to Table III were applicable to this model. The tunnel was progressively mined wider to determine the spans at which panel collapses are likely to occur.

The models depicted in Figure 19 show that FOGs occur at every tunnel width, as expected, because of the shallow-dipping thrust structure. At a span of 6 m a collapse occurred up to triplet I, a height of 1.3 m. The collapse height migrated up to 2.0 m (triplet II) at a span of 8 m, and up to 2.7 m (triplet III) at a span of 10 m. Collapse heights of 4 m and 6 m occurred at spans of 14 m and 20 m respectively.

A set of models was run with 18 mm diameter, 1.8 m long full-column resin roofbolts, spaced 1.5 m × 1.5 m. The reinforcement properties shown in Table Table IV were applied in the models, which provided a support resistance of 48 kN/m² over the length of the bolts. The results of the investigation are shown in Figure 20.

Stable conditions with minor FOGs were observed until a span of 8 m. Note that the reach of the bolts extended to just beyond triplet I. The panel collapse occurred up to triplet II at

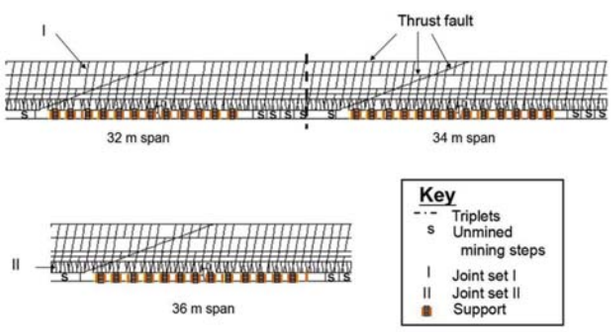

Figure 18—Results of the UDEC model for a support resistance of 200 kN/m². The support-to-face distance was kept to a maximum of 2.8 m

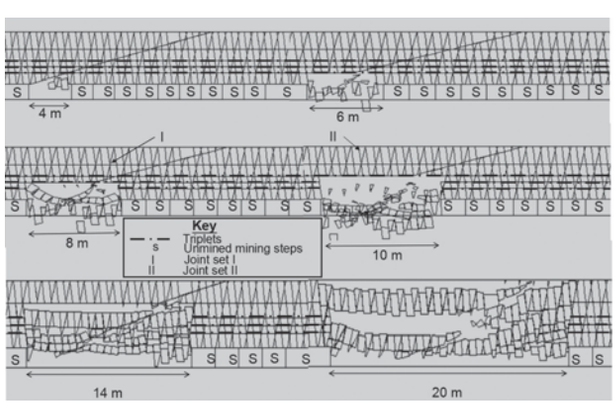

Figure 19—Unsupported model, vertical deformation exaggerated 10×

Table IV

Reinforcement properties of the rockbolts and resin

Parameter	Value
Bolt Young's modulus	210 GPa
Bolt yield force	110 kN
Bolt failure strain	0.19
Resin shear stiffness	300 MN
Resin shear strength	460 kN

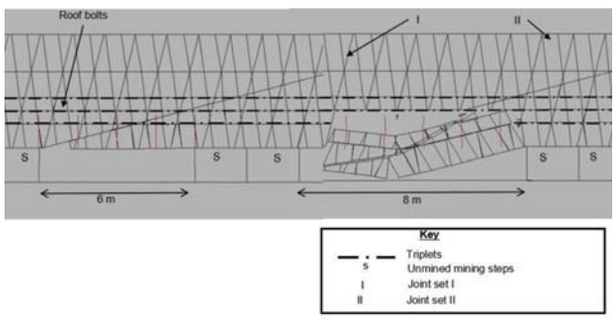

Figure 20—Results of the UDEC model with 18 mm diameter, 1.8 m long, full-column resin roofbolts; vertical deformation exaggerated 10×

exactly the same span as in the unsupported models. Importantly, the supported models were able to control most of the FOGs. Suitable surface support is needed to control the small falls between the bolts.

A set of models was run to test the effects of increasing the bolt length to 2.4 m. The results showed unstable conditions at a span of 8 m and a collapse at 10 m (Figure 21). The unstable conditions at 8 m were probably the result of parting on triplet II and bolt yield. A collapse occurred up to triplet III at a span of 10 m; again as observed in the unsupported model.

Some models were run to determine the behaviour of supported rock where the triplets are much closer to the excavation. The triplets were shifted down by 1.4 m, but the distances between the triplets remained unchanged. The thrust faulting and jointing were kept the same as in the previous models. A list of orientations and depths of the geological discontinuities in the new models is shown in Table V. The model results (Figure 22) show more stable conditions at a span of 8 m than the case where the bolts did not penetrate through the third triplet (Figure 21). However, a panel collapse still occurred up to the third triplet at a span of 10 m. The collapse occurred because the thrust fault extended above the reach of several rows of roofbolts.

A similar set of models was run with the thrust fault angle adjusted up to 30° to the strata. The results were the same as for the 20° fault, and again a collapse occurred at a span of 10 m.

The model shown in Figure 22 (thrust fault at 20°) was re-run once more with a pre-tension of 38 kN on each bolt at installation. A collapse occurred at a smaller span (Figure 23). The reason for the earlier failure is not clear. Previous modelling work by consultants showed that a small pre-tension on tendon support elements definitely improves deflection and thus stability. However, the thrust structure was not included in those models.

An investigation was conducted to determine the effect of changing the support resistance on stability. The spacing of roofbolts used in Figure 21 was reduced to 1.5 m × 0.8 m. The support resistance was thus increased from 48 kN/m^2 to 92 kN/m^2, but the length and diameter of the bolts were kept the same. The results showed an improvement in span with support resistance, with the critical span increasing from 10 m to 12 m (Figure 24). A similar set of models (with the higher support resistance) was run with the triplets at 1.3 m

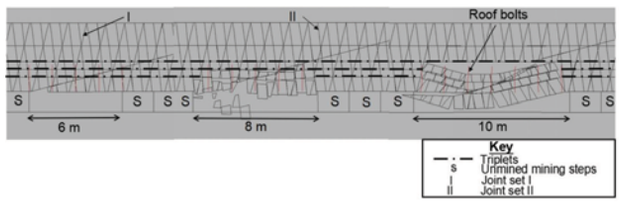

Figure 21—Results of the UDEC model with 18 mm diameter, 2.4 m long, full-column resin roofbolts; vertical deformation exaggerated 10×

Table V

Orientations and depths of geological discontinuities in the following models

Discontinuity	Height above stope (m)	Dip angle (degrees)
Triplet I	0.2	0
Triplet II	0.9	0
Triplet III	1.6	0
Thrust fault	4.1 and 6.1	0
Thrust fault		20
Joint set I		80
Joint set II		-85

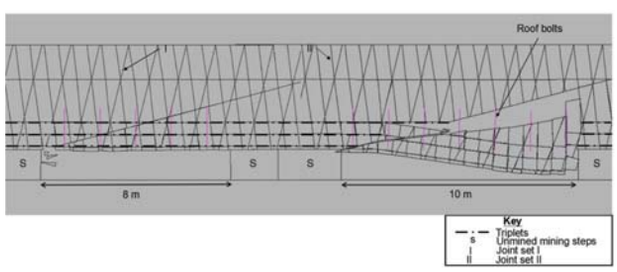

Figure 22—Results of the UDEC model with 18 mm diameter, 2.4 m long, full-column resin roofbolts (triplet at 0.2 m); vertical deformation exaggerated 10×

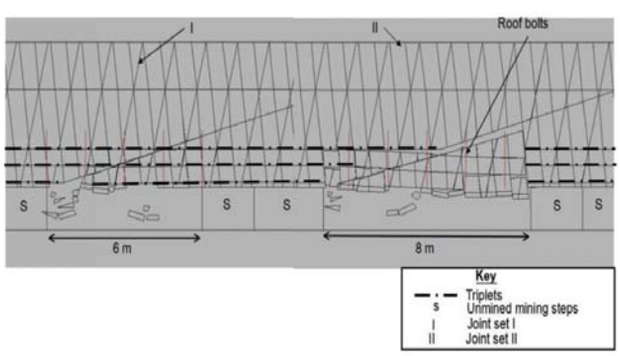

Figure 23—Results of the UDEC model with pre-tensioned 18 mm diameter, 2.4 m long, full-column resin roofbolts (triplet at 0.2 m); bolts pre-tensioned to 38 kN, vertical deformation exaggerated 10

(same as in Figure 21). In this instance the bolts did not penetrate through the upper triplet, but the critical span remained at 12 m (Figure 25). However, significantly more vertical displacement was calculated at a span of 10 m in this model than when the triplets were closer to the reef, due to

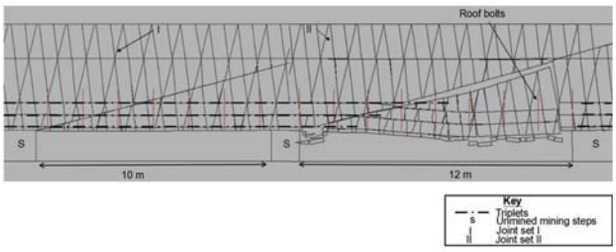

Figure 24—Results of the UDEC model with 18 mm diameter, 2.4 m long, full-column resin roofbolts at a spacing of 1.5 m × 0.8 m (triplet at 0.2 m); vertical deformation exaggerated 10×

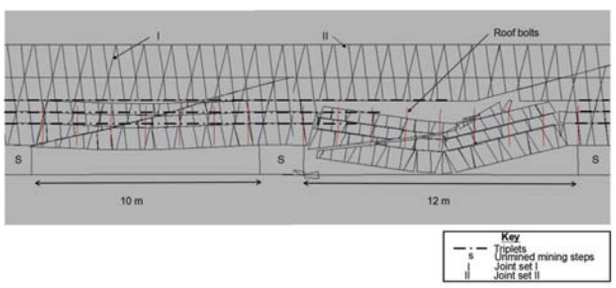

Figure 25—Results of the UDEC model with 18 mm diameter, 2.4 m long, full-column resin roofbolts at a spacing of 1.5 m × 0.8 m (triplet at 1.3 m); vertical deformation exaggerated 10×

parting on the upper triplet. Parting took place on this upper triplet at the same span as a collapse in the unsupported scenario (10 m), but the support was able to prevent a collapse and increased the critical span by 2 m.

A set of models was run to determine the effect of k-ratio on stability. The height and orientations of discontinuities were as shown in Table V, and all parameters as for the model depicted in Figure 22, except the k-ratio, which was reduced to 0.5. The results show that k-ratio does affect stability conditions, and the decrease in k-ratio resulted in a decrease in stable-span width (Figure 26) for the given support and geotechnical conditions. A collapse occurred at 8 m (2 m less than in Figure 22). A similar set of models was run at depths of 200 m and 1000 m, keeping the k-ratio at 0.5. The stable span was the same at 200 m, but there was an improvement at 1000 m (Figure 27).

For completeness, a model was run with the triplets shifted up. Triplet I was adjusted to 1.9 m above the hangingwall, *i.e.* just above the reach of the 1.8 m long roofbolts (Figure 28). The results were the same as when triplet I was at 1.3 m (Figure 20).

Evaluation of the numerical modelling results

The models were calibrated on conventional stopes where elongate and pack support was used. Shallow-dipping thrust faults were included in all the analyses as these structures occurred at the calibration site and have been observed across the Bushveld Complex platinum reefs. At the calibration site, stable conditions were predicted up to minor spans of 40 m, if an active support system, of 100 kN (at installation) and a maximum capacity of 200 kN was installed early. This support resistance was sufficient to

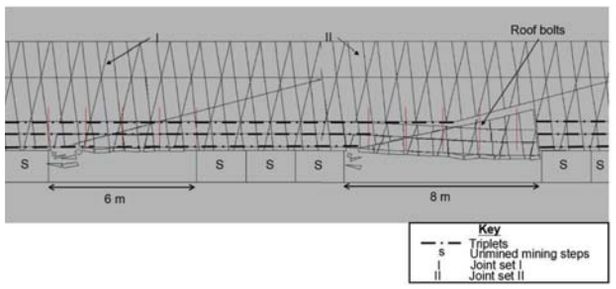

Figure 26—Results of the UDEC model with 22 mm diameter, 2.4 m long, full-column resin roofbolts (triplet at 0.2 m and k = 0.5) at 400 m depth below surface ; vertical deformation exaggerated 10×

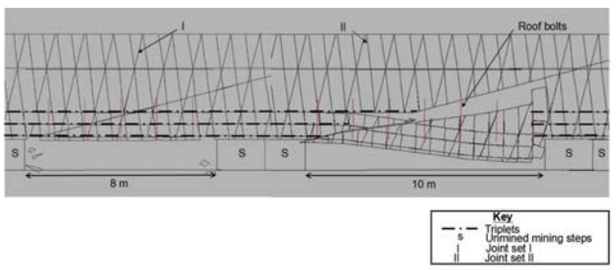

Figure 27—Results of the UDEC model with 22 mm diameter, 2.4 m long, full-column resin roofbolts (triplet at 0.2 m and k = 0.5), at 1000 m depth below surface; vertical deformation exaggerated 10×

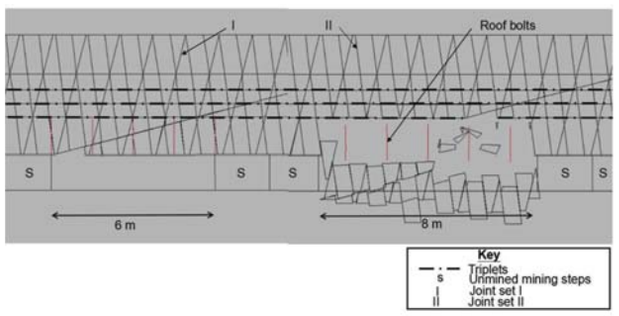

Figure 28—Results of the UDEC model with 18 mm diameter, 1.8 m long, full-column resin roofbolts, lowest triplet beyond the reach of the roofbolts; vertical deformation exaggerated 10×

maintain stability over the said minor span, even when parting planes existed above the reach of the support.

The conventional mining model was modified to cater for more general UG2 mining conditions. The aim of this exercise was to determine safe mining spans in a mechanized environment where roofbolts are used. Shallow-dipping thrust structures were again included in the sensitivity analyses. The results of the investigation show that provided 1.8 m long full-column resin roofbolts are installed early on a support resistance of 48 kN/m^2 (bolt spacing of 1.5 m × 1.5 m), a span of 6 m can be safely mined, irrespective of the height of the triplets or magnitude of the k-ratio. However, it should be noted that this finding is restricted to the conditions and parameters used in the models and described here. There may be conditions that were not modelled, and those cases should be treated differently.

The models show that surface support is required between bolts where shallow-dipping thrust structures cut through the hangingwall or if triplet 1 is close to the hangingwall. It is interesting to note that the less intense vertical jointing above triplet I in the conventional models resulted in similar collapse spans as in the mechanized models when comparing the unsupported results (Figures 12 and 19). The finding agrees with the statistical evaluation of the rock mass ratings, which shows that shallow-dipping, persistent discontinuities are the predominant factor in stable span determination and overshadow the other geotechnical parameters when they are present. An increase in bolt length to penetrate the second triplet at 2.0 m improved conditions, with a collapse at 10 m, although unstable conditions were predicted at 8 m. When the heights of the triplets were dropped to ensure that the bolts were able to penetrate all the triplets, stable conditions were shown at 8 m and a collapse occurred at 10 m. An improvement in critical span was also observed when the support resistance was increased, even though the elements remained the same length and did not penetrate all the triplets. A sensitivity analysis was done on support resistance by progressively reducing the spacing of support elements. In this analysis the support length was 1.8 m and the height of triplet l was 1.3 m. In these models the bolts penetrated only through triplet I, as shown in Figure 20. The results indicate an almost linear relationship between span and support resistance for the given geotechnical conditions and support type (Figure 29).

The angle of the shallow-dipping thrust fault was changed to 30° to the strata to determine if a slightly steeper angle would increase the height of instability at a particular span, and thus reduce the stable span for a given set of conditions. However, no discernible difference was observed. Hutchinson and Diederichs (1996) also show equal severity across the range of dip angles between 10° and 30° to the strata, and suggest that the worst discontinuity angles are within that range (Figure 5).

Pre-tensioning of the bolts resulted in premature unstable ground conditions at 8 m. The reason for the earlier collapse is not clear. Note that much larger lumps fell out during the collapses, which is also observed underground in areas supported with roofbolts.

Interestingly, the models using roofbolt support showed two failure mechanisms: beam failure and wedge failure.

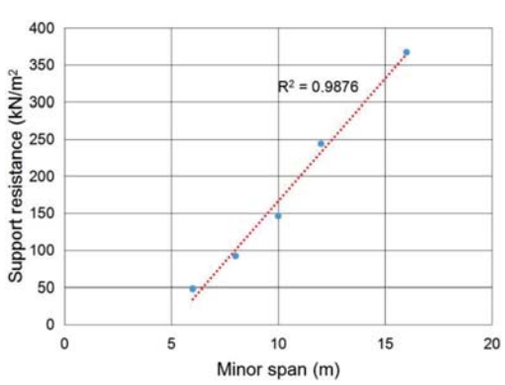

Figure 29—Relationship between span and support resistance for 1.8 m long roofbolts and triplets above 1.3 m

If a collapse occurred on a plane above the reach of the bolts, beam failure took place. Where this plane was below the bolt penetration (and the support resistance was sufficient to carry the weight of the rock below the plane), wedge failure was noted. This wedge failure occurred when a shallow-dipping thrust structure cut through the parting planes. Failure initiated in the zone where the structure was above the reach of the bolts and subsequently caused the bolts that penetrated the plane in tension to fail, one row at a time under a cantilever action.

Under ideal conditions, the maximum achievable stable span with a bolt spacing of 1.5 m × 1.5 m (48 kN/m²) was shown to be about 8 m. Larger stable spans are often observed underground, even with the same tendon support as used in the models. It should be emphasized, though, that the shallow-dipping thrust fault is not always in the vulnerable position modelled. The models are showing a worst-case scenario. Should it be possible to determine where these structures exist with a high degree of confidence, it would be possible to mine safely at larger spans, accounting for these structures where they exist. At mine B the thrust structures were easily identifiable. Spans of 10 m were mined successfully in areas where the thrust structure did not intersect the stope hangingwall. This scenario agrees with the results shown by the model without a thrust structure (Figure 11). However, the areas affected by the thrust structure had to be properly supported on a separate support system using 4.5 m and 6.0 m long anchors on a close spacing. The actual length and support resistance were calculated at the height of the structure above the hangingwall. Since the introduction of this system, instances of large FOGs have reduced almost to zero, except for instances of human error.

It should be noted that the model assumed an infinitely long panel (into the page). However, in reality there are intersections, or holings, between orthogonal panels. These intersections represent areas of larger span and should also be treated differently, or the spans of the panels should be reduced to ensure that the diagonal across the intersection does not exceed the critical span. For an 8 m critical span, a safe panel span for two equal sized panels intersecting would be 5.6 m (Figure 30).

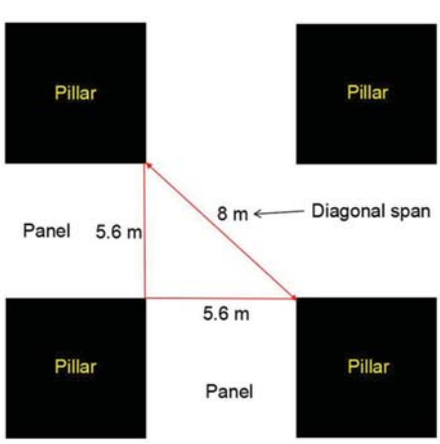

Figure 30—Excavation spans to accommodate a critical diagonal span across an intersection

Leading practices to combat FOGs

Several leading practices have been developed over the past 10 years to enable the early detection of potentially hazardous structures, as well as to determine appropriate local support in the hangingwall of stopes. Some of these practices are summarized below.

- Triggered Action Response Plan (TARP) systems were developed as a hazard identification tool to assist production personnel in the identification of potentially hazardous ground conditions. A TARP consists of a set of documented and known workplace hazards that need to be continuously identified (MOSH, 2017).
- Ground-penetrating radar (GPR) is a risk management tool that can facilitate the identification of potential parting planes and/or critical block-, slab- or wedge-forming discontinuities (Godden, 2011). Potentially unstable ground can often be identified for a distance of approximately 5.0 m above a cut stope hangingwall. Other instrumentation such as borehole cameras in regularly spaced boreholes is also increasingly being used in mechanized stopes to develop isopach plans of potential parting planes.
- Identification of deformation event precursors (Hartzenberg *et al.*, 2017). Effective identification of the precursors can assist in the planning and design processes to ensure appropriate design and layout strategies.
- Support design from a mechanistic understanding of the rock behaviour (Hartzenberg, du Plessis, and Friese, 2016).
- An understanding of instabilities from an understanding of the structural geology (du Plessis, Hartzenberg, and More O'Ferrall, 2017).

Summary and conclusions

The analysis of the FOG reports studied for the PlatMine project showed that FOG height is not restricted by the VTZ if a shallow-dipping fault structure cuts through the strata. Most FOGs have been shown to be connected with shallow-dipping or curved structures. Generally, these structures are associated with thrust faulting, which appears to be endemic across the Bushveld Complex. Dome structures are formed where this structure dips in and out of the reef hangingwall.

The results of the statistical evaluation of the rock mass ratings indicate that, under the conditions of the conventionally mined panels in the database, changing the support resistance would yield better results than changing the panel span. However, this should be understood in the context of a maximum minor span of 30 m, the type of support used in the evaluated panels, and the depth below surface ranging between 32 m and 970 m. The effect of increasing support resistance on stable span was also shown by the stope modelling. In a conventional mining scenario, stable conditions were predicted up to a minor span of at least 36 m if a prestressed mine pole and pack support system was installed at an average prestress load of 100 kN/m^2 and a peak resistance of 200 kN/m^2, regardless of the height of parting planes. This model was tested on the same mine and the collapses that had been regularly occurring ceased.

Both the FOG reports and the RMR database showed the importance of considering the effects of shallow-dipping thrust faulting on stability. A 2D UDEC model was calibrated on a conventional mining case study at mine A and subsequently modified to cater for generalized bolted, mechanized sections. Sensitivity analyses assumed the worst-case scenario, with a thrust structure present, and were done on:

- The height of the parting planes
- Length and support resistance of bolts
- Prestressing of bolts
- Depth below surface
- k-ratio.

The results of the investigation showed that 6 m is a safe panel span when 1.8 m long, full-column resin bolts are used at a support resistance of 48 kN/m^2. This span was found to be safe regardless of the k-ratio or height of the triplets. However, it should be noted that there could be conditions not considered in the models. Any conditions dissimilar to those described in the report should, therefore, be treated differently. Surface support is required between bolts where shallow-dipping discontinuities cut through the hangingwall or the lowest triplet is near the stope surface. Under ideal conditions, *i.e.* bolt penetration of all three triplets, a maximum span of 8 m seems feasible at the same support resistance. However, an increase in support resistance can improve stability and increase the stable span, even if the triplets are not penetrated by the bolts. It should be noted, though, that the 2D model does not account for intersections, which should be treated separately. Alternatively, the critical span at an intersection should be calculated by using the diagonal across the intersection.

In areas where there are no thrust structures, much larger spans can be mined with less support, but the structures need to be supported separately where they occur. Several leading practices have been developed in recent years to identify hazardous structures and determine appropriate support for localized hazards.

Acknowledgements

The CSIR and PlatMine are acknowledged for facilitating the success of the original research work described in this paper.

Dr J.A. Ryder and Dr D.P. de Carcenac are thanked for the guidance provided in the statistical evaluations of the Rock Mass Rating system. Mine management and rock engineering personnel on the mines are acknowledged for the assistance provided during data collection.

References

Barton, N., Lien, R., and Lunde, J. 1974. Engineering classification of rock masses for the design of tunnel support. *Rock mechanics*, vol. 6, no. 4. pp 189–236.

Bieniawski, Z.T. 1989. Engineering Rock Mass Classifications. Wiley, New York.

Brummer, R.K., Gay, N.C., Jager, A.J., McKinnon, S.D., Piper, P.S., Roberts, M.K.C., Ryder, J.A., Spottiswoode, S.M., and Wojno, L.J. 1988. An industry guide to methods of ameliorating the hazards of rockfalls and rockbursts. Chamber of Mines of South Africa, Johannesburg.

Du Plessis M., Hartzenberg, A.G., and More O'Ferrall G. 2017. Rock mass instability associated with the formation of regional geological structures along the Bushveld Complex as encountered during the extraction of the UG2 chromitite layer at Lonmin PLC. *Proceedings of the 13th ISRM International Congress of Rock Mechanics*, Montreal, Canada, 10-13 May.

https://www.onepetro.org/conference-paper/ISRM-13CONGRESS-2015-185

GODDEN, S. 2011. The use of remote sensing techniques on the AQPSA mines. S. Godden & Associates Ltd.

HARTZENBERG, A.G., DU PLESSIS M., and FRIESE, A.E.W. 2016. Structurally-related hangingwall alterations contributing to UG2 stope instabilities at Lonmin. *Proceedings of EUROCK2016, the 2016 International Symposium of the International Society for Rock Mechanics (ISRM 2016)*, Ürgüp, Cappadocia Region, Turkey, 29-31 August 2016. CRC Press.

HARTZENBERG, A.G., DU PLESSIS M., and FRIESE, A.EW. 2017. Unravelling the structural mysteries of the 'Bermuda Triangle' at Lonmin's Saffy Shaft. *Proceedings of Rock Mechanics for Africa (AfriRock 2017)*, Cape Town, 3–5 October. Southern African Institute of Mining and Metallurgy, Johannesburg.

HUTCHINSON, D.J. and DIEDERICHS, M.S. 1996. Cablebolting in Underground Mines. BiTech, Vancouver. 406 pp.

KIRKALDIE, L. 1988. Rock classification systems for engineering purposes. *STP 984*. ASTM International, West Conshohocken, PA. 167 pp.

LAUBSCHER, D.H. 1990. A geomechanics classification system for the rating of rock mass in mine design. *Transactions of the Institution of Mining and Metallurgy*, vol. 90. pp. 257–273.

MATHEWS, K.E., HOEK, E., WYLLIE, D.C., and STEWART, S.B.V. 1981. Prediction of stable excavations for mining at depths below 1000 m in hard rock. *CANMET Report*. DSS Serial no. OSQ80-00081, DSS File no. 17SQ.23440-0-9020. Deptartment of Energy, Mines and Resources, Ottawa.

MOSH (Mining Industry Occupational Safety and Health). 2017 Chamber of Mines, Johannesburg. http://www.mosh.co.za

POTVIN, Y. 1988. Empirical open stope design in Canada. PhD thesis, Department. of Mining and Mineral Processing, University of British Columbia. 343 pp.

ROBERTS, M.K.C. 2002. Addressing the problem of joints sub parallel to pillar lines. Contract report number 2002-0339. Johannesburg.

SWART, A.H., STACEY, T.R., WESSELOO, J., JOUGHIN, W.C., LE ROUX, K., WALKER, D., and BUTCHER, R. 2000. Investigation of factors governing the stability/instability of stope panels in order to define a suitable design methodology for near surface and shallow mining operations. *SIMRAC Project Report* OTH 501. Safety in Mine Research Advisory Committee (SIMRAC), Johannesburg.

SHI, G. and GOODMAN, R.E. 1987. Block theory and its application to rock engineering. Prentice Hall, Englewood Cliffs, NJ.

WATSON, B.P. 2003. The feasibility of using rock mass ratings for the design of panel spans and support in the shallow to intermediate depth Bushveld platinum mines. MSc thesis, Department of Mining Engineering, University of the Witwatersrand, Johannesburg.

WATSON, B.P., DE CARCENAC, D.P., ROBERTS, D.P., and ROBERTS, M.K.C. 2007. The determination of stable spans in stratified UG2 excavations. *PlatMine project report* 3.9. Miningtek Division of CSIR, Johannesburg. ◆

The SAIMM Journal all you need to know!

- ☆ Less 15% discount to agents only
- ☆ PRE-PAYMENT is required
- ☆ The Journal is printed monthly
- ☆ Surface mail postage included
- ☆ ISSN 2225-6253

The SAIMM Journal gives you the edge!

- ✻ with cutting-edge research
- ✻ new knowledge on old subjects
- ✻ in-depth analysis

SUBSCRIBE TO 12 ISSUES
January to December 2018
of the SAIMM Journal

R2157.10 LOCAL
OR
US$551.20 OVERSEAS

per annum per subscription

SAIMM
THE SOUTHERN AFRICAN INSTITUTE OF MINING AND METALLURGY

For more information please contact: Tshepiso Letsogo
The Journal Subscription Department
Tel: 27-11-834-1273/7 • e-mail: saimmreception@saimm.co.za or journal@saimm.co.za
Website: http://www.saimm.co.za

A serious, 'must read' that equips you for your industry—Subscribe today!

http://dx.doi.org/10.17159/2411-9717/2018/v118n5a7

Effect of mould geometry, coating, and plate thickness on the thermal profile of continuous casting moulds

by A. Gupta, R.K. Singh, A. Paul, and S. Kumar

Synopsis

A three-dimensional model for heat transfer analysis of continuous casting mould plate has been developed to predict the hot face temperature. Actual geometry has been considered by incorporating the bolt holes used for fixing bolts to tighten the plate with the backup water box, and the effect of these bolt holes on the hot face temperature of the mould plate is analysed. The high thermal conductivity of copper makes it suitable for use as mould plate material where high heat transfer rates are required. However, copper has poor resistance to abrasion and this disadvantage becomes apparent in the lower part of the mould, where severe wear of the copper surface takes place. To eliminate this problem, high-hardness materials like nickel are coated over the copper surface. This does not affect the heat transfer significantly. The purpose of this study is to investigate the effect of the bolt holes, as well as the nickel coating, on the hot face temperature.

Keywords
continuous casting, heat transfer, mould coating.

Introduction

Remarkable advances have been made in the continuous casting of steel, as demonstrated by the increasing use of continuous casting around the globe (Figure 1). Various developments have improved the efficiency of operation and product quality (Janik *et al.*, 2004; Janik and Dyja, 2004; Liu and Zhu, 2006; Thomas *et al.*, 1997; Thomas, 2001; Park *et al.*, 2000, 2002; Samarasekera and Brimacombe, 1979, 1982; Chow *et al.*, 2002; Meng and Thomas, 2003; Santillana *et al.*, 2008).

The mould, which is regarded as the heart of the continuous casting machine, plays a prominent role in the efficiency of the process and strand quality. Owing to the importance of the mould, various significant studies (Janik *et al.*, 2004; Janik and Dyla, 2004; Liu and Zhu, 2006) and model development have been carried out on the thermo-mechanical characteristics of the mould. The central objective of all these studies has been to obtain better heat transfer, dimensional accuracy of cast strands, better surface quality of strands, and longer mould life, *etc*.

Thomas *et al.*, (1997), Thomas (2001), and Park *et al.*, (2000) used a finite element model for prediction of temperature, distortion, and residual stresses on the mould plate. Park *et al.*, (2000), Samarasekara and Brimacombe (1979, 1982), and Chow *et al.*, (2002), on the other hand, developed mathematical models for predicting the shape of moulds and the temperature field as a function of operating design variables. Similar investigations (Meng and Thomas, 2003; Park *et al.*, 2002; Santillana *et al.*, 2008) are also available in the literature, and all of these point towards strict control of the mould hot face temperature to avoid distortion and thus produce better quality products. Also, generation of thermal stresses on the mould hot face must be avoided to minimize the distortion and resulting wear.

Figure 2a is a schematic of the continuous casting process. Molten steel from the ladle is poured into the tundish and from there into the moulds. In the mould, heat is extracted and the molten steel starts solidifying. As it cools, the steel strand is subsequently pulled downwards by the support rolls and finally cut into slabs. The dimensions of the slab are governed by the dimensions of the mould, which consists of a set of four plates (two narrow side-plates and two broad side-plates) as shown in Figure 2b. The side of the plate in contact with liquid steel or solidifying strand is known as the hot face and the side in contact with the water box is known as the cold face (Figure 2c). On the cold face of the plate an array of water cooling channels is provided to circulate cooling water at high flow rates to extract heat from the plate. Thus heat flows from the molten steel to the cooling water across the mould plate thickness.

Mould heat transfer is the most important parameter in continuous casting in terms of efficiency and quality. The heat removal rate from the mould has to be strictly controlled.

* *Research and Development Center for Iron and Steel, Steel Authority of India Limited.*

© *The Southern African Institute of Mining and Metallurgy, 2018.* *ISSN 2225-6253. Paper received June 2017; revised paper received Dec. 2017.*

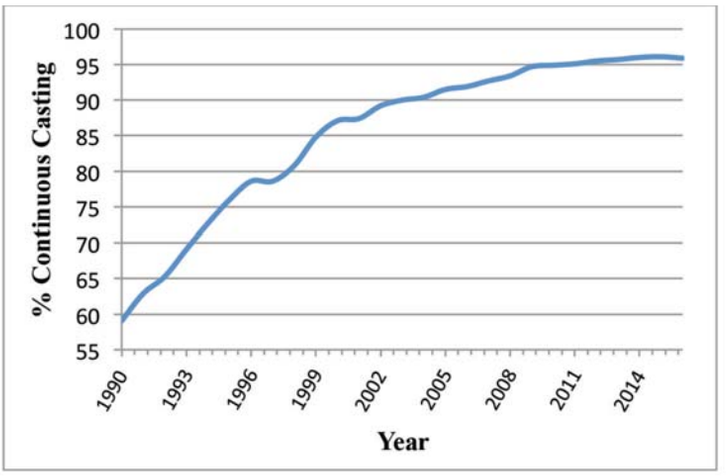

Figure 1—Increasing utilization of continuous casting process - global trends (World Steel Association. 2000, 2009, 2017)

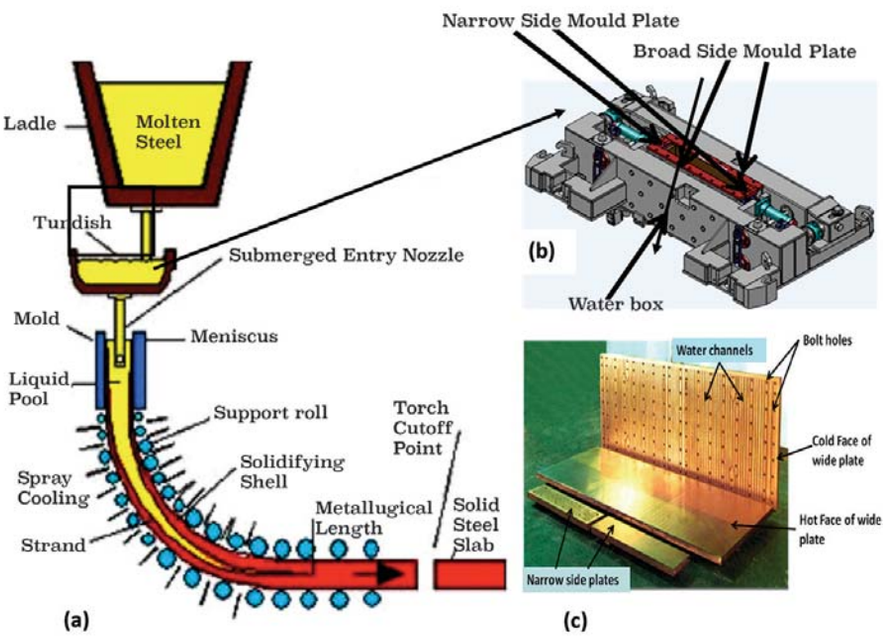

Figure 2—(a) Schematic of the continuous casting process (Continuous Casting Consortium, 2011), (b) mechanical assembly of mould (CISDI Engineering, 2011), (c) wide side and narrow side mould plates Tradekey, 2018)

Too high a rate of heat removal may lead to formation of a thicker shell near the mould exit. This causes rapid wear of the mould surface, thereby decreasing mould life and affecting the product quality. Conversely, a lower mould heat transfer rate may lead to a thinner shell, increasing the chance of a breakout at the mould exit and thus reducing process efficiency.

An effective and widely used way of improving the mould life is by coating the inside surface (hot face) with high-hardness materials. This coating, in turn, affects the heat transfer rate across the mould thickness and the hot face temperature of the mould. As highlighted above, both of these factors plays a vital role in any casting machine, and therefore the coating material and thickness of the coating must be chosen judiciously. In addition to this, the bolts used for clamping the mould plate to the water box reduce the thickness of the copper locally. This causes sudden variation in temperature at these localized spots, which may induce two-dimensional thermal stresses, eventually leading to distortion and wear of the mould plate. The present work focuses on a parametric study of the variation in copper thickness and the coating material on mould plates. The variation in the temperature of the hot face with variable coating thickness is analysed, along with the effect of the bolt holes. The results from this study will help in selecting the permissible limit of coating thickness to copper thickness ratio for continuous casting moulds.

Model Description

Geometric modelling

The dimensions of the modelled plate are 2000 mm × 900 mm. To take advantage of symmetry, only half of the plate is modelled, together with the cooling water channels

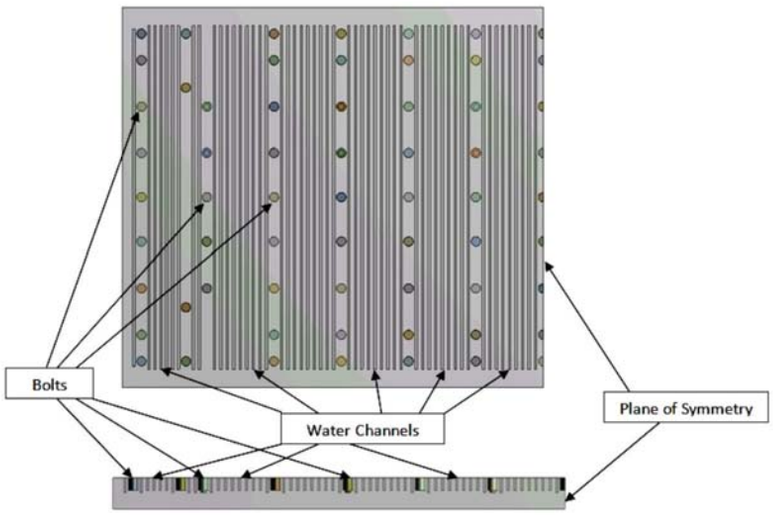

Figure 3—Front view and plan view of modelled geometry

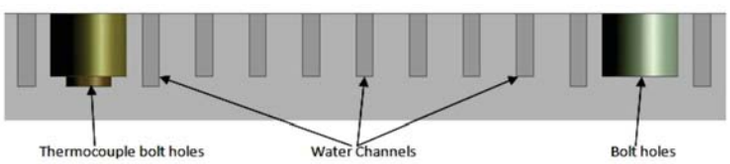

Figure 4—Detail view at thermocouple bolts, showing bolts and water channels

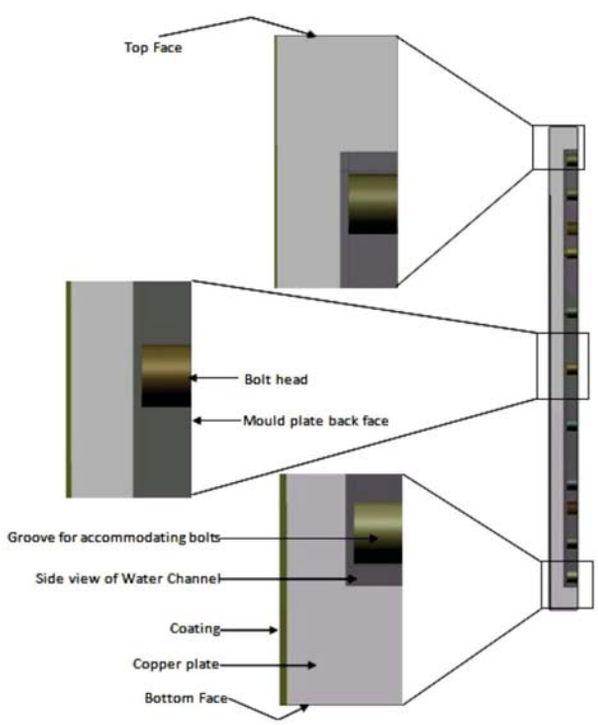

Figure 5—Variation in coating thickness over copper plate with mould length

and clamping bolts. Figure 3 represents the frontal and plan views of the modelled geometry.

The water channels adjacent to the bolts are extended deeper into the plate to take care of the extra heat flux, since there is no heat extraction at the bolt locations. Thermocouple bolts are also set a little deeper into the plate to accommodate the thermocouples. Figure 4 shows a detail view of these locations for clarification.

The coating pattern on the mould plate can be understood by referring to Figure 5. The figure shows the

tapered nature of the coating, starting with a thickness of 0.5 mm at the top and increasing to 2.5 mm at the bottom, thus keeping the plate thickness constant. This variable coating thickness is necessary because the shell thickness increases with increasing depth in the mould, and thus the pressure on the mould walls, and in turn the wearing tendency, increases. More wear is expected near the bottom of mould, and to counteract this a thicker coating of hard material is applied. The thickness of the copper is therefore reduced to compensate for increased hard material thickness, in order to keep the total plate thickness constant. Reducing the copper thickness will decrease the rate of heat extraction, so the thickness of the coating material has to be chosen judiciously and optimized considering the trade-off between increased strength for wear resistance and the resultant reduction in heat transfer.

Experimental design

Table I shows the experimental design for the parametric study on the effect of coating thickness on hot face temperature.

Table I

Experimental design

Case no.	Plate thickness	Coating description
1	45 mm (including coating)	Tapered coating - linearly varying from 0.5 mm at top to 2.5 mm at bottom
2	45 mm	Without coating
3	42.5 mm (including coating)	Tapered coating - linearly varying from 0.5 mm at top to 2.5 mm at bottom
4	42.5 mm	Without coating
5	40 mm (including coating)	Tapered coating - linearly varying from 0.5 mm at top to 2.5 mm at bottom
6	40 mm	Without coating
7	37.5 mm (including coating)	Tapered coating - linearly varying from 0.5 mm at top to 2.5 mm at bottom
8	37.5 mm	Without coating
9	35 mm (including coating)	Tapered coating - linearly varying from 0.5 mm at top to 2.5 mm at bottom
10	35 mm	Without coating

Mathematical heat flow model

In the mould plate, heat is transferred to the hot face from the solidifying molten steel and removed by water flowing in the water channels on the cold face. The objective of this work requires obtaining the thermal profile of the hot face of the mould plate. The presence of cooling channels and the bolt holes requires the heat transfer to be calculated in three dimensions, and so the Fourier equation for three-dimensional heat transfer across the plate, along with applicable boundary condition, is applied (Meng and Thomas, 2003; Park *et al.*, 2002; Santillana *et al.*, 2008).

$$\frac{d^2T}{dx^2}+\frac{d^2T}{dy^2}+\frac{d^2T}{dz^2}=0 \quad [1]$$

where T is temperature and x, y, z are the length, thickness, and width of the mould plate.

Figure 6 is a schematic representation of the heat transfer model. The heat flux profile on the hot face is also shown.

Assumptions

- The casting speed is assumed to be constant throughout the analysis period (Park *et al.*, 2000)
- The solidifying shell is assumed to be in perfect contact with the copper plate, without any gap (Santillana *et al.*, 2008).

Boundary conditions applied

- The hot face is applied with the heat flux boundary condition as shown in Figure 6. The heat flux profile is calculated based on plant measurements of mould water flow rate and rise in water temperature. This incorporates the effects of different layers formed within the mould (air gap, liquid slag, powder, and liquid steel). The applied heat flux profile is linear from the mould top to the peak heat flux location (slightly below the meniscus). Below the peak heat flux location, the heat flux profile in the mould is calculated based on the power law equation (Thomas *et al.*, 1997; Thomas, 2001; Park *et al.*, 2000; Meng and Thomas, 2003; Paul *et al.*, 2000) as in Equation [2].

$$q = at^{-b} \quad [2]$$

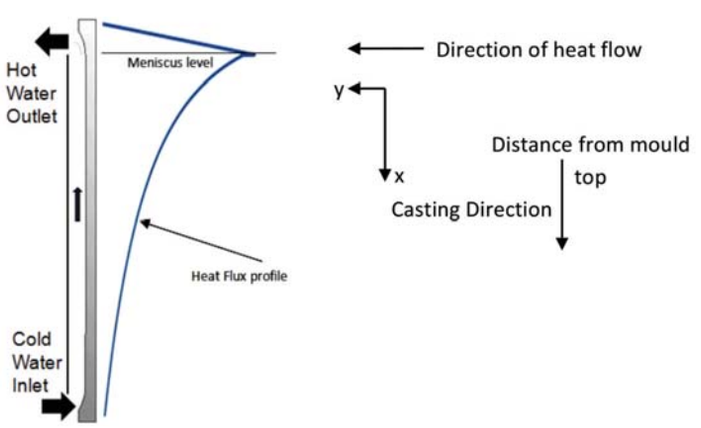

Figure 6—Schematic of the heat transfer model

where

q = mould heat flux (w/m^2)

t = residence time inside mould (seconds)

'a' and *'b'* are empirical constants adjusted based on total heat removed from the plate.

Since the casting speed is assumed to be constant, the distance x travelled inside the mould will be directly proportional to time (t). For the considered case where mould length is 900 mm and the meniscus is 70 mm below the top of the mould, based on plant calculations heat flux 'q' is given as:

$$q = \begin{cases} \frac{1815.555}{0.1115}x & for\ \ 0 < x < 0.1115 \\ 1815.555 \times \left(\frac{0.1115}{x}\right)^{0.4} & for\ \ 0.1115 < x < 0.90 \end{cases}$$

where x is the distance in metres from the mould top (refer Figure 6).

- The mould plate back face, bolt heads, mould plate top face, and mould plate bottom face are taken as being adiabatic and zero wall heat flux is given as the boundary condition
- The faces of the water channels will be the walls from which heat is removed by cooling water through convective heat transfer (Figure 6). Heat extracted q_{out} (w/m^2) is given as

$$q_{out} = h_w\left(T_{surf} - T_w\right) \quad [3]$$

where

T_w (K) is the temperature of the cooling water, for which a linear distribution is assumed from inlet to outlet

T_{surf} (K) is the surface temperature of the water channel

h_w (w/m^2.K) is the water channel heat transfer coefficient, calculated using the Sleicher Rouse equation (Burmesiter, 1993; Sleicher and Rouse, 1975) as

$$h_w = (5 + 0.15 * Re^{C1} * Pr^{C2}) * \frac{K}{D} \quad [4]$$

where

$$C1 = 0.88 - \frac{0.24}{4 + Pr}\ ,\ \ C2 = 0.333 + 0.5 * e^{-0.6*Pr}$$

$$\text{Reynolds Number, } Re = (\rho * V * D)/\mu$$

$$\text{Prandtl s Number, } Pr = \frac{\mu * Cp}{K}$$

$$K = 0.59 + 0.001 * (T_w - 273) \ and\ D = \frac{4 * A}{P}$$

where

ρ = density of water (kg/m^3)

μ = viscosity of water (kg/m.s)

V = velocity of water in cooling channels (m/s)

C_p = specific heat capacity of water (J/kg.K)

D = hydraulic diameter of water channel (m)

K = thermal conductivity of water (W/m.K)

A = cross-sectional area of the water channel (m^2)

P = perimeter of the cross-section of water channel (m).

Results and discussion

Temperature distribution across the mould plate

The typical temperature distribution (in K) across the mould plate is shown in Figures 7 and 8. The maximum temperature values can be observed at the meniscus, where peak heat flux is applied, with lower temperatures at locations further into the mould.

It can be observed from Figure 9 that there is an almost linear temperature gradient across the mould plate from the hot face to the roots of the water channels.

Effect of coating on peak hot face temperature

A nickel coating has been applied over the hot face of the

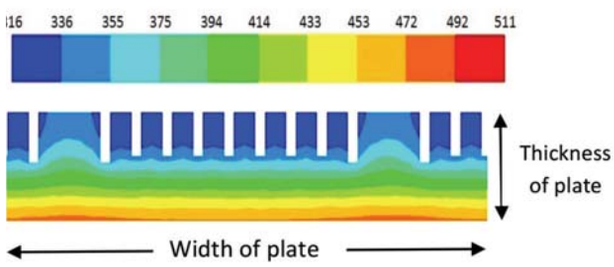

Figure 7—Temperature (K) profile across mould plate near meniscus region

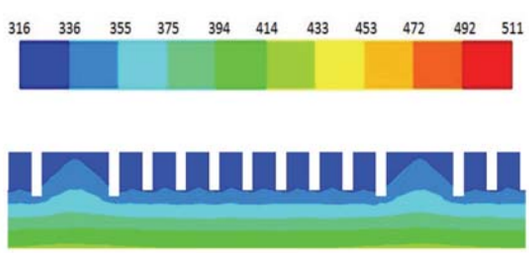

Figure 8—Temperature (K) profile across mould plate 350 mm below meniscus region

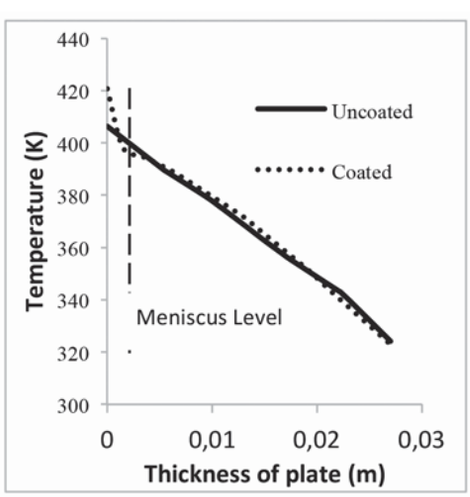

Figure 9—Temperature variation through the thickness of the plate

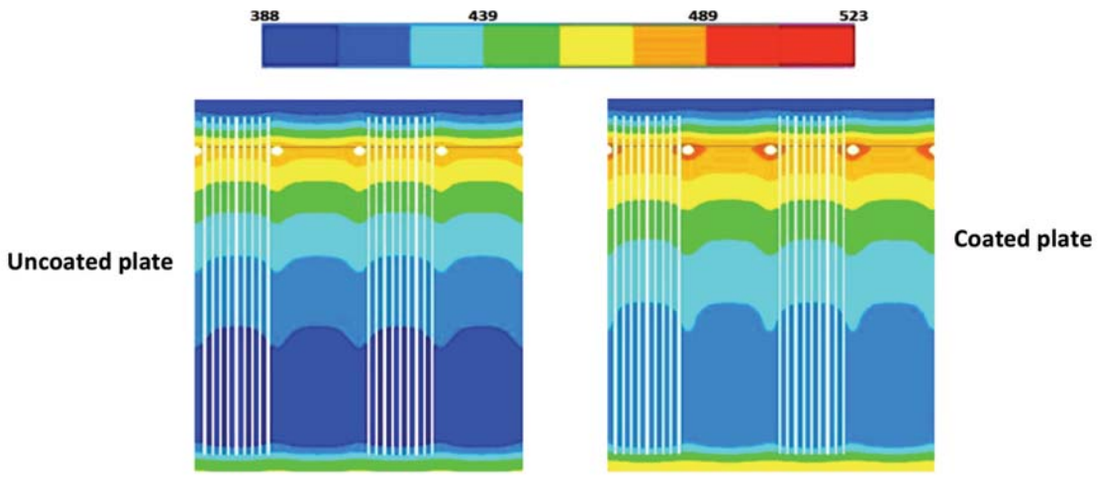

Figure 10—Temperature (K) variation on hot face of uncoated and coated plate

mould as indicated in Figure 5. The temperature distribution on the hot face for both coated and uncoated plates is shown in Figure 10. It is clearly evident that the temperatures are higher on the coated plate.

The temperature profile appears as regularly undulating horizontal bands. Regions where no water channel is present show a higher temperature than those where a water channel is present, for both the coated and the uncoated plate. Since the highest heat flux is located slightly below the meniscus region, the highest temperature bands are near the meniscus in both cases (Figure 10). Hot spots on the hot face opposite bolt locations form in both the plates, although the intensity of the hot spots is much higher in coated plates. This rise in temperature is due to lower conductivity of the coating material – 91 W/mK for nickel compared to 401 W/mK for copper (TibTech, 2018).

The sudden rise in temperature observed near the bottom of plate may be attributed to the absence of water channels at that location. At these locations, higher temperatures are observed in the case of coated plates compared to uncoated plates.

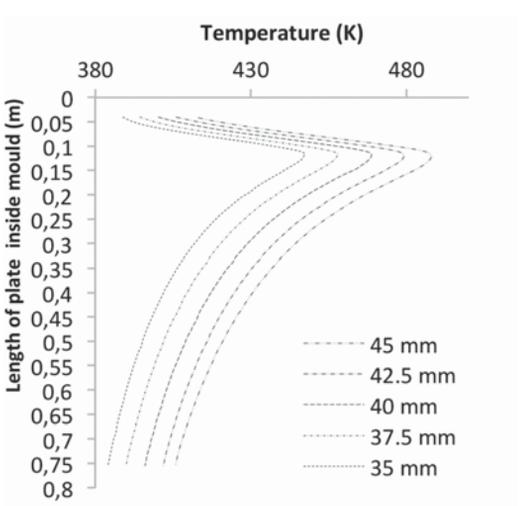

Figure 11—Temperature variation along the length of mould for different plate thicknesses

Effect of plate thickness on hot face peak temperature

Five different thicknesses of mould plate, as described in the experimental design, were chosen for analysing the effects of (a) variations in mould plate thickness and (b) plate coatings of different thicknesses on hot face temperature.

These analyses were conducted keeping all other boundary conditions constant. The hot face temperature profile mimics the heat flux profile applied, indicating clearly that, barring the regions close to bolt holes or water channels, the heat transfer across the plate is largely one-dimensional. Similar results have been reported in the literature (Thomas, 2001; Santillana *et al.*, 2008). Figure 11 shows the temperature variation on the hot face along the length (x) of the mould for different plate thicknesses. The figure also indicates that thicker plates have a higher hot face temperature due to the greater resistance to heat flow.

Table II

Increase in peak hot face temperature due to coating

Case no.	Plate thickness	Peak hot face temperature (K)	Temperature increase due to coating (K)
1	45 mm (including coating)	496.3	12.6
2	45 mm	483.7	
3	42.5 mm (including coating)	487.9	13.4
4	42.5 mm	474.5	
5	40 mm (including coating)	479.4	14.0
6	40 mm	465.4	
7	37.5 mm (including coating)	469.9	14.5
8	37.5 mm	455.4	
9	35 mm (including coating)	463.5	14.9
10	35 mm	448.6	

Table II lists peak hot face temperatures recorded for various plate thicknesses under the same boundary conditions and tabulates the rise in temperature due to coating on different plate thicknesses. Coated mould plates have a higher temperature profile and also show higher peak temperatures. This is as expected since the coating material has a lower thermal conductivity (91 W/mK) than the copper (401 W/mK) (TibTech, 2018), and hence the rate of heat transfer through the coating material will be lower.

It is quite evident that the effect of the coating increases with decreasing plate thickness, as shown by the greater rise in temperature for thinner plates. This can be attributed to the fact that, for same coating thickness, the ratio of coating material to copper increases. Thus the resistance to heat transfer due to the coating $\left(\frac{d_{coating}}{k_{coating}}\right)$ increases in comparison to the resistance offered by copper plate $\left(\frac{d_{coating}}{k_{coating}}\right)$, where d is the thickness of material and k is the thermal conductivity. The subscripts have the usual meanings.

A hot face temperature profile with and without coating for one of the cases is shown in Figure 12. Towards the lower end of the mould, the divergence between the thermal profiles of the coated and uncoated mould increases. This can be explained by the variation in coating thickness, i.e. 0.5 mm at the top of the plate, increasing linearly to 2.5 mm at the bottom of the plate. The greater the contribution of the coating material to the total plate thickness; the greater the temperature difference between the hot face thermal profiles of coated and uncoated moulds. At the lower end of the mould (beyond 0.8 mm) there is a significant rise in temperature for both coated and uncoated moulds. This is due to the absence of cooling channels in this position, owing to design considerations. For a thinner plate, this rise in temperature can be large enough to cause incipient boiling in the cooling channels in the lower portion. This would cause a sudden reduction in heat transfer in the lower portion of mould, which may have a serious impact on the quality of cast slabs.

Effect of bolt holes on hot face temperature

Bolts are essential as they are used to fix the water box to

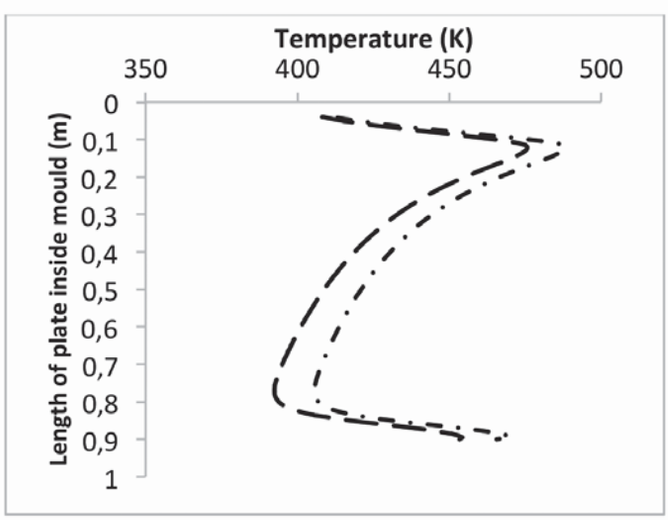

Figure 12—Comparison of hot face temperature profile with and without coating

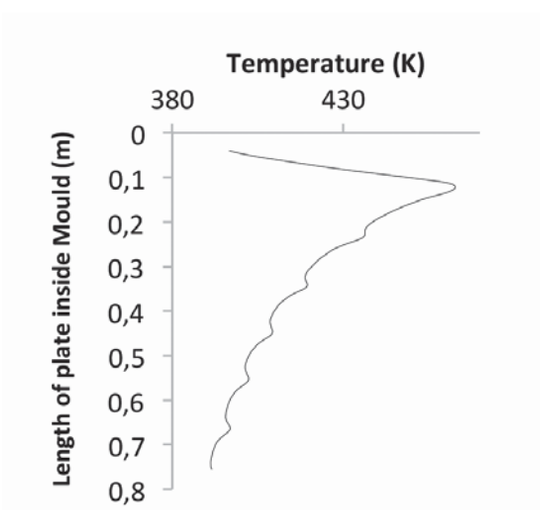

Figure 13—Variation of temperature due to tightening bolts along the length of the mould plate

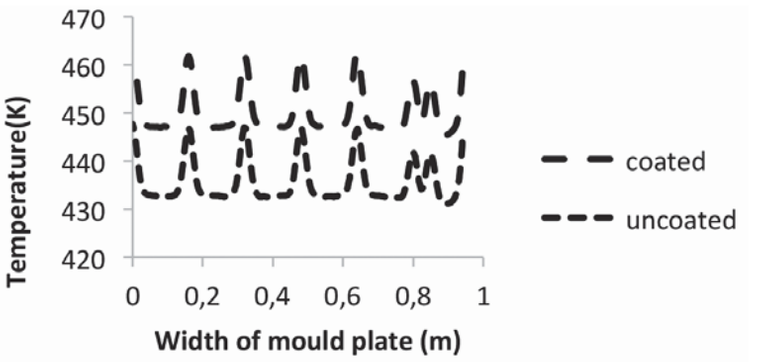

Figure 14—Variation of temperature due to tightening bolts along the width of the mould plate

the mould plate. Although bolts are required for completion of the mould assembly and to provide rigidity, they restrict the placing of water channels on the back cold face. Owing to the bolts, hot face temperature fluctuations appear across the width (z) as well as length (*x*) of the plate. Temperature variation along the length is due to the reduced thickness of copper at the bolt locations, whereas along the width it is due to the absence of water channels at the locations where bolts are positioned. These temperature fluctuations are significant and will cause two-dimensional thermal stresses to develop on the mould hot face, resulting in wear at the locations on the hot face opposite the bolts.

Figures 13 and 14 represent typical variation patterns of mould hot face temperature along the length and the width of the plate respectively. Figure 13 is a longitudinal cross-section along the mould length taken on the hot face opposite to the bolt holes. In Figure 14, zero represents the centre of the plate, and 1 the side.

The inflexions in the curve along the length of mould are at the locations of bolt holes. These zones experience localized temperature fluctuations on the mould plate hot face. Similarly, in Figure 14 the peaks along the curve represent the rise in temperature of the hot face at the bolt locations. This resembles a two-dimensional temperature fluctuation on the hot face at locations where tightening bolts are present on back side, which may result in localized regions of thermal stress, possibly leading to wear and damage of the mould plate and coating at these spots.

The effect of bolts on the hot face temperature becomes more pronounced as the thickness of the mould plate decreases. This is evident from Figure 15, which compares the hot face temperature profiles of plates with different copper thicknesses.

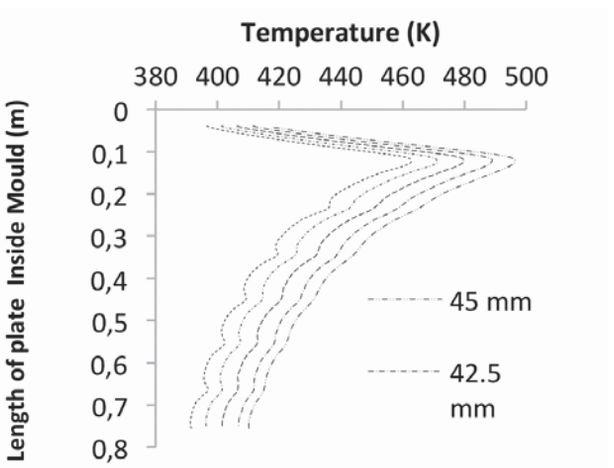

Figure 15—Hot face temperature profile showing effect of bolts for different plate thicknesses

Table III

Temperature fluctuations along the width of plate due to the presence of bolts

Case no.	Plate thickness (mm)	Uncoated plate hot face temperature (K)			Coated plate hot face temperature (K)		
		Above water channel	Above bolt location	Temperature fluctuation	Above water channel	Above bolt location	Temperature fluctuation
1	45	474.9	482.9	8.0	487.6	495.7	7.9
2	42.5	464.3	473.6	9.3	477.9	487.7	9.8
3	40	453.7	464.5	10.8	467.8	479.1	11.3
4	37.5	443.2	454.9	11.7	457.8	470.1	12.3
5	35	432.6	446.7	13.9	447.5	462.4	14.9

Table III compares the peak hot face temperature and the temperature opposite the cooling channel at the same location below the mould, for both coated and uncoated mould plates. The difference is around 8K for thicker plates. For thinner plates this difference rises to around 14K for an uncoated plate and 15K for a coated plate. The results indicate that the temperature variation across the width of the mould is practically same for both coated and uncoated thicker plates. However, in thinner plates a slight variation in temperature appears, with the coated plate showing a higher temperature.

This variation in temperature can be significant enough to cause thermal distortion on the mould plate. Thus, there is an optimum thickness of the mould plate below which the mould plates can be used with strict monitoring of cast steel quality parameters. In case of a coated mould plate this control is much more critical as the variation in mould face temperature is greater.

It can be noted that with a decrease in plate thickness, the highest temperature on the mould plate decreases. This is applicable for both coated and uncoated plates for all corresponding locations. A lower hot face temperature indicates improved heat transfer across the plate. Also, a thinner plate will be less costly than a thicker plate. Thus, it can be seen that a reduction in plate thickness on the one hand enhances the heat transfer, while on the other hand, thinner copper plates lead to greater variation in hot face temperature across the width of the mould in the meniscus region. This results in higher thermal stresses on thinner mould plates, which may result in accelerated wear of the mould. Coating of such mould plates may aggravate the situation as coated mould plates show a higher temperature variation compared to uncoated mould plate.

Conclusion

This work explains the thermal variations that can be observed along different dimensions of a mould plate due to factors like coating, tightening bolts, coating thickness, plate thickness *etc*. Temperature variation along the cross-section is more or less one-dimensional, hence 1D analysis could be helpful while focusing on overall temperature distribution. However, 1D analysis cannot capture the fluctuations due to the presence of bolt holes, absence of water channels at certain locations, and variation in temperature along the mould length due to a varying heat flux profile. 3D analysis hence plays an important role in capturing these details of mould heat transfer phenomena.

The results of the analysis show that hot face temperatures decrease with reduction in plate thickness at similar cooling water conditions. A reduction in hot face temperature is desirable as it increases the heat transfer rate. On the other hand, a reduction in plate thickness leads to greater temperature fluctuations at the bolt hole locations, which in turn will result in higher thermal stresses with a reduction in plate thickness. Thus, the optimum mould plate thickness has to be selected judiciously, taking into account both these contradictory features. There is an optimum thickness for the mould plates, below which the mould plates should not be used for casting, whether coated or uncoated.

Acknowledgment

The authors would like to thank the managements of RDCIS, SAIL India, and Bokaro Steel Limited (BSL) India for permission to publish this document. Special thanks are due to the casting personnel of the BSL continuous casting shop for their involvement and help with plant measurements.

References

Burmesiter, L.C. 1993. Convective Heat Transfer. 2nd edn. Wiley, New York.

Chow, C., Samarasekera, I.V., Walker, B.N., and. Lockhart, G. 2002. High speed continuous casting of steel billets—part 2: mould heat transfer and mould design. *Ironmaking and Steelmaking*, vol. 29, no. 1. pp. 61–69.

CISDI Engineering. 2011. CISDI successfully develops China's first hydraulic width-adjustable mold. http://www.cisdigroup.com/news4-843.html

Continuous Casting Consortium. 2011. Introduction to continuous casting. University of Illinois. http://ccc.illinois.edu/introduction/overview.html#techniques

Janik, M. and Dyja, H. 2004. Modelling of three-dimensional temperature field inside the mould during continuous casting of steel. *Journal of Materials Processing Technology*, vol. 157–158. pp. 177–182.

Janik, M., Dyja, H., Berski, S., and Banaszek, G. 2004. Two-dimensional thermomechanical analysis of continuous casting process. *Journal of Materials Processing Technology*, vol. 153–154. pp. 578–582.

Liu, X. and Zhu, M. 2006. Finite element analysis of thermal and mechanical behaviour in a slab continuous casting mold. *ISIJ International*, vol. 46, no. 11. pp. 1652–1659.

Meng, Y. and Thomas, B.G. 2003. Heat-transfer and solidification model of continuous slab casting. *Metallurgical and Materials Transactions B*, vol. 34, no. 5. pp. 685–705.

Park, J.K,. Thomas, B.G,. Samarasekera, I.V., and Yoon, U.S. 2002. Thermal and mechanical behavior of copper molds during thin-slab casting. (I). Plant trial and mathematical modelling. *Metallurgical and Materials Transactions B*, vol. 33B. pp. 1–12.

Park, J.K., Samarasekera, I.V., Thomas, B.G., and Yoon, U.S. 2000. Analysis of thermal and mechanical behavior of copper mould during thin slab casting. *Proceedings of the 83rd Steelmaking Conference*, Pittsburgh, PA, 26–29 March 2000. Iron and Steel Society, Warrendale, PA.

Paul, A., Pradhan, N., Ray, A.K., Bhor, P.K., Mazumdar, S., and Korath, J.M. 2000. Assessment of heat extraction through slab caster mould. *Scandinavian Journal of Metallurgy*, vol. 29, no. 4. pp. 139–145.

Samarasekera, I.V. and Brimacombe, J.K. 1979. The thermal field in continuous-casting moulds. *Canadian Metallurgical Quarterly*, vol. 18, no. 3. pp. 251–266. pp. 9–21.

Samarasekera, I.V. and Brimacombe, J.K. 1982. Mechanical behaviour of continuous-casting billet moulds. *Ironmaking and Steelmaking*, vol. 9, no. 1. pp. 1–15.

Santillana, B,. Hibbler, L.C., Thomas, B.G., Hamoen, A., Kamperman, A., and van der Knoop, W.V.D. 2008. Heat transfer in funnel-mould casting: effect of plate thickness. *ISIJ International*, vol. 48, no. 10. pp. 1380–1388.

Sleicher, C.A. and Rouse, M.W. 1975. A convenient correlation for heat transfer to constant and variable property fluids in turbulent pipe flow. *International Journal of Heat and Mass Transfer*, vol. 18, no. 5. pp. 677–683.

Thomas, B.G. 2001. Modeling of the continuous casting of steel - past, present and future. Brimacombe Lecture: *Proceedings of the 59th Electric Furnace Conference*, Phoenix, AZ . Iron and Steel Society, Warrendale, PA.

Thomas, B.G., Li, G., Moitra, A., and Habing, D. 1997. Analysis of thermal and mechanical. behavior of copper molds during. continuous casting of steel slabs. *Proceedings of the 80th Steelmaking Conference*, Chicago, IL, 13-16 April 1997. Iron and Steel Society, Warrendale, PA.

TibTech. 2018. Properties table of stainless steel, metals and other conductive materials. http://www.tibtech.com/conductivity.php

Tradekey. 2018. Mould copper plates for slab caster. http://www.tradekey.com/product-free/Mould-Copper-Plates-For-Slab-Caster-984450.html

World Steel Association. 2000, 2009, and 2017. Steel Statistical Yearbook. https://www.worldsteel.org/steel-by-topic/statistics/steel-statistical-yearbook.html ◆

Realising possibilities from mine to market.

Resource Evaluation — Mine Planning — Mining & Mine Development — Materials Handling — Environment & Approvals

Mineral Processing — Tailings & Waste Management — Smelting & Refining — Transport to Market — Non-Process Infrastructure

WorleyParsons adds value through our full scope of services from pit to port including studies, mine planning, impact assessments, permitting and approvals, project management, construction management and global procurement.

Our Mining Centre of Excellence in Johannesburg has niche expertise in underground and open cast mining and provides quality project development and engineering solutions for small to large projects across all areas of base metals, the coal supply chain, chemicals, ferrous metals, alumina, aluminium and iron ore.

Supported by the WorleyParsons global group, we pride ourselves on customising solutions for local environments and committing to our customers' goals.

WorleyParsons
resources & energy

www.worleyparsons.com wprsainfo@worleyparsons.com

SAMCODES
THE SOUTH AFRICAN MINERAL REPORTING CODES

SAMREC — THE SOUTH AFRICAN CODE FOR THE REPORTING OF EXPLORATION RESULTS, MINERAL RESOURCES AND MINERAL RESERVES

SAMVAL — THE SOUTH AFRICAN CODE FOR THE REPORTING OF MINERAL ASSET VALUATIONS

THE SAMREC and SAMVAL CODES

Advanced Workshop: Can you face your peers?

15–16 August 2018

The Wits Club, University of the Witwatersrand Johannesburg

The object of the interactive workshop is to address the more complex application of the codes through case studies. It will be assumed that the participants are fully conversant with the SAMREC and SAMVAL codes and are able to discuss their perspective on aspects of the case studies. The emphasis will be on being able to face one's peers and include both compliance and best practice aspects of the codes.

The workshop will take the form of group discussions of various case studies to facilitate discussion. Various topics have been selected and will be discussed in conjunction with discussions around Precious Metals, Coal, Diamonds and Valuation covering Exploration Results, Mineral Resources, Mineral Reserves and Valuations.

Participants will be supplied with material to review prior to the workshop. They will be placed in groups to discuss and dissect the material – 2 or 3 groups will be asked to present their findings at the end of each session. Each case study is designed for a 3 hour morning or afternoon session.

The workshop is intended to allow mining industry professionals to improve their knowledge and application of the advanced aspects of the SAMREC and SAMVAL Codes.

For further information contact:
Yolanda Ndimande, Conference Co-ordinator
Saimm, P O Box 61127, Marshalltown 2107
Tel: +27 (0) 11 834-1273/7
E-mail: yolanda@saimm.co.za
Website: http://www.saimm.co.za

GSSA Geological Society of South Africa

SAIMM THE SOUTHERN AFRICAN INSTITUTE OF MINING AND METALLURGY

NB: Documents for the workshop will be provided electronically on receipt of registration/payment

http://dx.doi.org/10.17159/2411-9717/2018/v118n5a8

Automatic generation of feasible mining pushbacks for open pit strategic planning

by X. Bai*†, D. Marcotte*, M. Gamache†, D. Gregory‡, and A. Lapworth°

Synopsis

The design of pushbacks in an open pit mine has a significant impact on the mine's profitability. Automatic generation of practical pushbacks is a highly desirable feature, but current automatic solutions fail to sufficiently account for complex geometric requirements of pushbacks, including slopes, phase bench and bottom width, smoothness, and continuity. In this paper, we present a tool to fill this gap. Our proposed algorithm is based on modification of sets of blocks obtained by parametric optimization of the pit using a maximum flow method. A set of geometric operators is developed to modify the sets to present a feasible geometry for mining. The geometric operators are essentially derived from mathematical morphological tools. Case studies show that the proposed method generates practical pushback designs that meet all geometric constraints. The algorithm can be used to create a solution for medium-size pits in minutes. This significantly improves the efficiency of designing pushbacks for open pit mines.

Keywords
pushbacks, geometric constraints, bench width, open pit planning, image processing, mathematical morphology.

Introduction

In surface mining, planning over the entire mine life is called long-term planning or strategic mine planning. It involves creating mine designs and schedules on a strategic scale, and provides a financial vision for a project as well as an engineering guidance for short-term production. One of the tasks of strategic planning is to design pushbacks, also referred as cutbacks, periods, or stages (Hustrulid and Kuchta, 1995; Whittle, 2011). Pushbacks (Figure 1) are essentially a series of manageable exploitation phases for an open pit mine. A pushback is ideally composed of a unique, spatially contiguous volume that can be mined with available mining equipment and that meets practical geometric mining constraints. A pushback is typically excavated in a continuous period of one to two years, and the extracted material needs to be able to feed the requirement of processing plants. Sometimes, if mining capacity is available, multiple pushbacks are mined concurrently, to produce sufficient ore to meet production schedules. Practical considerations result in two categories of constraints on pushback design: (i) geometric constraints; space is required for haul road design and machine access, and geotechnically controlled slope angles must be honoured for safety, and (ii) quality and overall size constraints on the content of each pushback to meet production targets, required blends and mill processing capacity *etc.* Recent literature has primarily focussed on the second category of constraints. Important, but commonly neglected, geometric constraints include minimum mining width, continuity and smoothness. The minimum mining width depends on the mining method and the selected equipment. Smoothness and continuity are critical (Hustrulid and Kuchta, 1995) for facilitating mining operations, specifically by reducing costly movement of equipment and fostering the design of even low-gradient access ramps with the least possible number of turns. Automated pushback design methodologies that implement these constraints are rarely reported in the public domain. This paper seeks to fill this gap.

Many publications on pushback generation emphasize maximization of NPV under resource constraints, with little attention paid to geometric considerations (Consuegra and Dimitrakopoulos, 2010; Goodfellow and Dimitrakopoulos, 2013; Meagher, Dimitrakopoulos, and Vida, 2015). Crucial operational parameters such as mining width, pit smoothness, and continuity have been neglected, resulting in impractical pushbacks. Designs typically include narrow benches and

* *Department of Civil, Geological and Mining Engineering, Polytechnique Montréal, Canada.*
† *GERAD & Department of Mathematics and Industrial Engineering, Polytechnique Montréal, Canada.*
‡ *Datamine Software Ltd., Sudbury, Canada.*
° *Datamine Software Ltd., Wells, UK.*

© *The Southern African Institute of Mining and Metallurgy, 2018.* *ISSN 2225-6253. Paper received Mar. 2017; revised paper received Feb. 2018.*

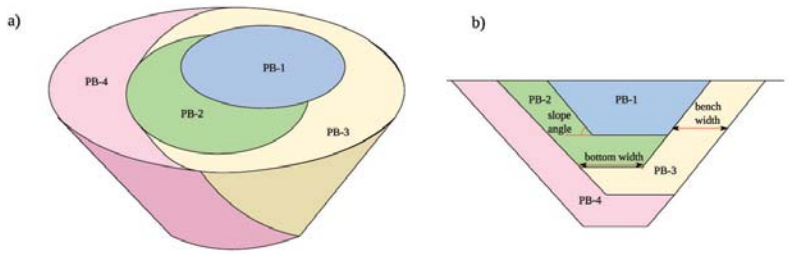

Figure 1—Pushbacks and the geometric constraints: (a) 3D view, (b) a cross-section

pit bottom, irregular boundaries, and multiple separated components. Post-modification of impractical pushbacks so as to be mineable is a questionable matter. It requires lengthy manual intervention, destroys value, and violates the resource constraints used to obtain the initial design. It is clear that the geometric problem must be dealt with prior to, or simultaneously with, the resources constraints. This is the main aim of this paper.

A few practical pushback generation tools that aimed at creating practical geometries have appeared in the commercial field. GEOVIA Whittle has a Mining Width Module that allows mining width templates to be specified in the X and Y directions and is applied to modify a set of pit shells to fulfil width requirements on benches and at pit bottoms (Whittle, 1998). It can also tolerate benches tapering towards highwalls. NPV Scheduler also includes a pushback generator that modifies nested pits to cater for mining width (Datamine, 2014). BHP Billiton's in-house software 'Blasor' incorporates a tool that can assist manual pushback modification (Stone *et al.*, 2004). More recently, DeepMine software reported a solution that can create the cohesive pushbacks and follows basic operational constraints (Juárez *et al.*, 2014). The tool uses an approximate dynamic programming method for searching the solution space of possible phase configurations. The technical description of these commercial tools is not publicly accessible, and very little detailed information is revealed on the critical functions of controlling pushback geometries.

A few attempts to automatically include geometric constraints are found in the underground mining literature (Bai, Marcotte, and Simon, 2014, 2013a, 2013b; Deraisme, Fouquet, and Fraisse, 1984; Nelis *et al.*, 2016). In particular, Deraisme, Fouquet, and Fraisse (1984) used mathematical morphology operators to produce mineable underground stopes. We exploit this idea in the more challenging context of open pit mining.

In this paper, we focus on the satisfaction of geometric constraints while maintaining a global NPV close to the one obtained using parametric nested pits that do not consider the geometric constraints of minimum width, smoothness, and continuity. We present a new tool to automatically generate pushbacks with all the geometrical constraints fulfilled. The tool is based on a series of new and existing geometric operators that automatically modify an initial parametric pushback to be practical. The geometric operators are based on image processing tools, mainly the mathematical morphological techniques. The tools are embedded in a strategy ensuring that: (i) the resulting NPV remains close to the one obtained with parametric nested pits, and (ii) the ore tonnage available at each period stays within specified bounds.

The paper is structured as follows. We first review the concepts of block model, ultimate pit, and parametric pit. Then, we define the three new geometric constraints (minimum size, smoothness, and continuity) that we want to impose. The notations and the basic mathematical morphological (MM) tools are described. Then, we present step-by-step the new algorithm based on MM to modify a pushback so as to satisfy the new constraints. We then compare the method to the pushbacks based on parametric nested pits that are available in some of the most popular commercial software. We test the algorithm on a simulated deposit and a real copper deposit and discuss its performance. We briefly discuss the computational aspect before concluding.

Definitions and notations

In this section, we review the main stages of pushback generation, the notation, and the MM operators used in our approach.

Main stages of pushback generation

The pushback generation involves three main components:

- The resource model
- The ultimate pit (UPit) and
- The generation of pushbacks.

The resource model

The geological resource is usually represented by a 3D block model. Each block has associated values of attributes such as grade, mineral content (valuable mineral or gangue minerals), processing recovery factors, grindability, *etc.* The block model is generated using exploration sample data and geostatistical modelling to estimate the block variables at unsampled locations (Chilès and Delfiner, 1999). The block model can be either deterministic, which reflects the best estimates, or stochastic, which provides possible alternative scenarios that reflect the uncertain geological and economic conditions (Marcotte and Caron, 2013).

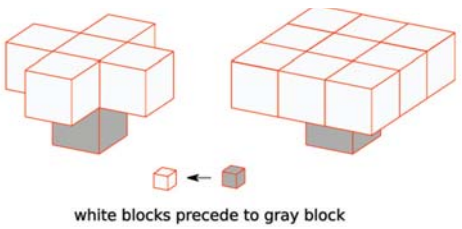

Figure 2—Typical link patterns to control pit slope constraints: to mine the block in grey, its predecessors at the upper level must be removed first

The ultimate pit

The ultimate pit is the pit that yields the maximum (undiscounted) profit for the given resource model. It comprises a subset of blocks that represent the volume within which the pushbacks should ideally be designed. The pit slope angle requirements are defined by precedence relationships between blocks and can vary at different locations in the mine or along different directions. A simple precedence pattern is shown in Figure 2.

In operations research, the UPit problem is defined as finding a set of blocks that follows precedence constraints and that yields maximum profit, which is a type of maximum closure problems. The Lerchs-Grossmann (LG) algorithm provides the optimal solution for such a problem (Lerchs and Grossmann, 1965). The equivalent problem can be solved much more efficiently with maximum flow (max-flow) algorithms such as the push-relabel method (Goldberg and Tarjan, 1988) and pseudo-flow method (Chandran and Hochbaum, 2009; Hochbaum, 2008). It is worth noting that the common UPit optimization methods do not consider the minimum mining width of the pit bottom or benches, nor the required smoothness and continuity. Consequently, they usually generate an impractical UPit with areas too narrow to mine or with too many satellite groups of blocks. The UPit, therefore, needs to be modified to ensure feasibility from a mining point of view. The tools developed in this paper can obviously be used for this purpose.

Generation of pushbacks

This step creates spatially connected sets of blocks within the ultimate pit that meet the practical requirements for mining. Common commercial packages use the nested shells method to lead pushbacks generation. Block values can be parameterized by applying revenue factors or cost factors (Whittle, 1988), while running LG or maximum flow on the parameterized models give a series of parametrical pits. As the parameter increases, a series of nested pits can be generated. Each pit only obeys slope constraint and is optimal for the particular economic parameter. Also, inner pits contain higher value per block and are mined before outer pits, therefore optimizing the NPV in a heuristic way. The created pit shells are then selected and modified to form pushbacks that cater for mining width and resources requirements. The great advantage of the nested shell method is that it delivers a range of pit shells for modification very quickly. The efficiency of the method allows large problems to be dealt with.

The procedure for nested pits method can be flexible. A simple way is to use an arbitrary set of revenue parameters and obtain a range of nested pits for further selection and modification, which is adopted by the Whittle tool. A standard optimization-based method is the parametric maximum flow method (Hochbaum and Chen, 2000). Another alternative is to optimize the parameter selection to find pits that best meet the resource constraints. Specifically, the procedure is to iteratively vary the parameter and run max-flow, then check the satisfaction of resource constraints. A satisfied phase is adopted and the procedure moves forward to create following phases. We name this procedure the 'successive max-flow' method. Since our proposed method shares similar workflow, we describe the details of the successive max-flow in Algorithm [11], together with our proposed high-level algorithm.

Geometric constraints for pushbacks: definitions

The slope angle is usually controlled by the precedence relation of blocks. This is a well-documented technique and will not be addressed here. Three other important geometric constraints for pushbacks are: (1) width constraints, (2) smoothness, and (3) continuity.

Width

Sufficient width (typically 100 m) is required on pushback benches (the horizontal sections of one pushback) and pit bottoms, to allow large equipment to work efficiently (Hustrulid and Kuchta, 1995). On the other hand, narrow benches may be mineable with smaller equipment that has a higher cost and lower productivity. Narrow benches should be avoided except in some cases, for example at the edges of pushbacks that are adjacent to a previously mined pit, required to create smooth pit contours. Therefore, the practical requirement of width can be described as two conditions: an area with sufficient target width (TW), or a sub-wide area adjacent to the wide area and to previously mined portions.

Smoothness

The boundaries of pushbacks are preferably designed to be smooth. Irregular shapes can result in operational difficulties. Irregular shapes can be caused by either small cavities or protuberances at pushback boundaries. The smoothness can be expressed by two conditions: (1) a pit must consist of at least NS consecutively adjacent blocks in both the x and y directions; and (2) if a block is outside the current pushback, it should also have at least NS consecutive adjacent blocks, in both the x and y directions, which are also outside the current pushback. The NS here is the parameter to control the smoothness. The first condition is to eliminate the protuberances of the current pushback, as in case I in Figure 3. The second conditions remove the cavities inside the current pushback, as in case II in Figure 3.

Continuity

Another requirement of pushbacks is their continuity. The haulage network is a consequence of the pushback design. A pushback comprising multiple disconnected parts would result in separate road access points. This should be avoided because equipment would need to be relocated more frequently within a given period of time, which increases the ramp development and mining costs and the complexity of the operation.

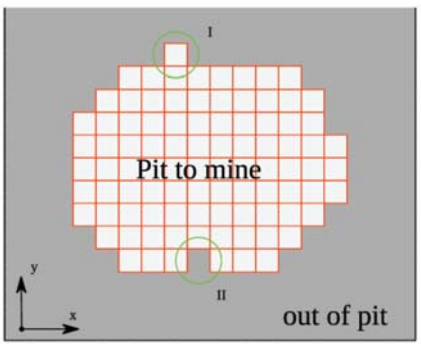

Figure 3—Cases of irregular pit boundaries, with smooth factor NS = 3

Notation

Indexes

i, j, and k	Coordinates of a block where k is the level
α, β, and γ	Coordinates of a block where γ is the level
t	A phase or pushback

Parameters

n_{PB}	The number of pushbacks
T^t_{ore}	Tonnage of ore of the phase t
TW	The number of blocks to form a wide area for efficient mining operation
AW	Auxiliary width parameter to control tolerable sub-wide areas
SE	Structural element for morphological operations
SES(w)	Structural element of square with width w
NS	The parameter to control smoothness

Block elements and sets:

$x_{i,j,k}$	A block located at (i, j, k)
$s_{\alpha,\beta,\gamma}$	A block located at (α, β, γ)
$\mathfrak{B}$	A set of blocks
$\mathfrak{B}_k$	A set of blocks on level k
$\mathfrak{B}_k^{1\to t}$	A set of blocks on level k extracted during phases 1 to t
$\mathfrak{B}_k^t$	A set of blocks that have been extracted during phase t, *i.e.* $\mathfrak{B}_k^{1\to t} \setminus \mathfrak{B}_k^{1\to t-1}$ where $\mathfrak{B}_k^{1\to 0} = \phi$ and $\mathfrak{B}_k^1 = \mathfrak{B}_k^{1\to t}$
$\mathfrak{B}_k^{t,new}$	Duplicated or modified $\mathfrak{B}_k^t$
$\mathfrak{B}_k^{1\to t,new}$	
$\mathfrak{B}_k^{1\to t,new0}$, $\mathfrak{B}_k^{1\to t,new1}$	Duplicated or modified $\mathfrak{B}_k^{1\to t}$
$\mathfrak{B}^{wide}$	A set of blocks in a temporarily accepted wide area in the iteration of width controlling algorithm (Algorithm [5])
$\mathfrak{B}_k^{unsettled}$	A set of blocks on level k that are repetitively shifted from modifying pushback and unplanned pushbacks. This is a specific set used in Algorithm [10].
$\mathfrak{B}_k^{unsettled,new}$	A duplicated or modified $\mathfrak{B}_k^{unsettled}$
$\mathfrak{B}_k^{unsettled,large}$	Dilated (enlarged) set $\mathfrak{B}_k^{unsettled}$
$pred(\mathfrak{B}_k)$	The set of predecessors of blocks $\mathfrak{B}_k$, *i.e.* the blocks that must be extracted if $\mathfrak{B}_k$ is extracted
$succ(\mathfrak{B}_k)$	The set of successors of blocks $\mathfrak{B}_k$, *i.e.* the blocks that have $\mathfrak{B}_k$ among their predecessors
$succ(\mathfrak{B}_k)^t$	The set of successors of blocks $\mathfrak{B}_k$ in t^{th} pushback

Basic mathematical morphological tools

From an image processing point of view, a pushback design is a 3D greyscale object where each voxel is valued by the period in which it is mined. A pushback *t* is a subset of blocks with voxel value *t*. It can also be represented as a binary image: the voxels in the pushback are indicated by values of unity; others by zeros. Since the width constraints concerns only the horizontal planes, when modifying the width of a pushback, one can focus on the 2D '1-0' image on each level *k*, where we note $\mathfrak{B}_k$ is the set of 'unities' .

Mathematical morphological methods are common tools to modify the geometry of images (Serra, 1982) . They are simple and efficient and are very useful for modifying the geometry of objects reflected in the object in an image. The methods are widely applied in image enhancement for the purpose of sharpening, smoothing, edge detection, *etc*. The characters of the methods are suitable for processing a pushback geometry in our context. The basic morphological tools operate on a binary image, or equivalently a set $\mathfrak{B}_k$, with a structural element (SE). The structural element, as a parameter, is a small binary image of a certain shape, like a square, diamond, or other simple shapes. A few basic functions include: (1) dilating, (2) eroding, (3) opening, and (4) closing.

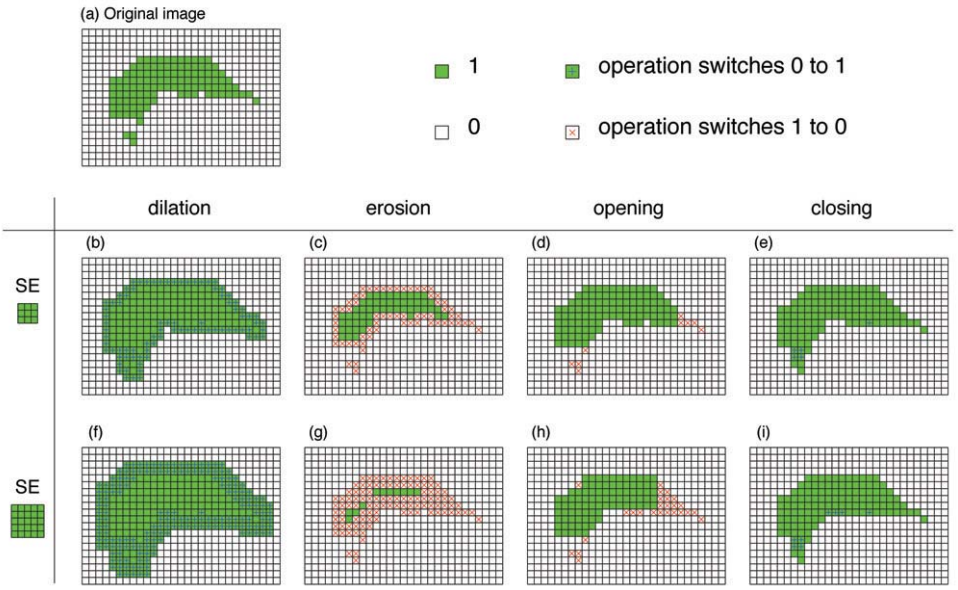

Figure 4—Effects of basic morphological operations. (a) Original image. Results of operations with SE of 3 × 3 square by dilating (b), eroding (c), opening (d), and closing (e). Results of operations with SE of 5 × 5 square by dilating (f), eroding (g), opening, (h), and closing (i)

Dilating

The dilation consists of placing the centre of SE on each element of the set $\mathfrak{B}_k$ and adding the elements located on SE to the dilated set (see Algorithm [1]). As a result, it returns an extension of the area of '1's in the original image. The dimension and shape of SE defines how the area is enlarged. For example, Figures 4b and 4f show the effect of dilation on the image in Figure 4a respectively with SE of 3 × 3 square and 5 × 5 square.

Eroding

The erosion operation (described in Algorithm [2]) has the opposite effect of dilation, *i.e.* shrinkage of the set $\mathfrak{B}_k$. It is also a dual operation of dilation, as eroding a set is equivalent to dilating its complementary set. Similarly, the SE controls the magnitude of erosion. The effect is shown in Figures 4c and 4g.

Opening

The opening operation comprises first eroding then dilating (Algorithm [3]). It behaves like matching the pattern of a structural element in the image, and returning only the matched elements. For example, opening with an element of 3 × 3 square on the image of Figure 4a generates the image in Figure 4d, where the parts smaller than 3 × 3 blocks are removed. Similarly, opening with SE of 5 × 5 square returns areas with a minimum width of 5 blocks (Figure 4h). It can be seen that the opening is very useful to measure and control the width, as it removes the clusters of blocks that are smaller than the structural element, and keeps the wide areas unaltered.

Closing

The closing operation is done by first dilating and then eroding the image (Algorithm [4]). The effect is to join the isolated components that are close to one another, as shown in Figures 4e and 4i.

Methodology

Globally, our algorithm defines feasible pushbacks sequentially from the first period to the last. Each pushback is created by modifying the optimal pit obtained by max-flow optimization with a specific price parameter. The parameter value is selected such that the capacity constraints are reached within specified bounds after the enforcement of the geometric constraints. The modification of each pushback proceeds level-by-level, from bottom to top. On each level, the morphological algorithms enforce the constraints of width, smoothness, and continuity, which is the core component of the algorithm. Any modification to a given level implies additional reallocation of blocks on upper or lower levels so as to maintain the slope (or precedence) constraints. Hence, a block added to a given level must come with all its predecessors on upper levels not yet mined in previous pushbacks. Similarly, all the successors of a block removed from a level must also be removed from the current pushback. Once a pushback is obtained, it is considered mined and the max-flow parametric optimization and geometric modifications are rerun on the remaining deposit. This ensures that the new pushback fully accounts for the effect of the geometric constraints applied on the previous pushback.

In next sections, we present the details of algorithms from a low level to high level. We first introduce the 2D geometric operations to control the new geometric constraints. The algorithm to generate a single 3D pushback is then presented. Finally, the main algorithm to create sequentially all pushbacks is discussed.

Geometric operators to control new constraints

We describe in detail the three main new geometric operators used to impose minimal width, smoothness, and continuity.

Width operator: adaptive opening

Obtaining the acceptable width of a pushback bench requires two conditions to be controlled: (1) the wide area has a width at least equal to target width (TW), and (2) a small sub-wide area can be mined only if it is adjacent to a wide area and is not too elongated. The first condition is easy to control by the opening operation. For the second condition, the sub-wide area is defined to be acceptable when its shape is roughly a triangle of base length AW, as shown in Figure 5. In this case, the width varies linearly over AW from TW to a single block. The control parameter AW corresponds to the maximum distance a single block can be from the adjacent

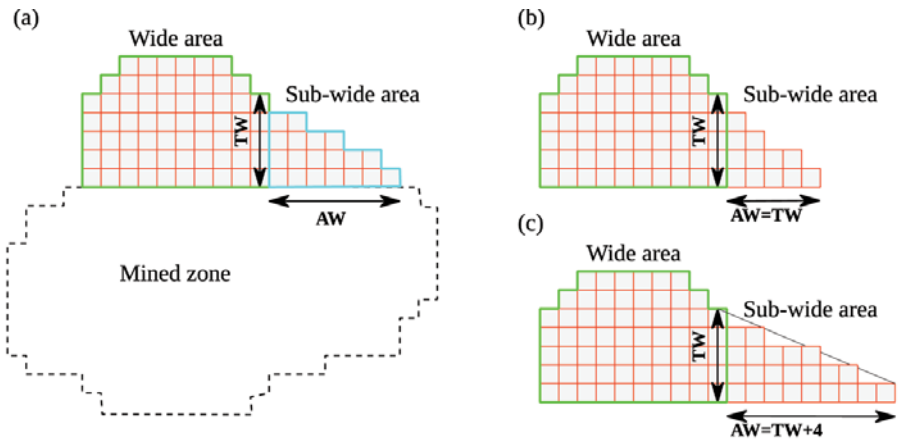

Figure 5—(a) Illustration of width of pushback with parameter TW and AW; (b) and (c), the influence of auxiliary parameter AW; AW *vs* TW controls the transition smoothness from a wide area to an existing pit

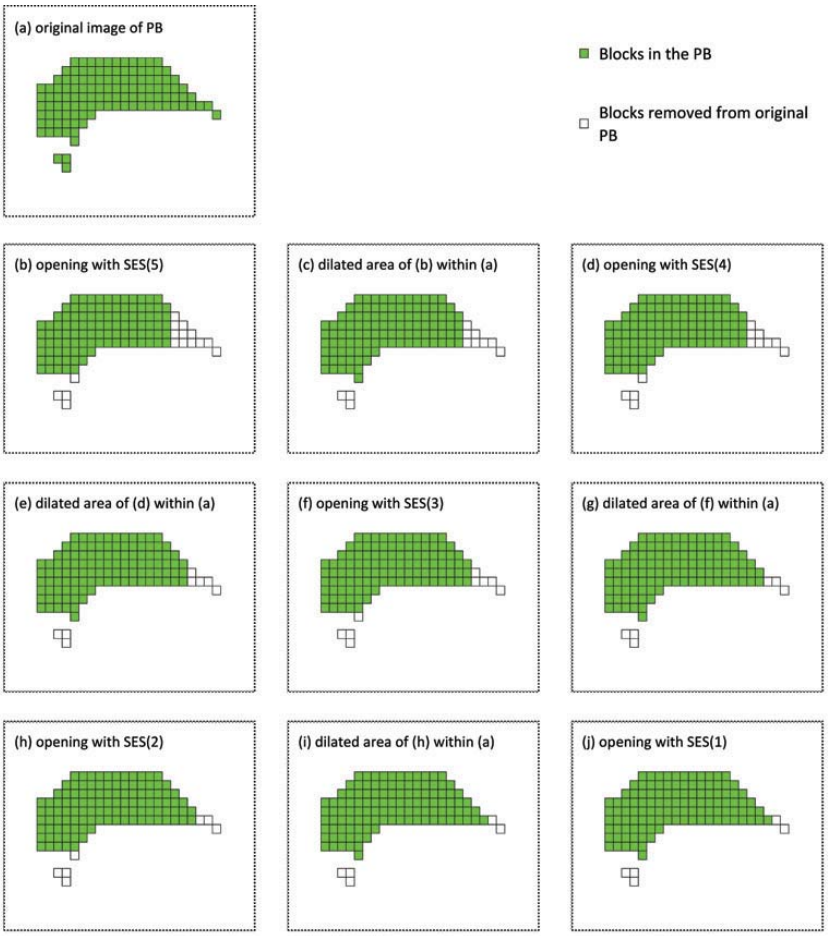

Figure 6—Illustration of evolution of pushback with adaptive opening operation, TW = 5, AW = 5. Green blocks indicate one pushback t, white blocks are removed by the operation

wide area. Clearly, increasing AW creates a sharper and longer sub-wide zone.

To modify a pushback to have a practical width, we propose a new compound operator based on opening, named 'adaptive opening'. The idea is to first find a set of blocks that satisfy the first width condition, *i* with minimum width TW. This is done by operating opening on the pushback binary image with a square structural element of size TW (note as SES(w = TW)). This step keeps the blocks that constitute the areas wider than or equal to w, in a set noted as $\mathfrak{B}^{wide}$, and removes the others blocks. We then check the abandoned blocks in the original pushback set. If an acceptable sub-wide area adjacent to the wide area can be found, it is added to the wide area $\mathfrak{B}^{wide}$. For this, we repeat AW times the following procedure: dilate the area of $\mathfrak{B}^{wide}$ within the original pushback set, reduce the width requirement w, check if the reduced width can be satisfied on the dilated set, and update the $\mathfrak{B}^{wide}$ with the newly fulfilled area. The procedure of the adaptive opening is described in Algorithm [5]. A step-by-step evolution of the image during adaptive opening is illustrated in Figure. 6.

Smoothness operator

To create smooth pushback boundaries, both opening and closing operations are used. Closing can fill the small cave on the edge of pushback, as is shown in Figure 4d. The opening operation cuts the small bumps on the edge of pushback. It should be noted that performing opening on one pushback can also remove the sub-wide transition area created by the adaptive opening. To avoid this side-effect and perform purely smoothing, the opening is operated on the combined set of current and earlier pushbacks, instead of only the current pushback. This procedure is described in Algorithm [6], and is noted as OpenSmoothing. The smoothing factor NS should be smaller than TW, otherwise the smoothing can over-reduce the PB blocks in the area wider than TW. Figure 7 illustrates the effect of OpenSmoothing with factor NS = 3. In Figure 7a, a series of pushbacks is obtained after applying adaptive opening, which is not smooth. In Figure 7b, the yellow blocks represent the union of the current PB and previous PB. We then apply opening with SES(3) on the union of both sets, and obtain Figure 7c. After that, we exclude the previous PB from Figure 7c, and get the new current PB, shown in Figure 7d. These two steps remove the small bumps on the boundary of the current PB, and also avoid removing accepted sub-wide area created during the previous adaptive opening. The result of smoothed pushbacks is displayed in Figure 7e.

Continuity operator

To control the continuity of a pushback, an algorithm to detect connected components (Conn-Comp) is used (Hopcroft

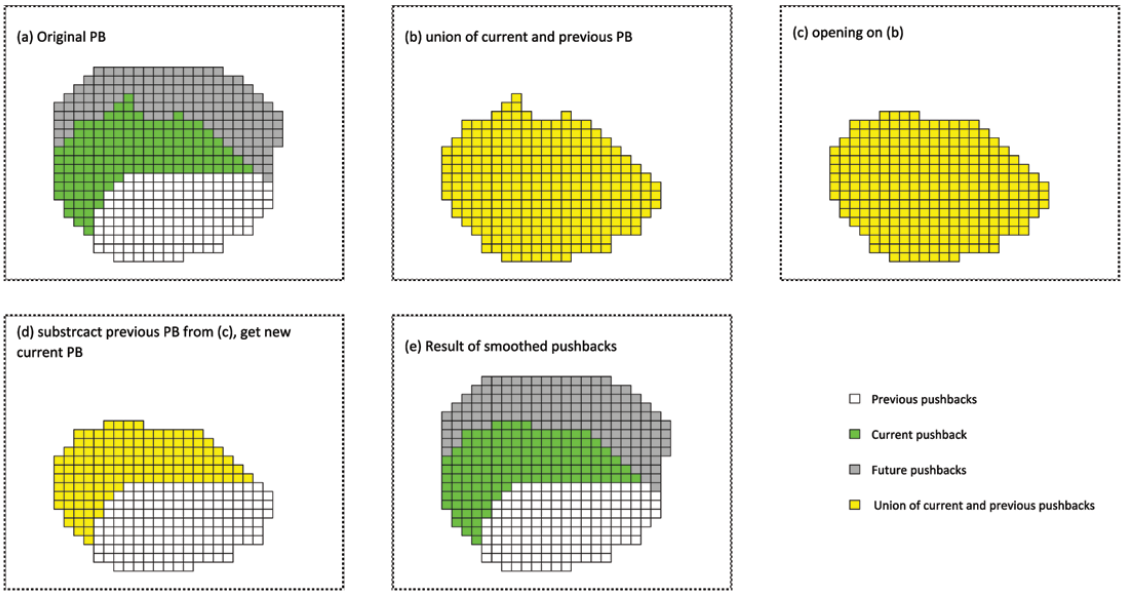

Figure 7—Effect of smoothing operations, NS = 3. Green blocks indicate one pushback t, white blocks are removed by the operation

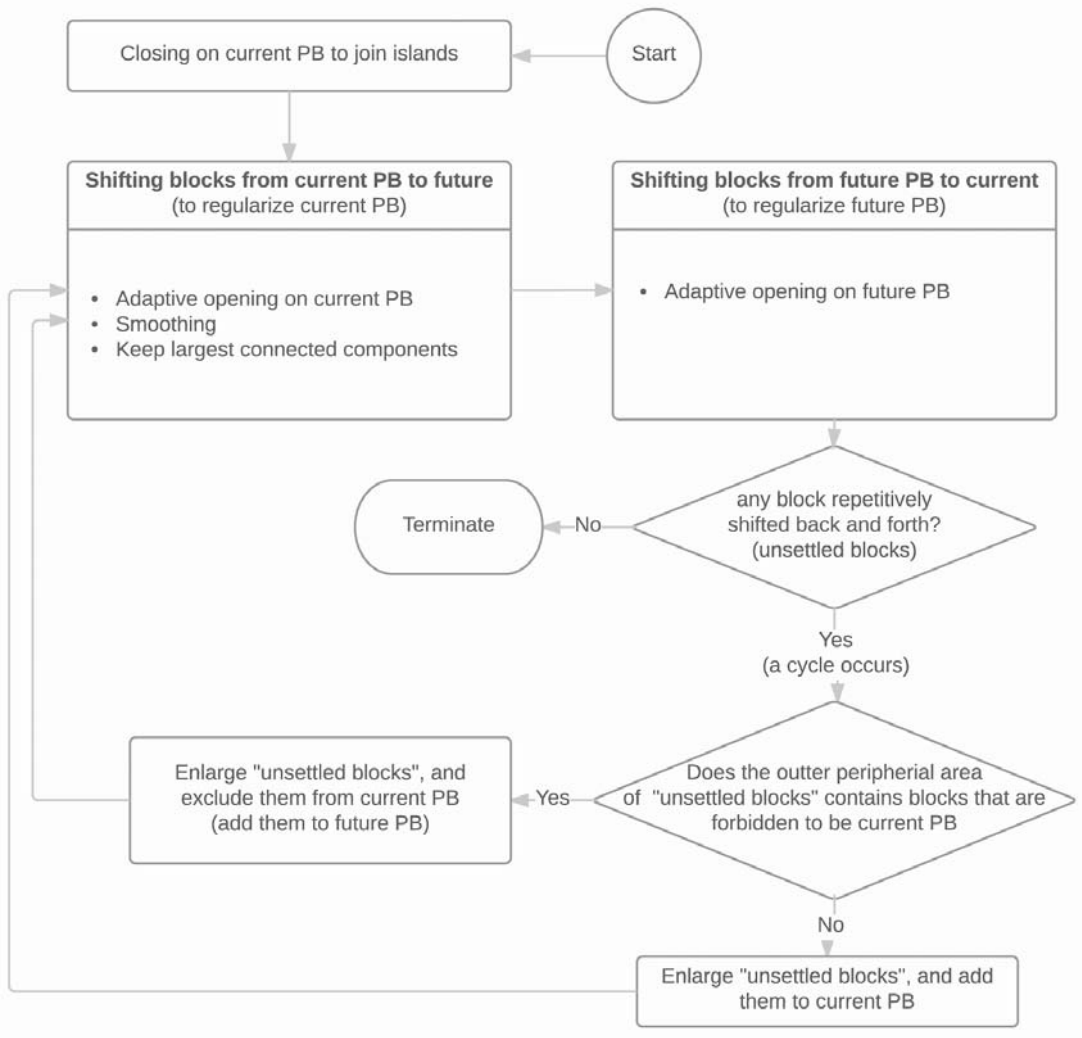

Figure 8—Flow chart of the procedures of modification on a bench (Algorithm [9])

and Tarjan, 1973) . Two cubic blocks can be considered to be connected if they have a shared face. The Conn-Comp identifies the isolated components. The largest connected component is kept; the smaller ones are postponed to later pushbacks. The continuity should be examined not only in 3D, but also in 2D on each level, to avoid an isolated set of blocks on the same level being allocated to the same pushback. The procedure to maintain continuity (KeepLargeConnComp) is described in Algorithm [7].

Synchronizing new geometric operators

The geometric tools described above control the constraints of width, smoothness, and continuity respectively for one bench of one single pushback. The following sequence of operations is adopted: (1) control the width; (2) smooth (by OpenSmoothing) the pushback edge; (3) keep the largest connected component. The sequence is selected so as to avoid posterior operations altering the previously fulfilled constraints. The three procedures generally remove blocks from the PB. Hence, the 'KeepLargeConnComp' simply removes the disconnected components, and does not change the established width and smoothness. Also, the opening operator in smoothing usually removes the clusters narrower than NS that are not adjacent to previous pushbacks, like the case shown in Figures 7b to 7e. This does not modify the width constraints. The procedure is described in Algorithm [8], and is noted as ModifyMultiConstr.

Multiple pushbacks on a single level

The method to control the geometric constraints for multiple pushbacks is described. Recall that in our algorithm the pushbacks are sequentially generated. When modifying one specific pushback t, the blocks in the ultimate pit ($\mathfrak{B}^{1\to n_{PB}}$) can be clustered into three groups: previous pushbacks ($\mathfrak{B}^{1\to t-1}$), which include the earlier pushbacks; current pushback ($\mathfrak{B}^{t}$); and future pushback ($\mathfrak{B}^{t+1\to n_{PB}}$), *i.e.* the unplanned pushbacks in the ultimate pit. Obviously, the previous pushbacks are already treated and are feasible. For the current PB, modifications should ensure all the geometrical constraints are fulfilled. Also, it should not be ignored that the future PB, the unplanned part, needs also to fulfill the width constraint. Otherwise it can happen that when treating later phases, no valid geometry can be found.

Algorithm [9], noted as 'ModifyBenchGeometry', describes the procedure on a 2D phase bench image. The flow chart is shown in Figure 8. The algorithm includes first a closing operation, in order to join isolated clusters and form a solid area. The closing also has a smoothing effect on the current PB. Then, we apply the geometric functions iteratively on current and future pushbacks, until both of them satisfy all the constraints. For current and future pushbacks, different operations are used. First, the function ModifyMultiConstr (Algorithm [8]) is performed on the current pushback, to make it satisfy the constraints of width, smoothness, and continuity. Then, for future phases, the adaptive opening is operated, because only the width constraint needs to be maintained for the future phase. The iteration essentially shifts blocks repetitively between current and future pushbacks. When operating on current pushbacks, excessive blocks are removed and postponed to future pushbacks, leaving the the current pushback feasible. Similarly, when modifying the future pushback, the removed blocks are moved to constitute the current one. Sometimes, the shifting may not find feasible configuration for both sets of current and future pushbacks, *i.e.* a cluster of blocks (note

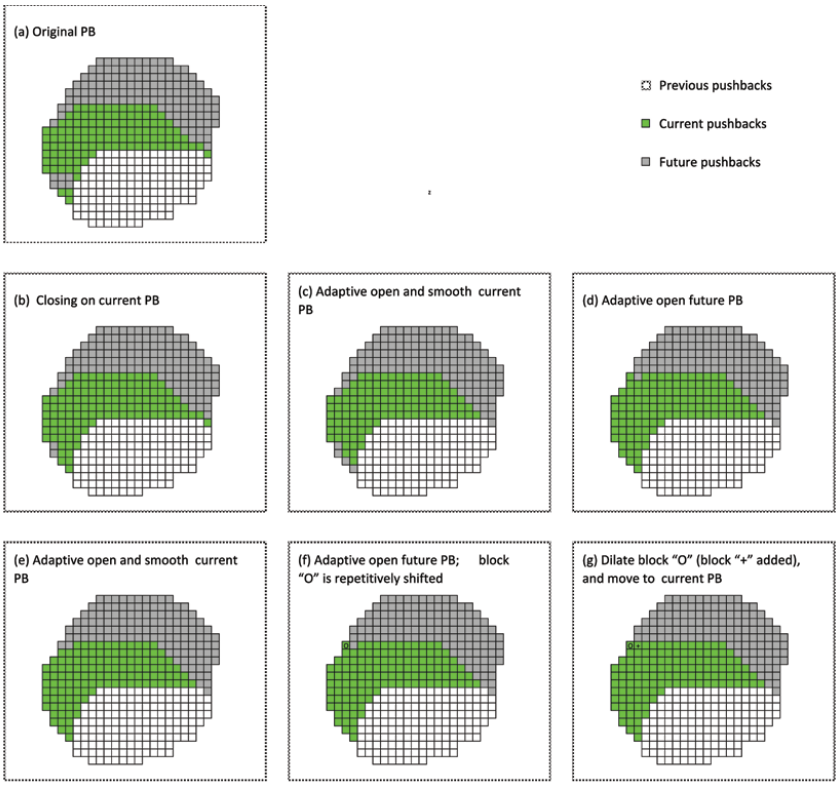

Figure 9—Step-by-step illustration of evolution of pushback in Algorithm [9] with TW = 5, AW = 5. Procedure goes from (a) to (g) to gradually achieve a practical pushback bench

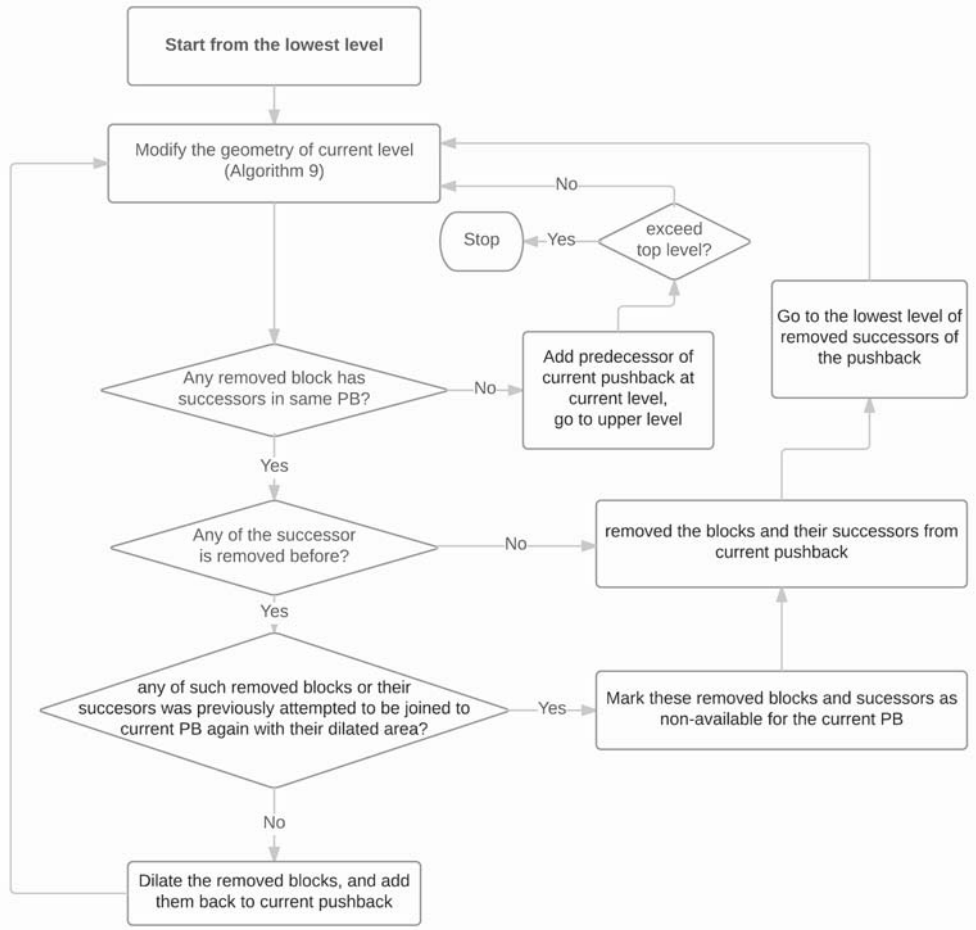

Figure 10—Flow chart of procedure for modifying the geometry of a single pushback (Algorithm [10]

as $\mathfrak{B}_k^{unsettled}$) is shifted back and forth, and cannot be accepted by either set. This is because the repeated operations change shapes in the same fashion and lack flexibility. In this case, two choices are available: (1) enlarge such cluster and append it to the current pushback, or (2) aggregate neighbouring blocks from the current pushback to enlarge the future pushbacks. The second choice is selected if any of $\mathfrak{B}_k^{unsettled}$ is forbidden from appearing in the current pushback t, otherwise the first choice is applied. The reason a block is banned from pushback t is that some of its predecessors are excluded at upper levels.

Figure 9 illustrates a step-by-step evolution of the pushback bench in Algorithm [9]. Figure 9a shows the original pushbacks, where green blocks stand for the current PB, the white ones for the previous PB, and the grey ones for the future PB. First, we run closing on the current PB, and the isolated blocks are joined (Figure 9b). Next, apply procedure ModifyMultiConstr (Algorithm [8]) on the current PB to make it feasible (see Figure 9c). Then, use adaptive opening on the future PB, to make it wide enough, and move the narrow clusters (grey blocks at left-bottom of Figure 9c) to the current PB. This obtains the result in Figure 9d. After that, repeatedly applying geometrical operations on the current and future PB, obtains Figures 9e and 9f, respectively. It can be seen that a block marked as 'O' is shifted back and forth and cannot be settled. So, we dilate the blocks 'O' inside the union of current and future PBs, then move the dilated block set (block 'O' and '+') to the current PB, and obtain Figure 9g. The procedure ends up with current and future PB both satisfying the geometric constraints.

3D modification of single pushback

To create a pushback satisfying the three new geometrical constraints at all levels and keeping the slope constraints, we propose Algorithm [10], with the flow chart shown in Figure 10. The procedure essentially repeats the 'ModifyBenchGeometry' procedure (Algorithm [9]) level by level, from bottom to top. When generating the t^{th} pushback, these operations result in two effects: (1) delaying some blocks from pushback t to later, and (2) bringing some blocks forward to pushback t. Therefore, after the morphological operations, the precedence relationship should be accounted for. Specifically, if a block is brought forward to pushback t, its predecessors in future pushbacks should be moved to pushback t as well, in order to ensure the accessibility of the block (Figure 11a). Otherwise, if a block is delayed, its successors should also be delayed (Figure 11b), as the blocks at lower levels are no longer accessible. If any of its successors are delayed, the procedure will go back to the lowest level of the delayed block, and redo Algorithm [9]. Sometimes, the delayed successors may be recovered by the geometrical operations at these lower levels, thus a cycle can occur. When a cycle is detected, the delayed blocks are dilated and added back to pushback t. The dilation is repeated a few

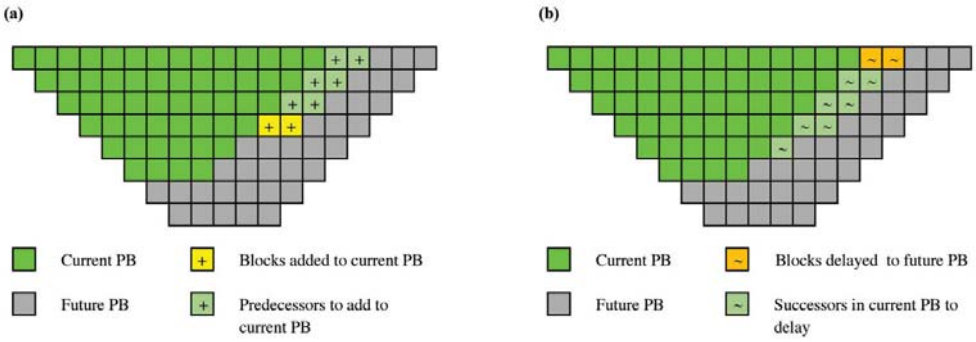

Figure 11—Synchronization of slope constraint and new geometrical constraints. (a) Blocks moved from future PB to current PB (yellow) must be accompanied by their predecessors in the future PB (dark green). (b) Blocks moved from current PB to future PB (orange) must go with their successors in the current PB (dark green)

times if necessary to try to break the cycle. If after a few dilations the cycle remains, the blocks in question are expelled from pushback t and added to a Tabu list, which is sent to the geometric operators so as to prohibit appending these blocks again to pushback t.

Main algorithm: modified parametric maximum flow

To achieve our goal of generating practical pushbacks with all geometrical constraints fulfilled, we need a high-level algorithm that utilizes Algorithm [10] to create multiple feasible pushbacks. We introduce Algorithm [11] for doing this. Since the structure of Algorithm [10] requires a pushback at earlier stages to be feasible, applying it on several nested pits simultaneously will not necessarily create multiple pushbacks with feasible geometry, nor guarantee satisfaction of resource constraints. Therefore, Algorithm [11] is designed to create pushbacks sequentially, from the first to last. When generating a new pushback, previous pushbacks are considered to be mined, so that modification only works on unplanned blocks. We use max-flow to create a parametric pit as an initial pit to be modified by Algorithm [10]. The modified pushback is then checked to assure the fulfillment of the production capacity constraints. A pushback that satisfied the constraints will be accepted; otherwise, it will be abandoned, then the price parameter will be adjusted and the max-flow and modification procedure repeated until the capacity requirement is met. The definition of resource constraints here can be very flexible, and the selection can depend on the specific application case. Here, for simplicity of description, we use only the ore tonnage constraint.

Algorithm [11] without geometrical modification (step 9) outlines a variant of the nested shells method, which is referred as 'successive max-flow' in the text above. This is similar to Whittle's nested shell solution in terms of selecting pit shells to match resource constraints. but works in an automatic way. We use it as a comparative method in following case studies.

Test results and discussion

The proposed algorithm is tested with two deposit models, one synthetic and one real. The goals of the test are to (1) evaluate the fulfillment of the new geometrical constraints in the created pushbacks, (2) analyse the variation of tonnage and size of pushbacks before and after geometrical modification, (3) assess the change of profit due to imposing new geometrical constraints, comparing with successive max-flow method, and (4) evaluate the computation time. The descriptions of testing data and design parameters are listed in Table I. The ultimate pits in the tests are created by a maximum flow algorithm and then modified by the geometric operators to ensure sufficient smoothness and enough width at pit bottom.

The first test data is from an artificial deposit created by FFTMA (Fast Fourier Transformation Moving Average) geostatistical simulation method (Ravalec, Noetinger, and Hu, 2000). The model contains 134 × 134 × 47 blocks. The unit block is 15 m × 15 m × 15 m. Pushback design uses the unique slope angle of 45° over the domain, and target width of 90 m, *i.e.* six blocks. Auxiliary width control parameter AW is 135 m (*i.e.* nine blocks). The smoothing factor NS adopts four blocks. The final pit is divided into five PBs. The tonnages of ore (blocks with positive profit) in each pushback are constrained to lie between 11.7 to 17.6 Mt (*i.e.* between 11 556 and 17 383 ore blocks at 3 t/m^3). Note that the ore tonnage range is flexible and should be adjusted considering the capacity tolerance of processing plants and the possible use of one or more stockpiles.

The second test data is from a real copper mine; the name and location are undisclosed for confidentiality reasons. A part of the deposit was previously mined, and pushbacks need to be designed for the remaining material. The testing data consists of 81 × 63 × 41 blocks, with a block size of 10 m × 10 m × 10 m. The slope is 45° over the domain, the target width is 70 m, *i.e.* seven blocks wide. Auxiliary width control parameter AW is 100 m (*i.e.* 10 blocks). The smoothing factor NS is five blocks. The ore blocks are sent to a single mill. The mining production plan is divided into six periods. The tonnages of ore in each pushback are

Table I

Testing data and parameters of pushback design

Parameter	Data 1	Data 2
Number of blocks	134 × 134 × 47	81 × 63 × 41
Unit block size (m)	15 × 15 × 15	10 × 10 × 10
TW (blocks)	6	7
AW (blocks)	9	10
NS (blocks)	4	5
Resource constraints in each PB (Mt)	[11.7, 17.6]	[6.0, 11.0]
Number of PBs	5	6

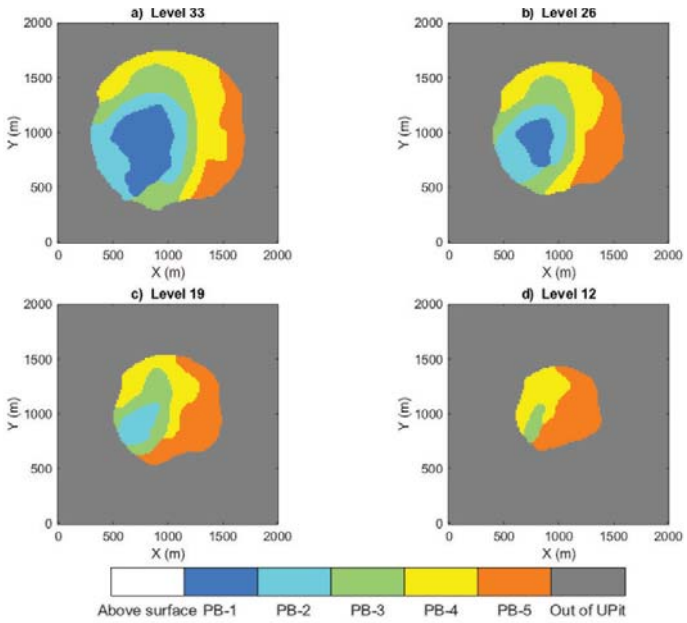

Figure 12—Case 1, automatically generated pushbacks plan view on level 33, 26, 19, and 12. Larger level numbers denotes higher elevation

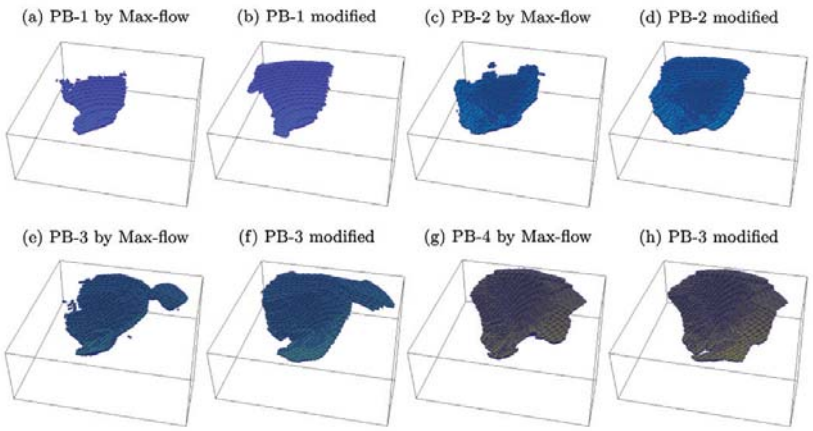

Figure 13—Case 1, comparison of modified pushbacks and original in 3D. Modified pushbacks show more continuity and smoothness

constrained to lie between 6.0 and 11.0 Mt *(i.e.* between 2000 and 3667 ore blocks at 3 t/m^3).

Geometric constraints, NPV, and tonnage

For the calculation of NPV, we first create a simple block sequence in each pushback and then discount the value of each block according to its sequence number. The block sequencing mimics the actual mining sequence, with three levels of precedence: (1) the blocks in an earlier pushback precede those in later pushbacks; (2) in one pushback, the blocks on higher bench levels are extracted before those at lower levels; (3) on each bench, the blocks are mined from east to west. The discount period is the time required to mine a single block (ore or waste). The discount rate for each block is 1.259×10^{-5}. The UPit contains 37 858 blocks. The discount factor for the last block in the UPit is $1/(1 + 1.259 \times 10^{-5})^{37858} = 0.62$. The (impractical) pushbacks generated by the nested shells method inside the same UPit are computed to provide a reference NPV. Note that these PBs do not respect the constraints of width, smoothness, and continuity. Hence, the reference NPV cannot be reached in practice. It is simply used as an indicator.

Figures 12 and 15 display the generated pushbacks on selected levels for the two cases. As is shown, the new geometrical constraints are all satisfied in the generated pushbacks. Most areas of the pushback benches are wider than the target minimum width. The pushback boundaries are regular and have smooth transitions with the pit of earlier periods. Also, each pushback has a single continuous component. In comparison, the pushbacks using the successive max-flow method do not show these desirable properties (shown in Figures 13 and 16). Those pushbacks are not mineable, as they present many isolated parts and are too irregular to be practical, especially in the real case no. 2. Figure 14 (for case 1) and Figure 17 (for case 2) show the change of the third pushback on different levels. In case 1, on level 20 (Figures 14a and 14b), the narrow bench is broadened to the target width, due to the effect of dilation. A

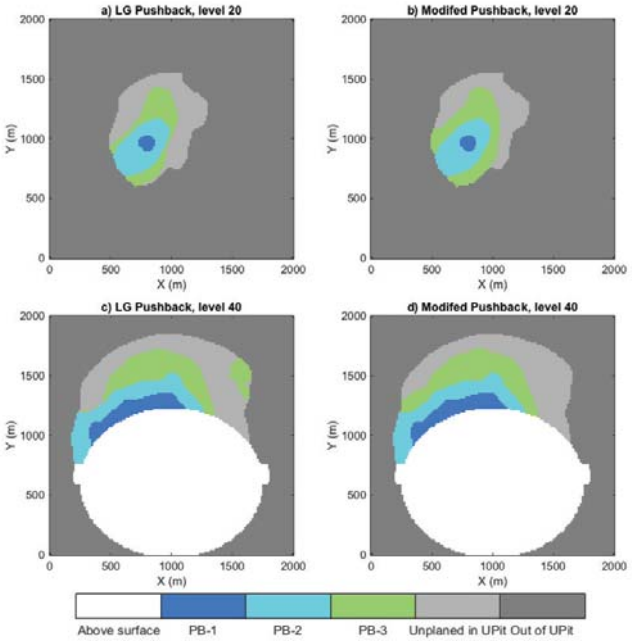

Figure 14—Case 1, comparison of LG pushback (a and c) and modified pushback (b and d) when modifying the third pushback (in light green). The narrow bench in (a) is widened in (b). The isolated green satellite zone in (c) disappears in (d)

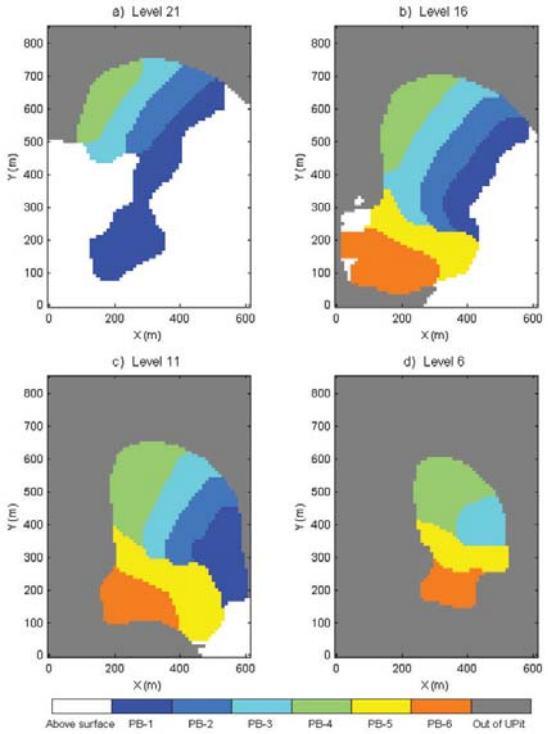

Figure 15—Case 2, automatic generated pushbacks plan view on levels 6, 11, 16, and 21. Larger level numbers denotes higher elevation

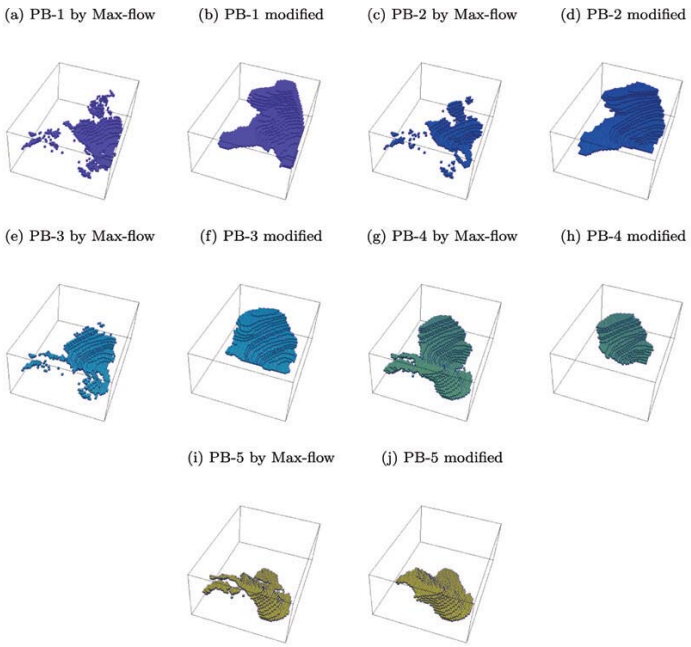

Figure 16—Case 2, comparison of modified pushbacks and original in 3D. The modified PBs become more cohesive, smoother, and regular. All isolated blocks or areas are filtered out

similar effect can be seen on level 17 in case 2 (Figures 17c and 17d). On level 40 of case 1, the smaller isolated green areas of Figure 14c disappear in Figure 14d. A similar effect appears in case 2 level 10 (Figures 17a and 17b). Also, the larger cluster with irregular boundary in Figure 14a is smoothed.

Ore tonnages of modified pushbacks are plotted in Figure 18 along with the relative change in ore tonnage compared to the initial max-flow pit. Note that the capacity constraints are not applied on the max-flow pit as they are the solutions used to initiate our PB, which are the ones constrained by the processing capacity. The last pushback is not shown as it contains only the residual material, the ore tonnage for which does not cover an entire period. The application of the geometric operators globally enlarged the initial max-flow. For case 1, modified pushback ore tonnages are increased by 13% to 55% compared to the initial parametric pits obtained

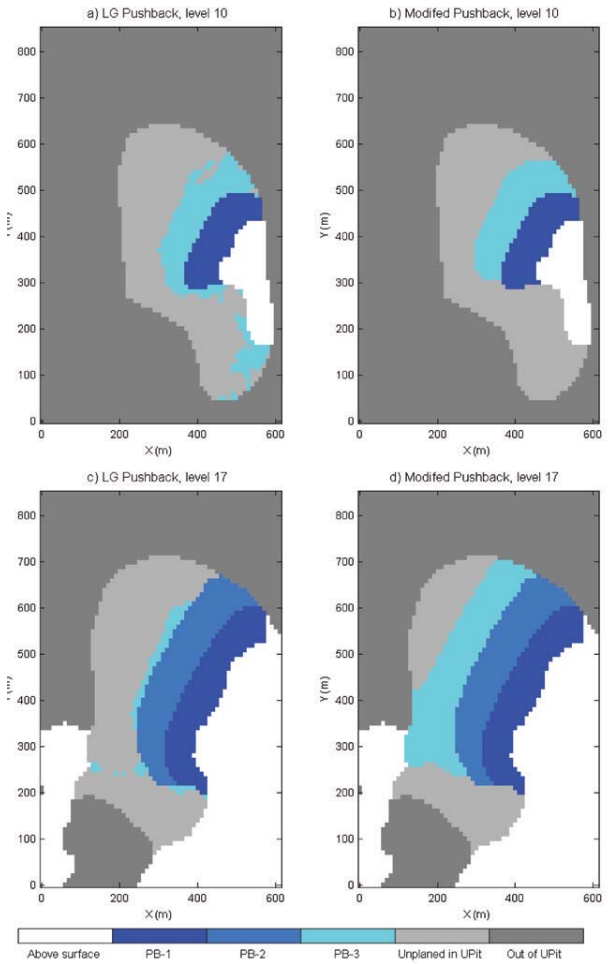

Figure 17—Case 2, comparison of LG pushback (a and c) and modified pushback (b and d) when modifying the third pushback (in cyan). The irregular boundary in (a) is smoothed in (b) and small disconnected components are removed. Narrow benches in (c) are broadened in (d)

after 'mining' the previous PB. For case 2, the tonnage increase reaches 50% to 166%. The increase is mostly due to dilation applied at lower levels that requires appending a large number of predecessors at upper levels. One exception is the fourth pushback in case 2, where the tonnage is reduced by 46%. As shown in Figures 18a and 18c, the ore tonnages of the first five pushbacks are well within the capacity thresholds. The final pushback has insufficient tonnage feed, but this will not cause a practical problem, as it can be considered to be the production for a shorter period until the end of the mine life.

Figure 19 shows the NPV per ton of the different PBs. Note that the NPV per ton is computed over a substantially larger tonnage for the modified PB than for the successive max-flow PB, so it is difficult to directly compare these results. However, over the life of the mine, and then for the same UPit, the modified PB NPVs diminish compared to those obtained with the (non-mineable) successive max-flow PB, by 0.5% ($4.18 billion *vs.* $4.26 billion) for case 1, and by 7.3% ($685million *vs.* $739 million) for case 2. As expected, imposing more constraints reduces the NPV. Note, however, that in case 2, the 7.3% NPV reduction is due mostly to the first three PBs, where the successive max-flow PBs are clearly non-mineable (see Figure 16).

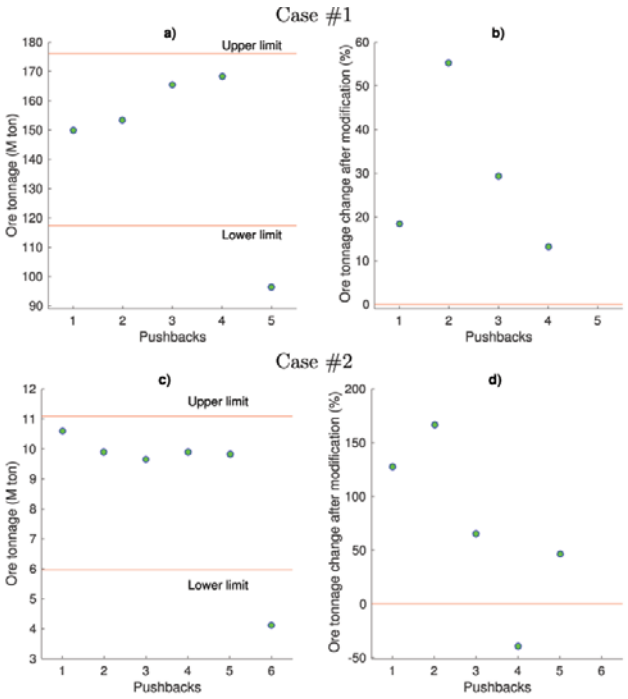

Figure 18—(a) and (c) Ore tonnage in modified pushbacks; (b) and (d) relative change of pushback ore tonnage after geometrical modifications

The NPV of the new method could be improved in a number of ways. First, the sequencing within each PB could be improved easily compared to the ad-hoc simple sequencing used here. Secondly, local search methods could be used to try to perturb the current PB definition by exchanging sets of blocks at the boundaries between the different PBs while still enforcing the geometric constraints to keep all the PBs mineable. This method is currently under investigation.

To analyse the sensitivity of the method to the new constraints, pushbacks are generated for a set of different mining widths. For case 1, the TW varies from two to six blocks; for case 2, it varies from three to seven blocks. To ensure that total value of the pit is same for comparison, the UPit for each case is created with the largest TW, *i.e.*, six blocks for case 1 and seven blocks for case 2. We measure the NPV loss ratio relative to the successive max-flow method for these varying TWs, which is shown in Figure 20. It shows clearly that NPV decreases steadily with the increase of mining width.

In addition to the three new constraints introduced here, real-world pushback design also needs to take into account more requirements, such as ramp access and infrastructure constraints. These are detailed requirements that may impact the final pushback design on different scales. They are nevertheless difficult to measure in standard ways, unlike pit slope and mining width. Integrating the full set of design constraints and delivering automated designs is an area for further research.

Computational aspects

Figure 21 shows the main steps and associated variables in the proposed algorithm. Since the pushbacks are generated sequentially, the number of pushbacks scales linearly with

the computation time. For the definition of a given pushback, the computing time for maximum flow depends on the spatial distribution of values in the block model. The application of geometrical constraints works bench-by-bench from bottom to top, but possibly with many ups and downs due to the removal of blocks on the upper level that have successors at lower levels in the same pushback. The computing time depends on the geometry of the pushback created by maximum flow, the complexity of the contour of already-mined zones, and the boundary of the ultimate pit.

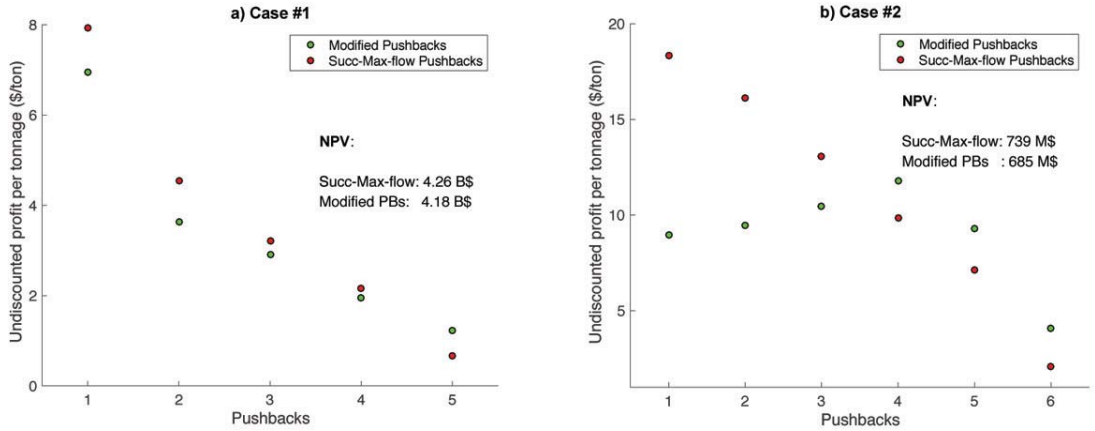

Figure 19—Comparison of average profit per ton in different pushbacks and NPV

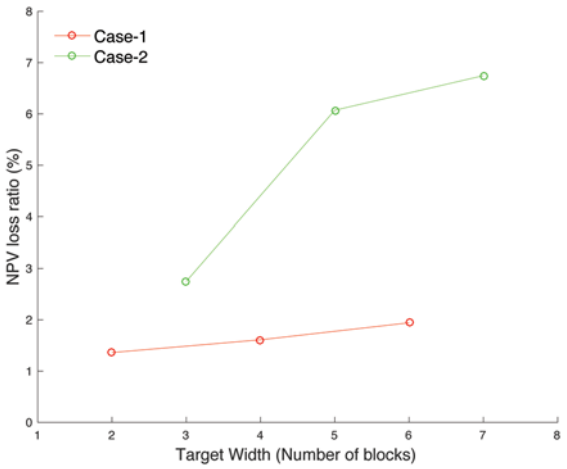

Figure 20—NPV loss ratio of geometrically constrained solution compared to successive max-flow solutions without constraints for different target mining widths. NPV loss ratio computed as 100 (NPVunconstrained-NPVconstrained) / NPVunconstrained)

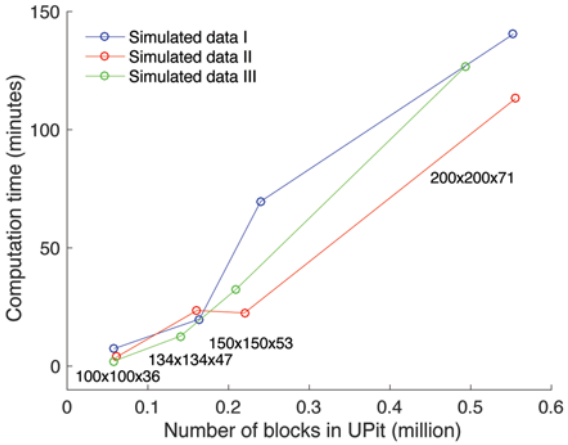

Figure 22—Computation time as a function of the block model size

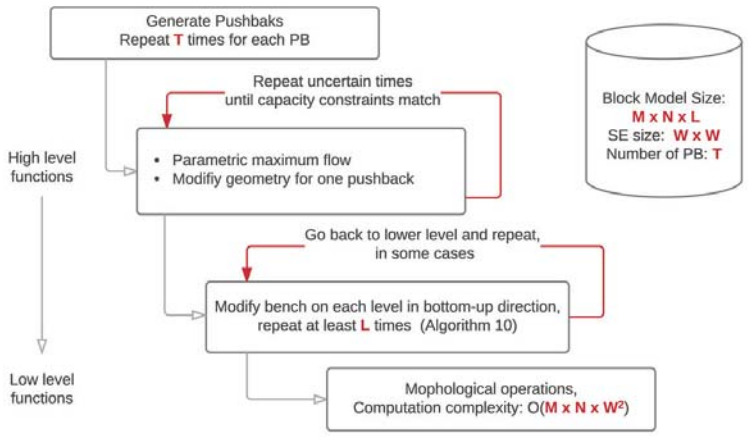

Figure 21—Main algorithm steps and variables affecting the computational efficiency

The bench modification utilizes a series of morphological operations. Typically, the computational complexity of morphological algorithms is (MNW^2) , where M and N are the dimensions of the block model in a horizontal plane, and W is the width of the structural element used in the operation. One can consider that between six and ten mining blocks usually suffice to create enough width for the equipment. Hence, the dominant terms for computing time are clearly the size of the deposit, M and N.

We used three simulated deposit of different sizes: 100 × 100 × 34, 134 × 134 × 47, 150 × 150 × 53, and 200 × 200 × 71. Figure 22 displays the computation time as a function of the size of the UPit for a fixed number of pushbacks. The design uses TW = 7 blocks. Tests were done on a laptop computer with Intel Core i5 2.5G CPU and 8 GB RAM. The programs were run in Matlab. Figure 22 shows that the program takes around 4 minutes to process a UPit with less than 100 000 blocks, and around 2 hours for a UPit with 550 000 blocks. Moreover, the computation time appears to globally scale quasi-linearly with the UPit size. This demonstrates that the algorithm is able to handle a medium-size block model in an affordable time, especially when compared to the time required for manual editing. Admittedly, processing a block model with more than 1 million blocks in the UPit would benefit from slight improvements to the current implementation of the method. One promising avenue is to use the more efficient implementation of morphological operations described in Dokládal and Dokládalová (2011), or simply to use a C++ compiled version or alike.

Conclusion

In this paper we propose a new algorithm to automatically generate mining pushbacks with practical geometries. The algorithm can manipulate the new geometrical constraints, including pushback bench and bottom width, smoothness, and continuity. A case study demonstrates that by reshaping the non-mineable initial pushbacks, one can obtain modified mineable pushbacks with marginal loss on the NPV value. The method is computationally efficient and has the potential to significantly contribute toward the automation of highly practical pushback designs.

Acknowledgments

This research was financed by NSERC Engage and Engage Plus Grants, Mitacs Accelerate, as well as Datamine Software Inc. and D. Marcotte NSERC research grant RGPIN-2015-06653. Two anonymous reviewers provided constructive suggestions for improving the draft.

References

Bai, X., Marcotte, D., and Simon, R. 2014a. A heuristic sublevel stope optimizer with multiple raises. *Journal of the Southern African Institute of Mining and Metallurgy*, vol. 114. pp. 427–434.

Bai, X., Marcotte, D., and Simon, R. 2013b. Underground stope optimization with network flow method. *Computers and Geosciences*, vol. 52. pp. 361–371. https://doi.org/10.1016/j.cageo.2012.10.019

Bai, X., Marcotte, D., and Simon, R., 2013c. Incorporating drift in long-hole stope optimization using network flow algorithm. *Proceedings. of the 36th International. Symposium on Application of Computers and Operations Research in the Mineral Industry*. (APCOM), Porto Alegre, Brazil. Costa, J.F., Koppe, J., and Peroni, R. (eds). Fundação Luiz Englert, Porte Alegre. pp. 391–400. https://doi.org/10.13140/2.1.3534.6880

Chandran, B.G. and Hochbaum, D.S. 2009. A computational study of the pseudoflow and push-relabel algorithms for the maximum flow problem. *Operations Research*, vol. 57, no.2. pp. 358–376. https://doi.org/10.1287/opre.1080.0572

Chilès, J.-P. and Delfiner, P. 1999. Geostatistics: Modeling Spatial Uncertainty. Wiley.

Consuegra, F.R.A. and Dimitrakopoulos, R. 2010. Algorithmic approach to pushback design based on stochastic programming: method, application and comparisons. *Mining Technology*, vol. 119. pp. 88–101. https://doi.org/10.1179/037178410X12780655704761

Datamine. 2014. NPV Scheduler. The complete strategic mine planning system. http:// www.dataminesoftware.com/npv-scheduler/

Deraisme, J., de Fouquet, C., and Fraisse, H. 1984. Geostatistical orebody model for computer optimization of profits from different underground mining methods. *Proceedings of the 18th APCOM Symposium*. London, UK. Institution of Mining and Metallurgy, London. pp. 583–590.

Dokládal, P. and Dokládalová, E. 2011. Computationally efficient, one-pass algorithm for morphological filters. *Journal of Visual Communication and Image Representation*, vol. 22. pp. 411–420. https://doi.org/10.1016/j.jvcir.2011.03.005

Goldberg, A.V. and Tarjan, R.E. 1988. A new approach to the maximum-flow problem. *Journal of the Association for Computing Machinery*, vol. 35. pp. 921–940.

Goodfellow, R. and Dimitrakopoulos, R. 2013. Algorithmic integration of geological uncertainty in pushback designs for complex multiprocess open pit mines. *Mining Technology,* vol. 122. pp. 67–77. https://doi.org/10.1179/147490013X13639459465736

Hochbaum, D.S. 2008. The pseudoflow algorithm: a new algorithm for the maximum-flow problem. *Operations Research*, vol. 56. pp. 992–1009. https://doi.org/10.1287/opre.1080.0524

Hochbaum, D.S. and Chen, A. 2000. Performance analysis and best implementations of old and new algorithms for the open-pit mining problem. *Operations Research*, vol. 48. pp. 894–914.

Hopcroft, J. and Tarjan, R. 1973. Algorithm 447: efficient algorithms for graph manipulation. *Communications of the Association for Computing Machinery*, vol. 16. pp. 372–378. https://doi.org/10.1145/362248.362272

Hustrulid, W. and Kuchta, M. 1995. Open Pit Mine Planning & Design: Fundamentals. Balkema.

Juárez, G., Dodds, R., Echeverría, A., Guzmán, J.I., Recabarren, M., Ronda, J., and Vila-Echague, E. 2014. Open pit strategic mine planning with automatic phase generation. *Proceedings of the Orebody Modelling and Strategic Mine Planning Symposium 2014*. Australasian Institute of Mining and Metallurgy, Melbourne. pp. 147–154.

Lerchs, H. and Grossmann, I.F. 1965. Optimum design of open-pit mines. *Transactions of the Canadian Institute of Mining, Metallurgy, and Petroleum*, vol. LXVIII. pp. 17–24.

Marcotte, D. and Caron, J. 2013. Ultimate open pit stochastic optimization. *Computers and Geosciences*, vol. 51. pp. 238–246. https://doi.org/10.1016/j.cageo.2012.08.008

Meagher, C., Dimitrakopoulos, R., and Vidal, V. 2015. A new approach to constrained open pit pushback design using dynamic cut-off grades. *Journal of Mining Science*, vol. 50. pp. 733–744. https://doi.org/10.1134/S1062739114040140

Nelis, G., Gamache, M., Marcotte, D., and Bai, X. 2016. Stope optimization with vertical convexity constraints. *Optimization and Engineering*, 2016, no. 4. pp. 1–20. https://doi.org/10.1007/s11081-016-9321-6

Ravalec, M., Noetinger, B., and Hu, L. 2000. The FFT Moving Average (FFT-MA) Generator: An efficient numerical method for generating and conditioning Gaussian simulations. *Mathematical Geology*, vol. 32. pp. 701–723. https://doi.org/10.1023/A:1007542406333

Serra, J.P. 1982. Image Analysis and Mathematical Morphology. Academic Press, New York.

Stone, P., Froyland, G., Menabde, M., Law, B., Rasyar, R., and Monkhouse, P. 2004. Blasor - blended iron ore mine planning optimisation at Yandi, Western Australia. *Proceedings of the International Symposium on Orebody Modelling and Strategic Mine Planning*. Australasian Institute of Mining and Metallurgy, Melbourne. pp. 285–288.

Whittle, D. 2011. Open-pit planning and design. *SME Mining Engineering Handbook.* Darling, P. (ed.), Society for Mining, Metallurgy and Exploration (SME) Inc., Littleton, CO. pp. 877–902.

Whittle, J. 1998. Four-X user manual. Whittle Programming Pty Ltd, Melbourne. ◆

Appendix

Algorithm 1: Dilating operation

```
Procedure Dilate(B_k, SE)
    Input: B_k, SE
    Output: B_k^new
    B_k^new ← {x + s | x ∈ B_k, s ∈ SE}
End
```

Algorithm 2: Eroding operation

```
Procedure Erode(B_k, SE)
    Input: B_k, SE
    Output: B_k^new
    B_k^new ← {x | ∀s ∈ SE, x + s ∈ B_k}
End
```

Algorithm 3: Opening operation

```
Procedure Open(B_k, SE)
    Input: B_k, SE
    Output: B_k^new
    B_k^new ← call Erode(B_k, SE)
    B_k^new ← call Dilate(B_k^new, SE)
End
```

Algorithm 4: Closing operation

```
Procedure Open(B_k, SE)
    Input: B_k, SE
    Output: B_k^new
    B_k^new ← call Dilate(B_k, SE)
    B_k^new ← call Erode(B_k^new, SE)
End
```

Algorithm 5: Adaptive Opening

```
Procedure AdaptiveOpen(B_k^t, TW, AW) /* Modify one bench of pushback to have practical width */
    Input: B_k^t, TW, AW
    Output: B_k^{t,new}
    m ← TW/(AW + 1)  /* gradient of diminishing of w */
    B_k^{t,new} ← call Open(B_k^t, SES(TW))  /* The area wider than TW */
    for d from 1 to AW do  /* For different distance to the wide area */
        B^{wide,ext} ← call Dilate(B_k^{t,new}, SES(1))  /* extend wide area */
        B^{wide,ext} ← B^{wide,ext} ∩ B_k^t  /* get the extended wide area in original pushback set */
        w = floor(AW + 1 − d) * m)  /* renew acceptable width in sub-wide area */
        B_k^{t,new} ← call Open(B^{wide,ext}, SES(w))  /* update the accepted sub-wide area */
    end
End
```

Algorithm 6: Smooth the edge of a pushback

```
Procedure OpenSmoothing(B_k^t, B_k^{1→t−1}, NS)
    Input: B_k^t, B_k^{1→t−1}, NS
    Output: B_k^{t,new}
    B_k^{1→t} ← B_k^{1→t−1} ∪ B_k^t
    B_k^{1→t,new} ← call Open(B_k^{1→t}, SES(NS))  /* Opening on the union of current and previous pushbacks */
    B_k^{t,new} ← B_k^{1→t,new} \ B_k^{1→t−1}
End
```

Algorithm 7: Keep largest Conn-Comp of a PB on one level

```
Procedure KeepLargeConnComp(B_k^t)
    Input: B_k^t
    Output: B_k^{t,new}
    Search the Conn-Comp in B_k^t
    B_k^{t,new} ← The largest Conn-Comp in B_k^t
End
```

Algorithm 8: Modify a pushback bench to fulfil multiple constraints

```
Procedure ModifyMultiConstr(B_k^t, B_k^{1→t−1}, TW, AW, NS)
    Input: B_k^t, B_k^{1→t−1}, TW, AW, NS
    Output: B_k^{t,new}
    B_k^{t,new} ← call AdaptiveOpen(B_k^t, SES(TW), AW)
    B_k^{t,new} ← call OpenSmoothing(B_k^{t,new}, NS)
    B_k^{t,new} ← call KeepLargeConnComp(B_k^{t,new})
End
```

Algorithm 9: Modify pushbacks geometry at one bench

```
Procedure ModifyBenchGeometry(B_k^t, B_k^{1→t−1}, B_k^{1→n_PB}, TW, AW, NS)
    Input: B_k^t, B_k^{1→t−1}, B_k^{1→n_PB}, TW, AW, NS
    Output: B_k^{t,new}
    B_k^{t→n_PB} ← B_k^{1→n_PB} \ B_k^{1→t−1}
    B_k^{t,new} ← call Close(B_k^t, SES(TW))  /* Join the small islands in current phase */
    B_k^{t+1→n_PB,new} ← B_k^{t→n_PB} \ B_k^{t,new}  /* update future pushback */
    B_k^{unsettled} ← ∅
    repeat
        /* Shift blocks from current pushback to future: step 6 */
        B_k^{t,new0} ← call ModifyMultiConstr(B_k^{t,new}, B_k^{1→t−1}, TW, AW, NS)
        /* Shift blocks from future pushback to current: step 7-9 */
        B_k^{t+1→n_PB,new} ← B_k^{t→n_PB} \ B_k^{t,new0}  /* future pushback */
        B_k^{t+1→n_PB,new1} ← call AdaptiveOpen(B_k^{t+1→n_PB,new}, SES(TW), AW)
        B_k^{t,new1} ← B_k^{t→n_PB} \ B_k^{t+1→n_PB,new1}
        B_k^{unsettled,new} ← B_k^{t,new0} \ B_k^{t,new1}  /* blocks shifted back from future to current, cycle occurs if there is any */
        if B_k^{unsettled,new} \ B_k^{unsettled} = ∅ then
            B_k^{unsettled,large} ← enlarged B_k^{unsettled,new}
            if any B ∈ B_k^{unsettled} is forbidden at t then
                B_k^{t,new} ← B_k^{t,new} \ B_k^{unsettled,large}
            else
                B_k^{t,new} ← B_k^{t,new} ∪ B_k^{unsettled,large}
            end
        end
        B_k^{unsettled} ← B_k^{unsettled,new}
    until B_k^{unsettled} = ∅
End
```

Algorithm 10: Modify the geometry of single pushback

```
Procedure ModifySinglePushback
    Input: B^t, B^{1→n_PB}, B^{1→t−1}, TW, AW, NS  /* Current pushback, Ultimate pit, Previous pushbacks, Targets width, Auxiliary width parameter, Smooth factor */
    Output: B^t  /* Modified current Pushbacks */
    k ← minimum level of B^t
    repeat
        B̈_k^t ← call ModifyBenchGeometry(B_k^t, B_k^{1→t−1}, B_k^{1→n_PB}, TW, AW, NS) /* Apply geometric operation on the pushback of current level */
        B^{rm} ← B_k^t \ B̈_k^t if succ(B^{rm})^t = ∅ then
            B^t ← B^t ∪ (pred(B_k^t) \ B^{1→t−1})  /* Add predecessors of current pushback at level */
            k ← k + 1  /* go to upper level */
        else
            if any blocks of succ(B^{rm})^t previously was removed then
                if B^{rm} was enlarged before then
                    B^{rm} ← enlarged B^{rm}
                    B^t ← B^t ∪ B^{rm}
                else
                    B^t ← B^t \ succ(B^{rm})^t
                    B^{exclusion} ← B^{exclusion} ∪ succ(B^{rm})
                    k ← lowest level of succ(B^{rm})^t  /* go to the lowest level of the removed successors */
                end
            else
                B^t ← B^t \ succ(B^{rm})^t
                k ← lowest level of succ(B^{rm})^t  /* go to the lowest level of the removed successors */
            end
        end
    until k > k_max
End
```

Algorithm 11: Main algorithm to generate pushbacks

```
Procedure ModifiedPara-Max-Flow
    Input: Economic block model, UPit and other parameters
    Output: Pushbacks: B^{t|t=1,...,n_PB}
    Construct graph G
    for t from 1 to n_PB − 1 do
        T_ore^t ← 0  /* ore tonnage of pushback t */
        Exclude previous pushbacks (B^{1→t−1}) from graph G
        repeat
            Adjust price and update accordingly the profit weight in the graph G
            Apply maximum flow on graph G, get current pushback: B^t
            Modify the geometry of pushback B^t to be feasible, get updated B_k^t (Algorithm 10)  /* The comparative method works without this line */
            Update T_ore^t for the new pushback B^t
        until T_ore^t satisfies mill constraints
    end
End
```

http://dx.doi.org/10.17159/2411-9717/2018/v118n5a9

A new approach for predicting bench blasting-induced ground vibrations: a case study

by X. Hu and S. Qu

Synopsis

The paper describes efforts to find an effective and reasonable method for predicting ground vibrations induced by bench blasting. In order to reflect the effect of actual topography and geological conditions, two concepts – the equivalent path and equivalent distance – are introduced to take into account the effects of topographic features and properties of the rock and rock mass. An equivalent–path-based equation, the EPB equation, is thus proposed, which takes into account the impacts of maximum charge quantity and explosion heat of the explosive, acoustic impedance of the rock, integrity coefficient of the rock mass, as well as the equivalent distance. A total of 48 field seismic monitoring tests were carried out and the constants of the EPB equation were determined. Comparison of the predicted peak particle velocity values with those measured shows that the average error of the prediction is much lower, demonstrating the applicability of the EPB equation in the prediction of bench blasting-induced ground vibrations.

Keywords

bench blasting, ground vibration, peak particle velocity, prediction, equivalent path, equivalent distance.

Introduction

Drill-and-blast is the most common method in rock excavation engineering. Usually, these blasting operations are performed at sites close to inhabited places or factory premises(Xia *et al.*, 2014), where ground vibrations induced by blasting may have an adverse effect on nearby buildings or facilities that need to be protected, such as slopes of open pit mines. For this reason, it is essential to make an acceptably accurate prediction of the vibrations, and therefore, define a safe charge of explosives during blasting (Kuzu, 2008; Nateghi, 2011). The prediction of ground vibrations induced by blasting is always a topic of general interest and numerous investigations have been carried out. Some commonly used and representative formulae are:

Sadaovsk's formula (Li, Ling, and Zhang, 2009):

$$\mathrm{PPV} = K\left(Q^{1/3}/R\right)^{\alpha} \quad [1]$$

USBM (Duvall and Fogelson) formula (Ambraseys and Hendron, 1968):

$$\mathrm{PPV} = K\left(Q^{1/2}/R\right)^{\alpha} \quad [2]$$

Langefors-Kihlstrom formula (Langefors and Kihlstrom., 1963):

$$\mathrm{PPV} = K\left(Q^{2/3}/R\right)^{\alpha} \quad [3]$$

Indian Standard formula (Bureau of Indian Standards, 1973):

$$\mathrm{PPV} = K\left(Q^{3/2}/R\right)^{\alpha} \quad [4]$$

where PPV stands for the peak particle velocity at the measuring point, Q is the maximum explosive charge per delay period, K and α are the site constants which are related to the blasting condition and the rock features, and R is the distance between the explosion source and the measuring point. As mentioned above, there is a general form:

$$\mathrm{PPV} = KQ^{\beta}/R^{\alpha} \quad [5]$$

where β is another constant. The equations express the correlation between the vibration intensity, explosive quantity, and the distance. However, because of factors relating to the explosion source, the terrain, and geological conditions, the results from the above formulae may deviate substantially from the measured values, and fall outside the permissible error range (Nateghi, 2011; Khandelwal and Singh, 2007).

Many studies have been conducted in order to find an effective method for the prediction of blasting vibration. For example, Bouckovalas and Papadimitriou (2005 explored the effects of slope geometry, predominant excitation frequency and duration, as well as the dynamic soil properties on seismic ground motion. They found that topography may lead to intense amplification

* *University of Science and Technology Beijing, China.*

© *The Southern African Institute of Mining and Metallurgy, 2018.* *ISSN 2225-6253. Paper received Mar. 2017; revised paper received Jun. 2017.*

or suppression at neighbouring points behind a slope crest, and a general trend of amplification near the crest and suppression near the toe of the slope seems to hold for the horizontal motion. Nguyen and Gatmiri, (2007 conducted a numerical study on the 2D scattering of seismic waves by local topography using the direct boundary element method, and found that local topographic irregularities play an important role in the modification of seismic ground motion at the irregular features themselves and in the neighbourhood. Kuzu, 2008 showed the effect of geological factors in predicting the level of blast-induced ground vibrations. Fiore (2010) focused on the evaluation of seismic site effects and their relation to the local topographical slope and proposed an empirical method to estimate the seismic amplification in the regular slope far from the crest and valley zones. Nateghi (2011) described ground motions induced by blasting near underground and surface concrete structures during the construction of upper Gotvand Dam, analysed the effects of different rock formations, different detonators and explosives, and evaluated the relationship and the predicted influence on neighbouring concrete structures according to the USBM method. Trip, Kontoe, and Wong (2013) analysed the effects of slope topography on ground motion in deep soil layers and found that the topographic amplification and soil layer amplification effects interact, suggesting that in order to accurately predict topographic effects, the two factors should be considered together. Some scholars have revised the formulae on the basis of Sadaovsk's formula (*e.g.* Song and Xiao,2010). With the development of computing science, an artificial neural network (ANN) method has also been increasingly used in PPV prediction in recent years (Amnieh, Mozdianfard and Siamaki, 2010; Amnieh, Siamaki, and Soltani, 2012,).

In the present research we aimed to find a new method for prediction of PPV for ground vibrations induced by bench blasting. In order to achieve this aim, firstly, the influencing factors of bench blasting vibration from two aspects, including the explosion source factors and the propagation path factors, were analysed. Then, a new formula for predicting bench blasting induced ground vibrations was established based on the analysis. Finally, the accuracy and rationality of this method were analysed and validated by statistical analysis and a comparative approach.

Analysis and discussion of influencing factors

Factors associated with the explosion source

It is globally recognized that the PPV increases with the maximum explosive charge quantity Q fired per delay in multi-hole millisecond delay bench blasting. In the governments regulations (People's Republic of China, 2014) and in the empirical equations mentioned (Li, Ling, and Zhang, 2009; Ambraseys and Hendron, 1968; Langefors and Kihlstrom, 1963; Bureau of Indian Standards, 1973), the Q value has been taken as a key parameter in estimating blasting-induced ground vibrations. Ground vibration arises from the energy released by the detonation of explosives. The strength of commercial explosives differs greatly from type to type. Therefore, it seems reasonable, and indeed necessary, to take the energy release properties of the explosives into account. In other words, it may be useful to take the explosive charge quantity Q and energy release of the explosive simultaneously into consideration in order to ensure reliability of blasting vibration predictions.

An explosive is a chemical compound or mixture of compounds that undergoes a very rapid reaction when initiated, and little heat is lost by transmission and radiation before it generates seismic waves propagating outward. As a result, the detonation of an explosive charge can be considered as a constant volume process, and the explosion heat Q_V of an explosive at constant volume can be used to describe the influence of explosive energy capacity, so the relation between PPV and the total energy of explosive per delay can be expressed as:

$$\mathrm{PPV} = f\left(Q \cdot Q_V\right) \quad [6]$$

The propagation path of a seismic wave from blasting

Influence of topography on the propagation path

As shown in Figure 1, the topography in open pit mines usually consists of benches, slope, and pits, with limited flat ground surface. In the application of the above-mentioned empirical equations to a flat ground surface (Figure 2), the distance R is simply considered to be the length of the straight line from the explosive charge to the monitoring geophone at the measuring point.

However, as Figure 3 shows, when monitoring geophones are positioned on a slope over the pit or even at a point outside of the mine, the topography can be much more complex and it is likely that there is no straight line along which the seismic wave propagates to reach the geophone. Unfortunately, this situation often occurs, so an effective and usable definition of the distance from the blast to the measuring point is needed in this kind of topography.

Figure 1—Topography of an open pit mine

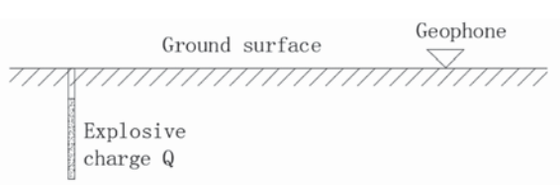

Figure 2—Diagrammatic sketch of seismic monitoring on a flat ground surface

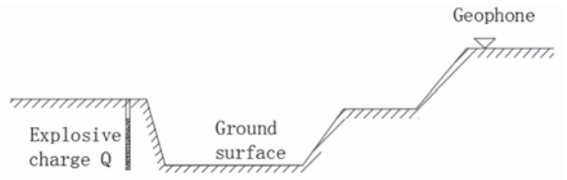

Figure 3—Diagrammatic sketch of seismic monitoring across a pit

As is shown in Figure 3, the seismic wave generated by detonation of the explosive charge Q will propagate under the ground surface to the measurement point but never passes through the atmosphere above the surface. We assume here that the shortest path through which the seismic wave can travel beneath the ground surface be used as the distance from the explosion source to the measuring point. If this assumption is valid, this minimum distance will function equivalently to the parameter R of the above-mentioned empirical equations in flat ground surface circumstances, and can thus be termed the 'equivalent distance'. Consequently, the path corresponding to the equivalent distance can then be defined as 'equivalent path' in a conceptive sense.

(1) Equivalent path on a bench-like surface

Benches are the main topographic features of open pit mines. For bench-like topography cases as shown in Figure 4, the equivalent path can be determined as follows.

1. Take the blast-hole centre P_0 of the maximum explosive charge as the starting point and draw a half-line l_0.
2. Take the straight line passing point P_0 and normal to the page as the axis, rotate l_0 under the ground surface towards the measuring point M, stop when l intersects the surface, mark the intersection point as P_1 and the length from P_0 to P_1 as R_0.
3. Then take the straight line passing through point P_1 and normal to the page as the axis, rotate l_1 (a half-line starting at point P_1) under the ground surface towards the measuring point M. Stop when it intersects the surface, and mark the intersection point as P_2 and the length from P_1 to P_2 as R_1.
4. Repeat the above procedures until l_i (a half-line starting at point P_i) reaches the measuring point M.

The series of straight-line segments P_0P_1, P_1P_2, P_2P_3,... is the so-termed 'equivalent path' and the equivalent distance can thus be defined as the sum of the straight-line segments from point P_i to point P_{i+1}, *i.e.*

$$R = \sum_{i=0}^{i=n} R_i, i = 0.12... \quad [7]$$

However, in accordance with the Huygens-Fresnel principle, the amplitude of seismic waves will decrease with the intersection angle θ_i, the angle of the wave propagation direction to the ground surface, as shown in Figure 4. The Kirchhoff obliquity factor can be expressed as (Gwenaël, Judicaël, and Guillaume, 2011):

$$K = (\theta_i) = (1 + \cos\theta_i)/2, i = 0,1,2,3... \quad [8]$$

To take the influence of Kirchhoff's obliquity factor into consideration, Equation [7] can be rewritten as

$$R = \sum_{i=0}^{i=n} [R_i / K(\theta_i)] = \sum_{i-0}^{i=n} [2R_i / (1 + \cos\theta_i)], \quad i = 0,1,2,3... \quad [9]$$

(2) Equivalent path on recessed surface

Besides bench-like surfaces, recesses and bumps are two other major features of the topography in open pit mines. Experiences show that bumps have little influence on the equivalent path, while recesses have much.

Propagation of seismic waves within the recessed surface is a complicated process and it is not possible to express it mathematically at present. However, the equivalent path concept may provide an opportunity to give an answer to the problem, at least to a certain degree. Take the case shown in Figure 5 as an example. In this case the recess is from point P_2 to point P_3. The equivalent path on the recessed surface can be approximately determined by the following procedure.

1. Draw a straight line l_1 from point P_1 passing point P_2.
2. Draw a straight line l_2 from point M and rotate it with point M as axis until it becomes tangent to point P_4.
3. Suppose the two straight lines intersect at point P_3'. Mark the nearest point from point P_3' to the ground surface as P_3'', and mark the midpoint of the line segment $P_3'P_3''$ as P_3.
4. Then the equivalent path between point P_2 and point P_4 can be defined as two parts: R_2 from P_2 to P_3 and R_3 from P_3 to P_4.

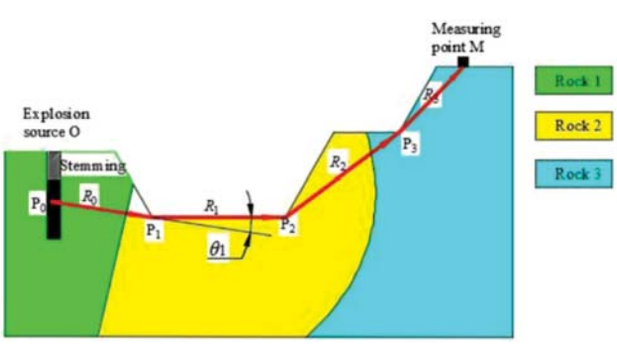

Figure 4—The equivalent path (red line) on bench-like surface without considering geological conditions

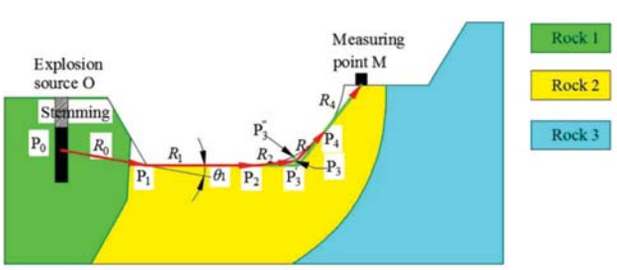

Figure 5—The equivalent path (red line) on a recessed surface without taking into account geological conditions

Influence of the rock property factor on the propagation path

In addition to the influence of topography on the propagation path, the site-specific characteristics should also be incorporated into the model for predicting blasting-induced vibration. As Kuzu (2008) noted, the site-specific ground characteristics must be taken into account, particularly if the ground conditions are variable, like in this case. Because of the complexity of the relationship between geological conditions and rock characteristics and the process of wave transmission, identifying one or more parameters that can comprehensively describe the characteristics of the rock mass appears particularly important. Fortunately, the elastic wave impedance and the integrity coefficient of rock can describe the physical and mechanical properties of the rock mass, such as the joint frequency and fracturing (Wang, 2010).

The relationship between the stress and the particle vibration velocity v can be written as:

$$\sigma = \rho c_m v \quad [10]$$

where ρ and c_m are respectively the density and longitudinal wave propagation velocity of the rock. So if the stress value is constant, there is a positive correlation between the PPV and the value of wave impedance of rock ρc_m.

The rock mass in reality often contains geological discontinuities such as fissures, fractures, and faults. Research and experience indicate the important role of geological discontinuities in the decay of seismic waves [2, 3]. As it is hard to define the impedance of the rock mass in an ideally theoretical manner, it seems reasonable to define the impedance z of the rock mass as the following:

$$z = \rho c_m / \eta \quad [11]$$

where ρ is the rock density in g·cm^{-3}, c_m is longitudinal wave propagation velocity in m·s^{-1}, and η is the integrity factor of the rock mass, $\eta = (c_m / c_r)^2$, where cr is the longitudinal wave propagation velocity of the rock in m·s^{-1}.

Therefore, the impedance z of the rock mass and PPV are negatively correlated, which can be expressed temporarily as

$$\mathrm{PPV} = f(z) \quad [12]$$

Construction of prediction model

Based on the above analysis, a formula relating PPV to the equivalent distances and the rock properties can be constructed as:

$$\mathrm{PPV} = K\left[\frac{(Q\cdot Q_V)^{1/3}\cdot(1+\cos\theta_i)}{\sum_{i=0}^{i=n}(2R_i\rho_i c_{mi}/\eta_i)}\right]^{\alpha} \quad [13]$$

(hereafter termed the EPB equation).

where i = 0,1,2,3...

PPV is peak particle velocity) cm·s^{-1}}

Q is the maximum explosive charge fired per delay (kg)

Q_V is the explosion heat of explosive at constant volume (kJ·kg^{-1})

P_i is the demarcation point of rock properties and the inflection point of propagation direction on the equivalent path

R_i is the equivalent distance from point P_i to point P_{i+1} (m)

θ_i is the intersection angle of the wave propagation direction to the ground surface at the P_i (degrees) (obviously, θ_i equals zero when point P_i is at the point P_0 or the demarcation point of rock properties)

ρ_i is the density of rock on the equivalent path, whose equivalent distance is R_i (g·cm^{-3})

η_i is the integrity coefficient of the rock mass on the equivalent path, whose equivalent distance is R_i, and $\eta_i = (c_m / c_r)_i^2$, in which c_m and c_r are the wave velocity of the rock mass and rock respectively (m·s^{-1})K and α are constants.

As shown in Figure 6, P_1 and P_4 are the demarcation points of rock properties, and P_2, P_3, and P_5 are the inflection point of the propagation direction. θ_3 is the intersection angle at point P_3.

Verification of prediction model

Field seismic monitoring tests

Seismic monitoring tests were conducted in Si-Jia-Ying iron mine, a large-scale open pit mine where multi-hole millisecond-delay bench blasting is applied. The layout of the blast-holes is triangular and the initiation method is hole-by-hole. The burden is 5 m, the distance between holes is 7 m, and the distance between rows is 6 m. The values and numbers of the parameters involved in the EPB equation were measured and collected systematically for each of the tests, for determining the values of the constants K and α and also for examining the accuracy and reliability of the EPB equation in prediction of blasting-induced PPV.

Equipment and procedure

Ten blasting seismographs (model NUBOX-6016, Figure 7) were used in this programme. Each seismograph uses an integrated triaxial geophone to convert ground movement/velocity into a voltage, which is simultaneously recorded by the seismograph in the manner of waveforms as shown in Figure 8. The seismic analysis software of the instrument provides features for graphical output of the

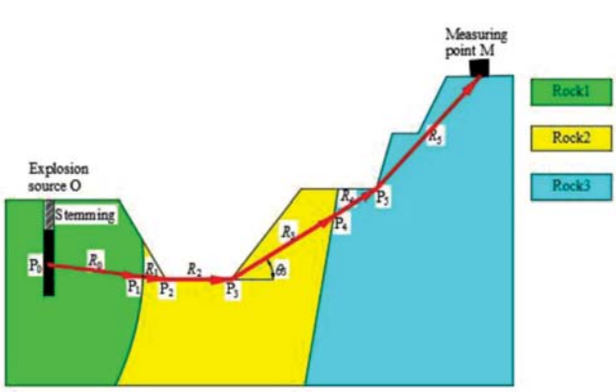

Figure 6—The equivalent path taking into account the topography and the rock properties

Figure 7—Seismograph and geophone used for monitoring of blasting-induced ground vibrations

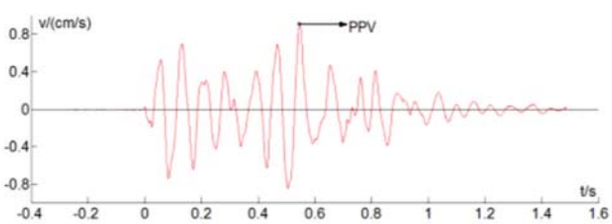

Figure 8—Example of blasting-induced seismic waveform: particle vibration velocity *v* vs. time *t*

waveforms in each of the three axes. PPV and dominant frequency *f* are measured automatically by the software from the waveform that results from the vector composite of the three mutually perpendicular components.

Geophones are fixed to a hard surface with plaster, or linked with sharp steel pins 20 cm in length to other types of ground surface, for coupling of the instrument to the ground and assuring a fair recording quality.

As shown in Figure 9, the geophones were fixed in a line at different distances from the blast, with the line oriented toward the mass centre of explosive charge Q of the blast.

The coordinates of the geophones and the charge for each blast were measured and documented for use in the analysis.

Parameters and results of tests

A total of 48 seismic monitoring tests were conducted. In each of the tests, condition parameters such as explosion heat at constant volume, the properties of the rock and rock mass, as well as rock type distribution in the mine were recordedollected. Waveforms in each of the three mutually perpendicular geophones and the resultant velocity-time curve for each seismograph were recorded. PPV correlation analyses were then carried out to determine the constants K and α of the EPB equation and for error analysis.

Condition parameters

Two types of explosive products, an ANFO and an emulsion, are available for blasting at the Si-Jia-Ying open pit mine. The explosion heat Q_V at constant volume is 3840 kJ·kg^{-1} for ANFO and 3200 kJ·kg^{-1} for emulsion (EM). Properties of the rock and rock mass are shown in Table I.

Result of the tests

The results of the 48 tests are shown in Table II.

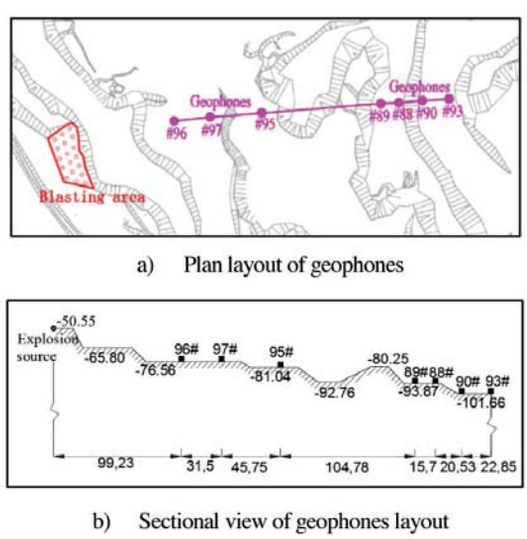

Figure 9—An example of a geophone (■) layout for monitoring blasting-induced ground vibrations

Table I

Properties of rock and rock mass at Si-Jia-Ying iron mine

Rock type		Rock density ρ(g·cm$_{-3}$)	Wave velocity of rock (km·s^{-1})	Wave velocity of rock mass c´ (km·s^{-1})	Integrity coefficient of rock mass η
Fe1	Fe11	3.526	5.33	3.35	0.395
	Fe12	3.526	5.33	4.13	0.600
	Fe13	3.526	5.33	4.62	0.750
Fe2	Fe21	3.461	5.13	2.29	0.200
	Fe22	3.461	5.13	3.15	0.376
SS	SS1	2.577	5.01	2.74	0.300
	SS2	2.577	5.01	3.71	0.550
	SS3	2.577	5.01	4.58	0.836
	SS4	2.577	5.01	4.75	0.900

Table II

Results of field seismic monitoring tests

Test no.	Q (kg)		R_i (m)			PPV (cm·s^{-1})	f (H)z
	EM	ANFO	Fe1	Fe2	SS		
1	540	360	135.99	0	153.25	1.09	4.88
2	540	360	156.58	0	225.56	0.58	6.84
3	540	360	156.58	0	478	0.29	11.72
4	0	750	0	0	149.86	2.74	40.04
5	0	750	0	0	220.59	1.61	18.55
6	0	750	129.00	67.61	452.24	0.13	12.7
7	450	0	0	258.92	98.2	0.6	26.37
8	450	0	0	261.76	27.71	0.97	10.74
9	450	0	34.29	140.71	123.45	0.8	4.88
10	270	450	0	0	553.66	0.43	33.2
11	270	450	0	0	553.66	0.49	33.2
12	270	450	0	0	741.59	0.25	12.7
13	0	450	70.71	0	45.16	3.15	34.18
14	0	450	70.71	0	45.16	3.15	34.18
15	0	450	72.04	232.42	148.95	0.2	16.6
16	0	450	90.73	285.6	148.95	0.22	10.74
17	400	0	53.96	32.81	124.72	1.03	20.51
18	400	0	0	33.22	71.54	4.81	38.09
19	400	0	0	156.01	65.04	1.47	43.95
20	400	0	0	151.19	117.22	1.44	36.13
21	0	480	69.11	221.91	179.37	0.34	6.84
22	0	480	45.84	221.91	179.37	0.42	6.84
23	0	480	31.16	185.37	160.29	0.7	10.74
24	0	480	8.42	185.32	160.29	0.66	29.3
25	0	480	0	176.92	160.29	0.63	4.88
26	0	480	0	124.8	137.68	1.57	43.95
27	0	480	0	54.92	92.85	4.01	36.13
28	0	480	101.94	207.28	208.07	0.17	29.3
29	0	480	63.99	170.74	188.99	0.31	17.58
30	0	480	41.24	170.69	188.99	0.39	11.72
31	0	480	32.83	110.17	166.38	0.59	18.55
32	0	480	57.97	0	64.35	4.34	9.77
33	0	480	0	43.34	17.97	9.89	35.16
34	0	480	16.11	65.07	38.06	4.16	36.13
35	700	0	51.49	0	4.72	14.65	4.88
36	400	0	194.18	122.48	78.23	0.28	27.34
37	400	0	191.36	122.48	99.68	0.19	6.84
38	400	0	190.34	122.48	117.69	0.15	6.84
39	400	0	190.83	122.48	169.74	0.13	5.86
40	0	450	39.59	0	62.61	4.82	8.79
41	0	450	71.1	0	62.61	2.23	34.18
42	0	450	119.32	0	165.89	0.46	37.11
43	0	450	119.41	0	181.59	0.43	34.18
44	0	450	119.41	0	202.37	0.44	38.09
45	0	450	7.68	4.28	220.96	0.46	34.18
46	0	420	7.68	31.64	113.92	3.4	34.18
47	0	420	7.68	50.28	113.92	3.42	38.09
48	0	420	7.68	89.09	120.22	1.92	35.16

Analysis and discussion

The values of the constants K and α of the EPB equation were determined by correlating the measured PPV with the equivalent distance of the 48 seismic monitoring tests. The least-squares method was applied in this procedure and the relevance coefficient R_c and root mean square error RMSE of the correlation were obtained. Taking the logarithm of the EPB equation yields:

$$\ln \mathrm{PPV} = \ln K + \alpha \cdot n \left[\frac{(Q \cdot Q_V)^{1/3} \cdot (1+\cos\theta_i)}{\sum_{i=0}^{i=n} (2R_i \rho_i c_{mi} / \eta_i)} \right] \quad [14]$$

where i = 0,1,2,3L L

Then let y = ln PPV,

$$x = \ln \left[\frac{(Q \cdot Q_V)^{1/3} \cdot (1+\cos\theta_i)}{\sum_{i=0}^{i=n} (2R_i \rho_i c_{mi} / \eta_i)} \right], \; a = \ln K, \; b = \alpha,$$

Equation [13] can thus be written as

$$y = a + bx \quad [15]$$

As shown in Figure 10, by correlating the EPB equation with the data listed in Table I and Table II at a confidence level of 95% the constants K and α are found to be 1528 and 1.91 respectively. Therefore, the EPB equation can then be written as the following:

$$\mathrm{PPV} = 1528 \left[\frac{(Q \cdot Q_V)^{1/3} \cdot (1+\cos\theta_i)}{\sum_{i=0}^{i=n} (2R_i \rho_i c_{mi} / \eta_i)} \right]^{1.91} \quad [16]$$

Figure 10 also shows that the correlation coefficient R_c equals 0.9825 and equals 0.2268 at a confidence level of 95%, indicating that the PPV of bench-blasting ground vibrations is highly correlated with the equivalent distance, the maximum explosive charge per delay, and explosion heat of the explosive, as well as the wave impedance of rock and integrity coefficient of the rock mass over the entire equivalent distance.

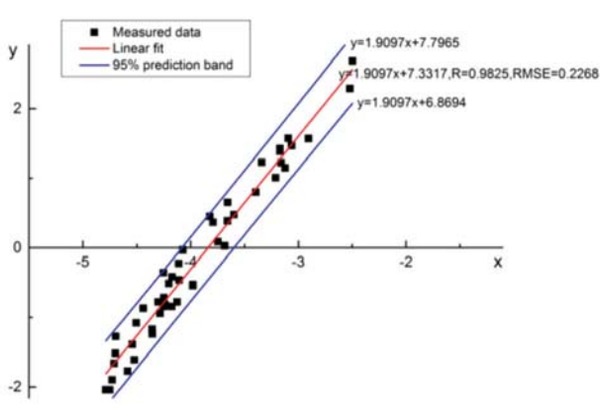

Figure 10—Result of linear regression of PPV with the EPB equation

The relative errors are obtained by comparing the predictive PPV values with the measured values in field seismic monitoring tests. The results of the relative errors, ε, are presented in Table IV.

The same operation was conducted with Sadaovsky's equation method. In the process of analysis, the distance parameter in Sadaovsky's equation (PPV = $K(Q^{1/3}R^{-1})$ is substituted with the horizontal distance R_h and spatial distance R_s from the blast to measuring point respectively. The fitting results are shown in Figures 11 and12. The correlation coefficient of the regressions is shown in Table III. Furthermore, errors from Sadaovsky's equation are also calculated and compared for an evaluation purpose. The results of the relative errors, ε, are shown in Table IV.

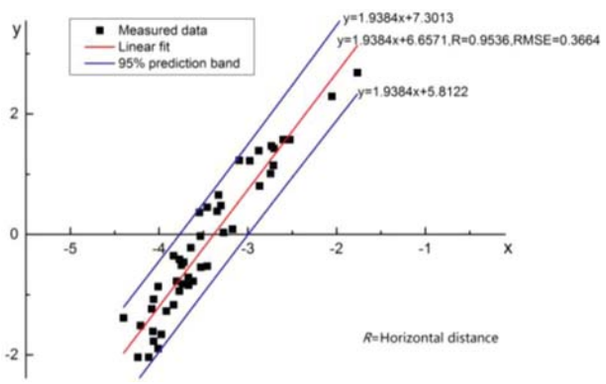

Figure 11—Linear regression of measured PPV with Sardovsky's equation as $R = R_h$

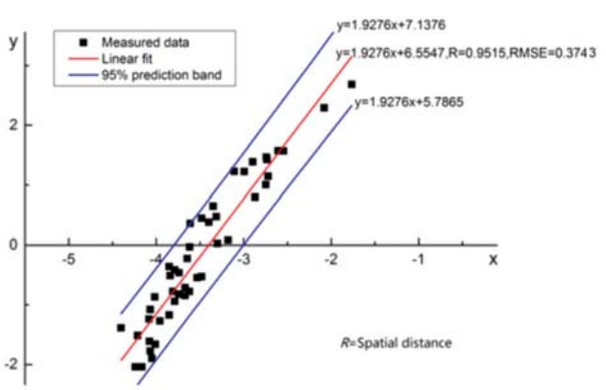

Figure 12—Linear regression of measured PPV with Sadaovsky equation as $R = R_s$

Table III

Result of linear regression of measured PPV with Sardovsky's equation

Parameter	$R = R_h$	$R = R_s$
K	704.2265	702.54
α	1.9384	1.9274
R_c	0.9536	0.9515
RMSE	0.3664	0.3743

Table IV

Comparison of the PPVs predicted by the EPB equation and Sardovsky's equation with monitored data

Test no.	Measured PPV	Sardovsky's equation				EPB equation	
		$R = R_h$		$R = R_s$			
		Predictied PPV	ε (%)	Predicted	ε (%) PPV	Predicted	ε (%) PPV
1	1.09	1.50	37.96	1.54	41.24	1.19	9.56
2	0.58	0.75	29.96	0.78	34.31	0.76	31.71
3	0.29	0.26	11.07	0.27	7.02	0.37	28.50
4	2.74	3.45	26.01	3.53	28.80	3.32	21.16
5	1.61	1.17	27.49	1.18	26.62	1.59	1.45
6	0.13	0.19	46.81	0.20	52.57	0.18	35.09
7	0.60	0.49	18.06	0.43	28.40	0.50	16.85
8	0.97	0.75	23.17	0.66	31.94	0.64	33.94
9	0.80	0.60	24.51	0.63	21.49	0.60	25.57
10	0.43	0.57	33.35	0.60	38.79	0.46	6.17
11	0.49	0.57	17.03	0.60	21.79	0.46	6.83
12	0.25	0.14	44.44	0.15	41.92	0.26	4.51
13	3.15	3.67	16.47	3.72	18.21	3.92	24.48
24	3.15	3.67	16.47	3.72	18.21	3.92	24.48
15	0.20	0.27	32.55	0.27	35.72	0.27	35.43
16	0.22	0.20	8.14	0.21	4.88	0.19	11.85
17	1.03	1.23	19.74	1.22	18.06	1.35	30.73
18	4.81	5.26	9.45	5.23	8.80	5.94	23.50
19	1.47	1.07	27.11	1.00	31.80	1.41	3.85
20	1.44	0.73	49.36	0.67	53.42	1.09	24.11
21	0.34	0.27	21.14	0.28	41.24	0.28	17.49
22	0.42	0.30	29.37	0.31	34.31	0.32	24.52
23	0.7	0.42	40.55	0.42	7.02	0.45	35.25
24	0.66	0.47	28.60	0.48	28.80	0.53	19.79
25	0.63	0.52	17.43	0.52	26.62	0.60	4.98
26	1.57	0.87	44.87	0.86	52.57	1.03	34.29
27	4.01	2.67	33.34	2.65	28.40	3.58	10.75
28	0.17	0.27	57.72	0.28	31.94	0.24	41.14
29	0.31	0.42	34.24	0.42	21.49	0.37	19.86
30	0.39	0.47	20.83	0.48	38.79	0.43	9.53
31	0.59	0.87	46.71	0.86	21.79	0.77	29.82
32	4.34	3.52	18.94	3.58	41.92	4.41	1.50
33	9.89	13.18	33.26	12.78	18.21	12.39	25.25
34	4.16	3.72	10.65	3.63	18.21	3.58	13.98
34	14.65	23.01	57.03	23.46	35.72	12.99	11.34
36	0.28	0.35	26.49	0.34	4.88	0.20	30.15
37	0.19	0.32	67.10	0.31	18.06	0.19	0.13
38	0.15	0.30	97.45	0.29	8.80	0.18	22.34
39	0.13	0.24	85.50	0.23	31.80	0.16	25.94
40	4.82	4.55	5.52	4.65	53.42	4.16	13.68
41	2.23	2.72	21.95	2.79	18.72	2.34	4.86
42	0.46	0.64	38.88	0.66	27.35	0.58	25.68
43	0.43	0.58	33.89	0.59	39.92	0.53	22.54
44	0.44	0.51	15.11	0.52	28.00	0.47	6.56
45	0.46	0.44	3.69	0.46	17.08	0.41	10.09
46	3.4	2.20	35.42	2.19	45.38	3.66	7.57
47	3.42	1.74	49.00	1.76	33.93	2.59	24.25
48	1.92	1.11	42.44	1.11	62.56	1.42	26.13
ε´	---	32.0%		32.69%		19.14%	

From Figures 10–12, it is not difficult to find that although the correlation coefficients with Sardovsky's equation are also fairly high (0.9536 and 0.9515), they increase to 0.3364 and 0.3743 respectively, compared to 0.2268 for the EPB equation. Furthermore, the distribution of the measured data points in Figure 10 becomes more concentrated compared with Figures 11and 12, which indicates the effectiveness of the EPB equation.

It can also be observed in Table IV that ε', the mean value of the relative error ε of the PPV predicted by the EPB equation to the measured PPV, is 19.14% , while ε' comes to 32.00% and 32.69% with $R=R_h$ and $R=R_s$ respectively using Sardovsky's equation .

Summary and conclusions

Under the condition of the consistency of site factors, including site topographic and geological conditions, the effectiveness of early empirical prediction equations such as Sadaovsky's equation is obvious. However, these equations are unsuitable for irregular topography such as benches and complicated geological conditions. A new method for predicting blasting-induced vibration, using the EPB equation, is suggested, which takes into account the irregular topography and complicated geological conditions.

In many cases of field bench blasting, the topography between a blast and points of concern is highly irregular, and hence the seismic waves do not propagate along a single straight line to the measuring points. In this paper, it is assumed that the equivalent path and equivalent distance can be used to characterize the distance dimension based on the minimum distance principle. Meanwhile, the wave impedance of rock and integrity factor of the rock mass are used to model the effect of rock properties and discontinuity characteristics of the rock mass on the path of wave propagation.

In this paper, it is considered that PPV is positively related to the energy released from detonation of the maximum explosive charge quantity fired per delay period in a blast. Different explosives release different energies when detonated, so here we use the product of the detonation heat (Q_V) and the maximum explosive charge quantity (Q) to represent the energy released by detonation.

As a result of linear correlation analysis on PPV data obtained in 48 field bench-blasting measurements, the constants K and α of the EPB equation are determined to be 1528 and 1.91 respectively. By comparing the predicted values with the measured data from field seismic monitoring tests, the error of the prediction with the EPB equation is found to be about 19.14%, much lower than that of Sadaovsky's equation (32.00% and 32.69%), indicating that the EPB equation is capable of describing the relationship of peak particle velocity with equivalent distance with high reliability, and is fairly reliable for use in predicting bench blasting-induced ground vibrations.

In conclusion, the EPB equation can easily be used in open pit mines where the factors in the equation such as the equivalent path and distance, rock density and wave velocity, and integrity coefficient of the rock mass can be easily measured. However, further study is needed to confirm the usefulness and reliability of the EPB equation in underground environments.

Acknowledgement

This study was supported by the National Natural Science Foundation of China (Grant No. 51274020).

References

Ambraseys, N.R. and Hendron, A.J. 1968. Dynamic behaviour of rock masses. *Proceedings of Rock Mechanics in Engineering Practices*. Wiley, London. pp.203–207.

Amnieh, H.B., Mozdianfard, M.R., and Siamaki, A. 2010. Predicting of blasting vibrations in Sarcheshmeh copper mine by neural network. *Safety Science*, vol. 48. pp. 319–325.

Amnieh, H.B., Siamaki, A., and Soltani, S. 2012. Design of blasting pattern in proportion to the peak particle velocity (PPV): Artificial neural networks approach. *Safety Science*, vol. 50. pp. 1913–1916.

Bouckovalas, G.D. and Papadimitriou, A.G. 2005. Numerical evaluation of slope topography effects on seismic ground motion. *Soil Dynamics and Earthquake Engineering*, vol. 25. pp. 547–558.

Bureau of Indian Standards. 1973. Criteria for safety and design of structures subjected to underground blast. *ISI Bulletin*, IS-6922.

Fiore, D.V. 2010. Seismic site amplification induced by topographic irregularity: Results of a numerical analysis on 2D synthetic models. *Engineering Geology*, vol. 114. pp.109–115. doi:http://dx.doi.org/10.1016/j.enggeo.2010.05.006

Gwenaël, G., Judicaël, P., and Guillaume, D. 2011. Time-domain impedance equationtion for transmission line matrix modelling of out door sound propagation. *Journal of Sound and Vibration*, vol. 330. pp. 6467–6481

Khandelwal, M. and Singh, T.N. 2007. Evaluation of blast-induced ground vibration predictors. *Soil Dynamics and Earthquake Engineering*, vol. 27. pp. 116–125.

Kuzu, C. 2008. The importance of site-specific characters in prediction models for blast-induced ground vibrations. *Soil Dynamics and Earthquake Engineering*, vol. 28. pp. 405–414.

Langefors, U and Kihlstrom, B. 1963.The Modern Techniques of Rock Blasting. Wiley, New York.

Li, X.B., Ling, T.H., and Zhang, Y.P. 2009. Analysis of Blast Vibration Signals-Theories and Methods. Science Press, Beijing. pp. 161.

Nateghi, R. 2011. Prediction of ground vibration level induced by blasting at different rock units. *International Journal of Rock Mechanics and Mining Sciences*, vol. 48. pp. 899–908.

Nguyen, K.V. and Gatmiri, B. 2007. Evaluation of seismic ground motion induced by topographic irregularity. *Soil Dynamics and Earthquake Engineering*, vol. 27. pp. 183–188.

People's Republic of China. 2014.National Standards Compilation group of safety regulations for blasting (GB6722-2014). Standards Press of China, Beijing.

Song, G.M. and Xiao, Q.H. 2000. Research on the methods of measurement and evaluation of blasting vibration in open-pit mines. *Nonferrous Metal (Mining)*, vol. 4. pp. 24–27.

Tripe, R., Kontoe, S., and Wong, T.K.C. 2013. Slope topography effects on ground motion in the presence of deep soil layers. *Soil Dynamics and Earthquake Engineering*, vol. 50. pp. 72–84.

Wang, X.G. 2010. Handbook of Blasting. Metallurgical Industry Press, Beijing. pp. 225.

Xia, X., Li, H.B., Niu, J., Li, J., and Liu, Y. 2014. Experimental study on amplitude change of blast vibrations through steps and ditches. *International Journal of Rock Mechanics and Mining Sciences*, vol.71. pp. 77–82. ◆

http://dx.doi.org/10.17159/2411-9717/2018/v118n5a10

Effect of cooling conditions on the leachability of chromium in Cr_2O_3-containing steelmaking slag

by Y. Yu*, D. Wang*, J. Li*†, M. Li‡, and Z. Xue*

Synopsis

The effects of temperature and atmosphere during cooling on the leachability of chromium from stainless steel slag were investigated. Experiments were performed under an oxidizing atmosphere in a muffle furnace and in a reducing atmosphere in an induction furnace. The slags were subjected to leaching tests using the standard procedure prEN12457-2. Results indicated that an oxidizing atmosphere enhances the leachability of chromium and that the extent of leaching increases with temperature. A reducing atmosphere tends to suppress the leaching of chromium. Differences between the chromium leached from the samples cooled under different atmospheres revealed that it is difficult for CO to completely reduce chromium Cr^{6+} to Cr^{3+} once hexavalent chromium has been generated. Therefore, it is necessary to utilize a neutral or reducing atmosphere for cooling the slag so as to prevent the formation of hexavalent chromium.

Keywords

atmosphere, oxidation, hexavalent chromium, stainless steel slag, chromium leaching.

Introduction

Stainless steel slags are generated in electric arc furnace (EAF), argon oxygen decarburization (AOD) furnace, and vacuum oxygen decarburization furnace operations. The transition metal chromium (Cr), which is an essential alloying element in stainless steel, is prone to oxidation because of its high reactivity during melting (Li *et al.*, 2013), and chromium oxides float in the molten slag phase. Trivalent and hexavalent chromium are the most common oxidation states in chromium compounds. Trivalent chromium is the most stable state under normal atmospheric conditions, whereas hexavalent chromium is toxic because of its strong oxidative property (Zhong *et al.*, 2015). The leaching of chromium from stainless steel slags can lead to economic and ecological issues (Loock-Hattingh *et al.*, 2015). Therefore, it is imperative to examine the mechanism involved in the leaching of chromium and design some effective treatments to stabilize chromium in slags.

Several studies have reported the leaching and stabilization of chromium (Engstrom, 2010; Durinck *et al.*, 2008; Albertsson, 2011; Tae and Morita, 2017; Gelfi, Cornacchia, and Roberti, 2010; Song and Garbers-Craig, 2016; Du Preez *et al.*, 2017). Engstrom (2010) and Albertsson (2011) reported that the leachability of chromium depends mainly on the distribution of chromium in the slag. Stainless steel slag comprises various minerals. Some of these minerals, such as merwinite ($Ca_3MgSi_2O_8$), larnite (Ca_2SiO_4), akermanite ($Ca_2MgSi_2O_7$), and gehlenite ($Ca_2Al_2SiO_7$), are slightly soluble in water. In contrast, other minerals, such as wüstite, and spinel, are resistant to dissolution and oxidation. The $MgCr_2O_4$ spinel phase, *i.e.*, magnesiochromite, in the slag is known to be important for controlling the leaching properties of chromium from the slag (Pillay, Von, and Petersen, 2003). Garcia-Ramos *et al.*, (2008) investigated the immobilization of chromium in CaO-SiO_2-Cr_2O_3-Al_2O_3-MgO synthetic slags by MgO. Their results indicated that MgO-based slag exhibits the lowest chromium leachability, owing to the immobilization of chromium in MgO-spinel. Engström *et al.*, (2010) and Peter *et al.*, (2010) developed a new method for treating EAF slag obtained from stainless steelmaking. The agents that enhance the formation of the spinel solid solution are added into a transfer ladle during tapping of the steel and slag. The effect of the additions on spinel formation can be described as follows:

$$factor\ sp_{opt.} = 0.2^{*}MgO + 1.0^{*}Al_2O_3 + x_{opt.}\ FeO_n - 0.5^{*}Cr_2O_3\ [\%wt.]$$

where $x_{opt.}$ depends on the oxidation state of the EAF slag.

* *State Key Laboratory of Refractories and Metallurgy, Wuhan University of Science and Technology, China.*

† *Key Laboratory for Ferrous Metallurgy and Resources Utilization of Ministry of Education, Wuhan University of Science and Technology, China.*

‡ *Yonggang Group Co.,LTD, China.*

© *The Southern African Institute of Mining and Metallurgy, 2018.* *ISSN 2225-6253. Paper received Mar. 2017; revised paper received Sep. 2017.*

For EAF slags with high values of $sp_{opt.}$, the leachable chromium content is almost negligible. These studies focused on the suppression of chromium leaching by adjusting the composition. Few studies have been reported regarding the effect of atmosphere on the leaching of chromium during cooling of stainless steelmaking slag. Considering the production of ferrochrome alloys from chromite ores, Beukes, Dawson, and Zyl (2010) reported that the generation of Cr(VI) is related to the presence of oxygen at a high temperature.

In this study, to increase understanding of the mechanism involved in the leaching of chromium from stainless steel slags, the effects of atmosphere and temperature on the leachability of chromium during the cooling of liquid slag were investigated by experiments performed in muffle and induction furnaces.

Experimental

Raw material

Table I summarizes the chemical composition of the slags obtained from the stainless-steelmaking process. Samples S1 and S2, which were generated in an AOD furnace, had an extremely high calcium oxide content, 61.54 wt% and 54.46 wt%, respectively, whereas the chromium oxide content in both slags was quite low, only 0.19 wt% and 0.51 wt%, respectively. Sample S3, the EAF slag, had the lowest basicity (CaO/SiO_2), albeit with a fairly high Cr_2O_3 content (5.78 wt%).

Experimental set-up and procedure

The experimental set-up included the muffle and induction furnaces (Figure 1). The maximum temperature of the muffle furnace was 1200°C. A graphite crucible was used as the heating element for the induction furnace, with a maximum power of 60 kW and frequency of 3 kHz. Figure 2 shows the experimental procedure. First, 270 g of each of the slag samples was crushed to less than 4 mm. Then, 90 g of particles was used for the leaching test, which was conducted according to the European standard leaching procedure prEN12457-2. The remaining 180 g was charged in an Al_2O_3 crucible and heated in the muffle furnace at 600°C and 1000°C for 180 minutes under air. Then, 90 g of the oxidized slag obtained from the muffle furnace in the previous step was used in the leaching test, and the remaining 90 g was heated in the induction furnace at the same temperature as in the muffle furnace for 180 minutes. Finally, the reduced slags were subjected to the leaching test. The leachates obtained from the tests were analysed using inductively coupled plasma emission spectrometry (ICP-OES, IRIS Advantage ER/S), and HSC Chemistry 5.1 was employed to perform thermodynamic calculations for some reactions.

The standard procedure is in compliance with the leaching of granular waste materials and sludge, and a one-stage batch test is conducted at a liquid-to-solid ratio of 10 L/kg for materials with a particle size of less than 4 mm. The complete leaching procedure included the following steps:

(i) Add 90 g of slag into a 1 L polypropylene bottle
(ii) Add 900 mL of deionized water to the bottle
(iii) Place the capped bottle in a rotary agitator (GGC-D, Guohuan Institute of High-tech Automation)
(iv) Agitate for 24 ± 0.5 hours at a rate of 10 r/min
(v) Filter the mixture using a vacuum filtration device (TTGM, 2000 mL, Lianlink).

Atmosphere in an induction furnace

Notably, a graphite crucible is used as the heating element in the induction furnace; thus, the interactions between O_2, CO_2, and CO occur at a high temperature (Huang, 2006).

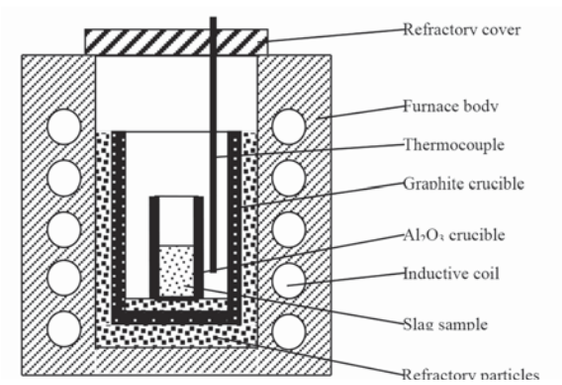

Figure 1—Experimental set-up of the induction furnace

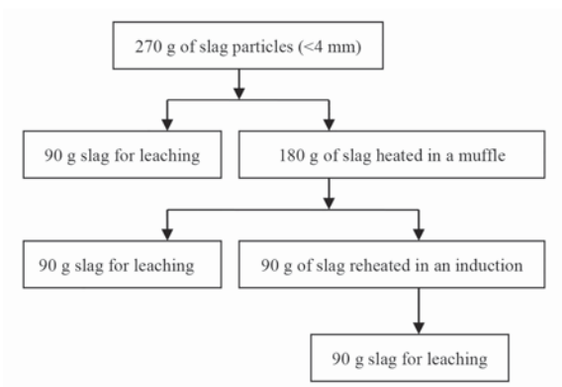

Figure 2—Flow chart of the procedure for the treatment of stainless steel slag under different atmospheres

Table I

Composition of the stainless steel slags, wt%

No.	CaO	SiO_2	MgO	Al_2O_3	Cr_2O_3	MnO	TiO_2	FeO	CaO/SiO_2
S1	61.54	30.27	6.65	1.31	0.19	0.55	0.45	0.31	2.03
S2	54.46	29.57	7.90	5.39	0.51	0.42	0.53	0.29	1.84
S3	34.14	26.23	9.71	6.64	5.78	2.50	6.95	0.96	1.30

$$C_{(graphite)} + O_2 = CO_2 \quad [1]$$

$$\Delta G_1^\theta = -395350 - 0.54T \ \text{J·mol}^{-1} \quad [2]$$

$$2C_{(graphite)} + O_2 = 2CO \quad [3]$$

$$\Delta G_3^\theta = -228800 - 171.54T \ \text{J·mol}^{-1} \quad [4]$$

$$C_{(graphite)} + CO_2 = 2CO \quad [5]$$

$$\Delta G_5^\theta = 166550 - 171T \ \text{J·mol}^{-1} \quad [6]$$

$$2CO + O_2 = 2CO_2 \quad [7]$$

$$\Delta G_7^\theta = -5619000 - 170.46T \ \text{J·mol}^{-1} \quad [8]$$

The partial pressures of O_2, CO, and C_2 are calculated at 600°C and 1000°C at the equilibrium state of the C–O system. A non-oxidizing atmosphere is present at high temperatures (Table II). CO was used for the reduction of slag. Niemelä , Krogerus, Oikarinen, (2004) and Kleynhans *et al.* (2016) have revealed that CO does not reduce Cr_2O_3. The possibility of the reduction of chromium from the hexavalent to the trivalent state by CO is discussed in the following sections.

Experimental results

The slag samples were heated at 600°C and 1000°C in the muffle furnace for 180 minutes and then leached according to the standard leaching procedure prEN12457-2. Higher chromium concentrations were observed in the leachates of the oxidized slags compared with those in the original slag samples. The chromium concentration increases with temperature (Figure 3). After sample S1 had been subjected to oxidation at 600°C and 1000°C, the concentrations of chromium in the leachates were 466% and 2197% greater than those of the original slag, respectively. The corresponding values for sample S2 increased to 4.82 mg/L and 56.90 mg/L. These values are considerably greater than that of the original slag (1.80 mg/L). Moreover, the concentrations of chromium in the leachates of sample S3 increased by 333% and 3270% compared with the original slag.

After reduction of the slag in the induction furnace, the content of chromium in the leachate decreases in comparison with that in the original slag (Figure 4). The three slag samples exhibited the same tendency: the highest chromium content in the leachate is observed for the original slag, whereas the lowest concentration chromium is observed for the slag reduced at 600°C. When S1 was oxidized at 600°C in the muffle furnace and then reduced at 600°C in the induction furnace, the leachate chromium content decreased from 2.15 to 0.15 mg/L. When the sample was processed at 1000°C following the same procedure, the concentration of chromium in the leachate fell from 8.73 to 0.37 mg/L. The concentrations of leached chromium for the reduced samples of S2 and S3 were dramatically less than those observed for the corresponding oxidized samples. The decrease is greater for reduction at 1000°C than at 600°C. For example, the concentrations of chromium in the leachate from the reduced samples of slag S3 were 0.61% and 0.15% of those of the samples oxidized at 600°C and 1000°C, respectively. Furthermore, the concentrations of chromium in the leachates collected from the samples reduced at 1000°C were always greater than those at 600°C.

Table II

Parameters of O_2, CO, and CO_2 in the C–O system at a constant pressure of 1 atm

	600°C	1000°C
p_{CO}	0.26	0.99
p_{CO}/p_{CO2}	0.36	99
p_{O2}	1.54×10^{-24}	4.42×10^{-19}

Discussion

Effect of atmosphere on chromium leaching

Thermodynamically, the amount of chromium dissolving into water from the stainless steel slag depends on the $CaCrO_4$ content (Lee and Nassaralla, 1997), which is expressed by the following reactions:

$$2CaO + Cr_2O_3 + \frac{3}{2}O_2 = 2CaCrO_4 \quad [9]$$

$$\Delta G^\theta = -RT \ln \frac{a_{CaCrO_4}^2}{a_{CaO}^2 \cdot a_{Cr_2O_3} \cdot p_{O_2}^{3/2}} \quad [10]$$

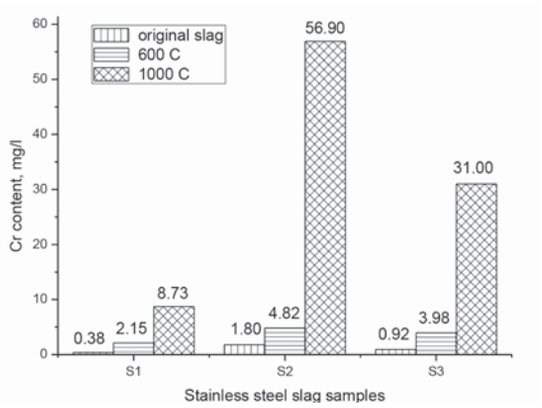

Figure 3—Effect of temperature on the leaching of chromium under an oxidizing atmosphere

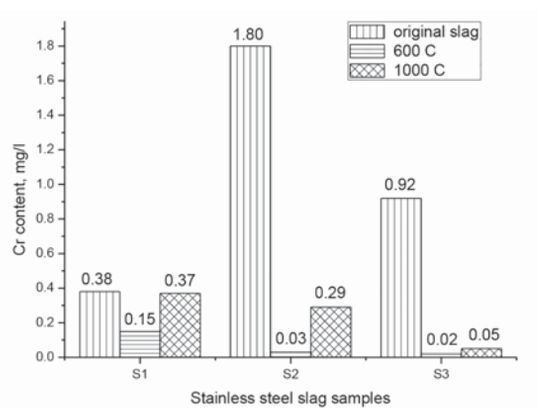

Figure 4—Effect of temperature on the leaching of chromium under a reducing atmosphere

$$CaO + CaCr_2O_4 + \frac{3}{2}O_2 = 2CaCrO_4 \quad [11]$$

$$\Delta G^{\theta} = -RT \ln \frac{a^2_{CaCrO_4}}{a_{CaO} \cdot a_{CaCr_2O_4} \cdot p^{3/2}_{O_2}} \quad [12]$$

where a is the activity and p is the partial pressure. When pure solid CaO, Cr_2O_3, $CaCr_2O_4$, and $CaCrO_4$ are chosen as the standard states of activities, the standard Gibbs energy of formation for solid $CaCrO_4$ is expressed as follows:

$$\Delta G^{\theta} = \frac{3}{2}RT \ln p_{O_2} \quad [13]$$

The slags were heated in the muffle furnace under air; thus, the partial pressure of oxygen was constant at 0.21. According to Equation [13], the standard Gibbs energy changes of reactions [9] and [11] can be expressed as a function of temperature, namely:

$$\Delta G^{\theta} = -19.46T \quad [14]$$

Hence, the treatment of slag in the muffle furnace enhances the formation of $CaCrO_4$, and a high temperature may also favour the reactions. The concentration of chromium in the leachate therefore increases as a result of heating in the muffle furnace, and it increases with temperature.

As stated in the section 'Atmosphere in an induction furnace', the atmosphere in the induction furnace maintains strong reducibility. The data shown in Table II revealed that the partial pressure of oxygen is less than 4.42×10^{-19} at a temperature of less than 1000°C, and it increases with temperature in the induction furnace. The soluble component, $CaCrO_4$, will decompose according to reactions [15] and [16]:

$$2CaCrO_4 + 3CO(g) = 2CaO + Cr_2O_3 + 3CO_2(g) \quad [15]$$

$$2CaCrO_4 + 3CO(g) = CaO + CaCr_2O_4 + 3CO_2(g) \quad [16]$$

According to thermodynamic calculations performed using the FactSage 7.0 thermodynamic database, the standard Gibbs energy change of Equation [15] is expressed as follows:

$$\Delta G^{\theta} = -247.39 - 0.33T \ \ (kJ) \quad [17]$$

Consequently, $CaCrO_4$ formed in the muffle furnace can be reduced by CO produced by the interaction between graphite and air in the induction furnace, and the chromium contained in the slags transforms from the soluble state (Cr^{6+}) into the stable states (Cr_2O_3 and $CaCr_2O_4$), leading to a significant decrease in the amount of chromium leached.

Moreover, the difference between the amounts of chromium dissolved from the three slags can be interpreted in terms of kinetics. The oxidation and reduction of chromium are gas–solid reactions, for which the interface is known to be a key factor. Pillay, Von, and Petersen, (2003) reported that the oxidation of a mixture of CaO and Cr_2O_3 supposedly occurs at the boundaries between CaO and Cr_2O_3 via the diffusion of oxygen along the particle boundaries, whereas that of Cr^{3+} occurs across the boundaries, leading to the formation of $CaCrO_4$. In the furnace slags in which CaO and Cr_2O_3 would form a solid solution, oxidation possibly occurs at the exposed surface of particles containing this type of solid solution.

The chromium content dominates the distribution on the surface of the slag particles. Hence, S2 exhibits a higher amount of dissolved chromium compared with S1 because of the higher chromium content. However, S3 exhibits the highest chromium concentration, and the amount of dissolved chromium is less than that in S2 after treatment in a muffle furnace at 600°C and 1000°C (Figure 3). This discrepancy can be explained by the mode of occurrence of chromium in the furnace slags. Notably, chromium exists mainly as a solid solution, such as merwinite, akermanite, and matrix, which is related to the extremely low content in the AOD slag. However, for the EAF slag, the majority of the chromium would occur in spinel minerals, such as $MgCr_2O_4$ and $FeCr_2O_4$, which are thought to be resistant to oxidation and dissolution in water (Samada, Miki, and Hino, 2011).

Effect of temperature on chromium leaching

Notably, temperature has a considerable effect on the dissolution of chromium in the lixiviant (Figures 3 and 4). At a high temperature, a large amount of $CaCrO_4$ is formed in the muffle furnace, which is reduced by CO in the induction furnace. These reactions can be explained by Arrhenius's Law, as shown in Equation [18] (Hua, 2004), indicating that either the increase in temperature or decrease in the activation energy can increase the reaction rate.

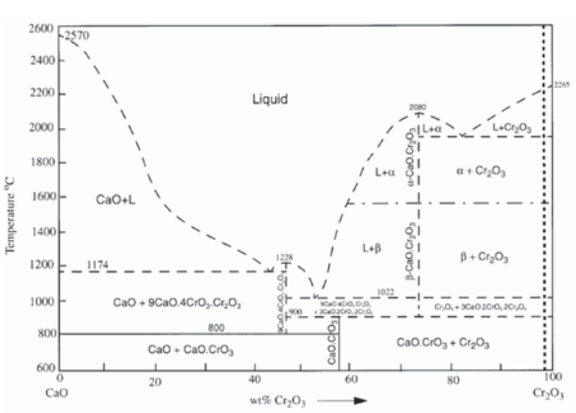

Figure 5—Phase diagram of the CaO–Cr_2O_3 system

$$k = Ae^{-\frac{E}{RT}} \quad [18]$$

where k is the reaction rate, A is the pre-exponential factor, E is the activation energy, and R is the universal gas constant.

Nevertheless, the formation of $CaCrO_4$ is restricted by temperature. Lee and Nassaralla (1998) reported that the formation of hexavalent chromium (Cr^{6+}) in a magnesite-chrome refractory is affected by the reaction temperature and chemical composition. According to the $CaO–Cr_2O_3$ phase diagram shown in Figure 5 (Lee and Nassaralla, 1997), the concentration of Cr^{6+} increases at a temperature below the critical point of 1022°C. Hexavalent chromium is thought not to exist in the liquid slag, indicating that Cr^{6+} is formed during cooling. Hence, the neutral or reducing atmosphere during cooling possibly suppresses the formation of Cr^{6+} and the subsequent leaching of chromium.

In addition, the difference in the chromium concentration in the leachates shown in Figure 4 indicated that once hexavalent chromium is formed, it is difficult to completely reduce Cr^{6+} to Cr^{3+}, suggesting that it is necessary to utilize a protective atmosphere for the cooling of slag to inhibit the formation of Cr^{6+}.

Conclusions

To further understand the mechanism involved in the leaching of chromium from stainless steel slags, the effects of atmosphere and temperature on the leaching of chromium from slags were investigated at temperatures of 600°C and 1000°C in a muffle furnace under an oxidizing atmosphere and an induction furnace under a reducing atmosphere, and an efficient method for suppressing the leachability of chromium was identified.

Chromium can be oxidized to the hexavalent state by oxygen, and a high amount of chromium can leach into water at a high temperature under an oxidizing atmosphere. After the oxidation of sample S1 at 600°C and 1000°C, the concentrations of chromium were respectively 466% and 2197% these values are greater than that of the original slag.

Under a reducing atmosphere, $CaCrO_4$ can be reduced to calcium oxide and chromium oxide by CO, leading to a decrease in the chromium concentration in the leachates. After sample S2 was first oxidized and then reduced at 1000°C, the concentration of leached chromium decreased from 56.90 to 0.29 mg/L. Once hexavalent chromium was formed, it was difficult to completely reduce to Cr^{3+}. Thus, a neutral or reducing atmosphere can favour the suppression of chromium leaching.

Acknowledgement

The research was supported by National Natural Science Foundation of China (No.51404173), Hubei Provincial Natural Science Foundation (No. 2016CFB579), China Postdoctoral Science Foundation (No.2014M562073), and State Key Laboratory of Refractories and Metallurgy (No.2014QN21). We thank Dr Q. Yang and Professor A. Xu for assistance in preparing the samples.

References

Albertsson, G.J. 2011. Investigations of stabilization of Cr in spinel phase in chromium- containing slags. PhD thesis, Royal Institute of Technology, Sweden.

Beukes, J.P., Dawson, N.F., and Zyl, P.G.V. 2010. Theoretical and practical aspects of Cr(VI) in the South African ferrochrome industry. *Journal of the Southern African Institute of Mining and Metallurgy*, vol. 110, no. 12. pp. 743–750.

Du Preez, S.P., Beukes, J.P., Dalen, W.P.J.V., Zyl, P.G.V., Paktunc, D., and Loock-Hattingh, M.M. 2017. Aqueous solubility of Cr(VI) compounds in ferrochrome bag filter dust and the implications thereof. *Water SA*, vol. 43, no. 2. pp. 298–309.

Durinck, D., Engström, F., Arnout, S., Heulens, J., Jones, P.T., and Bo, B. 2008. Hot stage processing of metallurgical slags. *Resources Conservation and Recycling*, vol. 52, no. 10. pp. 1121–1131.

Engstrom, F. 2010. Mineralogical influence on leaching behaviour of steelmaking slags. PhD thesis, Luleå University of Technology, Sweden.

Engström, F., Pontikes, Y., Geysen, D., Jones, P.T., Bo, B., and Blanpain, B. 2011. Review: Hot stage engineering to improve slag valorisation options. *Proceedings of the Second International Slag Valorisation Symposium: The Transition to Sustainable Materials Management*, Leuven, Belgium, 18–20 April 2011. KU Leuven. pp. 231–251.

García-Ramos, E., Romero-Serrano, A., Zeifert, B., Flores-Sánchez, P., Hallen-López, M., and Palacios, E.G. 2008. Immobilization of chromium in slags using MgO and Al_2O_3. *Steel Research International*, vol. 79, no. 5. pp. 332–339.

Gelfi, M., Cornacchia, G., and Roberti, R. 2010. Investigations on leaching behavior of EAF steel slags. *Proceedings of the 6th European Slag Conference*, Madrid, 20–22 October 2010. Publication no. 5. EUROSLAG, Duisburg-Rheinhausen, Germany. pp. 1–13.

Hua, Y. 2004. Kinetics of Metallurgical Process. Metallurgical Industry Press, Beijing [in Chinese].

Huang, X.H. 2006. Principle of Ferrous Metallurgy. Metallurgical Industry Press, Beijing.

Kleynhans, E.L.J., Neizel, B.W., Beukes, J.P., and Zyl, P.G.V. 2016. Utilization of pre-oxidized ore in the pelletized chromite pre-reduction process. *Minerals Engineering*, vol. 92. pp. 114–124.

Lee, Y. and Nassaralla, C.L. 1997. Minimization of hexavalent chromium in magnesite-chrome refractory. *Metallurgical and Materials Transactions B*, vol. 28, no. 5. pp.855–859.

Lee, Y. and Nassaralla, C.L. 1998. Formation of hexavalent chromium by reaction between slag and magnesite-chrome refractory. *Metallurgical and Materials Transactions B*, vol. 29, no. 2. pp. 405–410.

Li, J.L., Xu, A.J., He, D.F., Yang, Q.X., and Tian, N.Y. 2013. Effect of FeO on the formation of spinel phases and chromium distribution in the $CaO-SiO_2-MgO-Al_2O_3-Cr_2O_3$ system. *International Journal of Minerals, Metallurgy and Materials*, vol.20, no.3. pp. 253–258.

Loock-Hattingh, M.M., Beukes, J.P., Zyl, P.G.V., and Tiedt, L.R. 2015. Cr(VI) and conductivity as indicators of surface water pollution from ferrochrome production in South Africa: four case studies. *Metallurgical and Materials Transactions B*, vol. 46, no. 5, pp. 1–11.

Niemelä, P., Krogerus, H., and Oikarinen, P. 2004. Formation, characterisation and utilisation of CO-gas formed in ferrochrome smelting. *Proceedings of the 10th International Ferroalloys Congress*, Cape Town, South Africa, 1–4 February 2004. Southern African Institute of Mining and Metallurgy, Johannesburg. pp. 68–77.

Peter, D., Andreas, E., Michael, K., and Dirk, M. 2010. Recent development in slag treatment and dust recycling. *Steel Research International*, vol. 80, no. 10. pp. 737–745.

Pillay, K., Von, B.H., and Petersen, J. 2003. Ageing of chromium(III)-bearing slag and its relation to the atmospheric oxidation of solid chromium(III)-oxide in the presence of calcium oxide. *Chemosphere*, vol. 52, no. 10. pp. 1771–1779.

Samada, Y., Miki, T., and Hino, M. 2011. Prevention of chromium elution from stainless steel slag into seawater. *ISIJ International*, vol. 51, no. 5. pp. 728–732.

Song, S. and Garbers-Craig, A.M. 2016. Formation, leachability and encapsulation of hexavalent chromium in the $Al_2O_3-CaO-Fe_2O_3-Cr_2O_3$ system. *Journal of the European Ceramic Society*, vol. 36, no. 6. pp. 1479–1485.

Tae, S.J. and Morita, K. 2017. Immobilization of Cr (VI) in stainless steel slag and Cd, As and Pb in wastewater using blast furnace slag via a hydrothermal treatment. *Metals and Materials International*, vol. 23, no. 3. pp. 576–581.

Zhong, L., Yang, J., Liu, L., and Xing, B. 2015. Oxidation of Cr(III) on birnessite surfaces: The effect of goethite and kaolinite. *Journal of Environmental Sciences*, vol. 37, no. 11. pp. 8–14. ◆

SAIMM
THE SOUTHERN AFRICAN INSTITUTE OF MINING AND METALLURGY

Geometallurgy Conference 2018

BACK TO THE FUTURE

Supported by

GSSA Geological Society of South Africa
MINSA Mineralogical Association of South Africa
SAIMM THE SOUTHERN AFRICAN INSTITUTE OF MINING AND METALLURGY
WESTERN CAPE BRANCH

6th August 2018–Technical Workshop • 7-8th August 2018–Conference
Lagoon Beach Conference Venue, Cape Town, South Africa

Background

The theme of this first geometallurgy conference '**Back to the future**' is inspired by looking both into the past and the future: the concept of Geometallurgy goes back to some of the earliest mining activities when mineral recognition, mining, separation and concentration were undertaken simultaneously. Over time, changes in operational structures, product expansion and specialisation ultimately led to the diminishment and breakdown of this holistic approach.

In the last two decades 'Geometallurgy' has become a sophisticated yet entirely logical return to this integrated approach to mine planning. In a world of exponentially increasing ore heterogeneity and economic complexity, Geometallurgy is effectively a highly structured, integrated multi-disciplinary collaboration for optimising the value of an ore deposit. The approach is premised on acquiring multi-dimensional, spatially constrained (blocked) ore body knowledge that quantifies and qualifies all aspects of ore body variability. This data must include each element's response to blasting, excavation, crushing, grinding, separability and the environment and of course, its economic factors. These discrete elemental data sets are modelled to optimise a mine plan which takes into account the respective threshold criteria for each of the dataset components. Geometallurgy provides for truly integrated mine planning, ore flow management and processing from exploration to operations and through to final closure and rehabilitation. (Think of it as 4D Whittle on steroids, but for the entire mine life cycle, not just the optimised pit or stope envelope for the mining operation).

Looking into the future, we need to visualise what our 'ideal' mining operation in Southern Africa should look like, how it will function, and be equipped to articulate what we need to do to achieve this. Geometallurgy is a critical tool in achieving this.

Keynotes

Prof. Alice Clark
Director of Production Centres, SMI-BRC & SMI-JKMRC, University of Queensland, Australia

Sello Kekana
Head of Technical Training and Development, Ivanhoe Mines

Alistair Macfarlane, *Minerals Council South Africa*

Matt Mullins
Director: Tecoma Strategies

Dr Carlo Philander
Regional Manager South Africa Mineral Resources Development Tronox

Sponsors

Geovariances
SCANTECH www.scantech.com.au
winsam SCIENTIFIC
TESCAN PERFORMANCE IN NANOSPACE

For further information contact: Head of Conferencing, Camielah Jardine, SAIMM, P O Box 61127, Marshalltown 2107
Tel: +27 11 834-1273/7, Fax: +27 11 833-8156 or +27 11 838-5923, E-mail: camielah@saimm.co.za, Website: http://www.saimm.co.za

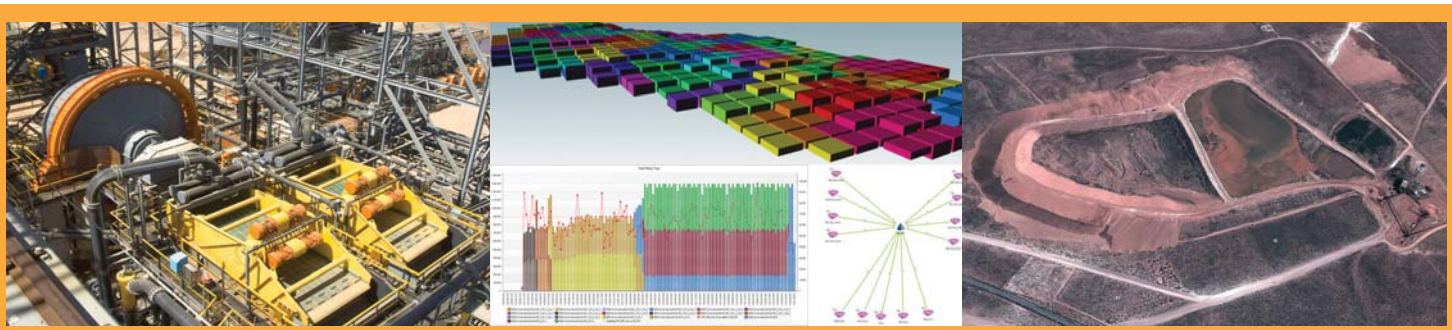

Conference Announcement

http://dx.doi.org/10.17159/2411-9717/2018/v118n5a11

Mathematical simulation and water modelling of liquid steel interaction with an argon bubble curtain in a one-strand continuous casting tundish

by A. Cwudziński

Synopsis

The injection of argon into a continuous casting tundish stimulates the zones of active flow (plug and ideal mixing flow) in the liquid steel and reduces the stagnant volume flow. In this research, numerical simulations and laboratory experiments were conducted on the use of a gas-permeable barrier (GPB) in the one-strand tundish. The investigations were aimed at increasing active liquid steel flow in the tundish, without using standard flow-control devices, under variable thermal conditions. The software program ANSYS-Fluent was used to perform numerical simulations. A water model was used to validate the numerical model. The water motion vector fields confirm the hydrodynamic patterns obtained from the computer simulations. The argon flow rate, location of the GPB, and the thermal conditions influence the liquid steel motion in the tundish. The best GPB positions were identified based on the lowest value of stagnant flow at argon injection flow rates of 15 and 5 Nl/min.

Keywords

tundish, argon injection system, steel flow, residence time distribution curves, mathematical modelling, water model.

Introduction

The use of argon in steelmaking protects the liquid steel against the influence of the atmosphere and promotes effective mixing to improve the thermal and chemical homogeneity (Chang, Zhong, and Zou, 2016; Chattopadhyay *et al.*, 2010; Liu and Thomas, 2015; Bai and Thomas, 2001; Smirnov, Efimova, and Kravchenko, 2014; Joo and Guthrie, 1992; Maldonado-Parra *et al.*, 2011; Ganguly and Chakraborty, 2004). The movement of argon bubbles within the liquid steel volume intensifies the mass and momentum exchange processes, thus intensifying the dissolution of technical alloys or scrap, as well as promoting the removal of nonmetallic inclusions during liquid steel refining. Feeding of argon to liquid steel, especially at the tundish stage, should not only provide the expected flow pattern modification, but also ensure the stable operation of the tundish, mould, and secondary cooling zone. The tundish should ensure that the required superheating level in the liquid steel is maintained and protect the steel against oxidation via stable behaviour of the tundish powder (Ilegbusi and Szekely, 1989; Chakraborty and Sahai, 1991; Barreto, Barron Meza, and Morales, 1996; Cloete *et al.*, 2015; Mabentsela, Akdogan, and Bradshaw, 2017). Gas-permeable barriers are used in different tundish types, and it is important to establish their optimal locations in the tundish (Chen *et al.*, 2014; Vargas-Zamora *et al.*, 2004; Smirnov, Efimova, G. and Kravchenko, 2013, 2014; Zhong *et al.*, 2006; Chang, Zhong, and Zou, 2015; Wang *et al.*, 2008; Jiang *et al.*, 2010; Cwudziński, 2010a, 2010b, 2010c). The injection of argon stimulates the zones of active flow (plug and ideal mixing flow) and reduces the stagnant volume flow. In the tundish working space, the stagnant volume flow should be as low as possible because the liquid steel resides in these recirculation zones longer than twice the average residence time of steel in the tundish. Therefore, recirculation regions of this type may favour the lowering of temperature, retard the chemical homogenization process in the liquid steel, and hinder impurities, such as nonmetallic inclusions, from floating up to the free surface of the liquid steel. Dispersed plug flow is beneficial in the case of consecutive casting of steel grades with different chemical compositions, because in this flow regime, all fluid elements move in the same direction and at the same velocity, which minimizes the possibility of interpenetration of the streams and mixing of successive steel batches. In contrast, ideal mixing volume flow is advantageous for the chemical and thermal homogenization of liquid steel, which during long casting sequences favourably influences

* *Department of Metals Extraction and Recirculation, Faculty of Production Engineering and Materials Technology, Czestochowa University of Technology, Poland.*

© *The Southern African Institute of Mining and Metallurgy, 2018.* *ISSN 2225-6253. Paper received Feb. 2017. revised paper received Nov. 2017.*

the quality of liquid steel flowing to the mould. For this reason, the overall hydrodynamic pattern should be characterized by the lowest possible contribution of stagnant volume flow and a well-balanced range of dispersed plug flow and ideal mixing volume flow. Argon flow rates in tundishes are much lower than in ladle furnace (LF) treatment, therefore a measurable effect can be achieved in the form of an improved hydrodynamic pattern for reasonable costs related to argon consumption. A further advantage is the reduced quantity of refractory materials (no classical flow-control devices) in the internal working volume of the tundish. This paper presents the results of numerical simulations and laboratory experiments (using a water model) concerning the use of a gas-permeable barrier (GPB) in the one-strand tundish.

Tundish and argon curtain system

Figure 1a shows the one-strand tundish currently used in industry. The nominal capacity of the tundish is 30 t. Currently, the tundish is furnished with a low dam, 0.12 m in height, installed before the bottom step in the stopper-rod system area. The dam incorporates two 0.14 × 0.05 m overflow windows arranged symmetrically relative to the tundish axis. The inner diameters of the ladle shroud supplying liquid steel to the tundish and tundish nozzle supplying steel to the mould are identical, being equal to 0.07 m. Figure 1b illustrates the locations P1, P2, and P3 of GPB installations in the tundish working volume. In all of the proposed tundish furnishing variants, the flow control device in the form of a low dam was retained. Three argon flow rates, *i.e.* 5, 10, and 15 Nl/min, were tested. In a 75 mm-high GPB, a 50 × 750 mm porous plug is positioned in such a manner that, immediately at the sidewalls of the tundish, no argon will flow into the liquid steel. This design was aimed at protecting the tundish brickwork and maintaining the hydrodynamic liquid steel flow condition at the tundish sidewalls, which is characteristic of a tundish not furnished with an argon feed system (Cwudziński, 2015). In previous research (Cwudziński, 2010a, 2010b, 2010c) the optimal position of the GPB in the tundish was found to be in the mid-length of the bottom (position P2, Figure 1b). During the course of the current investigation, two additional gas-permeable barrier locations, shifted by 375 mm from the middle position, were considered, one being shifted towards the stopper-rod system and the other towards the pouring zone (Table I).

Mathematical model

For building the virtual model, the Gambit computer program was used. The numerical domain included tet/hybrid elements of the Tgrid type. The created virtual tundishes with GPB were composed of computational grid, from 161 900 to 165 700 elements. The software program ANSYS-Fluent was used to perform numerical simulations of the behaviour of liquid steel during continuous casting of slabs. The basic mathematical model equations describing the phenomena under consideration examination are as follows (Szekely, 1979; Mazumdar and Evans, 2010):

$$\frac{\partial \rho}{\partial t} = -\left[\frac{\partial}{\partial x}(\rho u) + \frac{\partial}{\partial y}(\rho u) + \frac{\partial}{\partial z}(\rho u)\right] \quad [1]$$

$$\frac{\partial}{\partial t}(\rho u) = -\left[\frac{\partial}{\partial x}(\rho u u) + \frac{\partial}{\partial y}(\rho u u) + \frac{\partial}{\partial z}(\rho u u)\right] - \left[\frac{\partial p}{\partial x} + \frac{\partial p}{\partial y} + \frac{\partial p}{\partial z}\right] - \left[\frac{\partial}{\partial x}\tau + \frac{\partial}{\partial y}\tau + \frac{\partial}{\partial z}\tau\right] + \rho g \quad [2]$$

$$\frac{\partial}{\partial t}(\rho E) = -\left[\frac{\partial}{\partial x}(u\rho E + p) + \frac{\partial}{\partial y}(u\rho E + p) + \frac{\partial}{\partial z}(u\rho E + p)\right] + \frac{\partial}{\partial x}\left(k_{eff}\frac{\partial T}{\partial x}\right) + \frac{\partial}{\partial y}\left(k_{eff}\frac{\partial T}{\partial y}\right) + \left(k_{eff}\frac{\partial T}{\partial z}\right) \quad [3]$$

where g is the gravitational acceleration (m/s^2), E the energy (J), k_{eff} the effective thermal conductivity (W/mK), p the pressure (Pa), t the time (s), T the temperature (K), u the velocity (m/s), τ the stress tensor (Pa), and ρ the density (kg/m^3).

Table I

Considered variants of tundish

Tundish variants	Type of flow control device				Argon flow rate, Nl/min		
	Low dam	GPB P1	GPB P2	GPB P3	5	10	15
1	×						
2	×	×			×		
3	×	×				×	
4	×	×					×
5	×		×		×		
6	×		×			×	
7	×		×				×
8	×			×	×		
9	×			×		×	
10	×			×			×

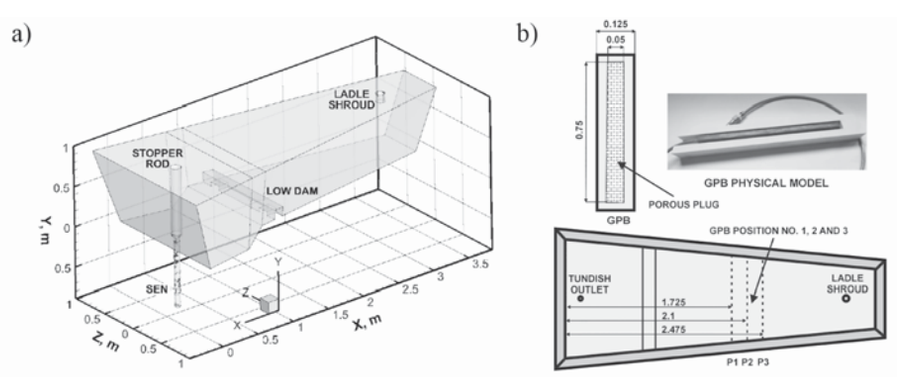

Figure 1—Tundish and gas-permeable barrier (GPB): (a) low dam tundish, (b) position mounting of GPB

For the description of interactions between liquid steel and argon, the discrete phase model was chosen. The coupled procedure was used to model the influence of argon bubbles on the movement of liquid steel. The thermal energy model included transport energy by conduction and convection under turbulent conditions. For the non-isothermal conditions of steel flow through the tundish, the magnitudes of heat fluxes on particular tundish walls and bottom were determined to be –2600 W/m^2, and –1750 W/m^2 on the regulator walls. The losses on the steel free surface were –15 000 W/m^2. The heat fluxes were determined on the basis of industrial trials, and have been repeatedly used by many researchers and also tested for the considered tundish (Chakraborty and Sahai, 1992; Morales *et al.*, 1999; Miki and Thomas, 1999; Barron-Meza, Barreto-Sandoval, and Morales, 2000; Lopez-Ramirez *et al.*, 2001; Morales *et al.*, 2001; Singh, Paul, and Ray, 2003; Lopez-Ramirez *et al.*, 2004; Zhang, 2005). The wall condition with zero tangential stress was assumed on the free steel table surface. A user-defined scalar (UDS) transport equation was used to calculate the motion of the tracer in the liquid steel. For the description of the turbulence of steel flow through the tundish, the realizable k-ε turbulence model was adopted. In the realizable k-ε turbulence model, constants take on the following values: C1 =1.44, C2=1.9, k=1.0, σ_ε=1.2 (Shih *et al.*, 1995). For the realizable k-ε turbulence approach, turbulent viscosity C_μ is not constant, and is calculated on the basis of the actual level of kinetic energy, dissipation rate, and fluid angular velocity (Majumdar, 2011). The physical parameters of the liquid steel are as follows: viscosity 0.007 kg/m s, heat capacity 750 J/kg K, thermal conductivity 41 W/m K, and thermal expansion 0.0001 1/K (Cwudziński, 2010). The density of liquid steel was described by the polynomial function ρ = 8300 – 0.7105T (Cwudziński, 2014a). At the tundish inlet, a liquid steel inflow of 1.316 m/s was assumed with turbulence kinetic energy of 0.0173 m^2/s^2 and rate of energy dissipation 0.065137 m^2/s^3. The kinetic energy and dissipation rate were calculated from the relationships presented by Morales *et al.* (2000) and Lopez-Ramirez *et al.* (2001). The initial liquid steel velocity corresponded the continuous casting of 1.5 × 0.225 m slabs at a speed of 0.9 m/min. The initial liquid steel temperature in the non-isothermal computer simulation was 1823 K.

Physical water model

The 210 litre-capacity tundish model was constructed on a scale of 0.4 (Figure 2). In accordance with the criteria of similarity, the medium simulating the liquid steel was water,

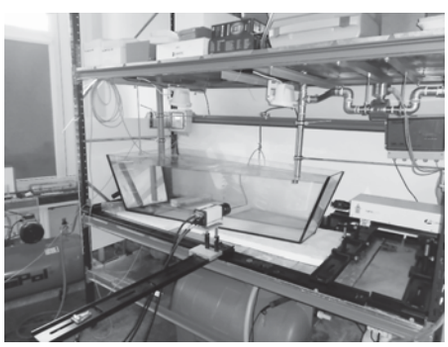

Figure 2—Tundish water model

which at 20°C has a kinematic viscosity identical to that of liquid steel. The argon gas was simulated by air. It is obvious that air has different physical properties to argon, but it is nearly always use during water modelling of steelmaking processes. The laboratory experiments for the water-air system were performed while meeting the Froude criterion, which ensured the similarity between the gravitational and inertial forces occurring in the physical tundish model and in the actual metallurgical plant was preserved (Krishnapisharody and Irons, 2013).

$$\left(\frac{u^2}{gL}\right)_m = \left(\frac{u^2}{gL}\right)_p \quad [4]$$

where L is the characteristic length (m), u the velocity of the continuous medium (m/s), and g the acceleration due to gravity (m/s^2).

The basic expression describing the initial volumetric flow rate of water and air in the physical model is as follows:

$$Q_{w/air} = \lambda^{2.5} Q_{ls/Ar} \quad [5]$$

where $Q_{w/air}$ is the water/air volumetric flow rate (m^3/s), $Q_{ls/Ar}$ the liquid steel/argon volumetric flow rate (m^3/s), and λ the scale factor.

Water flowed into the tundish model at an average flow rate of 30 Nl/min. Air at a flow rate of 0.5, 1, and 1.5 Nl/min was blown into the physical tundish model through a specially designed gas-permeable injection barrier. A camera and a double-cavity laser with a pulse energy of 200 mJ and a wavelength of 532 nm with an optical light knife system with a light beam was used during laboratory trials. For the analysis of the vector flow field, the DaVis 8.0 software program with the 2DPIV module was employed. Seeding in the form of 5 ml glass balls with a density of 1100 kg/m^3 (±50 kg/m^3) and an average diameter from 9 to 13 μm was introduced to the water flowing through the tundish model. The measurement of the vector flow field (PIV) in the physical tundish model was started after four average residence times had elapsed (time of casting one heat). After a steady field of flow was attained in the physical model's working volume, the laser was activated; the beam, passing through the optical system, formed a light plane in which the trajectories of glass ball motion was recorded. The glass balls flowed in accordance with flow directions forming in the water stream. Then a camera equipped with a filter adjusted to the wavelength of light emitted by the laser was activated. The purpose of the filter was to eliminate any ambient interference during recording. For the recording of residence time distribution (RTD) curves, a multimeter with titanium conductometric cells suitable for the measurement of variations in water salinity was used. For the pulse method of adding tracer a 2% salt solution was added to the water. During the stepwise addition of tracer, the batch of water in the tundish model was characterized by a salt concentration about 350 mg/l, whereas the concentration of salt in the water flowing from the ladle model to the tundish model was about 200 mg/l.

Residence time distribution curves and buoyancy number

The hydrodynamic condition in the tundish is described by

the RTD characteristics of types (E) and (F), which illustrate the motion of fluid elements between entering and exiting a specific system (Westerterp, van Swaaij, and Beenackers, 1984; Nauman and Buffham, 1983; Wen and Fan, 1975). The relationship between the residence time and the concentration of the substance results from the fact that the fluid elements have a varying time of residence in the system under consideration. A RTD curve can be drawn by adding a tracer in the form of a chemical substance to the fluid flowing into the facility and recording it at the outflow. The tracer can be introduced to the liquid in two ways: either by continuous feeding (step method) in a specific quantity, which enables F-type characteristics to be plotted; or by batchwise feeding of the tracer, so-called pulse tracer feeding, during which an E-type curve is recorded (Rosner, 1986; Levenspiel, 1999; Szekely and Ilegbusi, 1989; Himmelblau and Bischoff, 1968). The flow can be assessed by analysis of the graphic decomposition of the curve. For the quantitative analysis based on the volumes of individual flow types in the type of facilities under consideration in this work, the formulae provided by Sahai and Emi (1996), Mazumdar and Guthrie (1999), and Thomas (2003) can be used. In reality, industrial tundish designs are determined by the sizes of the stagnant volume, dispersed plug and ideal mixing volume flows, and the transient zone. Their quantitative assessment enables the selection of optimal design solutions for a given industrial tundish. Based on the results of Cwudziński's (2008) investigations carried out in industrial conditions, a transition zone in the range from 0.2 to 0.8 of (dimensionless) concentration of chemical element was chosen as representative for the tundish under consideration. In order to explain the phenomena occurring in the tundish working volume in relation to the influence of thermal stratification on steel flow, the buoyancy number (*Bu*), as described by Equation [6], was calculated.

$$Bu = \frac{g\beta\Delta TL}{u_{avg}^{2}} \qquad [6]$$

where g is the gravitational acceleration (m/s^2), L the depth of liquid steel (m), ΔT the temperature difference between the liquid steel flowing to the tundish and the liquid steel flowing to the mould (K), u_{avg} the average velocity of the steel flow (m/s), and β the thermal expansion (1/K).

The buoyancy number describes the effect of natural convection on the fluid flow pattern, and expresses the ratio of buoyancy forces to inertial forces in the system. A *Bu* value above 5 indicates that the liquid steel flowing through the tundish will be affected by natural convection, whereas a value < 1 will indicate the influence of forced convection on the motion of the steel.

Results and discussion

Isothermal conditions – flow structure

Numerical simulations and laboratory experiments were carried out for all considered variants of GPB position and argon flow rate. It was found that, in overall terms, the hydrodynamic system in the central part of the tundish did not change significantly with increasing argon flow rate, while the modification of the liquid steel movement was determined chiefly by the position of the injection barrier. The results of computer simulations and laboratory experiments are presented in Figures 3–5 for the considered GPB positioning locations and an argon flow rate of 5 Nl/min. In the central part of the tundish with the GPB in position P1, a clear influence of the argon phase on the liquid steel motion is apparent, whereby the liquid steel stream ascends towards the free surface (Figure 3a). On the stopper-rod system side, part of the liquid steel streams descending towards the tundish bottom turn back at the low dam to flow up to the argon injection region. The remaining descending streams in this part of the tundish flow towards the tundish nozzle. On the pouring zone side, a region of interaction of the streams flowing from the argon curtain and the pouring zone is apparent. Both flow regimes meet in the mid-measurement

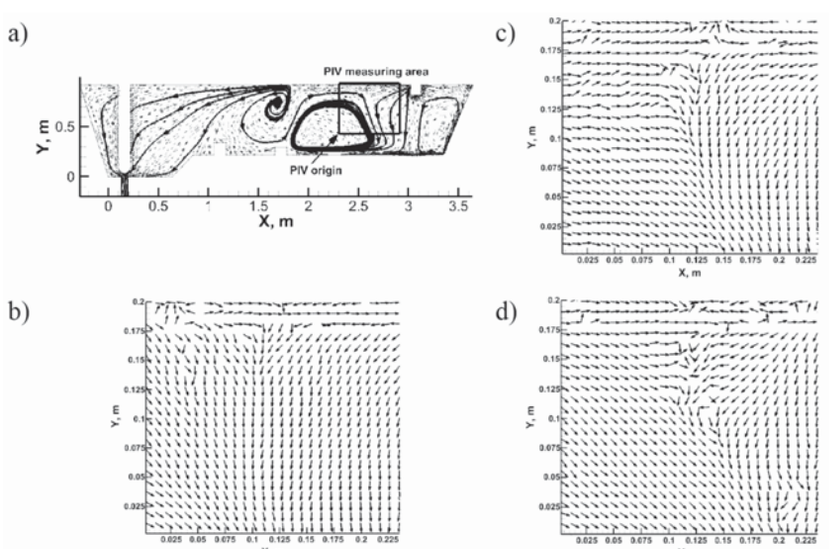

Figure 3— Vector flow fields for P1 GPB position: (a) numerical simulation of liquid steel flow (Ar flow rate 5 Nl/min), (b) physical modelling of water flow – trial no. 1, (c) physical modellling of water flow – trial no. 2, (d) physical modelling of water flow – trial no. 3

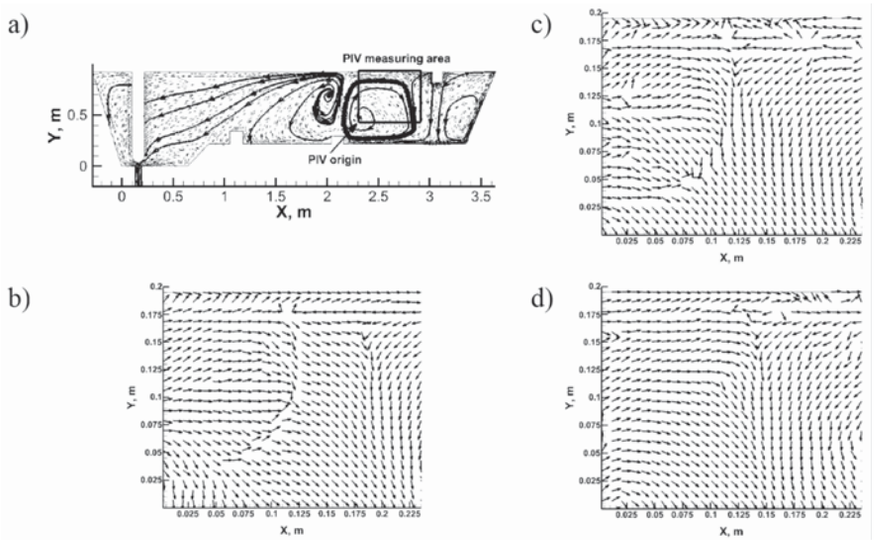

Figure 4—Vector flow fields for P2 GPB position: (a) numerical simulation of liquid steel flow (Ar flow rate 5 Nl/min), (b) physical modelling of water flow – trial no. 1, (c) physical modelling of water flow – trial no. 2, (d) physical modelling of water flow – trial no. 3

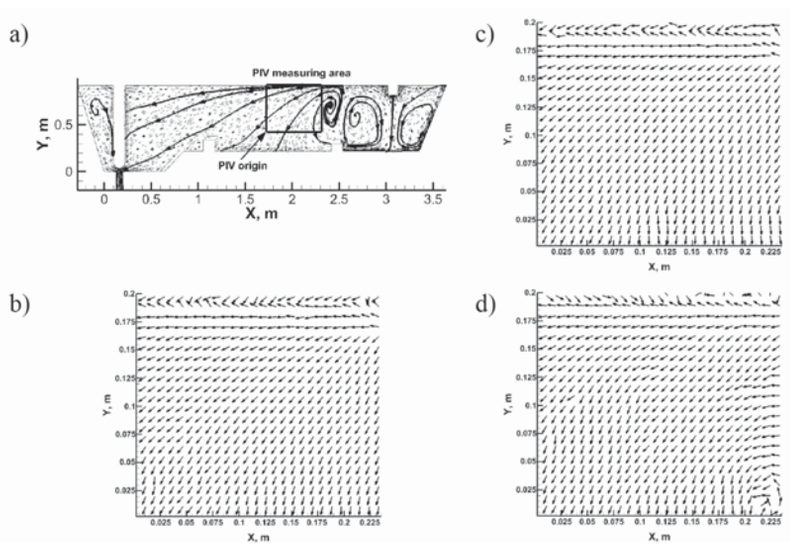

Figure 5—Vector flow fields for P3 GPB position: (a) numerical simulation of liquid steel flow (Ar flow rate 5 Nl/min), (b) physical modelling of water flow – trial no. 1, (c) physical modelling of water flow – trial no. 2, (d) physical modelling of water flow – trial no. 3

region, whereas the streams flowing from the argon curtain grow in strength as they approach the tundish bottom, penetrating through the tundish feeding streams. Shifting the GPB to position P2 did not significantly influence the overall hydrodynamic pattern in the central part of the tundish (Figure 4a). In this case also, the streams flowing from the GPB and from the pouring zone interact with each other; however, the region of interaction is shifted more towards the pouring zone. Shifting the GPB to position P3 reduces the liquid steel circulation region between the injection barrier and the liquid steel stream flowing into the tundish (Figure 5a). In that case an intensive region of circulation oriented to the free surface, descending according to the feed stream motion, flowing along the bottom towards the GPB, and then being entrained by argon bubbles, forms. In the zone between the GPB and the stopper-rod system, the hydrodynamic pattern in the central part of the tundish features streams descending from the free surface towards the bottom and the nozzle of the tundish. The water motion vector fields for GPB positions no. 1 and 2 confirm the occurrence in the measurement region of the lines of interaction of water streams flowing in from two directions, *i.e.* from the GPB and from the tundish model feed zone (Figures 3b, 3c, and 3d, 4b, 4c, and 4d). It is evident that the position of the zone of interaction of the abovementioned hydrodynamic patterns gradually moves with time. Disturbances in the vector field are also visible in some places, indicating a dynamism of water movement. Also, the water motion vector fields in the measurement region for the tundish with the GPB in position P3 confirm the hydrodynamic patterns obtained from the computer simulations (Figures 5b, 5c, and 5d). In either case, both the liquid steel and the water flow from the free surface towards the tundish bottom and the stopper-rod system.

Isothermal conditions – residence time distribution curves

Figure 6a shows E-type RTD curves for all tundish furnishing variants under consideration and the argon flow rates tested. In the tundish with the GPB in position no. 1, at an argon flow rate of 15 Nl/min a distinct shift in the curve peak from the Y axis occurs, which indicates an increase in the dispersed plug flow contribution to the overall flow pattern developing in the working space of the facility. When the GPB was moved to position no. 2, on the other hand, the largest increase in the contribution of dispersed plug flow volume was obtained at an argon flow rate of 5 Nl/min. In that tundish variant, a lowering of the peak position relative to the X axis was also obtained, which indicates intensification of the process of tracer spreading within the liquid steel volume, that is, the diversification of the flow pattern. With subsequent shifting of the GPB towards the pouring zone, the argon flow rate significantly influences the dispersed plug flow contribution, because the peaks for the tundish variants under consideration are positioned fairly close to one another relative to the Y axis. In contrast, their positions relative to the X axis differ, which is, obviously, closely related to the mixing power generated by the gas columns, which is the greater the higher the argon flow rate. For the GPB under discussion, laboratory casting sequences (water model) were performed. The F-RTD curves, in the form of points, were juxtaposed with the computer simulation results (Figure 6b). A fairly satisfactory agreement between the water-air experiments and the liquid steel-argon numerical simulations was achieved. Figure 7 presents the percentage contributions of the stagnant volume, dispersed plug, and ideal mixing volume flows. In the case of the GPB, for two locations of its installation and argon flows of 5 and 15 Nl/min, a reduction of the extent of stagnant volume flow was obtained. In the low-dam tundish currently in use commercially, stagnant volume flow accounts for 28%, and dispersed plug flow only 14% (Cwudziński, 2014b). An increase in the immersed dispersed plug flow was also obtained by increasing the ratio of dispersed plug flow to well-mixed volume flow from 0.24 for the tundish without a GPB to 0.38 and 0.47 for the tundish with the GPB. In the remaining GPB positioning variants and at the proposed argon flow rates, the stagnant volume flow contribution increased to as high as 40% in the tundish with the GPB in position no. 3. Shifting the GPB by another 375 mm towards the pouring zone caused not only an increase in stagnant volume flow, but also definitely decreased the dispersed plug flow contribution to the overall flow pattern to below 5%. Figure 8a shows F-type RTD curves for all tundish furnishing variants under consideration and argon flow rates tested. In the case of the GPB tundish, a definite effect of argon flow rate can be seen with different GPB positions. The laboratory experiments performed, by locating the obtained points in relation to the numerical curve, confirmed the correctness of numerical results for transitions zone behaviour during isothermal conditions (Figure 8b). The range of the transient zone is closely correlated with the dispersed plug flow portion of the overall pattern forming in the tundish working space. Therefore, reduction of the stagnant volume flow portion does not in itself assure hydrodynamic conditions favouring reduction of the extent of the transient zone. When a GPB was used, the most favourable reduction in transient zone range was obtained for the tundish with the GPB in position no. 2 at an argon flow rate of 5 Nl/min (Figure 9). In this case, the reduction of the transient zone decreased the weight of the transient steel slab by 1.5 t, compared to the tundish currently in use commercially. However, the investigation showed that the hydrodynamic conditions created by

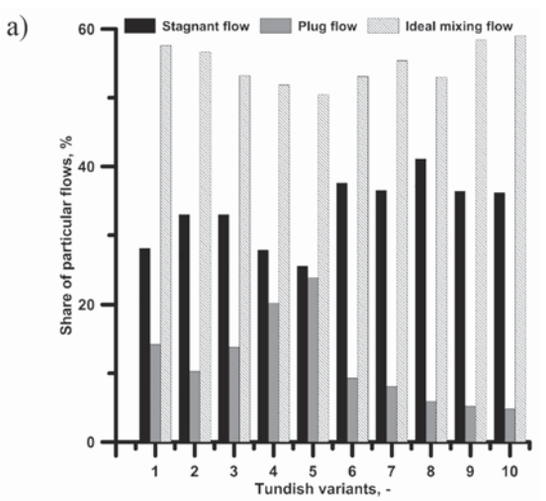

Figure 7—Hydrodynamic structure of liquid steel flow for isothermal conditions

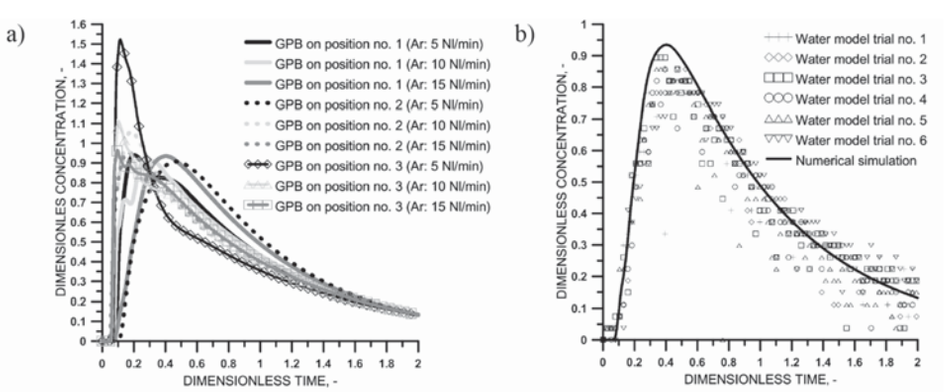

Figure 6—E-type RTD curves for tundish with GPB: (a) influence of GPB position and Ar flow rate on liquid steel flow structure, (b) numerical model validation

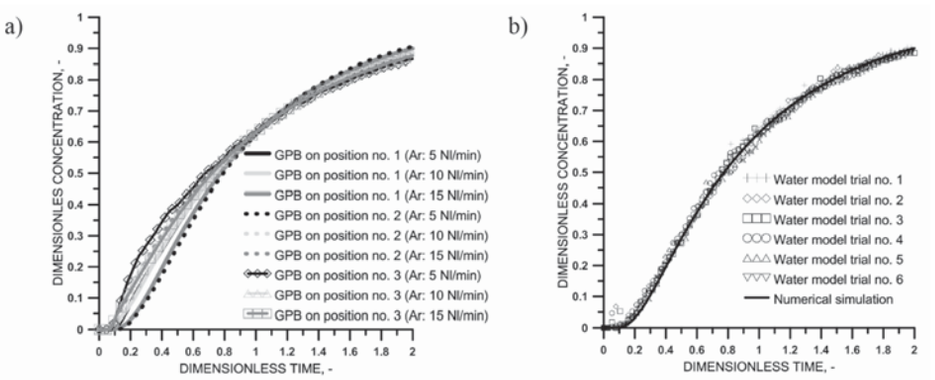

Figure 8—F-type RTD curves for tundish with GPB: (a) influence of GPB position and Ar flow rate on liquid steel flow structure, (b) numerical model validation

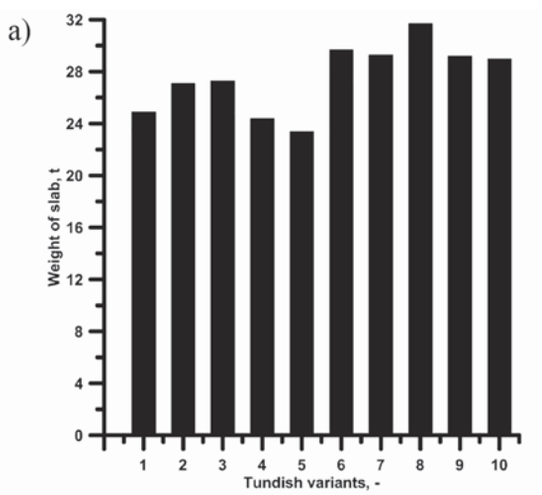

Figure 9—Weight of transition slab for isothermal conditions

interaction of the argon phase with liquid steel under isothermal conditions could considerably increase the extent of the transient zone, by as much as 6.8 Mg compared to the commercial tundish.

Non-isothermal conditions – flow structure

Figures 10 and 11 represent the results of computer simulations of liquid steel flow and temperature for non-isothermal conditions for the three most favourable GPB tundish variants, as selected based on the results obtained for isothermal conditions. The best tundish variants were characterized by the lowest value of stagnant flow for the considered GPB positions and argon flow rate. The hydrodynamic conditions in the low dam tundish (Figure 10a) are described in detail by Cwudziński (2014b, 2017). In the tundish with GPB in position P1 with an argon flow of 15 Nl/min, the GPB causes liquid steel to recirculate between the feed zone and the argon injection zone (Figure 10b). The

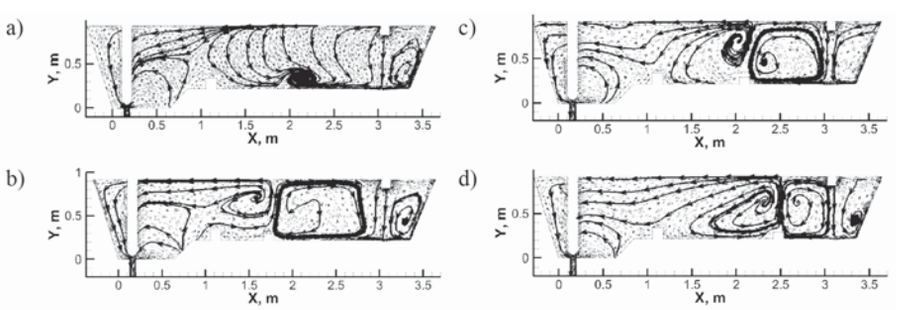

Figure 10—Liquid steel vector flow fields for tundish non-isothermal condition: (a) tundish with low dam, (b) tundish with P1 GPB position and Ar: 15 Nl/min, (c) tundish with P2 GPB position and Ar: 5 Nl/min, (d) tundish with P3 GPB position and Ar: 15 Nl/min

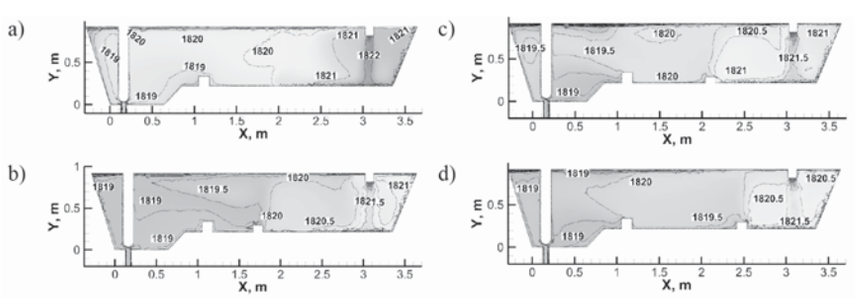

Figure 11—Liquid steel temperature fields for tundish non-isothermal condition: (a) tundish with low dam, (b) tundish with P1 GPB position and Ar: 15 Nl/min, (c) tundish with P2 GPB position and Ar: 5 Nl/min, (d) tundish with P3 GPB position and Ar: 15 Nl/min

recirculation region is also fed by the backward-flowing streams that flow into the GPB region and, by interacting with argon bubbles, are carried towards the free surface and partially transferred to the recirculation zone. In the zone between the GPB and the stopper-rod system, parts of the streams flow in a horizontal configuration at the free surface. In the stopper-rod system zone at the bottom, part of the streams ascends towards the free surface and the other part flows in parallel along the bottom. With the GPB in position P2 and at an argon flow rate of 5 Nl/min, the liquid steel recirculation zone in the pouring zone is retained (Figure 10c). In contrast, upstream of the low dam, the liquid steel streams clearly descend towards the bottom. The flow of liquid steel in the stopper-rod system zone of the tundish with the GPB in position P2 is similar to that with the GPB in position P1, with the stream descending above the low dam counteracting the formation of the backward-flowing stream. This is particularly evident when the GPB is shifted to position P3, because the feed streams fall towards the low dam and then flow horizontally towards the stopper-rod (Figure 10d). Knowledge of the distribution of liquid steel temperature in the tundish with argon injection system is essential, because argon at ambient temperature is introduced to a high-temperature system. Figure 11 shows maps of the liquid steel temperature fields. The use of the GPB did not cause any drop in the liquid steel temperature due to the plume of argon bubbles flowing through the liquid steel. In the stopper-rod system, also, the liquid steel temperature is 1819 K, which compared to the initial liquid steel temperature value of 1823 K, represents a decrease of only 4 K.

Non-isothermal conditions – residence time distribution curves

The quantitative analysis of the tundish operation in selected GPB positioning variants for non-isothermal conditions was based on the E- and F-type RTD curves. The RTD curves enabled the assessment of the influence of thermal gradients forming in the bulk of the liquid steel on the hydrodynamic patterns developing in the working space of the facility. Figure 12 shows F- and E-type RTD curves for four tundish furnishing variants. In all of the proposed variants qualified for non-isothermal simulations, an increase in dispersed plug flow was obtained (Figure 12a). The position of the peaks of the E-type RTD curves relative to the X and Y axes is similar, which indicates similar conditions of tracer dispersal in the bulk of the liquid steel. The dimensionless concentration value oscillates around unity, which indicates a considerable degree of dissipation of the feed streams flowing to the tundish. This is also confirmed by an approximately 50% ideal mixing volume flow portion of the overall steel movement pattern. The smallest stagnant volume flow portion of 30.4% was obtained for the tundish with the GPB installed closer to the stopper-rod system and at an argon flow rate of 15 Nl/min (Table II). The distribution of all F-type RTD curves is very similar (Figure 12b). The least advantageous RTD curve shape was obtained with the argon curtain in position no. 3 and an argon flow rate of 15 Nl/min. Compared to the low dam tundish variant, this indicates an increase in the extent of the transient zone and a 0.5 Mg increase in the quantity of steel of the intermediate chemical composition larger by. The remaining GPB positioning variants and the employed argon flow rates of 5 and 15 Nl/min contributed to a reduction in the transient zone extent by 0.6 Mg (Table III). An advantageous reduction in the quantity of the steel of intermediate chemical composition was obtained for two GPB locations, by stimulating the active steel flow and minimizing the stagnant volume flow. Table IV gives the *Bu* number calculated for the analysed tundish furnishing variants and for non-isothermal conditions. The introduction of argon to the working volume of the tundish caused an increase in average liquid steel flow velocity up to 0.051 m/s with the GPB in position P1. The increase in liquid steel velocity enhances the momentum in the system and increases the influence of inertial forces on the hydrodynamic structure. The minimum influence of natural convection on

Table II

Hydrodynamic structure of liquid steel flow for non-isothermal conditions

Tundish variants	Stagnant flow, %	Dispersed plug flow, %	Ideal mixing flow, %
1	31.3	11.2	57.5
4	30.4	18.3	51.3
5	30.6	16.7	52.7
10	32.8	14.2	53

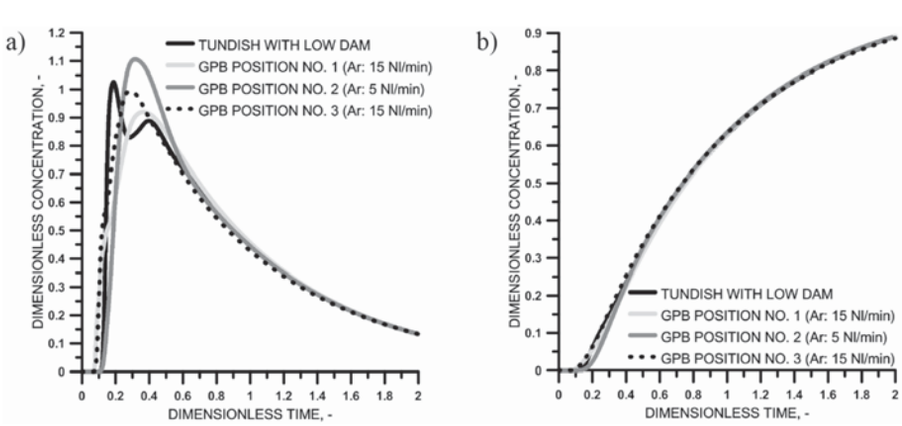

Figure 12—RTD curves for non-isothermal conditions: (a) type E, (b) type F

Table III

Transition zone for non-isothermal conditions

Tundish variants	Transition zone time, s	Slab length, m	Transition slab weight, Mg	Influence of GPB on transition slab weight, Mg
1	741	11.12	26.3	×
4	725	10.87	25.7	– 0.6
5	726	10.89	25.7	– 0.6
10	758	11.37	26.8	+ 0.5

Table IV

Buoyancy numbers for non-isothermal condition in the tundish

Tundish variants	Coefficient of thermal expansion, 1/K	Liquid steel average velocity, m/s	Temperature difference ΔT, K	Liquid steel level, m	*Bu* number
1	0.0001	0.036	5	0.7 0.92	2.65 3.48
4	0.0001	0.051	5	0.7 0.92	1.32 1.73
5	0.0001	0.041	5	0.7 0.92	2.04 2.68
10	0.0001	0.050	5	0.7 0.92	1.37 1.81

the hydrodynamic system is confirmed by the low *Bu* values of below 2. Slightly higher *Bu* values of 2.68 were obtained for the stopper-rod system zone, which is characterized by a greater height of the liquid steel column. It is chiefly in the region of the stopper-rod system that the largest difference in flow pattern was evident between computer simulations performed for non-isothermal and isothermal conditions.

Summary

- The GPB introduces additional momentum to the system by the interaction between the argon bubbles and the liquid steel, leading to an increase in flow velocity, thus highlighting the role of inertial forces in the modification of the hydrodynamic pattern
- Under non-isothermal conditions, the temperature stratification in the liquid steel will modify the steel flow in regions of the tundish working space remote from the argon injection and tundish feed zones, resulting in a change in the hydrodynamic pattern
- Shifting the GPB towards the feed zone does not favourably influence the extent of the transient zone. This is due to the intensification of the steel mixing process initiated by the feeding stream and the argon plume
- Advantageous hydrodynamic conditions in relation to the transient zone range were obtained for the tundish variant with the GPB positioned closer to the stopper-rod system in the mid-length of the bottom of the tundish feed zone
- The modification of the hydrodynamic pattern of liquid steel movement in the GPB tundish depends on the argon flow rate, which is closely correlated with the location of the GPB and the thermal condition of the steel grade being cast.

Acknowledgements

This research work was sponsored by the Ministry of Science and Higher Education under the IuventusPlus programme, project no. IP2014 006973, in the years 2015–2016.

References

Bai, H. and Thomas, B.G. 2001. Turbulent flow of liquid steel and argon bubbles in slide-gate tundish nozzles: Part II. Effect of operation conditions and nozzle design. *Metallurgical and Materials Transaction B*, vol. 32. pp. 269–284.

Barreto, J. de J., Barron Meza, M.A., and Morales, R.D. 1996. Physical and mathematical modeling of steel flow and heat transfer in tundish under non-isothermal and non-adiabatic conditions. *ISIJ International*, vol. 36, no. 5. pp. 543–552.

Barron-Meza, M.A., Barreto-Sandoval, J. de J., and Morales, R.D. 2000. Physical and mathematical models of steel flow and heat transfer in a tundish heated by plasma. *Metallurgical and Materials Transaction B*, vol. 31. pp. 63–74.

Chang, S., Cao, X., Zou, Z. Isac, M., and Guthrie, R.I.L. 2016. Microbubble swarms in a full-scale water model tundish. *Metallurgical and Materials Transaction B*, vol. 47. pp. 2732–2743.

Chakraborty, S. and Sahai, Y. 1991. Effect of varying ladle stream temperature on the melt flow and heat transfer in continuous casting tundishes. *ISIJ International*, vol. 31, no. 9. pp. 960–967.

Chakraborty, S. and Sahai, Y. 1992. Effect of holding time and surface cover in ladles on liquid steel flow in continuous casting tundishes. *Metallurgical and Materials Transaction B*, vol. 23. pp. 153–167.

Chang, S., Zhong, L., and Zou, Z. 2015. Simulation of flow and heat fields in a seven-strand tundish with gas curtain for molten steel continuous-casting. *ISIJ International*, vol. 55, no. 4. pp. 837–844.

Chattopadhyay, K., Hasan, M., Isac, M., and Guthrie, R.I.L. 2010. Physical and mathematical modeling of inert gas-shrouded ladle nozzles and their role on slag behavior and fluid flow patterns in a delta-shaped, four-strand tundish. *Metallurgical and Materials Transaction B*, vol. 41. pp. 225–233.

Chen, D., Xie, X., Long, M., Zhang, M., Zhang, L., and Liao, Q. 2014. Hydraulic and mathematics simulation on the weir and gas curtain in tundish of ultrathick slab continuous casting. *Metallurgical and Materials Transaction B*, vol. 45. pp. 392–398.

Cloete, J.H., Akdogan, G., Bradshaw, S.M., and Chibwe, D.K. 2015. Physical and numerical modelling of a four-strand steelmaking tundish using flow analysis of different configurations. *Journal of the Southern African Institute of Mining and Metallurgy*, vol. 115. pp. 355–362.

Cwudziński, A. 2008. Regulation of steel flow in the slab tundish. PhD thesis, Czestochowa University of Technology (in Polish).

Cwudziński, A. 2010a. Numerical simulation of liquid steel flow in wedge-type one strand slab tundish with a subflux turbulence controller and an argon injection system. *Steel Research International*, vol. 81, no. 2. pp. 123–131.

Cwudziński, A. 2010b. Numerical simulation of steel flow through a one strand slab tundish with steel flow control devices. *Canadian Metallurgical Quarterly*, vol. 49, no. 1. pp. 63–72.

Cwudziński, A. 2010c. Numerical simulation of liquid steel flow and behaviour of non-metallic inclusions in one-strand slab tundish with subflux turbulence controller and gas permeable barrier. *Ironmaking and Steelmaking*, vol. 37, no. 3. pp. 169–180.

Cwudziński,, A. 2014a. Numerical and physical prediction of hydrodynamic conditions in one strand slab tundish. *Metallurgical Research & Technology*, vol. 111, no. 1. pp. 45–55.

Cwudziński, A. 2014b. Numerical and physical modeling of liquid steel active flow in tundish with subflux turbulence controller and dam. *Steel Research International*, vol. 85, no. 5. pp. 902–917.

Cwudziński, A. 2015. Numerical, physical, and industrial studies of liquid steel chemical homogenization in one strand tundish with subflux turbulence controller. *Steel Research International*, vol. 86, no. 9. pp. 972–983.

Cwudziński, A. 2017. Physical and mathematical simulation of liquid steel mixing zone in one strand continuous casting tundish. *International Journal of Cast Metals Research*, vol. 30, no. 1. pp. 50–60.

Ganguly, S. and Chakraborty, S. 2004. Numerical investigation on role of bottom gas stirring in controlling thermal stratification in steel ladles. *ISIJ International*, vol. 44, no. 3. pp. 537–546.

Himmelblau, D.M. and Bischoff, K.B. 1968. Process Analysis and Simulation. Wiley, New York.

Ilegbusi, O.J. and Szekely J. 1989. Effect of magnetic field on flow, temperature and inclusion removal in shallow tundishes. *ISIJ International*, vol. 29, no. 12. pp. 1031–1039.

Jiang, J., Li, J.S., Wu, H.J., Yang, S.F., Li, T., and Tang, H.Y. 2010. Water modeling of molten steel flow in a multi-strand tundish with gas blowing. *International Journal of Minerals, Metallurgy and Materials*, vol. 17, no. 2. pp. 143–148.

Joo, S. and Guthrie, R.I.L. 1992. Modeling flows and mixing in steelmaking ladles designed for single- and dual-plug bubbling operations. *Metallurgical and Materials Transaction B*, vol. 23. pp. 765–778.

Krishnapisharody, K. and Irons, G.A. 2013. A critical review of the modified Froude number in ladle metallurgy. *Metallurgical and Materials Transaction B*, vol. 44. pp. 1486–1498.

Levenspiel, O. 1999. Chemical Reaction Engineering. Wiley, New York.

Liu, R. and Thomas, B.G. 2015. Model of gas flow through porous refractory applied to an upper tundish nozzle. *Metallurgical and Materials Transaction B*, vol. 46. pp. 388–405.

Lopez-Ramirez, S., Barreto, J. de J., Palafox-Ramos, J., Morales, R.D., and Zacharias, D. 2001. Modeling study of the influence of turbulence inhibitors on the molten steel flow, tracer dispersion, and inclusion trajectories in tundish. *Metallurgical and Materials Transaction B*, vol. 32. pp. 615–627.

Lopez-Ramirez, S., Barreto, J. de J., Vite-Martinez, P., Romero Serrano J.A., and Duran-Valencia C. 2004. Physical and mathematical determination of the influence of input temperature changes on the molten steel flow characteristics in slab tundishes. *Metallurgical and Materials Transaction B*, vol. 35. pp. 957–966.

Mabentsela, A., Akdogan, G., and Bradshaw S. 2017. Numerical and physical modeling of tundish slag entrainment in the steelmaking process. *Journal of the Southern African Institute of Mining and Metallurgy*, vol. 117. pp. 469–483.

Majumdar, P. 2011. Computational fluid dynamics analysis of turbulent flow. *Computational Fluid Dynamics Technologies and Applications*. Minin I.V. and Minin O.V. (eds.). Intech. Chapter 9, pp. 255–292.

Maldonado-Parra, F.D., Ramírez-Argáez, M.A., Conejo, A.N., and González, C. 2011. Effect of both radial position and number of porous plugs on chemical and thermal mixing in an industrial ladle involving two phase flow. *ISIJ International,* vol. 51, no. 7. pp. 1110–1118.

Mazumdar, D. and Guthrie, R.I.L. 1999. The physical and mathematical modelling of continuous casting tundish systems. *ISIJ International*, vol. 39, no. 6. pp. 524–547.

Mazumdar, D. and Evans, J.W. 2010. Modeling of Steelmaking Processes. CRC Press, Boca Raton, FL.

Miki, Y. and Thomas, B.G. 1999. Modeling of inclusion removal in a tundish. *Metallurgical and Materials Transaction B*, vol. 30. pp. 639–654.

Morales, R.D., Lopez-Ramirez, S., Palafox-Ramos, J., and Zacharias D. 1999. Numerical and modeling analysis of fluid flow and heat transfer of liquid steel in a tundish with different flow control devices. *ISIJ International,* vol. 39, no. 5. pp. 455–462.

Morales, R.D., Barreto, J. de J., Lopez-Ramirez, S., Palafox-Ramos J., and Zacharias D. 2000. Melt flow control in a multi-strand tundish using a turbulence inhibitor. *Metallurgical and Materials Transaction B*, vol. 31. pp. 1505–1515.

Morales, R.D., Lopez-Ramirez, S., Palafox-Ramos, J., and Zacharias, D. 2001. Mathematical simulation of effects of flow control devices and buoyancy forces on molten steel flow and evolution of output temperatures in tundish. *Ironmaking and Steelmaking*, vol. 28, no. 1. pp. 33–43.

Nauman, E.B. and Buffham, B.A. 1983. Mixing in Continuous Flow Systems, Wiley, New York.

Rosner, D.E. 1986. Transport Processes in Chemically Reacting Flow Systems. Butterworth, Stoneham, MA.

Sahai, Y. and Emi, T. 1996. Melt flow characterization in continuous casting tundishes. *ISIJ International*, vol. 36, no. 6. pp. 667–672.

Singh, R.K., Paul, A., and Ray, K. 2003. Modelling of flow behaviour in continuous casting tundish. *Scandinavian Journal of Metallurgy*, vol. 32. pp. 137–146.

Shih, T.-H., Liou, W.W., Shabbir, A., Yang, Z., and Zhu, J. 1995. A new k- eddy viscosity model for high Reynolds number turbulent flows. *Computers & Fluids*, vol. 24, no. 3. pp. 227–238.

Smirnov, A.N., Efimova, V.G., Kravchenko, A.V., and Pismarev, K.E. 2014. Flotation of nonmetallic inclusions during argon injection into the tundish of a continuous casting machine. Part 3. *Steel in Translation*, vol. 44, no. 3. pp. 180–185.

Smirnov, A.N., Efimova, V.G., and Kravchenko, A.V. 2013. Flotation of nonmetallic inclusions during argon injection into the tundish of a continuous casting machine. Part 1. *Steel in Translation*, vol. 43, no. 11. pp. 673–677.

Smirnov, A.N., Efimova, V.G., and Kravchenko, A.V. 2014. Flotation of nonmetallic inclusions during argon injection into the tundish of a continuous casting machine. *Part 2. Steel in Translation*, vol. 44, no. 1. pp. 11–16.

Szekely, J. 1979. Fluid Flow Phenomena in Metals Processing. Academic Press, New York.

Szekely, J. and Ilegbusi, O.J. 1989. The Physical and Mathematical Modelling of Tundish Operations, Springer-Verlag, Berlin.

Thomas, B.G. 2003. Modeling study of intermixing in tundish and strand during a continuous casting grade transition. *Continuous Casting Tundish Operations*. Schade, J. (ed.), vol. 10. pp. 115–127.

Vargas-Zamora, A., Morales, R.D., Díaz-Cruz, M., Palafox-Ramos, J., and Barreto-Sandoval, J. de J. 2004. Inertial and buoyancy driven water flows under gas bubbling and thermal stratification conditions in a tundish model. *Metallurgical and Materials Transaction B*, vol. 35. pp. 247–257.

Wang, J., Zhu, M.Y., Zhou, H.B., and Wang, Y. 2008. Fluid flow and interfacial phenomenon of slag and metal in continuous casting tundish with argon blowing. *Steel Research International*, vol. 15, no. 4. pp. 26–31.

Wen, CY. and Fan, L.T. 1975. Models for Flow Systems and Chemical Reactors. Marcel Dekker, New York.

Westerterp, K.R., van Swaaij, W.P.M., and Beenackers, A.A. 1984. Chemical Reactor Design and Operation. Wiley, New York.

Zhang, L. 2005. Fluid flow, heat transfer and inclusion motion in a four-strand billet continuous casting tundish. *Steel Research International*, vol. 76, no. 11. pp. 784–796.

Zhong, L., Li, L., Wang, B., Jiang, M., Zhu, L., and Chen, R. 2006. Water modeling experiments of argon bubbling curtain in a slab continuous casting tundish. *Steel Research International,* vol. 77, no. 2. pp. 103–106. ◆

http://dx.doi.org/10.17159/2411-9717/2018/v118n5a12

Particle size distribution and energy consumption during impact crushing of single granite particles

by H.Y. Fang, J.H. Yang, and Q. Chen

Synopsis

To study the effects of crushing parameters on particle size distribution and energy consumption of rock impact crushing, a custom-made experimental rig was used for impact crushing tests on single particles of granite. The particle size distribution of the crushed product was analysed, as well as the sand production ratio and energy consumption per unit sand product under different impact velocities and with different primary particle sizes. The results show that the particle size distribution of the crushed granite under different experimental parameters is in accordance with the Weibull distribution. With a decrease in the primary particle size, or a specified impact velocity, the discreteness of the particle size distribution of the fragments becomes greater. An optimal impact velocity exists at which the energy consumption per unit sand product is minimized. Also, it was found that the smaller the primary particle size, the lower the energy consumption per unit sand produced.

Keywords

granite, single-particle impact crushing, impact velocity, primary particle size, particle size distribution; specific energy consumption.

Introduction

In both civil and architectural engineering, sand is an important constituent of concrete, and the consumption of sand for such use is significant. In recent years, the supply of natural sand has become inadequate, resulting in a need to produce relatively large amounts of manufactured, high-quality sand. Research has shown that the vertical shaft impact (VSI) crusher can produce manufactured sand with high enough quality to compete with natural sands (Gopalakrishnan and Murugesan, 2015; Bengtsson and Evertsson, 2006; Johansson and Evertsson, 2014; Luo Yang, and Fang, 2014; Åkesson and Tjell, 2010).

There are many factors that affect the fragmentation characteristics of rock. Ovalle. (2014) analysed the effects of particle size on rock aggregate crushing strength, and concluded that strength decreases as particle size decreases. Nikolov (2002, 2004) presented a model for the particle size distribution of material crushed by hammer or VSI crusher, expressed as a function of the crusher rotor radius and angular velocity, the feed rate, and the feed size distribution. In the model of Bengtsson and Evertsson (2008), typical parameters of mass flow and absolute velocity of particles were incorporated to calculate the capacity and power of a VSI crusher. The model predictions were compared with experimental data obtained from a full-scale VSI crusher to select appropriate parameters to improve production of manufactured sand under conditions of minimum energy consumption. However, it was found that the conditions in the VSI crusher were not ideal for high-quality sand manufacturing, and instrumental monitoring of the sand-making process inside the crushing chamber was difficult.

From the research to date, it is evident that the velocity of particles ejected from the rotor is typically obtained theoretically, and based on many assumptions. In 2009 (Shi *et al.*, 2009), the Julius Kruttschnitt Mineral Research Centre (JKMRC) comminution research team developed a Rotary Breakage Tester (JKRBT) for testing of rapid particle fragmentation. In the device, a high-speed video camera was used to measure impact velocity, although the interactions of rocks inside the crushing chamber are complex and chaotic. As a result, it is difficult to determine the main factors that influence particle fragmentation characteristics and energy consumption.

These challenges can be addressed by using the experimental method of single particle impact crushing. Laboratory material fragmentation studies can be broadly classified into two groups based on the role of external forces applied: compression crushing and impact crushing. The representative test methods for the former are the twin pendulum (Weedon and Wilson, 2000; Sahoo, Weedon, and Roach, 2004a, 2004b; Narayanan, 1985; Cai *et al.*, 2016), drop weight tester (DWT) (Napier-Munn *et al.*, 1996; Saeidi, *et al.*, 2016; Hu *et al.*, 2015; Li, Zheng, and Du, 2013), and split Hopkinson pressure bar (SHPB) (Deng, *et*

* *College of Mechanical Engineering and Automation, Huaqiao University, China.*

© *The Southern African Institute of Mining and Metallurgy, 2018.* *ISSN 2225-6253. Paper received May 2017; revised paper received Jul. 2017.*

al., 2016; Li *et al.*, 2009; Zhang *et al.*, 2000). The experimental device presented in the literature by Jiang, Du, and Liu (2013) belongs to the latter group, given that the particles were accelerated by a drive belt and then crushed on an impact plate. In compression crushing, two solid working surfaces move from opposite directions, and when the distance between them is reduced to a certain value, the compressive stress on the particles reaches its limiting value and fragmentation occurs. In this scenario, the strain of the particle occurs between two solid working surfaces. In impact crushing, high-speed particles impact fixed or moving targets, causing the particles to be subjected to extremely rapid impact loading. When the ultimate value of stress is reached, fragmentation occurs. In this scenario, the strain on the particle occurs on one working surface, such as in a VSI crusher, in which the particles are broken during impact.

Particle fragmentation characterization aims to quantify the size distribution of the product and establish the relationship between specific energy inputs and resultant product through laboratory testing (Napier-Munn *et al.*, 1996). There are many published studies on particle size distribution of the rock product and the related energy consumption. Early in 1996, the relationship between t_{10} and specific comminution energy was developed by the JKMRC (Napier-Munn *et al.*, 1996; Bearman, Briggs, and Kojovic, 1997; Delaney *et al.*, 2015; Cleary *et al.*, 2017), wherein the factor t_{10} is the percentage of material passing 1/10th of the original feed size, and thus represents the degree of fragmentation.

Another common function used to represent the rock product of mechanical comminution is the Rosin-Rammler distribution, or Weibull distribution (Rosin and Rammler, 1933; Weibull, 1939, 1951). A number of investigators report that the Weibull distribution can be used to describe the mass accumulation distribution of brittle material fragments (Sanchidrián *et al.*, 2012, 2014; Paluszny *et al.*, 2015; Jiang, Du, and Liu, 2013; Li, Zheng, and Du, 2013). In the study of Jiang, Du, and Li (2013), according to the Griffith theory of brittle fracture, the surface energy formula is used to calculate the fracture energy formed in the new surface, and from such it is evident that the energy dissipation rate increases with impact velocity. To date, the effect of impact velocity and primary particle size on product particle size distribution, and the energy consumption per unit sand product, have been rarely mentioned in the literature. The suitability of a Weibull distribution model for describing the distribution of rock product grain size from impact crushing is also in question.

In this paper, the results of impact crushing experiments on single granite particles are presented for different impact velocities and different primary particle sizes. Based on a Weibull distribution model, the particle size distribution of the product is analysed, and the energy consumption per unit sand product is also discussed. This research is aimed at the selection of parameters for sand manufacturing using a VSI crusher.

Modelling

Weibull distribution model

The definition of Weibull distribution was first put forward by Maurice Fréchet. Rosin and Rammler (1933) applied a Weibull distribution model for the first time when studying the particle size distribution of coal. A Weibull distribution model that describes the particle size distribution obtained from impact crushing of a granite single particle can be expressed as:

$$R_{(d)} = 1 - \exp\left[-\left(\frac{d}{D}\right)^n\right] \quad [1]$$

where $R_{(d)}$ is the cumulative mass percentage of particles ≤d in size after crushing. The factor d denotes any particles in the size range of the crushed product, while D is the particle size when $R_{(d)}$ = 63.2%. The Weibull modulus, n, can be used to characterize the uniformity of particle size distribution. To analyse the particle size distribution, a logarithmic transform is applied to both sides of Equation [1] to obtain the particle size distribution function after crushing:

$$f_{(d)} = \ln\left(-\ln\left(1 - R_{(d)}\right)\right) = n\ln d - n\ln D \quad [2]$$

where $f_{(d)}$ is defined as the cumulative mass distribution function of the crushed granite with particles no larger than d.

In order to predict the degree of granite fragmentation under different experimental parameters, the dimensionless parameter is defined as:

$$\varphi = \frac{D_0}{D} \quad [3]$$

where D_0 is the primary particle size of the granite.

Energy consumption per unit sand product model

Manufactured sand is mainly used in concrete with strength grade ≤C60 for building, municipal, transportation, and other construction projects. The required particle size for such concrete is ≤4.75 mm. In a VSI crusher, sand particles are produced by accelerating aggregate particles in a rotor to a specified velocity (the particles have relatively large kinetic energy) and ejecting them to impact on a static anvil made of liner material or wear-resistant metal. The impact results in crushing of the particles at high velocity as the fragments decelerate extremely rapidly.

The economic viability of manufactured sand production is closely related to the energy utilization ratio of the processes of particle acceleration and impact. For the latter, the kinetic energy of the particles is the energy input. The energy output includes the energy required to generate a new surface, the residual kinetic energy of fragments, the distributed heat energy, and friction energy, among other. Unfortunately, the ratio of fragmentation energy to input energy is difficult to determine. In this study, the energy input required to produce a unit of finished product is chosen as a measure of energy utilization, and is represented as energy consumption per unit sand product in kWh/t.

A particle with velocity (v) has a mass-specific kinetic energy (E), which is independent of the particle shape and mass, as shown below:

$$E = \frac{1}{2}v^2 \quad [4]$$

The sand production ratio (S_p) is defined as the mass percentage of fragments which are not larger than 4.75 mm in size. The value of S_p is expressed as:

$$s_p = \frac{m_i}{m_0} \times 100\% \quad [5]$$

where m_i is the mass of fragments no larger than 4.75 mm in size and m_0 is the total mass of the fragments. The energy consumption per unit sand product (E_s) is expressed as:

$$E_s = \frac{E / 3.6 \times 10^6}{s_p} \quad [6]$$

Single particle impact crushing test on granite

Test apparatus and method

Single particle impact crushing experiments on granite were performed using a custom-made test platform constructed mainly of stainless steel, as shown in Figure 1. The apparatus uses high-pressure gas stored in a container to provide energy to the particles entering from a feeder into the launch tube. The gas pressure can be adjusted to control the launch velocity. The single granite particle enters the feeder, the gas valve is opened, and the particle is launched and is accelerated through the launch tube into the crushing chamber. In the chamber the particle impacts a hardened metal anvil at a high velocity and is crushed.

The front side of the crushing chamber includes a large transparent window of bulletproof glass, which enables photographs of particles to be taken before impact using a high-speed camera (up to 10 000 images per second). A ruler in the window is used to record the locations of the particle in the crushing chamber, as shown in Figure 2. The distance between the two positions shown can be determined to scale using the ruler, and the time between the two positions can be obtained from the frame numbers of the corresponding photographs, thus allowing the velocity of the particle to be calculated. After impacting the anvil with relatively high kinetic energy, the granite particle breaks into many fragments. Powder generated from the impact rises under its own buoyancy in the air and escapes to a dust collecting device mounted at the top of the crushing chamber. Under the force of gravity, the larger fragments fall from the discharge port into another collector located under the crushing chamber. The fragments from the two collectors are then sieved and weighed to obtain the mass of fragments within each range of particle sizes.

Test conditions

After coarse or medium crushing with a jaw or cone crusher, the broken granite particles have irregular shapes. Because the impact point on the surface of the particle when it strikes the anvil is usually random, the forces acting on the particle have different effects depending on the particle's orientation at impact, and the corresponding crushing effect will also be different. To reduce the influence of irregular shapes, the granite particles used in these tests were carefully processed beforehand so as to be as close to spherical as possible. Since granite is a brittle material a large number of samples was needed for reliable results to be obtained, thus 12 particles were used for each set of experiments.

Results and discussion

Influence of impact velocity on particle size distribution

During sand manufacturing with a VSI crusher, the stone particles are accelerated by the rotor to a velocity of 50–70 m/s and are then ejected. To correspond to these conditions, the crushing experiments were conducted using four groups of granite particles with a primary particle size of about

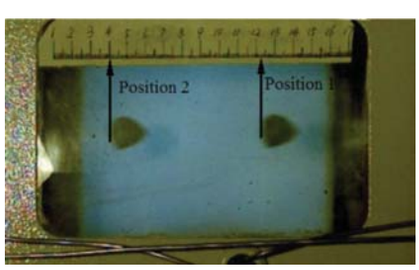

Figure 2—Photograph showing the transparent window of the crushing chamber fitted with a ruler to record the locations (two positions shown) of a particle, from which the velocity can be calculated

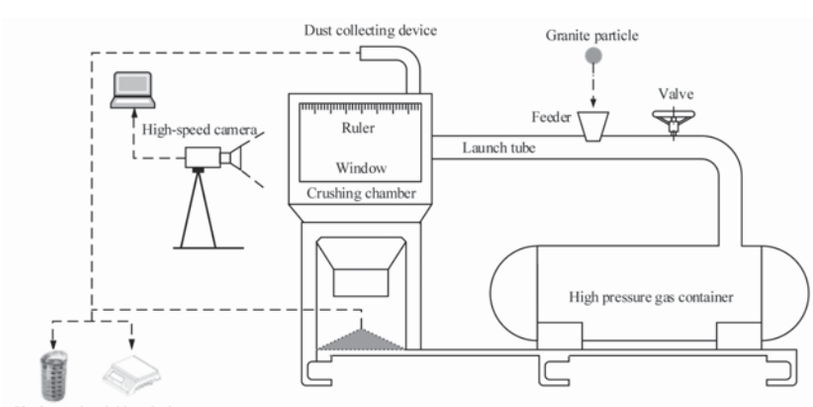

Figure 1—Schematic diagram of the custom-made stainless steel testing platform and measuring equipment used for single granite particle impact crushing experiments

15.30 mm, at velocities of 50.10 m/s, 59.43 m/s, 63.32 m/s, and 69.48 m/s. Repeatability tests were also conducted on each group to optimally control the velocity difference between each sample group. After comminution, the granite fragments of each group were collected, sieved, weighed, and the cumulative mass distributions were calculated, which are shown in Table I.

The least squares regression method was used for best-fit analysis of the particle size distributions at different impact velocities. The analysis was carried out on the cumulative mass distribution, and the results are shown in Figure 3. The distribution functions and correlation coefficients are presented in Table II. The distribution function is linear with respect to ln(d) under the experimental impact velocity. The correlation coefficients of the fitting equation are in the range 0.97–0.99, indicating that the Weibull distribution function can be used to describe the particle size distribution of the broken granite particles after impact crushing.

The relationship between the Weibull modulus n and the impact velocity is shown in Figure 4, from which it is evident that Weibull modulus initially decreases and then increases with increasing impact velocity. At an impact velocity of about 60 m/s, the discreteness of the particle size distribution reaches the maximum, suggesting that the mass distribution of progeny fragments in each size range is not uniform.

Figure 5 shows changes in the value of φ with changing impact velocity. As impact velocity increases, the value of φ increases rapidly and then tends to stabilize, demonstrating that the greatest fragmentation occurs at the highest impact velocity. As the degree of fragmentation increases, the ability of the granite particles to resist external forces gradually strengthens, and more energy is needed for further fragmentation. Thus, when the impact velocity reaches a relatively high value, about 63 m/s in this case, further increases in fragmentation decrease markedly.

Table

Cumulative mass distributions of crushed granite particles at different impact velocities

Impact velocity (m/s)	50.10	59.43	63.32	69.48
≤0.30 mm	2.15	3.40	4.39	3.11
≤0.60 mm	4.98	7.81	9.50	8.37
≤1.18 mm	9.53	14.52	16.31	16.21
≤2.36 mm	17.16	27.59	27.88	27.19
≤4.75 mm	32.97	49.44	52.65	49.94
≤9.50 mm	78.32	87.55	95.11	94.57
≤13.2 mm	100.00	100.00	100.00	100.00

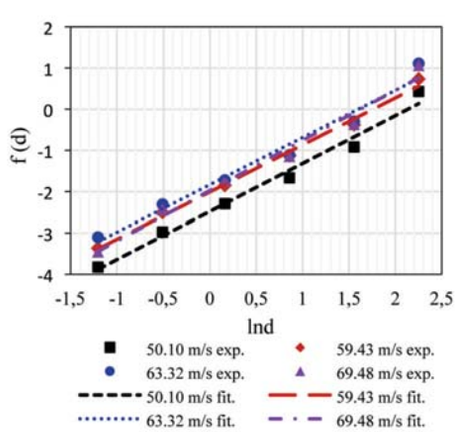

Figure 3—Particle size distributions of granite fragments at different impact velocities

Influence of primary feed size on particle size distribution

The average feed particle size of the granite used in VSI crushing is normally about 15 mm. To test the influence of feed particle size, a further four groups of spheroidal granite particles were prepared for further experimentation, with particle sizes of 12.56 mm, 14.23 mm, 16.50 mm, and 17.76 mm. The crushing experiments were conducted at impact velocities of about 60 m/s, with post-treatment of the

Table II

Fitting functions, *D* values, and correlation coefficients of particle size distributions of crushed granite particles obtained at different impact velocities

Impact velocity (m/s)	$f_{(d)}$	*D*	R^2
50.10	1.16ln(d) - 2.48	8.47	0.98
59.43	1.14ln(d) - 2.01	5.82	0.99
63.32	1.15ln(d) - 1.84	4.96	0.97
69.48	1.22ln(d) - 1.98	5.08	0.98

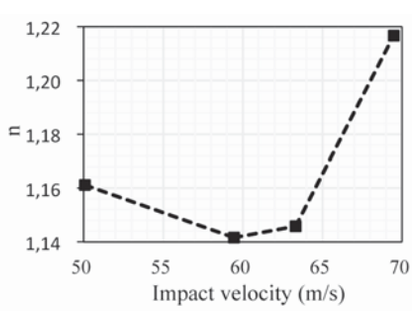

Figure 4—The Weibull modulus (n) as a function of impact velocity. Note that the maximum discreteness of the particle size distribution range occurs at a velocity of about 60 m/s

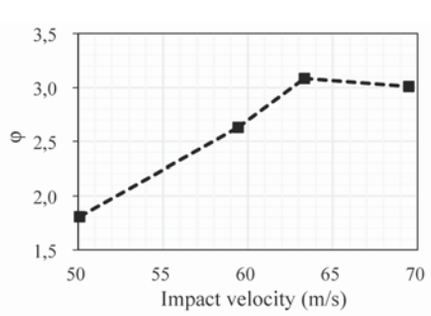

Figure 5—Changes in φ as a function of impact velocity. Note that φ stabilizes at a velocity of about 63 m/s, indicating that the tendency for further fragmentation of the granite particles beyond this velocity decreases markedly

granite fragments (collection, weighing and analysis) as before. The cumulative mass distributions of the sand products from these differently sized primary particles are shown in Table III.

As before, the least squares regression method was used for best-fit analysis of the particle size distributions based on differently sized primary particles, carried out on the cumulative mass distribution (Figure 6). The distribution function and correlation coefficients are presented in Table IV. The distribution function is again linear with respect to ln(d), with high correlation coefficients (0.98–0.99). This provides further evidence that the Weibull distribution function can be used to describe the particle size distribution of fragmented granite particles subjected to impact crushing.

Table III

Cumulative mass distributions of the crushed granite particles from differently sized primary particles

Primary particle size (mm)	12.56	14.23	16.50	17.76
≤0.30 mm	4.98	4.58	4.69	4.35
≤0.60 mm	11.41	9.65	10.27	8.75
≤1.18 mm	21.24	17.85	18.64	14.79
≤2.36 mm	41.02	30.96	33.16	23.91
≤4.75 mm	76.81	61.20	61.40	42.55
≤9.50 mm	100.00	95.38	94.02	85.54
≤13.2 mm		100.00	100.00	93.15
≤16.0 mm				100.00

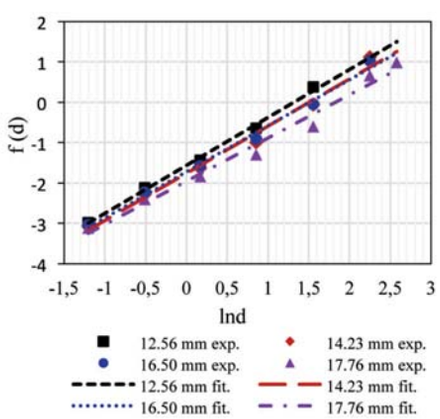

Figure 6—Particle size distributions of granite fragments obtained from differently sized primary particles crushed at 60 m/s

Table IV

Fitting functions, *D* values, and correlation coefficients of particle size distributions of crushed granite particles obtained from differently sized primary particles

Primary particle size (mm)	f (d)	D	R^2
12.56	1.19ln(d) - 1.56	3.73	0.99
14.23	1.17ln(d) - 1.76	4.50	0.99
16.50	1.14ln(d) - 1.83	5.02	0.99
17.76	1.07ln(d) - 1.95	6.20	0.98

The relationship between the Weibull modulus n and the primary particle size is shown in Figure 7, which indicates that n decreases as primary particle size increases. The discreteness of the particle size distribution of the crushed granite therefore becomes greater.

Figure 8 shows the relationship between φ and the primary particle size, and it is evident that as the primary particle size increases, the φ value decreases. This indicates that when the impact velocity is around 60 m/s, the degree of fragmentation of the granite particles decreases as the primary particle size increases. This is because granite is a brittle material with a variety of defects, including cleavage surfaces, micro-cracks, and macro-cracks. The large primary particles contain more macro-cracks. Under the instantaneous impact force, macro-crack extension occurs first, to a certain extent, and the particle is broken, which results in a decrease in particle size. However, in this process, the kinetic energy of the progeny fragments decreases rapidly and becomes insufficient for further crushing, so the particle size of the final progeny fragments is relatively large. For the small primary particle sizes, there is sufficient initial kinetic energy to overcome the resistance to micro-crack propagation and cleavage surface damage, and the degree of fragmentation is high.

Energy consumption per unit sand product

Particles no larger than 4.75 mm were isolated by sieving the fragments, and the mass percentage with respect to total fragments was calculated. The sand production ratio is shown as a function of impact velocity and particle size in Figures 9 and 10, respectively. Within the range of experimental parameters, the sand production ratio from

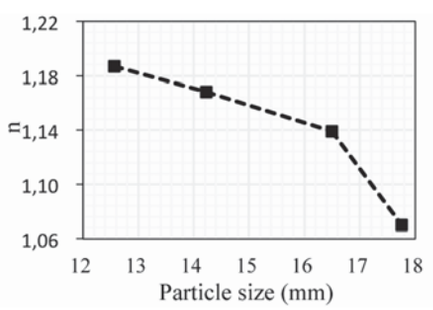

Figure 7—The Weibull modulus (n) as a function of primary particle size

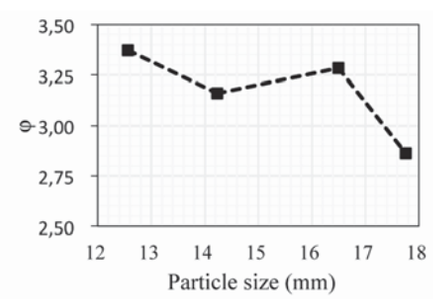

Figure 8—Changes in φ as a function of particle size

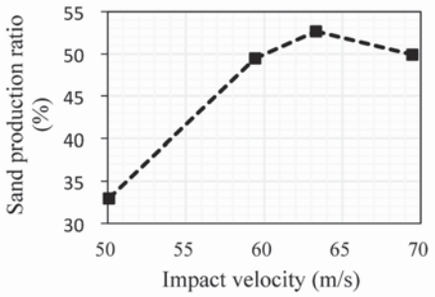

Figure 9—Sand production ratio as a function of impact velocity. Note the decrease in sand production at impact velocities greater than about 63 m/s

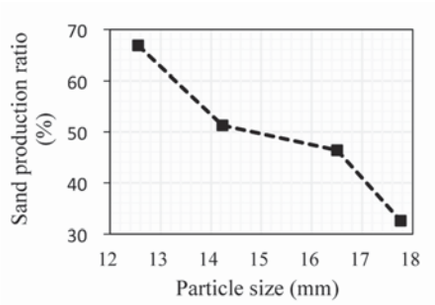

Figure 10—Sand production ratio as a function of particle size

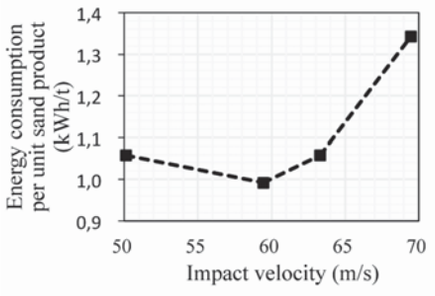

Figure 11—Energy consumption per unit sand product as a function of impact velocity. Note the significant increase in energy use at impact velocities greater than about 60 m/s

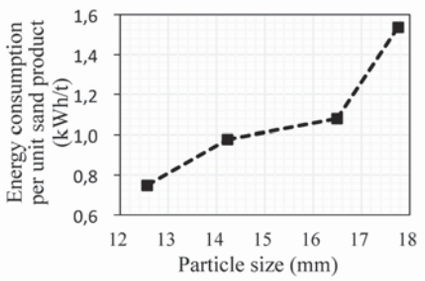

Figure 12—Energy consumption per unit sand product as a function of particle size. Note the marked increase in energy use for particle sizes larger than about 16.50 mm

granite particles by a single impact is in the 30–70% range. With increasing impact velocity, the sand production ratio first increases and then decreases. This trend is also evident with increasing particle size, as shown in Figure 10. There is an optimum impact velocity and primary particle size for obtaining the highest sand production ratio: 63 m/s and 15.30 mm, respectively. A high sand production ratio can also be obtained with the smaller primary particle sizes.

As the impact velocity increases, the initial kinetic energy of the particles increases accordingly. The effects of impact velocity and primary particle size on energy consumption per unit sand product are represented in Figures 11 and 12. The energy consumption per unit sand product for impact crushing is in the 0.70–1.60 kWh/t range, and as the impact velocity increases, the energy consumption per unit sand product first decreases, and then increases after about 60 m/s. This increase is also evident in relation to increasing particle size (Figure 12).

The minimum energy consumption per unit of finished product is at an impact velocity of about 60 m/s. It is also evident that small primary particle sizes should be selected to expend the least amount of comminution energy. However, this might be outweighed by the increased comminution energy required in the previous fragmentation stage to produce such small primary particles. Further study will be required to ascertain the balance between energy consumption in these two crushing stages.

Conclusion

In this study, we used single particle impact crushing to investigate the factors controlling rock fragmentation in VSI crushing. A high-velocity impact comminution apparatus was designed and built to dynamically fragment granite particles in order to quantify the effect of impact velocity and primary particle size with the aid of a high-speed camera.

The experimental results show that the particle size distribution of the granite fragments accords with the Weibull distribution function. The impact velocity and primary particle size have little effect on the distribution function, but are closely associated with the degree of fragmentation and the uniformity of particle size distribution. The energy consumption per unit sand product can be reduced if an appropriate impact velocity and smaller primary particle size are selected.

Recommendations

The VSI crusher is the preferred equipment for industrial production of manufactured sand. The size of the feed (primary) rock and rotational speed of the rotor are two key factors that affect the fragmentation characteristics. Based on the research findings presented in this paper, in industrial-scale VSI crushing, rocks with smaller primary particle size are recommended. The optimum rotational speed of the rotor (n_r) can be approximated by Equation [7]:

$$n_r = \frac{v_p}{r} \quad [7]$$

where v_p is the velocity of the particles ejected from the rotor, which is generally considered as the impact velocity of the particles, and r is the radius of the rotor.

Taking the minimum energy consumption per unit sand product as the major consideration, the impact velocity is set to about 60 m/s. The degree of fragmentation is moderate with this parameter. The required gradation of the manufactured sand can be achieved by further screening and recombination of the progeny fragments.

In order to verify the applicability of the research results to industrial-scale VSI crushing, some follow-up experiments should be done. For an existing VSI crusher with rotor radius of 470 mm, the recommended test parameters are shown in Table V. For all the experiments, the capacity of the VSI crusher will be set to the same value of approximately 100 t/h, and the rock used in the tests will be granite. The orthogonal experiment will be conducted, and the power consumption will be measured when the process is considered stable.

Acknowledgements

This work was financially supported by the Major Project Foundation of Science and Technology in Fujian Province (2014H6017, 2016H6013), a special project of the National and International Scientific and Technological Cooperation (2015DFA710402) and Joint Innovation Project of Industrial Technology in Fujian Province.

References

Åkesson, U. and Tjell, B. 2010. Geological parameters controlling the improvement of manufactured sand using vertical shaft impact crushers instead of cone crushers. *Proceedings of IMPC 2010: XXV International Mineral Processing Congress*, vol. 1. pp. 547–553.

Bearman, R.A., Briggs, C.A., and Kojovic, T. 1997. Applications of rock mechanics parameters to the prediction of comminution behaviour. *Minerals Engineering*, vol. 10, no. 3. pp. 255–264.

Bengtsson, M. and Evertsson, C.M. 2008. Modelling of output and power consumption in vertical shaft impact crushers. *International Journal of Mineral Processing*, vol. 88, no. 1–2. pp. 18–23.

Bengtsson, M. and Evertsson, C.M. 2006. Measuring characteristics of aggregate material from vertical shaft impact crushers. *Minerals Engineering*, vol. 19, no. 15. pp. 1479–1486.

Cai, G.P., Liu, Z.G., Xu, Q., and Yu, S.K. 2016. Experimental study on impact energy and crushing effect. *Mining Research and Development*, vol. 36, no. 1. pp. 106–110 (In Chinese).

Cleary, P.W., Sinnott, M.D., Morrison, R.D., Cummins, S., and Delaney, G.W. 2017. Analysis of cone crusher performance with changes in material properties and operating conditions using DEM. *Minerals Engineering*, vol. 100. pp. 49–70.

Delaney, G.W., Morrison, R.D., Sinnott, M.D., Cummins, S., and Cleary, P.W. 2015. DEM modelling of non-spherical particle breakage and flow in an industrial scale cone crusher. *Minerals Engineering*, vol. 74. pp. 112–122.

Deng, Y., Chen, Y., Jin, Y., and Zou, D.W. 2016. Theoretical analysis and experimental research on the energy dissipation of rock crushing based on fractal theory. *Journal of Natural Gas Science and Engineering*, vol. 33. pp. 231–239.

Table V

Test parameters for the industrial-scale VSI crusher

Rotational speed (r/min)	Primary particle size (mm)
1118	≤13
1220	≤15
1332	≤17
1423	≤19

Gopalakrishnan, K.M. and Murugesan, R. 2015. Effect of rock fractured materials replacement in concrete-its strength and durability study. *International Journal of Earth Sciences and Engineering*, vol. 8, no. 1. pp. 470–475.

Hu, Z.Z., Zhuang, Y.M., Cai, T.Y., and Chen, X.P. 2015. Experimental study on energy consumption and particle size distribution of single particle coal under impact crushing. *Journal of China Coal Society*, vol. 40. pp. 230–234 (In Chinese).

Jiang, H.X., Du C.L., and Liu S.Y. 2013. The effects of impact velocity on energy and distribution of rock crushing. *Journal of China Coal Society*, vol. 38. pp. 604–609 (In Chinese).

Johansson, R. and Evertsson, M. 2014. CFD simulation of a centrifugal air classifier used in the aggregate industry. *Minerals Engineering*, vol. 63. pp. 149–156.

Li, J.P., Zheng, K.H., and Du, C.L. 2013. The distribution discipline of impact crushed on coal and gangue. *Journal of China Coal Society*, vol. 38. pp. 54–58 (In Chinese).

Li, X.B., Zhou, Z.L., Zhao, F.J., Zuo, Y.J., Ma, C.D., Ye, Z.Y., and Hong, L. 2009. Mechanical properties of rock under coupled static-dynamic loads. *Journal of Rock Mechanics and Geotechnical Engineering*, vol. 1, no. 1. pp. 41–47.

Luo, M., Yang, J.H., and Fang, H.Y. 2014. An investigation on sand production of vertical shaft impact crusher using EDEM. *Advanced Materials Research*, vol. 1004–1005. pp. 1226–1230.

Napier-Munn, T.J., Morrell, S., Morrison, R.D., and Kojovic, T. 1996. Mineral Comminution Circuits: their Operation and Optimisation. Julius Kruttschnitt Mineral Research Centre, University of Queensland.

Narayanan, S.S. 1985. Development of a laboratory single particle breakage technique and its application to ball mill scale-up. PhD thesis, University of Queensland (JKMRC), Australia.

Nikolov, S. 2002. A performance model for impact crushers. *Minerals Engineering*, vol. 15, no. 10. pp. 715–721.

Nikolov, S. 2004. Modelling and simulation of particle breakage in impact crushers. *International Journal of Mineral Processing*, vol. 74, Supplement. pp. 219–225.

Ovalle, C., Frossard, E., Dano, C., Hu, W., Maiolino, S., and Hicher, P.Y. 2014. The effect of size on the strength of coarse rock aggregates and large rockfill samples through experimental data. *Acta Mechanica*, vol. 225, no. 8. pp. 1–18.

Paluszny, A., Tang, X.H., Nejati, M., and Zimmerman, R.W. 2015. A direct fragmentation method with Weibull function distribution of sizes based on finite- and discrete element simulations. *International Journal of Solids and Structures*, vol. 80. pp. 38–51.

Rosin, P. and Rammler, E. 1933. The laws governing the fineness of powdered coal. *Journal of the Institute of Fuel*, vol. 7. pp. 29–36.

Saeidi, F., Tavares, L.M., Yahyaei, M., and Powell, M. 2016. A phenomenological model of single particle breakage as a multi-stage process. *Minerals Engineering*, vol. 98. pp. 90–100.

Sahoo, R.K., Weedon, D.M., and Roach, D. 2004a, Single-particle breakage tests of Gladstone Port Authority's coal by a twin pendulum apparatus. *Advanced Powder Technology*, vol. 15, no. 2. pp. 263–280.

Sahoo, R.K., Weedon, D.M., and Roach, D. 2004b. Degradation model of Gladstone Port Authority's coal using a twin-pendulum apparatus. *Advanced Powder Technology*, vol. 15, no. 4. pp. 459–475.

Sanchidrián, J.A., Ouchterlony, F., Moser, P., Segarra, P., and López, L.M. 2012. Performance of some distributions to describe rock fragmentation data. *International Journal of Rock Mechanics and Mining Sciences*, vol. 53. pp. 18–31.

Sanchidrián, J.A., Ouchterlony, F., Segarra, P., and Moser, P. 2014. Size distribution functions for rock fragments. *International Journal of Rock Mechanics and Mining Sciences*, vol. 71. pp. 381–394.

Shi, F.N., Kojovic, T., Larbi-Bram, S., and Manlapig, E. 2009. Development of a rapid particle breakage characterisation device – The JKRBT. *Minerals Engineering*, vol. 22, no. 7–8. pp. 602–612.

Weedon, D.M. and Wilson, F. 2000. Modelling iron ore degradation using a twin pendulum breakage device. *International Journal of Mineral Processing*, vol. 59, no. 3. pp. 195–213.

Weibull, W. 1939. A statistical theory of the strength of materials. *Proceedings of the American Mathematical Society*, vol. 151, no. 5. pp. 1–45.

Weibull, W. 1951. A statistical distribution function of wide applicability. *Journal of Applied Mechanics*, vol.18. pp. 293–297.

Zhang, Z.X., Kou, S.Q., Jiang, L.G., and Lindqvist. P. 2000. Effects of loading rate on rock fracture: fracture characteristics and energy partitioning. *International Journal of Rock Mechanics and Mining Sciences*, vol. 37, no. 5. pp. 745–762. ◆

The Southern African Institute of Mining and Metallurgy

is proud to host the

FURNACE TAPPING 2018 CONFERENCE

14 October 2018 - Welcome Networking Cocktail & Entertainment

15–16 October 2018—Conference

17 October 2018—Technical Tours

Nombolo Mdhluli Conference Centre
Kruger National Park
South Africa

BACKGROUND

A controlled tapping process is essential for all pyrometallurgical smelting furnaces. Draining of metal and slag in a controlled fashion is as important as maintaining a closed tap-hole when required. From a furnace containment perspective, the tap-hole area is one of the high wear, and therefore high risk. Tap-hole failures can have devastating impacts on smelters. Risk mitigation steps therefore addresses safety and health of operators, consequential property damages, and loss of production (business interruptions). Tap-hole life-cycle design and management require development of high quality materials, equipment, and methods that not only take criteria for normal operating conditions into account, but also those of maintenance, repairs, and relines.

Furnace Tapping 2014 was a first of its kind event. The event focused on the challenges associated with furnace tap-hole life-cycle design and management, and on finding ways to address these challenges, for which no miracle one-size-fits-all solution exists. South Africa, which produced 18 commodities at more than 75 sites applying smelter technology, was an ideal breeding ground for such an event. Although it had a strong local focus, people from other parts of the world also gathered to share creative solutions to problems many had in common.

The SAIMM takes pride in announcing a follow-up conference, Furnace Tapping 2018, which will again be hosted in South Africa, in October 2018. The high standard of technical papers compiled in the peer-reviewed proceedings of Furnace Tapping 2014 will be maintained. The SAIMM envisage for Furnace Tapping 2018 further documentation of tapping practices by existing operators, more reviews of current operations, and descriptive case studies in which technologies available for tap-hole design, monitoring, closure, and maintenance were applied. Of special interests are feedback on research conducted in the field, and the impact of safety, health and environmental regulations from various parts of the world, on tap-hole life-cycle design and management.

Looking forward to meeting you at Furnace Tapping 2018!

OBJECTIVES

To provide an international forum for transfer of new knowledge on the design, maintenance, and operating practices surrounding the tapping of pyrometallurgical smelters, and to discuss methods and results of research conducted in the field.

KEYNOTE

Prof. P.C. Pistorius
(Carnegie Mellon University)

J.J. Sutherland
(Transalloys)

Dr. M.W. Kennedy
(Proval Partners)

Prof. J.P. Beukes
(North-West University)

Photographer ©Joalet Steenkamp

It doesn't interest me who you know or how you came to be here. I want to know if you will stand in the centre of the fire with me and not shrink back.
(from the poem, The Invitation, by Oriah Mountain Dreamer)

WHO SHOULD ATTEND

The conference is aimed at delegates from the pyrometallurgical industry operating smelters or those who support them, and includes:

- First line, middle, and senior management
- Plant/production engineers
- Process/development engineers
- Refractory engineers
- Design engineers
- Maintenance engineers
- Safety practitioners
- Researchers in the field

SAIMM
THE SOUTHERN AFRICAN INSTITUTE OF MINING AND METALLURGY

FOR FURTHER INFORMATION CONTACT:

Camielah Jardine, Head of Conferencing, Saimm
P O Box 61127, Marshalltown 2107, Tel: +27 (0) 11 834-1273/7
E-mail: camielah@saimm.co.za, Website: http://www.saimm.co.za

Sponsors

DANGO & DIENENTHAL (SOUTHERN AFRICA) (PTY) (LTD)

TMT Tapping - Measuring - Technology

MINTEK

EVOLVING YOUR TAPPING PROCESS
TREFIMET

Conference Announcement

NATIONAL & INTERNATIONAL ACTIVITIES

2018

6–7 June 2018 — Digitalization in Mining Conference
'Mining business make-over –Exploiting the digital resolution'
Focus Rooms, The Core, Sunninghill, Sandton
Contact: Yolanda Ndimande
Tel: +27 11 834-1273/7, Fax: +27 11 838-5923/833-8156
E-mail: yolanda@saimm.co.za, Website: http://www.saimm.co.za

11–14 June 2018 — SAIMM: Diamonds — Source to Use 2018 Conference
'Thriving in Changing Times'
Birchwood Hotel and OR Tambo Conference Centre, JetPark, Johannesburg
Contact: Camielah Jardine
Tel: +27 11 834-1273/7, Fax: +27 11 838-5923/833-8156
E-mail: camielah@saimm.co.za, Website: http://www.saimm.co.za

27 June 2018 — Global Mining Standards and Guidelines Group
'Interoperability and Underground Communications Infrastructure'
Mandela Mining Precinct, Cnr Rustenburg & Carlow Roads, Melville, Johannesburg
Contact: Yolanda Ndimande
Tel: +27 11 834-1273/7, Fax: +27 11 838-5923/833-8156
E-mail: yolanda@saimm.co.za, Website: http://www.saimm.co.za

9–12 July 2018 — Copper Cobalt Africa in association with The 9th Southern African Base Metals Conference
Avani Victoria Falls Resort, Livingstone, Zambia
Contact: Camielah Jardine
Tel: +27 11 834-1273/7, Fax: +27 11 838-5923/833-8156
E-mail: camielah@saimm.co.za, Website: http://www.saimm.co.za

30–31 July 2018 — Introduction to Process Engineering School 2018 Volume 1
Birchwood Hotel and OR Tambo Conference Centre, JetPark, Johannesburg
Contact: Yolanda Ndimande
Tel: +27 11 834-1273/7, Fax: +27 11 838-5923/833-8156
E-mail: yolanda@saimm.co.za, Website: http://www.saimm.co.za

6–8 August 2018—Geometallurgy Conference 2018 *'Back to the Future'*
Lagoon Beach Conference Venue, Cape Town
Contact: Camielah Jardine
Tel: +27 11 834-1273/7, Fax: +27 11 838-5923/833-8156
E-mail: camielah@saimm.co.za, Website: http://www.saimm.co.za

15–16 August 2018 — The SAMREC and SAMVAL CODES
'Advanced Workshop: Can you face your peers?'
The Wits Club, University of the Witwatersrand, Johannesburg
Contact: Yolanda Ndimande
Tel: +27 11 834-1273/7, Fax: +27 11 838-5923/833-8156
E-mail: yolanda@saimm.co.za, Website: http://www.saimm.co.za

29–31 August 2018 — MineSafe 2018 Technical Conference and Industry day
Gallagher Convention Centre, Johannesburg
Contact: Camielah Jardine
Tel: +27 11 834-1273/7, Fax: +27 11 838-5923/833-8156
E-mail: camielah@saimm.co.za, Website: http://www.saimm.co.za

4 September 2018 — Micro TBM Tunnelling Seminar 2018
'Come to the fore in South Africa'
The Wits Club, University of the Witwatersrand, Johannesburg
Contact: Yolanda Ndimande
Tel: +27 11 834-1273/7, Fax: +27 11 838-5923/833-8156
E-mail: yolanda@saimm.co.za, Website: http://www.saimm.co.za

10–11 September 2018 — ASM Conference 2018
'Fostering a regional approach to ASM transformation in sub-Saharan Africa'
Nasrec, Johannesburg (Electra Mining)
Contact: Yolanda Ndimande
Tel: +27 11 834-1273/7, Fax: +27 11 838-5923/833-8156
E-mail: yolanda@saimm.co.za, Website: http://www.saimm.co.za

18–19 September 2018 — 4th Young Professionals Conference
'Creating a sustainable African minerals industry through applied innovation'
Focus Rooms, The Core, Sunninghill, Sandton
Contact: Camielah Jardine
Tel: +27 11 834-1273/7, Fax: +27 11 838-5923/833-8156
E-mail: camielah@saimm.co.za, Website: http://www.saimm.co.za

14–17 October 2018 — Furnace Tapping 2018 Conference
Nombolo Mdhluli Conference Centre, Kruger National Park, South Africa
Contact: Camielah Jardine
Tel: +27 11 834-1273/7, Fax: +27 11 838-5923/833-8156
E-mail: camielah@saimm.co.za, Website: http://www.saimm.co.za

24 October 2018 — 15th Annual Student Colloquium
'Mining and metallurgy in a sustainable world'
Johannesburg
Contact: Yolanda Ndimande
Tel: +27 11 834-1273/7, Fax: +27 11 838-5923/833-8156
E-mail: yolanda@saimm.co.za, Website: http://www.saimm.co.za

25–26 October 2018 — Higher Education Development in the Extractive Industry Workshop 2018
Glenhove Conference Centre, Melrose Estate, Johannesburg
Contact: Yolanda Ndimande
Tel: +27 11 834-1273/7, Fax: +27 11 838-5923/833-8156
E-mail: yolanda@saimm.co.za, Website: http://www.saimm.co.za

2019

24–25 June 2019— Ninth International Conference on Deep and High Stress Mining 2019 Conference
Misty Hills Conference Centre, Muldersdrift, Johannesburg
Contact: Camielah Jardine
Tel: +27 11 834-1273/7, Fax: +27 11 838-5923/833-8156
E-mail: camielah@saimm.co.za, Website: http://www.saimm.co.za

13–15 November 2019 — XIX International Coal Preparation Congress & Expo 2019
New Delhi, India
Contact: Coal Preparation Society of India
Tel/Fax: +91-11-26136416, 4166 1820
E-mail: cpsidelhi. india@gmail.com, president@cpsi.org. inrksachdevO 1 @gmail.com, hi. sapru@monnetgroup.com

Company Affiliates

The following organizations have been admitted to the Institute as Company Affiliates

3M South Africa (Pty) Limited
AECOM SA (Pty) Ltd
AEL Mining Services Limited
Air Liquide (Pty) Ltd
AIRT Sheet Metal
Alexander Proudfoot Africa (Pty) Ltd
AMEC Foster Wheeler
AMIRA International Africa (Pty) Ltd
ANDRITZ Delkor(Pty) Ltd
Anglo Operations Proprietary Limited
Anglogold Ashanti Ltd
Arcus Gibb (Pty) Ltd
Atlas Copco Holdings South Africa (Pty) Limited
Aurecon South Africa (Pty) Ltd
Aveng Engineering
Aveng Mining Shafts and Underground
Axis House Pty Ltd
Bafokeng Rasimone Platinum Mine
Barloworld Equipment -Mining
BASF Holdings SA (Pty) Ltd
BCL Limited
Becker Mining (Pty) Ltd
BedRock Mining Support Pty Ltd
BHP Billiton Energy Coal SA Ltd
Blue Cube Systems (Pty) Ltd
Bluhm Burton Engineering Pty Ltd
Bouygues Travaux Publics
CDM Group
CGG Services SA
Minerals Council South Africa
Coalmin Process Technologies CC
Concor Opencast Mining
Concor Technicrete
Council for Geoscience Library
CRONIMET Mining Processing SA Pty Ltd
CSIR Natural Resources and the Environment (NRE)
Data Mine SA
Department of Water Affairs and Forestry
Digby Wells and Associates
DMS Powders
DRA Mineral Projects (Pty) Ltd
Duraset
Elbroc Mining Products (Pty) Ltd
eThekwini Municipality
Expectra 2004 (Pty) Ltd
Exxaro Coal (Pty) Ltd
Exxaro Resources Limited
Filtaquip (Pty) Ltd
FLSmidth Minerals (Pty) Ltd
Fluor Daniel SA (Pty) Ltd
Franki Africa (Pty) Ltd-JHB
Fraser Alexander (Pty) Ltd
G H H Mining Machines (Pty) Ltd
Geobrugg Southern Africa (Pty) Ltd
Glencore
Hall Core Drilling (Pty) Ltd
Hatch (Pty) Ltd
Herrenknecht AG
HPE Hydro Power Equipment (Pty) Ltd
IMS Engineering (Pty) Ltd
Ivanhoe Mines SA
Joy Global Inc.(Africa)
Kudumane Manganese Resources
Leco Africa (Pty) Limited
Longyear South Africa (Pty) Ltd
Lonmin Plc
Lull Storm Trading (Pty) Ltd
Magnetech (Pty) Ltd
Magotteaux (Pty) Ltd
MBE Minerals SA Pty Ltd
MCC Contracts (Pty) Ltd
MD Mineral Technologies SA (Pty) Ltd
MDM Technical Africa (Pty) Ltd
Metalock Engineering RSA (Pty)Ltd
Metorex Limited
Metso Minerals (South Africa) Pty Ltd
Minerals Operations Executive (Pty) Ltd
MineRP Holding (Pty) Ltd
Mintek
MIP Process Technologies (Pty) Limited
Modular Mining Systems Africa (Pty) Ltd
MSA Group (Pty) Ltd
Multotec (Pty) Ltd
Murray and Roberts Cementation
Nalco Africa (Pty) Ltd
Namakwa Sands(Pty) Ltd
Ncamiso Trading (Pty) Ltd
New Concept Mining (Pty) Limited
Northam Platinum Ltd - Zondereinde
PANalytical (Pty) Ltd
Paterson & Cooke Consulting Engineers (Pty) Ltd
Perkinelmer
Polysius A Division Of Thyssenkrupp Industrial Sol
Precious Metals Refiners
Rand Refinery Limited
Redpath Mining (South Africa) (Pty) Ltd
Rocbolt Technologies
Rosond (Pty) Ltd
Royal Bafokeng Platinum
Roytec Global (Pty) Ltd
RungePincockMinarco Limited
Rustenburg Platinum Mines Limited
Salene Mining (Pty) Ltd
Sandvik Mining and Construction Delmas (Pty) Ltd
Sandvik Mining and Construction RSA(Pty) Ltd
SANIRE
Sebilo Resources (Pty) Ltd
SENET (Pty) Ltd
Senmin International (Pty) Ltd
Smec South Africa
Sound Mining Solution (Pty) Ltd
SRK Consulting SA (Pty) Ltd
Technology Innovation Agency
Time Mining and Processing (Pty) Ltd
Timrite Pty Ltd
Tomra (Pty) Ltd
Ukwazi Mining Solutions (Pty) Ltd
Umgeni Water
Webber Wentzel
Weir Minerals Africa
Worley Parsons RSA (Pty) Ltd

MINESAFE 2018

Striving for Zero Harm

Driving Excellence through Compliance

Gallagher Convention Centre,
Johannesburg

Technical Conference and Industry day

29–30 August 2018—Conference
31 August 2018—Industry Awards Day

WHO SHOULD ATTEND

The conference should be of value to:

- Safety practitioners
- Mine management
- Mine health and safety officials
- Engineering managers
- Underground production supervisors
- Surface production supervisors
- Environmental scientists
- Minimizing of waste
- Operations manager
- Processing manager
- Contractors (mining)
- Including mining consultants, suppliers and manufacturers
- Education and training
- Energy solving projects
- Water solving projects
- Unions
- Academics and students
- DMR.

OBJECTIVES

The conference will focus on improving health, safety and the environmental impact in the mining and metallurgy industry and highlight actions to be taken. It will act as a platform for learning and allow people to share ideas on safety, health and the environment as well as local communities relationship (issues).

This conference aims to bring together management, DMR, Chamber of Mines, Unions and health and safety practitioners at all levels from the industry to share best practice and successful strategies for zero harm and a value-based approach to health and safety. It will address the main challenges in the mining industry such as logistics, energy and safety of employees, contractors and the communities.

SPONSORSHIP

Sponsorship opportunities are available. Companies wishing to sponsor or exhibit should contact the Conference Co-ordinator.

SAIMM
THE SOUTHERN AFRICAN INSTITUTE OF MINING AND METALLURGY

ASSOCIATION of MINE MANAGERS of SOUTH AFRICA

MMMA

THE S.A. COLLIERY MANAGERS' ASSOCIATION

SUPPORTED BY:

CHAMBER OF MINES of South Africa

Mine Health & Safety Council
MHSC

mineral resources
Department:
Mineral Resources
REPUBLIC OF SOUTH AFRICA

NUM
National Union of Mine Workers

UASA
THE UNION

AMCU

SOLIDARITEIT
SOLIDARITY

For further information contact:
Head of Conferencing
Camielah Jardine, SAIMM,
Tel: +27 11 834-1273/7
Fax: +27 11 833-8156 or +27 11 838-5923
E-mail: camielah@saimm.co.za
Website: http://www.saimm.co.za

Conference Announcement

BM
BASE METALS
2018

Copper Cobalt Africa

In Association with

The 9TH Southern African Base Metals Conference

9–12 July 2018

Avani Victoria Falls Resort, Livingstone, Zambia

SAIMM is proud to host the Second Copper Cobalt Africa Conference in the heart of Africa

To be held in Livingstone, Zambia, this anticipated and prestigious event provides a unique forum for discussion, sharing of experience and knowledge, and networking for all those interested in the processing of copper and cobalt in an African context, in one of the world's most spectacular settings - the Victoria Falls.

The African Copper Belt is again experiencing a resurgence of activity following the commodity downturn of recent years. A significant proportion of capital spending, project development, operational expansions, and metal value production in the Southern African mining industry take place in this region. The geology and mineralogy of the ores are significantly different to those in other major copper-producing regions of the world, often having very high grades as well as the presence of cobalt. Both mining and metallurgy present some unique challenges, not only in the technical arena, but also with respect to logistics and supply chain, human capital, community engagement, and legislative issues. This conference provides a platform for discussion of a range of topics, spanning the value chain from exploration, projects, through mining and processing, to recycling and secondary value addition.

For international participants, this conference offers an ideal opportunity to gain in-depth knowledge of and exposure to the African copper and cobalt industries, and to better understand the various facets of mining and processing in this part of the world.

Jointly hosted by the Mining and Metallurgy Technical Programme Committees of the Southern African Institute of Mining and Metallurgy (SAIMM), this conference aims to:

- Promote dialogue between the mining and metallurgical disciplines on common challenges facing the industry
- Enhance understanding of new and existing technologies that can lead to safe and optimal resource utilization
- Encourage participation and build capacity amongst young and emerging professionals from the Copper Belt region.

The organizing committee looks forward to your participation.

Conference Topics

- Mineralogy
- Exploration and new projects
- Open-cast mining
- Underground mining
- Rock engineering
- Mine planning
- Mineral resource management
- Geometallurgy
- Minerals processing
- Pyrometallurgy
- Hydrometallurgy
- Current operational practices and improvements
- Project development and execution
- Novel technologies for this industry
- Socio-economic challenges
- Recycling
- Waste treatment and minimization
- Environmental issues

Sponsors

AARD, ALS Minerals, AXISHOUSE, BASF We create chemistry, CiDRA Minerals Processing, CM solutions Metallurgical consultancy & Laboratories, DERRICK Authorized Distributor, Elkem Carbon, FLSmidth, GE, IMP Innovative Solutions, MASIMO Chemical Logistics, MASIMO Chemicals South Africa, Murray & Roberts, Murray & Roberts Cementation, Outotec, ProProcess, SCANTECH Process control specialists, SOLVAY asking more from chemistry, srk, ZEISS, SIBELCO

Media Sponsor MEI

To add your name to the mailing list and to receive further information, please e-mail your contact details to: Camielah Jardine: Head of Conferencing
SAIMM, P O Box 61127, Marshalltown 2107, Tel: +27 (0) 11 834-1273/7
E-mail: camielah@saimm.co.za, Website: http://www.saimm.co.za

SAIMM
THE SOUTHERN AFRICAN INSTITUTE OF MINING AND METALLURGY